Magnetic resonance of nuclear and electronic spins in molecules and semiconductors for quantum information processing

Mikhail V. Vaganov

New College

University of Oxford

A thesis submitted for the degree of

Doctor of Philosophy

Trinity 2025

Abstract

This thesis details three studies performed with the aim of deepening our understanding of how nuclear and electronic spins can be manipulated such that they might be used in quantum information processing.

I start by discussing the possibility of using pulses of static electric fields to coherently control qudits implemented on molecular magnets. The success of this control depends on the level of spin-electric coupling (SEC) which reflects how the respective Hamiltonian changes with the application of an electric field. I present our research on a family of Mn(II)-containing molecules in which the systematic control of SEC is realised by varying the coordination environment of their spin centre. Their trigonal bipyramidal molecular structure with C_3 symmetry leads to a significant molecular electric dipole moment. Due to this, as well as high polarisability of the ligands, an applied electric field induces enhanced structural distortions. This gives rise to significant experimentally observed SEC, which is further rationalised by wavefunction theoretical calculations.

I then discuss the SEC in a molecular magnet [Yb (trensal)], which similarly possesses C_3 symmetry, but instead of manganese, this molecule contains a rare-earth ion of ytterbium (III). At cryogenic temperatures, [Yb (trensal)] can be described by an effective spin-1/2 Hamiltonian. However, our study shows that the significant values of SEC exhibited by [Yb (trensal)] can be only explained if the Hamiltonian is additionally equipped with the extended Stevens operators. The unique property of [Yb (trensal)] is that it demonstrates linear SEC even when the E-field is oriented perpendicularly to the C_3-axis of the molecule, and that this perpendicular SEC is of the same order of magnitude as the parallel effect.

In the third study, I show how, by using electron-nuclear double resonance, we implement a logical qubit encoded on four states of an $I = 3/2$ nuclear spin hyperfine-coupled to an $S = 1/2$ electron spin qubit. The encoding protects against the dominant decoherence mechanism in such systems – fluctuations of the quantizing magnetic field. We explore the dynamics of the encoded state both under a controlled application of the fluctuation and under natural decoherence processes. Our results confirm the potential of these proposals for practical, implementable, fault-tolerant quantum memories.

Acknowledgements

First and foremost, thank you, dear reader, for taking the time to engage with the experiments, formulas, and findings laid out in this thesis, and for stepping, even briefly, into the world I have been immersed in for the past five years. Whether you read this out of interest, duty, or pure happenstance, I am deeply grateful for your time and attention.

There are a great many people who have helped and supported me throughout my DPhil journey.

I would like to express my gratitude to my supervisor, Prof Arzhang Ardavan, for giving me the opportunity to work in this exciting area of research, and for his insight, enthusiasm, and optimism, which encouraged me to think more positively myself. I am especially thankful to Dr Junjie Liu for his patient guidance, expertise, and constant support in nearly every aspect of my DPhil. It would be no exaggeration to say that Junjie is the person who truly taught me the art of experimental physics.

Special thanks also go to my former supervisor and mentor at the Institute of Continuous Media Mechanics, Prof Yuriy Raikher, who first introduced me to the world of science and gave me the vital initial impetus for my academic career.

I am grateful to Dr Gabriel Moise for acquainting me with the CAESR facility, its spectrometers, wet chemistry laboratory, and cryogenics. I thank Dr Sumin Lim for helping me to grasp the intricate connections between magnetic resonance techniques and quantum computing. I thank Niccolo Fontana for helping me prepare the probes for the SEC measurements, and for being a great DPhil colleague throughout. I would also like to acknowledge Dr William Myers for helping me tame the Bruker spectrometers in CAESR.

This work would not have been possible without the help and support of my colleagues and collaborators. I am thankful to Prof Stergios Piligkos and his group for synthesising the crystals of [Yb (trensal)], and to Prof Talal Mallah and his group for preparing the bi-pyramidal manganese complexes, and for allowing me to study them with ESR. It cannot be understated how important it was for us to have plenty of liquid helium, and in this regard, I owe a huge thank you to Rob Storey and Kieran McCall for ensuring the smooth supply of the LHe dewars.

Next, I have been fortunate to acquire new good friends in Oxford: Tianyi, Soyoung, Alyona, Hank, Igor, James, Max – thank you all for the dinners, the

Figure 1: New College. Hall, Chapel, Tower, and Library as seen from the Holywell quadrangle. Thank you to New College staff, MCR, and SCR for the great time at Oxford.

endless tea and chocolate, and for taking me for walks – all this kept me sane! I owe special thanks to Max, Hank, and Bang for kindly proofreading this thesis. Max especially, for he undertook the Herculean task of being the first person to read my entire thesis and helping me navigate the intricacies of English grammar, punctuation, and syntax. For this, he has my deepest and warmest gratitude.

I would like to express my profound appreciation to my family – my mom, dad, sister, and her family – for their unwavering love and support throughout my whole life, study, and career in Perm, Dresden, and Oxford. You are always in my heart.

Finally, I would like to graciously acknowledge the generous financial support of the Hill Foundation, which funded me throughout my DPhil.

It has been quite a long, yet exciting journey.

Thank you all sincerely!

Contents

List of Abbreviations

1D, 2D . . . . One- or two-dimensional, referring in this thesis to spatial dimensions in an image.

AC . . . . . Alternating current.

AWG . . . . . Arbitrary waveform generator.

CW . . . . . Continuous-wave.

DC . . . . . Direct current.

DFT . . . . . Density functional theory.

EDFS . . . . . Echo-detected field sweep.

ENDOR . . . Electron-nuclear double resonance.

E-field . . . . . Electric field.

EM . . . . . Electromagnetic.

ENCT . . . . . Electron-nuclear coherence transfer.

EPR . . . . . Electron paramagnetic resonance.

ESE . . . . . Electron spin echo.

ESO . . . . . Extended Stevens operators.

ESR . . . . . Electron spin resonance.

HF . . . . . Hyperfine term/splitting/constant.

MW . . . . . Anything related to microwaves.

NMR . . . . . Nuclear magnetic resonance.

PCB . . . . . The base of a printed circuit board. It is typically used to describe the PCB plates in the E-field experiment.

PSD . . . . . Phase-sensitive detection.

RF . . . . . Anything related to radiowaves.

SEC . . . . . Spin-electric coupling.

SNR . . . . . Signal-to-noise ratio.

ZFS . . . . . Zero field splitting – refers to one of the terms in the Hamiltonian, normally associated with the representation in terms of the ESO.

Chapter 1
Introduction

In 1998, Isaac Chuang, Neil Gershenfeld, and Mark Kubinec demonstrated the process of quantum computation on a 2-qubit quantum computer based on nuclear magnetic resonance (NMR) technology [1]. 25 years later, in October 2023, Atom Computing announced the release of its quantum processor with 1180 qubits created on an array of neutral atoms [2]. Then, in December 2023, IBM introduced its Condor quantum processor built on 1121 superconducting qubits [3]. The number of qubits in quantum computers has been increasing steadily since 1998, and between 2016 and 2023 it underwent almost exponential growth depicted in Figure 1.1.

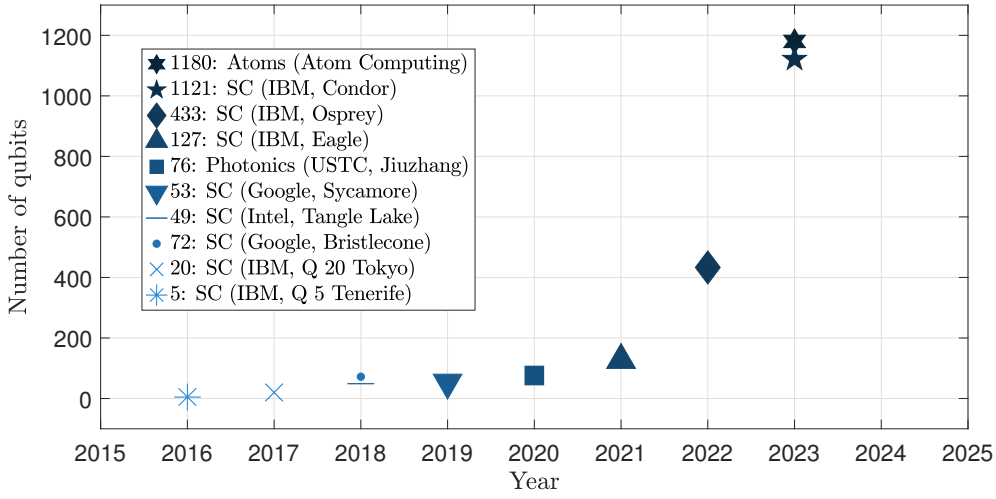

Figure 1.1: Number of qubits in quantum processors based on logic gates since 1998 [4].

Naturally, the quantum processors graphed in Figure 1.1 differ in their architecture and production technology, but the number of qubits they possess can roughly reflect the rate at which quantum technologies advance. While in quantum information theory, a qubit is a generalised term which stands for an elementary unit of quantum information, the physical implementation of qubits takes different forms. Some possible implementations might include optical photons [5–8], trapped ions and neutral atoms [9–12], nuclear and electron spins [13–18], quantum dots [19], nitrogen-vacancy centres in diamonds [20–22], various superconducting devices based on a Josephson junction [23], gapped topological systems [24, 25]. Each of these implementations has both advantages and inherent limitations, but they are all fascinating from a physics perspective [26–28]. The present thesis focuses on electron and nuclear spins in molecular magnets and in paramagnetic impurities of diamagnetic crystals.

1.1 Spins as qubits

Molecular magnets are molecules that carry a non-zero magnetic moment [29–34]. They typically consist of a paramagnetic centre surrounded by organic or inorganic ligands, but their precise chemical structure can be rationally tailored for the purpose of a particular task. Electronic and nuclear spins of molecular magnets are natural and ready-to-use candidates for the role of qubits [35, 36]. While a qubit is a two-state quantum-mechanical system which can be realised with a spin-1/2 particle such as a single electron or nucleus, molecular magnets with several unpaired electrons or a nucleus with spin greater than 1/2 possess more quantum states than is required for one qubit. In quantum information, an entity offering a d-dimensional Hilbert space is known as a qu**d**it (with $d = 2$ for a qu**b**it). The additional levels of a qudit can be used to directly encode several logical qubits or, alternatively, they can be used in less intuitive and more exciting ways such as quantum error correction (QEC), for instance [37]. In addition to molecular magnets, we can also employ single-ion paramagnetic impurities found in diamagnetic crystals as a source of electronic and nuclear spins.

The theory of quantum information assumes that it is possible to initialise qubits, entangle them, manipulate their states via a set of logical gates, and read-out their values when the computation is complete. Together with additional requirements for scalability and long coherence times, those assumptions constitute a set of necessary conditions formulated by David DiVincenzo [38] for designing a quantum computer. Electronic spins in condensed matter, with their well-defined quantum properties and long quantum coherence times [33, 34, 39–43], are natural candidates for embodying quantum information; their hyperfine-coupled nuclear spins, which tend to be even more coherent, offer potential as quantum memory elements. Indeed, such systems featured among the earliest theoretical condensed matter quantum information proposals such as that of Bruce Kane [44]. There are several challenges on the way to achieving DiVincenzo's criteria. This thesis addresses two of them: the fully electric control of qubits and quantum error-correction.

1.2 Research questions addressed in this thesis

Due to the natural coupling between the magnetic moment associated with the spin and an external magnetic field, the magnetic resonance technique is the tool of choice for manipulating spin-based qubits [45]. Today, there is a broad consensus in the literature [13] that NMR in principle provides a universal set of Hamiltonians which can be used to implement any desired unitary evolution, including quantum logic gates – the building blocks of quantum computing [26, 27]. The underlying physics of nuclear and electronic spins is very similar, so that magnetic resonance of electrons – electron spin resonance (ESR)[1] – should also possess this quality.

1.2.1 Electric control

Both NMR and ESR stipulate that in order to control a single qubit implemented by a molecular magnet, one needs to apply both static and oscillating magnetic fields at the scale of a single molecule. While not impossible [46], this imposes a significant engineering challenge because a divergence-less magnetic field is not

[1] Also known as electron paramagnetic resonance, EPR.

easy to confine. In contrast, an electric field (E-field) can be more easily routed, confined, and screened at a nanoscale which has been successfully proven by modern semiconductor electronics. Therefore, the possibility of electric spin control offers significant architectural advantages for classical or quantum spintronics: it can reduce energy consumption and facilitate logic operations on spins [47–50].

A candidate for the all-electric control would be a molecular compound whose spin Hamiltonian can be controlled via an electric field [43, 51–54]. The E-field itself can be easily generated between compact and oppositely charged electrodes [44]. The control is possible when there is a strong coupling between the spin system and an E-field via spin-orbit interaction or via crystal (ligand) field – we call it spin-electric coupling, or SEC for short. If the state of the system is affected by the electric field in any way, the change will be reflected in the system's Hamiltonian, and is, consequently, rendered into the variation in the ESR frequency [53, 55]. The possibility to change the resonance frequency of a chosen sample paves the way for the selective control of qubits implemented on spin-bearing molecules [56]. It has also been demonstrated that both coherent control and projective spin measurements may be achieved using the same set of electrodes [14, 57, 58].

In this thesis, I present our investigation into the SEC of two types of molecular magnets, one of which contains a transition metal ion of manganese (see Chapter 4) and another which has a rare earth ion of ytterbium (see Chapter 5). Both molecules were engineered to create molecular magnets with spin transitions that are both in an accessible energy range and sensitive to electric fields. In the manganese molecules, we demonstrate how we can control the SEC by changing a single atom. In the ytterbium molecules, we observed an unexpected SEC, different from those reported previously.

1.2.2 Quantum error correction

There is broad agreement that progress in quantum information technology is currently going through the era of noisy intermediate-scale quantum (NISQ) devices – the term coined by John Preskill [59]. Although the control fidelity in few-qubit

systems has reached two or three nines [60–63] and certain studies [64, 65] propose that quantum supremacy may be achievable even with NISQ devices, we are currently limited to certain specific computations on the scale of tens of qubits and maintaining the same level of precision becomes increasingly difficult as the size of the system is scaled up [59, 66]. The increase in the physical size of the system decreases the coupling between spatially separated qubits and increases the effect of noise. Noise in this context stems from all sorts of unwanted inter-qubit interactions and their coupling to the environment. Further progress on the way to a universal quantum computer will depend on the development of reliable mechanisms which are able to tackle this noise and associated computational errors.

Quantum error correction (QEC) protocols seek to address these challenges by enlarging the Hilbert space to store information with redundancy [67, 68]. Many current proposals are based on the idea of using multiple physical qubits to encode an individual logical qubit [69–72], yielding qubit-based error correction algorithms such as surface codes [73, 74]. The straightforward implementation of these proposals, which implies introducing more noisy qubits into the system, undermines itself by increasing the distance between the qubits, decreasing the signal to noise ratio, and therefore worsening the very issue it is supposed to solve.

An alternative paradigm deploys qu**d**its instead of qu**b**its. This approach reduces the overhead associated with additional qubits and can provide a hardware-efficient structure. Originally proposed by Gottesman, Kitaev, and Preskill [75], a range of theoretical [76–79] and experimental [80–85] explorations are ongoing into systems based on quantum harmonic oscillators with bosonic eigenstates. This kind of approach provides infinite dimensions in a spatially compact system, but at the cost of complexity in practical operations.

In this context, qudits realised by spins greater than 1/2 offer a promising alternative: a single physical object providing a multidimensional but finite and often well-isolated Hilbert space. These can be, for instance, electronic and nuclear spins in the solid state or molecular magnets. The hyperfine interaction between the electron and nuclear manifolds would work as an interface between these two

levels. A particularly simple error correcting protocol can be implemented on just one unpaired electron and four nuclear levels of a pertinent atom or ion [86]; that is, one electron qubit and one nuclear qudit. It is worth noting that a candidate system may have more than one unpaired electron and more available nuclear levels, but those can be used for something else – for storing another logical qubit, for instance.

The possibility of implementing an error-correction protocol on the electron-nuclear qudit of manganese impurities in zinc oxide is discussed in Chapter 6.

1.3 Bigger goal

The development of a quantum computer should not be seen as the only and final goal of research in quantum information. The physical implementation of qubits and their properties anticipated by the theory will lead to a better understanding of the physics of the quantum world, whereas calculations run on quantum computers will create unprecedented possibilities of simulating quantum systems which are practically unreachable on classical computers. Existing quantum systems have already demonstrated the possibility of the latter. For example, a programmable quantum simulator based on arrays of Rydberg atoms has recently been used for probing novel quantum spin liquid states [87], and a discrete time crystal was created and observed on 20 superconducting qubits of the Google Sycamore quantum processor [88].

This thesis represents my humble contribution to this bigger goal.

1.4 Structure of the thesis

The thesis consists of the introduction, five main chapters and the appendix.

Chapter 2 contains some of the mathematical foundation of quantum physics necessary for the discussion of consecutive chapters.

Chapter 3 describes our main experimental set-up. I started my DPhil in 2020 and spent the first year and a half by hiding from COVID-19 in our laboratory 020 in the Department of Physics while assembling this set-up.

The subsequent two chapters present our research into the SEC of molecular magnets. Thus, Chapter 4 focuses on the results of our finished project devoted to the Mn(II) trigonal bipyramidal complexes, while Chapter 5 describes the on-going research into the SEC in [Yb (trensal)].

In Chapter 6, I present and discuss our investigation into the possibility of implementing an error-correction protocol on the electron-nuclear qudit of manganese impurities in zinc oxide.

The appendix contains miscellaneous topics which support and supplement the content of the main chapters.

For all practical purposes...
Without loss of generality...
Easy to see...

And other ways to annoy a student.

Oxford University Lecturers

Chapter 2
Theoretical framework

Contents

Chapter 2 provides the theoretical foundation for the experimental investigations presented in Chapters 4, 5 and 6. It introduces the notation and formalism for describing the states of separate qubits and qudits, as well as the evolution of these states. The chapter then extends this framework to ensembles of spins, employing density matrix formalism to characterise their collective behaviour and their evolution under the action of MW and RF pulses. The chapter also describes several standard ESR techniques like EDFS and the sequences for measuring relaxation times. It culminates with a theoretical description of the E-field effect.

2.1 Fundamentals

For a quantum system to act as a qu**b**it its state should be fully described by a superposition of two orthogonal basis states to which the system collapses after a measurement:

$$|\psi\rangle = c_0 |0\rangle + c_1 |1\rangle \tag{2.1}$$

More generally, a qu**d**it is a system with d possible quantum states. An arbitrary pure state of a qudit can be written as a linear combination of d basis states $|i\rangle$:

$$|\psi\rangle = \sum_i^d c_i |i\rangle , \tag{2.2}$$

where $c_i \in \mathbb{C}$. The complex coefficients obey normalisation condition $\sum_i |c_i|^2 = 1$ to ensure that the probabilities of collapsing to different states sum to one.

According to the fundamental postulates of quantum mechanics, the time evolution of the state $|\psi\rangle$ of a quantum system is described by the Shrödinger equation:

$$\mathrm{i}\hbar \frac{\partial |\psi\rangle}{\partial t} = \hat{\mathcal{H}} |\psi\rangle , \tag{2.3}$$

where $\hat{\mathcal{H}}$ is the Hamiltonian – the operator corresponding to the total energy of the system.

In the projects presented in this thesis, the physical implementations of qubits and qudits was brought about by electronic and nuclear spins. The major technique which allows us to coherently control the spins is the magnetic resonance phenomenon.

2.1.1 Spin Hamiltonian

In the context of nuclear and electron magnetic resonances, operator $\hat{\mathcal{H}}$ is a function of the spatial coordinates and momenta of all the particles constituting the system (spatial part), and of their angular momenta. If the system geometry does not change significantly during measurement or the total time of measurement can be subdivided into time intervals during which the system geometry can be considered unchanged, the Hamiltonian $\hat{\mathcal{H}}$ can be simplified by integrating it over the spatial coordinates. What one obtains after such a procedure is the *static spin Hamiltonian* [89–91]. It is an operator which consists of a set of parameters and a combination of spin operators:

$$\begin{aligned}\hat{\mathcal{H}}_{\mathrm{S}} &= \hat{\mathcal{H}}_{\mathrm{EZ}} + \hat{\mathcal{H}}_{\mathrm{SOC}} + \hat{\mathcal{H}}_{\mathrm{NZ}} + \hat{\mathcal{H}}_{\mathrm{HF}} + \hat{\mathcal{H}}_{\mathrm{NQ}} + \hat{\mathcal{H}}_{\mathrm{ZFS}} = \\ &= \mu_{\mathrm{B}} g_J \boldsymbol{B}_0^{\mathrm{T}} \hat{\boldsymbol{J}} + \lambda \hat{\boldsymbol{S}}^{\mathrm{T}} \hat{\boldsymbol{L}} - \sum_k^n \mu_{\mathrm{N}} g_{\mathrm{N},k} \boldsymbol{B}_0^{\mathrm{T}} \hat{\boldsymbol{I}}_k + \sum_k^n \hat{\boldsymbol{J}}^{\mathrm{T}} \boldsymbol{A}_k \hat{\boldsymbol{I}}_k + \sum_k^n \hat{\boldsymbol{I}}^{\mathrm{T}} \boldsymbol{P}_k \hat{\boldsymbol{I}} + \\ &\quad + \sum_k \sum_{q=-k}^{k} B_k^q \hat{O}_k^q(\hat{\boldsymbol{J}}), \quad (2.4)\end{aligned}$$

where $\boldsymbol{B}_0$ is a static applied magnetic field, μ_{B} and μ_{N} are the Bohr and nuclear magnetons, g_J is the Landé g-factor, g_{N} is the nuclear dimensionless gyromagnetic ratio; $\boldsymbol{A}$ is the hyperfine tensor; $\hat{O}_k^q$ and B_k^q are the extended Stevens operators and their coefficients; and $\boldsymbol{P}$ is the nuclear quadrupole tensor. Operator $\hat{\boldsymbol{J}}$ stands for the total electron angular momentum, and for the ions discussed in this thesis it consists of the total intrinsic spin $\hat{\boldsymbol{S}}$ and orbital angular momentum $\hat{\boldsymbol{L}}$ (Russell-Saunders coupling). Operator $\hat{\boldsymbol{I}}$ represents the nuclear spin angular momentum. All angular momentum operators are vector operators and can be expressed in terms of, for instance, Cartesian components as $\hat{\boldsymbol{J}} = \left(\hat{J}_x, \hat{J}_y, \hat{J}_z\right)$.

Hamiltonian 2.4 describes the total energy of one or several unpaired electrons of a single ion that interact with n surrounding nuclei. It includes the electron $\hat{\mathcal{H}}_{\mathrm{EZ}}$ and nuclear $\hat{\mathcal{H}}_{\mathrm{NZ}}$ Zeeman energy terms describing the interaction of total electron and nuclear angular momenta $\hat{\boldsymbol{J}}$ and $\hat{\boldsymbol{I}}$ with the static magnetic field $\boldsymbol{B}_0$; the spin-orbit coupling (SOC) term $\hat{\mathcal{H}}_{\mathrm{SOC}}$, the hyperfine term $\hat{\mathcal{H}}_{\mathrm{HF}}$ describing the interaction between the electrons and nuclei; the zero-field splitting term $\hat{\mathcal{H}}_{\mathrm{ZFS}}$ incorporating

the crystal-field interaction (see Section 2.5.3), the electron dipole-dipole interaction, and the generalized anisotropic exchange interaction; and the nuclear quadrupole term $\hat{\mathcal{H}}_{\mathrm{NQ}}$ representing the interaction between the nucleus and the electric field of its environment. The spin Hamiltonian 2.4 is not the most general: high-order effects can be accounted by incorporating additional terms of the form $B_0^s \hat{\boldsymbol{J}}^r \prod_{k=1}^{n} \hat{\boldsymbol{I}}_k^{t_k}$ ($\{s, r, t_k\}$ are non-negative integers) with pertinent coefficients [90, 91]. Note that, apart from the hyperfine term, this Hamiltonian does not include terms representing the interaction between electrons and nuclei of separate ions.

In the following chapters, we are going to discuss systems with only one species of nuclear spins ($n = 1$), and without considering the nuclear quadrupole interaction $\hat{\mathcal{H}}_{\mathrm{NQ}}$. By further splitting $\hat{\mathcal{H}}_{\mathrm{SOC}}$ into two parts contributing to $\hat{\mathcal{H}}_{\mathrm{EZ}}$ and $\hat{\mathcal{H}}_{\mathrm{ZFS}}$ as described, for instance, in References [89, 91], we can use a simpler Hamiltonian:

$$\hat{\mathcal{H}}_0 = \mu_{\mathrm{B}} \boldsymbol{B}_0^{\mathrm{T}} \boldsymbol{g} \hat{\boldsymbol{J}} - \mu_{\mathrm{N}} g_{\mathrm{N}} \boldsymbol{B}_0^{\mathrm{T}} \hat{\boldsymbol{I}} + \hat{\boldsymbol{J}}^{\mathrm{T}} \boldsymbol{A} \hat{\boldsymbol{I}} + \sum_k \sum_{q=-k}^{k} B_k^q \hat{O}_k^q(\hat{\boldsymbol{J}}), \tag{2.5}$$

where $\hat{\boldsymbol{J}}$ now plays the role of an effective (or formal) spin, and $\boldsymbol{g}$ is a tensor incorporating both the Zeeman and spin-orbit coupling effects.

Equations 2.4 and 2.5 represent the energy of the spin system. The widely-used convention in the magnetic resonance literature is to give the values of the energy quantities and the parameters in units of frequency, most often in MHz. In this thesis, I will follow this convention and will be writing, for instance, $A = 200$ MHz instead of $A/h = 200$ MHz. However, where necessary, I shall include the Planck constant explicitly to avoid ambiguity.

2.1.2 Magnetic resonance phenomenon

The word 'static' in the definition of $\hat{\mathcal{H}}_0$ means that all the terms in Equation 2.5 can be considered constant during a certain period of time. The eigenvalues ϵ_i and eigenstates $|i\rangle$ of operator $\hat{\mathcal{H}}_0$ are the energy values and the stationary states of the system at which it can exist indefinitely long (as long as $\hat{\mathcal{H}}_0$ is truly

static), respectively. The eigenstates are found by solving the time-independent Schrödinger equation given by

$$\hat{\mathcal{H}}_0 \left|i\right\rangle = \epsilon_i \left|i\right\rangle . \tag{2.6}$$

For approximate calculation, one can discretise any evolution of a system into arbitrarily short steps during which the static $\hat{\mathcal{H}}_0$ takes a different form but the evolution of $|\psi\rangle$ progresses as

$$\left|\psi, t_2\right\rangle = e^{-\mathrm{i}\hat{\mathcal{H}}_0(t_2-t_1)/\hbar} \left|\psi, t_1\right\rangle . \tag{2.7}$$

In practice, however, a greater physics insight is gained by handling oscillatory additions to Hamiltonian 2.5 using the time-dependent perturbation theory.

When the system is subject to an oscillatory magnetic field $\tilde{\boldsymbol{B}}_{\mathrm{AC}} = \boldsymbol{B}_{\mathrm{AC}} e^{i\omega t}$, the static Hamiltonian $\hat{\mathcal{H}}_0$ is perturbed by an oscillatory term via the Zeeman coupling given by

$$\hat{\mathcal{H}}_{\mathrm{AC}} = \boldsymbol{B}_{\mathrm{AC}}^{\mathrm{T}} \left(\mu_{\mathrm{B}} \boldsymbol{g} \hat{\boldsymbol{J}} - \mu_{\mathrm{N}} g_{\mathrm{N}} \hat{\boldsymbol{I}}\right) e^{i\omega t}. \tag{2.8}$$

If the frequency ω is close to the difference $|\epsilon_j - \epsilon_i|/\hbar$, then in the first-order petrubation limit[1] the rate at which the system transitions between states $|i\rangle$ and $|j\rangle$ will be proportional to the mod-square of the corresponding matrix element:

$$W \propto \left|\left\langle j\right| \boldsymbol{B}_{\mathrm{AC}}^{\mathrm{T}} \left(\mu_{\mathrm{B}} \boldsymbol{g} \hat{\boldsymbol{J}} - \mu_{\mathrm{N}} g_{\mathrm{N}} \hat{\boldsymbol{I}}\right) \left|i\right\rangle\right|^2. \tag{2.9}$$

In its turn, this rate determines the intensity of the transition in spectroscopic experiments.

The described process constitutes the essence of the magnetic resonance phenomenon. The two terms of Equation 2.8 commute because they act on different spin species. Moreover, very often, terms $\mu_{\mathrm{B}} g_J$ and $\mu_{\mathrm{N}} g_{\mathrm{N}}$, which are associated with the separation of the electron and nuclear energy levels, differ by several orders of magnitude. For a wide range of chemical compounds, at 340 mT – the typical static

[1] The first-order limit used here is valid for small perturbations and short times only but it gives a good idea of what happens at the resonance even at strong oscillatory fields [92, 93]. The precise consideration of the evolution of a quantum system is presented in Section 2.2.3.

field historically used for the X-band EPR – these terms in $\hat{\mathcal{H}}_{\mathrm{EZ}}$ and $\hat{\mathcal{H}}_{\mathrm{NZ}}$ produce resonant frequencies in the range of GHz for electrons and of MHz for nuclei. All this allows us to consider electron and nuclear magnetic resonances separately.

2.1.3 Rotating and doubly-rotating frames

In a typical experimental set-up, the alternating magnetic field $\tilde{\boldsymbol{B}}_{\mathrm{AC}}$ is linearly polarised and can be decomposed into the sum of two circularly polarised fields rotating in opposite directions with frequencies $\pm\omega_{\mathrm{AC}}$. For theoretical calculations and a qualitative understanding of the effect of various pulse sequences, it is useful to consider the evolution of spins in the reference frame rotating together with one of the circular components of the excitation field [90, 94]. I will first briefly describe the classical treatment of the rotating frame and then present the quantum mechanical transformation in terms of operators.

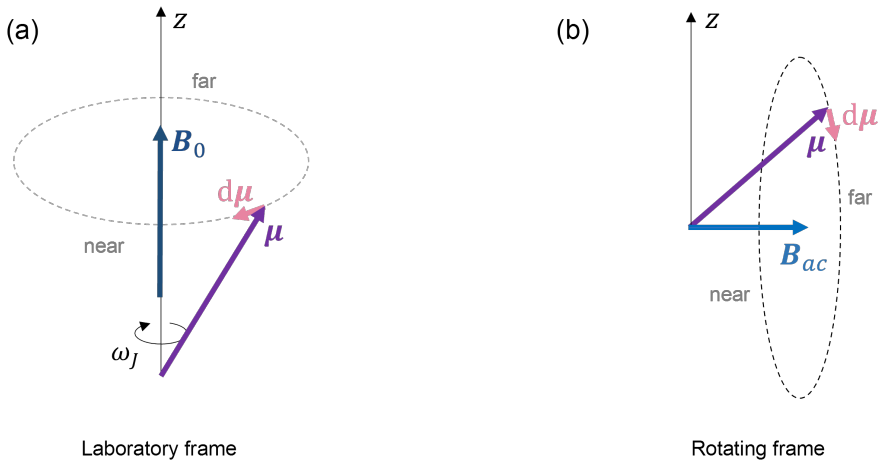

Figure 2.1: (a) Precession of a magnetic moment $\boldsymbol{\mu}$ in a static magnetic field $\boldsymbol{B}_0$. (b) The magnetic moment $\boldsymbol{\mu}$ and the alternating magnetic field $\boldsymbol{B}_{\mathrm{AC}}$ in the frame of reference rotating together with one of the circular components of $\tilde{\boldsymbol{B}}_{\mathrm{AC}}$.

To see the usefulness of the rotating frame, consider for now only an isotropic Zeeman interaction of a single species of spins with an external static magnetic field $\boldsymbol{B}_0$, whose direction defines the orientation of the laboratory z-axis (see Figure 2.1(a)). According to the semi-classical picture, in a static magnetic field $\boldsymbol{B}_0$, a magnetic moment $\boldsymbol{\mu}$ precesses about the z-axis with Larmor frequency $\omega_J = \gamma_J B_0$, where γ_J is the gyromagnetic ratio. We now turn on the oscillating field $\tilde{\boldsymbol{B}}_{\mathrm{AC}}$

in the laboratory frame and consider the behaviour of all the vectors in a frame rotating with angular velocity ω_{AC} (see Figure 2.1(b)). The magnetic resonance is observed when the frequency of the oscillating magnetic field ω_{AC} is close to ω_J. Under this condition, the magnetic moment $\boldsymbol{\mu}$ does not precess about the z-axis in the rotating frame as if field $\boldsymbol{B}_0$ was absent. However, field $\tilde{\boldsymbol{B}}_{\mathrm{AC}}$ is still there: it loses its alternating nature and is present as a static field $\boldsymbol{B}_{\mathrm{AC}}$ directed along the axis of its polarisation. Thus, in the rotating frame, spins precess only about $\boldsymbol{B}_{\mathrm{AC}}$ at frequency $\gamma_J B_{\mathrm{AC}}$. In case of the electron magnetic resonance, it is conventional to denote the vector-magnitude of the oscillating field as $\boldsymbol{B}_1$, whilst for the nuclear magnetic resonance this field is called $\boldsymbol{B}_2$. The corresponding Larmor frequencies are then $\omega_1 = \mu_{\mathrm{B}} g B_1/\hbar$ and $\omega_2 = \mu_{\mathrm{N}} g_{\mathrm{N}} B_2/\hbar$.

In the experimental set-up used for the projects presented in this thesis, the excitation fields $\boldsymbol{B}_1$ and $\boldsymbol{B}_2$ were generated independently, and all three fields $\boldsymbol{B}_0$, $\boldsymbol{B}_1$ and $\boldsymbol{B}_2$ were oriented mutually perpendicular to each other in the laboratory frame. The static $\boldsymbol{B}_0$ was generated by a resistive magnet – it defined the laboratory z-axis, which coincided with the z-axes of the rotating frames. Field $\boldsymbol{B}_1$ was directed along the vertical laboratory axis, and along the x-axis in the electron rotating frame. Field $\boldsymbol{B}_2$ was perpendicular to both $\boldsymbol{B}_0$ and $\boldsymbol{B}_1$.

The semi-classical picture of rotating magnetic moments is good for representing non-interacting spin-1/2 particles, and it corresponds to the representation in terms of the Bloch sphere. For higher spins, however, there is no intuitive analogy in the classical mechanics, and we need to treat the transformation to the rotating frame using the quantum mechanical formalism.

In the case of isotropic $\boldsymbol{g}$, the transition from the laboratory frame to the rotating frame is accomplished by transforming the total Hamiltonian $\hat{\mathcal{H}}_0 + \hat{\mathcal{H}}_{\mathrm{AC}}$ and the state $|\psi\rangle$ using the propagator

$$\hat{U} = e^{-\mathrm{i}\left(\omega_{\mathrm{MW}} \hat{J}_z - \omega_{\mathrm{RF}} \hat{I}_z\right) t}, \tag{2.10}$$

where ω_{MW} and ω_{RF} are the frequencies of $\boldsymbol{B}_1$ and $\boldsymbol{B}_2$, respectively.

The transformed Hamiltonian takes the following form:

$$\hat{\mathcal{H}}_0' = \left(\hbar\left[\frac{\mu_\mathrm{B} g B_0}{\hbar} - \omega_\mathrm{MW}\right]\hat{J}_z + \mu_\mathrm{B} g B_1 \hat{J}_x\right) - \\ - \left(\hbar\left[\frac{\mu_\mathrm{N} g_\mathrm{N} B_0}{\hbar} - \omega_\mathrm{RF}\right]\hat{I}_z + \mu_\mathrm{N} g_\mathrm{N} B_2 \hat{I}_x\right) + \\ + \hat{\mathcal{H}}^0_\mathrm{HF} + \hat{\mathcal{H}}^0_\mathrm{ZFS} + \\ + \text{time-dependent terms}, \quad (2.11)$$

where $\hat{\mathcal{H}}^0_\mathrm{HF}$ and $\hat{\mathcal{H}}^0_\mathrm{ZFS}$ represent those parts of the corresponding full terms, which commute with the full Zeeman interaction – they are usually called 'secular terms' in the literature (terms which commute only with $\hat{\mathcal{H}}_\mathrm{EZ}$ are known as 'pseudo-secular') [94, 95]. The remaining time-dependent part is usually ignored, because it leads to only small frequency shifts [90], although they might be important while considering the nuclear quadrupole interaction [94]. Each square bracket contains the difference between the resonance frequencies of a species of spins and the frequency of the corresponding excitation field. Exactly at resonance, the square brackets zero out and the Zeeman terms describe the interaction of spins with only the excitation fields, which are static in the rotating frame. For the anisotropic $\boldsymbol{g}$ one should use the propagator corresponding to the rotation about the axis defined by the product $\boldsymbol{B}_0^\mathrm{T}\boldsymbol{g}$. Details of the transformation can be found in References [90, 94, 95].

2.2 Density operator formalism

All the samples discussed in this work consisted of a large number of spins which in general evolve in slightly different environments. They can be represented as clusters (or ensembles) of identical spins experiencing the conditions of a particular environment. The collective state of such ensembles of spins cannot be described by a single state vector, and instead a different approach should be used: namely, the density matrix (operator) formalism.

2.2.1 Pure states

A *pure state* of a single spin J can be described as a superposition of $2J+1$ basis states $|i\rangle$ as

$$|\psi\rangle = \sum_{i=1}^{2J+1} c_i |i\rangle . \tag{2.12}$$

The purity of such a state lies in the fact that the complex amplitudes c_i are not random but have certain values, and some of them (but not all) can even be zero. The normalisation condition requires $\sum_i |c_i|^2 = 1$. This mathematical description is similar to the definition of a qudit given in Equation 2.2 with $d = 2J+1$.

The expectation value of an observable Q corresponding to some operator $\hat{Q}$ can be found via projective measurements (see Section 2.2.4.1) given by

$$\left\langle \hat{Q} \right\rangle = \langle \psi | \hat{Q} | \psi \rangle . \tag{2.13}$$

Another way of describing a single spin state is through an object called a density operator defined as

$$\hat{\rho} = |\psi\rangle \langle \psi| . \tag{2.14}$$

The closely related *density matrix* ρ is obtained by putting the density operator between basis bra-kets – the matrix elements will thus depend on the choice of the basis. Then the expectation value of $\hat{Q}$ takes the form

$$\left\langle \hat{Q} \right\rangle = \mathrm{Tr}(\rho Q). \tag{2.15}$$

If the quantum system under study consists of n heterogeneous spins, for instance, of a variety of electron and nuclear spins, the function describing a pure state of the composite system will be equal to the direct product of the states (Kronecker product for matrix representation) of individual spins:

$$\left|\psi^{(\mathrm{composite})}\right\rangle = \left|\psi^{(1)}\right\rangle \otimes \left|\psi^{(2)}\right\rangle \otimes \cdots \otimes \left|\psi^{(n)}\right\rangle . \tag{2.16}$$

Similarly, the density operators of the composite system will be equal to the direct product of individual density operators:

$$\hat{\rho}^{\mathrm{composite}} = \hat{\rho}^{(1)} \otimes \hat{\rho}^{(2)} \otimes \cdots \otimes \hat{\rho}^{(n)}. \tag{2.17}$$

The state of an ensemble of identical and perfectly coherent spins will be $|\psi\rangle^{\otimes N}$. The expectation value of an extensive quantity $\hat{Q}$ measured on this ensemble (ensemble average) is equal to the expectation value of measurement on a single spin times the number of spins in the ensemble: $N\left\langle\hat{Q}\right\rangle$ (see also Appendix A.1.1.1). Thus, there is no need to assemble a separate density operator for an ensemble of identical spins.

2.2.2 Mixed states

In a real sample all the spins find themselves in slightly different circumstances. The approach to describing this situation mathematically is to subdivide the initial ensemble of different spins into m clusters of N_j identical spins which can be assigned with particular state functions $\left|\psi^{(j)}\right\rangle^{\otimes N_j}$ and density operators $\hat{\rho}^{(j)} = \left(\left|\psi^{(j)}\right\rangle\left\langle\psi^{(j)}\right|\right)^{\otimes N_j}$. It is important to note that the set of elementary state functions $\left|\psi^{(j)}\right\rangle$ is well defined but we have no information as to what particular pure state each of the clusters is in. The lack of this information is addressed using statistical methods by assigning probabilities $p_j = N_j/N$ (or weights) to each of the possible pure states based on the number of spins in each cluster, as follows:

$$\left\langle\hat{Q}\right\rangle = \sum_{j=1}^{m} N_j \left\langle\psi^{(j)}\right|\hat{Q}\left|\psi^{(j)}\right\rangle, \tag{2.18}$$

$$\hat{\rho} = \frac{1}{N}\sum_{j=1}^{m} N_j \left|\psi^{(j)}\right\rangle\left\langle\psi^{(j)}\right| = \sum_{j=1}^{m} p_j \left|\psi^{(j)}\right\rangle\left\langle\psi^{(j)}\right|, \tag{2.19}$$

from which it is clear that the density operator can be expressed in its single-spin form, and that its eigenstates are the pure states of individual spins in separate clusters. Then the expectation value of an arbitrary extensive operator $\hat{Q}$ is again

$$\left\langle\hat{Q}\right\rangle = N\,\mathrm{Tr}(\rho Q). \tag{2.20}$$

It is instructive to discuss the meaning of the elements of density matrix ρ. Substituting 2.12 into 2.19, we obtain

$$\hat{\rho} = \sum_{j=1}^{m} p_j \sum_{i,k}^{2J+1} c_i^{(j)} c_k^{*(j)} \left|i\right\rangle\left\langle k\right| = \sum_{i,k}^{2J+1} \overline{c_i c_k^*} \left|i\right\rangle\left\langle k\right|, \tag{2.21}$$

where the overline denotes the ensemble average of $c_i c_k^*$.

In an orthonormal initial basis $|i\rangle$ the elements of the density matrix are

$$\rho_{ik} = \langle i| \hat{\rho} |k\rangle = \overline{c_i c_k^*}. \tag{2.22}$$

The diagonal elements $|c_i|^2$ show the population of the basis levels $|i\rangle$, whereas the non-diagonal terms are called *coherences* [90] and show how coherent different clusters of spins are with respect to each other. In ESR, the echo signal, for instance, is the transient transverse magnetization of a sample under study. The measured components of transverse magnetization are proportional to the expectation values of spin operators $\hat{J}_x$ and $\hat{J}_y$, whose matrices have only non-diagonal elements. From Equation 2.20, we deduce that the magnitude of the signal will depend on the absolute values of coherences in the density matrix. In other words, the intensity of the echo signal reflects the level of coherence between all spins in a sample, and it disappears when those spins become completely decoherent. For further details of the spin-echo sequence, see Section 2.4.3.

2.2.2.1 Initial density matrix and Pseudo-pure states

Normally, the initial state of a spin system is described by the density operator corresponding to the state of thermodynamic equilibrium given by

$$\hat{\rho}(t=0) = \frac{e^{-\frac{\hat{\mathcal{H}}}{k_\mathrm{B}T}}}{\mathrm{Tr}\left(e^{-\frac{\hat{\mathcal{H}}}{k_\mathrm{B}T}}\right)}, \tag{2.23}$$

where t is time, T stands for temperature and k_B is the Boltzmann constant.

Let us assume that the Zeeman energy term dominates the Hamiltonian (high-field approximation). Additionally, for most of frequencies and temperatures relevant for this thesis, the high-temperature approximation ($\hbar\omega \ll k_\mathrm{B}T$) is also valid, so that

$$\hat{\rho}(t=0) \approx \frac{\hat{\mathbf{1}} - \frac{g\mu_\mathrm{B}B_0}{k_\mathrm{B}T}\hat{J}_z}{\mathrm{Tr}\left(\hat{\mathbf{1}} - \frac{g\mu_\mathrm{B}B_0}{k_\mathrm{B}T}\hat{J}_z\right)} = \frac{1}{2J+1}\left(\hat{\mathbf{1}} - \frac{g\mu_\mathrm{B}B_0}{k_\mathrm{B}T}\hat{J}_z\right), \tag{2.24}$$

where $1/(2J+1)$ factor comes from the dimensionality of the operator matrices for angular momentum J.

The identity operator $\hat{\mathbf{1}}$ stays invariant throughout unitary evolution implemented by magnetic resonance measurements and can be dropped out. The constant coefficient is also not important if we are not interested in quantifying the intensity of a signal and/or the total number of spins in the system. Thus, the initial density matrix of an ensemble of spins J is associated with the matrix of operator $\hat{J}_z$ of the corresponding dimensionality, and we can write

$$\rho(0) = -J_z. \tag{2.25}$$

The notion of *pseudo-pure* states is closely connected with the initialization process of qubits in ESR and NMR. In order to execute any quantum computation, we want to put our system into a known initial state, which should be pure. However, all we have is the mixed initial density operator 2.23. Often, this state can be transformed into a *pseudo-pure* state of the form

$$\hat{\rho}_{\mathrm{PPS}} = \frac{(1-\alpha)\hat{\mathbf{1}} + 2\alpha\,|\psi\rangle\langle\psi|}{(1-\alpha)2^n + 2\alpha}, \quad -1 \leq \alpha \leq 1, \tag{2.26}$$

where $|\psi\rangle$ represents the initial pure state of a system of n qubits which we seek to achieve, and α can be thought of as a parameter controlling the purity of the state[2]. Thus, ρ_{PPS} is a unit trace Hermitian matrix of size $2^n \times 2^n$, with eigenvalues that lie in the interval $[0, 1]$, and with $(2^n - 1)$ of them degenerate [96].

2.2.3 Evolution of the density operator

Starting with the definition of the density operator 2.19 we can directly write the equation governing its evolution in time under the Spin Hamiltonian 2.5 as

$$\hat{\rho}(t) = \exp\left(-\frac{\mathrm{i}}{\hbar}\int_0^t \hat{\mathcal{H}}_0\,\mathrm{d}t\right)\hat{\rho}(0)\exp\left(+\frac{\mathrm{i}}{\hbar}\int_0^t \hat{\mathcal{H}}_0\,\mathrm{d}t\right) \tag{2.27}$$

[2]For a goal state with only one non-zero complex coefficient in the basis of the Hamiltonian, $\alpha = 1$ produces a system where only one energy level is occupied, whereas $\alpha = -1$ corresponds to the situation where all levels are equally populated except for one empty level.

2.2.3.1 The importance of unitary operators

The eigenvalues of a Hamiltonian $\hat{\mathcal{H}}_0$ of a closed system are energy values ϵ_i represented by real numbers, consequently such a Hamiltonian is a Hermitian one (together with its matrix). Now, consider the evolution of the density operator under a constant Hamiltonian (we can always choose a time interval where this condition can be satisfied). From Equation 2.27 it follows that

$$\hat{\rho}(t) = e^{-\frac{\mathrm{i}}{\hbar}\hat{\mathcal{H}}_0 t}\hat{\rho}(0)e^{\frac{\mathrm{i}}{\hbar}\hat{\mathcal{H}}_0 t} = \hat{U}(t)\hat{\rho}(0)\hat{U}^\dagger(t), \tag{2.28}$$

where the object $\hat{U}(t) = e^{-\mathrm{i}\hbar\hat{\mathcal{H}}t}$ is called a *transformation operator* (it transforms the initial density operator) or *propagator* (it propagates the density operator in time) with operator $\hat{\mathcal{H}}_0$ being a *generator* of that transformation. It is an *operator exponential* which has a particularly simple form if the generator is expressed in the basis of its eigenstates $|\epsilon_i\rangle$:

$$\hat{U} = \sum_i e^{-\mathrm{i}\frac{\epsilon_i}{\hbar}t}|\epsilon_i\rangle\langle\epsilon_i|, \quad \hat{\mathcal{H}}_0 = \sum_i E_i|\epsilon_i\rangle\langle\epsilon_i|. \tag{2.29}$$

From the definition, it is seen that $\hat{U}\hat{U}^\dagger = \hat{\mathbf{1}}$ meaning that $\hat{U}$ is a unitary operator.

So, it follows straight from the fundamental TDSE 2.3 that the evolution of a closed quantum system is described by a unitary operator.

As a corollary of 2.29, a unitary operator does not change the norm of a state vector but only affects the phases of its complex amplitudes – it follows from the form of the eigenstates of $\hat{U}$: complex exponential $e^{-\mathrm{i}\frac{\epsilon_i}{\hbar}t}$ has magnitude 1 and introduces a phase shift $\epsilon_i t/\hbar$.

It also follows from 2.29 and the definition of a unitary operator that $\hat{U}(-t) = \hat{U}^\dagger(t)$. Therefore, in order to reverse the action of one unitary transformation, we need to apply its adjoint to the state of the system left after the action of the direct operator.

Not every transformation is unitary though. Moreover, in real-world applications, we actually need to be able to accomplish non-unitary transformations such as SET and CLEAR gates, and readout. Non-unitary transformations are realised

via interaction of the quantum system with its environment. The undesired non-unitary transformations are sources of quantum decoherence, relaxation, and signal decay (see Section 2.2.5.)

2.2.3.2 Evolution of the density matrix

Following Equation 2.28, the evolution of the density matrix elements in the basis of the eigenstates of $\hat{\mathcal{H}}_0$ is given by

$$\rho_{kl} = \langle k|e^{-\frac{\mathrm{i}}{\hbar}\hat{\mathcal{H}}_0 t}\hat{\rho}(0)e^{\frac{\mathrm{i}}{\hbar}\hat{\mathcal{H}}_0 t}|l\rangle = e^{-\frac{\mathrm{i}}{\hbar}\mathcal{H}_{kk}t}\langle k|\rho(0)|l\rangle e^{\frac{\mathrm{i}}{\hbar}\mathcal{H}_{ll}t} = \rho_{kl}(0)e^{\frac{\mathrm{i}}{\hbar}(\mathcal{H}_{ll}-\mathcal{H}_{kk})t}, \quad (2.30)$$

where $\mathcal{H}_{ll}$ and $\mathcal{H}_{kk}$ are the diagonal matrix elements of $\hat{\mathcal{H}}_0$ corresponding to the indices of ρ_{kl}. This expression shows that, under a constant Hamiltonian, the diagonal elements of ρ stay unchanged whereas the non-diagonal elements (coherences) acquire additional phase. The phase of the coherences is reflected in the phase of the measured echo signal: we can use that information to study the effect of additional terms in the Hamiltonian introduced by external perturbations.

2.2.4 Projective and ensemble measurements

2.2.4.1 Projective measurements

By definition

$$\hat{P} = \sum_i^k |i\rangle\langle i| \quad (2.31)$$

is a projector on the subspace spanned by vectors $|i\rangle$. For instance, one can talk about subspaces generated by the eigenstates $|q\rangle$ of an operator $\hat{Q}$ corresponding to its certain eigenvalue q. The degeneracy of eigenvalues determine the dimensionality k of the corresponding subspace. If the eigenvalues are not degenerate, each subspace (i.e. eigenstate) will have a corresponding projector P_q. It also follows that such projectors are orthogonal and idempotent $\left(P_q^2 = P_q\right)$.

An observable represented by an operator $\hat{Q}$ can then be described in terms of the projectors onto its eigenspaces:

$$\hat{Q} = \sum_q^m q\,|q\rangle\langle q| = \sum_q^{m'} q\hat{P}_q, \quad (2.32)$$

where m is the total number of eigenvalues of $\hat{Q}$ and m' is the number of distinct eigenvalues. The set of q constitutes possible outcomes of measurements.

The probability of obtaining the value q in a measurement is equal to

$$p(q) = \langle\psi|\hat{P}_q|\psi\rangle \tag{2.33}$$

and the state $|\psi\rangle$ *collapses* after the measurement to

$$|q\rangle = \frac{\hat{P}_q\,|\psi\rangle}{\sqrt{p_q}}. \tag{2.34}$$

This type of measurement is known as a *projective measurement*. It is often juxtaposed with an *ensemble measurement* which does not lead to the collapse of superposition.

The average value of projective measurements is

$$\left\langle\hat{Q}\right\rangle = \sum_q^{m'} q\,\langle\psi|\hat{P}_q|\psi\rangle = \langle\psi|\left(\sum_q^{m'} q\hat{P}_q\right)|\psi\rangle = \langle\psi|\hat{Q}|\psi\rangle\,, \tag{2.35}$$

or equivalently

$$\begin{aligned}\left\langle\hat{Q}\right\rangle = \sum_q^{m'} q\,\langle\psi|\hat{P}_q|\psi\rangle = \sum_q^{m'}\sum_i^{k} q\,\langle\psi|i\rangle\,\langle i|\psi\rangle = \sum_q^{m} q\,\langle\psi|q\rangle\,\langle q|\psi\rangle = \\ = \sum_q^{m}\langle q|\hat{Q}|q\rangle\,\langle q|\psi\rangle\,\langle\psi|q\rangle = \sum_q^{m}\langle q|\hat{Q}\hat{\rho}|q\rangle = \mathrm{Tr}(\rho Q),\end{aligned} \tag{2.36}$$

which is the same as Equation 2.15.

2.2.4.2 Measurement of transverse magnetisation

In ESR and NMR one usually measures the transverse magnetisation of a spin system, so that the output signal is proportional to the expectation values of operators $\hat{J}_x$ and $\hat{J}_y$.

In particular, for a spin-1/2 system in an arbitrary state

$$|\psi\rangle = \alpha\,|0\rangle + \beta\,|1\rangle \tag{2.37}$$

with the density matrix

$$\rho = \begin{pmatrix} |\alpha|^2 & \alpha\beta^* \\ \alpha^*\beta & |\beta|^2 \end{pmatrix}, \tag{2.38}$$

the expectation values of the x- and y-magnetisation are

$$M_x \propto \mathrm{Tr}\{\rho J_x\} = \mathrm{Tr}\left\{\begin{pmatrix} |\alpha|^2 & \alpha\beta^* \\ \alpha^*\beta & |\beta|^2 \end{pmatrix} \frac{1}{2}\begin{pmatrix} 0 & 1 \\ 1 & 0 \end{pmatrix}\right\} = \frac{1}{2}(\alpha\beta^* + \alpha^*\beta), \tag{2.39a}$$

$$M_y \propto \mathrm{Tr}\{\rho J_y\} = \mathrm{Tr}\left\{\begin{pmatrix} |\alpha|^2 & \alpha\beta^* \\ \alpha^*\beta & |\beta|^2 \end{pmatrix} \frac{1}{2}\begin{pmatrix} 0 & -\mathrm{i} \\ \mathrm{i} & 0 \end{pmatrix}\right\} = \frac{\mathrm{i}}{2}(\alpha\beta^* - \alpha^*\beta). \tag{2.39b}$$

In order to simulate the quadrature detection (see Section 2.4.3), one can compose a complex signal as $M_x + \mathrm{i}M_y$.

2.2.4.3 Ensemble average measurement

For an ensemble of N spins, the formulae are very similar (following Equation 2.20):

$$M_x = N\,\mathrm{Tr}(\rho J_x), \tag{2.40}$$

$$M_y = N\,\mathrm{Tr}(\rho J_y), \tag{2.41}$$

where ρ has the dimension of a single spin, but now it is the density matrix representing the entire ensemble. Such measurements, being conducted on an ensemble of spins continuously, do not cause states of separate spins to collapse [27]. ESR measurement monitors the average values of two non-commuting operators by implementing an operator corresponding to the average of some observable evaluated over the whole ensemble [13]. This process is sometimes called weak measurement [26].

2.2.5 Note on decoherence and relaxation

The ultimate source of any decoherence and relaxation is uncontrolled interaction of the system with its environment, which can be labelled by a common term: noise. Noise can come from fluctuations in the parameters presented in a stated Hamiltonian, or it can come from completely unaccounted interactions.

Relaxation, or more precisely, processes causing a decrease in the signal intensity, are described mathematically by non-unitary operators. Considering that a Hamiltonian of a closed system is a hermitian operator generating a unitary propagator (see Section 2.2.3.1), it follows that noise must come from the failure of representing a system to be closed.

Some of the unaccounted interactions often mentioned in the literature [90, 97] are explained as follows. The spin-phonon coupling is responsible for the transition of energy between spins and the lattice (spin-lattice relaxation). Spectral diffusion is the process during which spins change their state between being in- and out-of-resonance with the applied EM radiation due to the relatively slow change in the local magnetic field; it includes motion of an anisotropic paramagnetic centre, electron-electron exchange, and electron-nuclear cross relaxation [97]. Spin diffusion is sometimes treated as a separate process which causes spectral diffusion due to the dipole-dipole interaction between the in- and out-of-resonance spins. Instantaneous diffusion is a similar effect which manifests itself via the dephasing of dipole-dipole coupled spins which are flipped by the excitation pulses in contrast to natural processes.

Noise can also come from accounted interactions: thus, slight fluctuations of the static magnetic field $\boldsymbol{B}_0$ can contaminate the phase information by introducing $\hat{J}_z$ error (see Chapter 6).

There are several characteristic times that describe the decoherence of spins, in particular, electron spins. The spin-lattice (longitudinal) relaxation time T_1 describes how fast the z-component of magnetisation approaches its equilibrium magnitude. The phase memory time T_m is the characteristic time over which the coherence between separate spins decays. This is the constant which is extracted from the decay of the echo intensity as a function of the interpulse delay using the stretched exponential (see Section 2.4.3). The spin-spin (transverse) relaxation time T_2 refers to the decay of the net transverse magnetisation of a spin system mostly due to the dipole-dipole interaction between spins which is considered to be homogeneous. Times T_2 and T_m have the same meaning when the decay of the echo intensity is purely exponential. Finally, time T_2^* is the characteristic time of the free-induction decay: it gives the overall decay rate for both homogeneous (T_2) and inhomogeneous contributions [98]. The decoherence effect of the inhomogeneous part is often referred as inhomogeneous broadening; this effect can be negated by means of refocusing (see Section 2.4.3).

The detailed treatment of relaxation processes can be a challenging task on its own and is out of the scope of this thesis. The definitions presented here might lack many subtleties found in more specialised sources. Nonetheless, they should suffice for understanding the physics discussed in later chapters. There, I will be interested principally in the apparent relaxation times which determine the interpulse spacing and the overall timescale of the measurements we used. More information can be found, for instance, in References [89, 90, 94, 95, 97, 99, 100].

2.3 Product operator formalism

Besides the particular example of the initial density operator in Section 2.2.2.1, it is conventional to express general $\hat{\rho}(t)$ in terms of angular-momentum operators $\hat{S}_i$ (or $\hat{J}_i$), $\hat{I}_i$, and the identity operator $\hat{\mathbf{1}}$. Moreover, the action of MW or RF excitation pulses can be described by spin operators $\hat{S}_{x,y}$ and $\hat{I}_{x,y}$ if the corresponding fields $\boldsymbol{B}_1$ and $\boldsymbol{B}_2$ are orthogonal to the static $\boldsymbol{B}_0$ defining the z-axis. In this section, I use the notation $\hat{\boldsymbol{J}}$ as a variable denoting an arbitrary spin operator.

2.3.1 Evolution of density operator under excitation pulses

The effect of the MW or RF excitation pulses is most conveniently described in the frame rotating together with the fields $\boldsymbol{B}_1$ or $\boldsymbol{B}_2$ at the corresponding angular frequencies (see Section 2.1.3). The general formula for the evolution of the density operator under the action of excitation pulses with a rotation (flip) angle θ is

$$\hat{\boldsymbol{J}}_i \xrightarrow{\theta\hat{\boldsymbol{J}}_j} \hat{\boldsymbol{J}}_i \cos(\theta) + \mathrm{i}\left[\hat{\boldsymbol{J}}_i, \hat{\boldsymbol{J}}_j\right] \sin(\theta) \quad \text{for} \quad \hat{\boldsymbol{J}}_i \neq \hat{\boldsymbol{J}}_j, \tag{2.42}$$

with the special case of operator $\hat{\boldsymbol{J}}_i$ acting on itself:

$$\hat{\boldsymbol{J}}_i \xrightarrow{\theta\hat{\boldsymbol{J}}_i} \hat{\boldsymbol{J}}_i. \tag{2.43}$$

The commutator relation between different components of the spin operator is

$$\left[\hat{J}_i, \hat{J}_j\right] = \mathrm{i} \sum_k \epsilon_{ijk} \hat{J}_k, \tag{2.44}$$

where ϵ_{ijk} is the Levi-Civita symbol.

2.3.1.1 Excitation pulses of variable phase

The spin operator representing an excitation pulse with the flip angle θ and a variable phase φ takes the form

$$\theta\hat{J}_\varphi = \theta\left(\hat{J}_x\cos(\varphi) + \hat{J}_y\sin(\varphi)\right). \tag{2.45}$$

The evolution under these two operators cannot be calculated using Equation 2.42 because $\hat{J}_x$ and $\hat{J}_y$ do not commute. The workaround is to decompose $\theta\hat{J}_\varphi$ into a rotation about the z-axis by $-\varphi$ followed by a rotation at angle θ about the x-axis and a rotation with angle φ again about the z-axis [90, 101].

$$\xrightarrow{\theta\hat{J}_\varphi} = \xrightarrow{-\varphi\hat{J}_z} \quad \xrightarrow{\theta\hat{J}_x} \quad \xrightarrow{\varphi\hat{J}_z} \tag{2.46}$$

If operator $\hat{J}_\varphi$ connects coherent levels and $\theta = \pi$, the action of $\theta\hat{J}_\varphi$ is to increment the phase of coherence by 2φ.

2.3.2 Product operators

Let us again consider a system of n heterogeneous spins with the state function

$$\left|\psi^{(\text{composite})}\right\rangle = \left|\psi^{(1)}\right\rangle \otimes \left|\psi^{(2)}\right\rangle \otimes \cdots \otimes \left|\psi^{(n)}\right\rangle \tag{2.47}$$

and the density operator

$$\hat{\rho}^{\text{composite}} = \hat{\rho}^{(1)} \otimes \hat{\rho}^{(2)} \otimes \cdots \otimes \hat{\rho}^{(n)}. \tag{2.48}$$

The dimensionality n_H of the composite Hilbert space of this system is the product of the number of basis states of each type of spin:

$$n_\text{H} = \prod_{i=1}^{n}(2J^{(i)} + 1). \tag{2.49}$$

The total spin Hamiltonian will then be equal to the sum of Hamiltonians of separate spins within a direct product with a unit matrix of the dimension equal to the composite dimensionality of the rest of the spins. This can be written as

$$\hat{\mathcal{H}}_0^{(\text{composite})} = \sum_{i=1}^{n}\hat{\mathbf{1}}^{(1)} \otimes \hat{\mathbf{1}}^{(2)} \otimes \cdots \otimes \hat{\mathbf{1}}^{(i-1)} \otimes \hat{\mathcal{H}}_0^{(i)} \otimes \hat{\mathbf{1}}^{(i+1)} \otimes \cdots \otimes \hat{\mathbf{1}}^{(n)}. \tag{2.50}$$

Individual spin operators extend their dimensionality in the same way:

$$\hat{\boldsymbol{J}}^{(\text{composite space},\, i)} = \hat{\mathbf{1}}^{(1)} \otimes \hat{\mathbf{1}}^{(2)} \otimes \cdots \otimes \hat{\mathbf{1}}^{(i-1)} \otimes \hat{\boldsymbol{J}}^{(i)} \otimes \hat{\mathbf{1}}^{(i+1)} \otimes \cdots \otimes \hat{\mathbf{1}}^{(n)}. \quad (2.51)$$

Many interaction terms in spin Hamiltonians contain a product of two spin operators such as

$$\hat{\boldsymbol{J}}^{(A)}\hat{\boldsymbol{J}}^{(B)} = \left(\hat{\boldsymbol{J}}^{(A)} \otimes \hat{\mathbf{1}}^{(B)}\right)\left(\hat{\mathbf{1}}^{(A)} \otimes \hat{\boldsymbol{J}}^{(B)}\right) = \\ = \left(\hat{\boldsymbol{J}}^{(A)}\hat{\mathbf{1}}^{(A)}\right) \otimes \left(\hat{\boldsymbol{J}}^{(B)}\hat{\mathbf{1}}^{(B)}\right) = \hat{\boldsymbol{J}}^{(A)} \otimes \hat{\boldsymbol{J}}^{(B)}. \quad (2.52)$$

This expression has not introduced new mathematics but is helpful in dealing with matrix representations.

The last rule concerns the evolution of the density operator under the action of a product operator given by

$$\hat{\rho}^{(A)} \otimes \hat{\rho}^{(B)} \xrightarrow{\theta\hat{\boldsymbol{J}}^{(A)}\otimes\hat{\boldsymbol{J}}^{(B)}} \hat{\rho}^{(A)} \otimes \hat{\rho}^{(B)} \cos(\theta) + \mathrm{i}\left[\hat{\rho}^{(A)} \otimes \hat{\boldsymbol{J}}^{(B)}, \hat{\boldsymbol{J}}^{(A)} \otimes \hat{\rho}^{(B)}\right] \sin(\theta). \quad (2.53)$$

2.3.2.1 Two-spin operators for qubits

Considering a system of two qubits implemented by spins $\hat{\boldsymbol{S}}$ and $\hat{\boldsymbol{I}}$, the product-operator basis in terms of Cartesian spin operators is given by

$$\left\{\hat{S}_x, \hat{S}_y, \hat{S}_z, \mathbf{1}\right\} \otimes \left\{\hat{I}_x, \hat{I}_y, \hat{I}_z, \mathbf{1}\right\} \xrightarrow{normalisation} \\ \left\{\frac{1}{2}\mathbf{1}, \hat{S}_x, \hat{S}_y, \hat{S}_z, \hat{I}_x, \hat{I}_y, \hat{I}_z, 2\hat{S}_x\hat{I}_x, 2\hat{S}_x\hat{I}_y, 2\hat{S}_x\hat{I}_z, 2\hat{S}_y\hat{I}_x, 2\hat{S}_y\hat{I}_y, 2\hat{S}_y\hat{I}_z, 2\hat{S}_z\hat{I}_x, 2\hat{S}_z\hat{I}_y, 2\hat{S}_z\hat{I}_z\right\} \quad (2.54)$$

By convention, the unit-operator is not shown, so for instance, a two-spin operator $\hat{S}_x$ is actually $\hat{S}_x \otimes \hat{\mathbf{1}}_I = \hat{S}_x\hat{\mathbf{1}}_I$, and, analogously, $\hat{I}_x = \hat{\mathbf{1}}_S \otimes \hat{I}_x = \hat{\mathbf{1}}_S\hat{I}_x$.

The following commutator relations between these operators will be useful in the proceeding sections:

$$\left[\hat{S}_i, 2\hat{S}_j\hat{I}_k\right] = 2\left[\hat{S}_i, \hat{S}_j\right] \otimes \hat{I}_k, \quad (2.55)$$

$$\left[\hat{I}_i, 2\hat{S}_j\hat{I}_k\right] = 2\hat{S}_j \otimes \left[\hat{I}_i, \hat{I}_k\right]. \quad (2.56)$$

As for the product operators which include non-trivial components of both spins, only those are non-zero which have at least one component along the same axis:

$$\left[2\hat{S}_i\hat{I}_k, 2\hat{S}_j\hat{I}_k\right] = 4\left[\hat{S}_i, \hat{S}_j\right] \otimes \hat{I}_k^2 = \left[\hat{S}_i, \hat{S}_j\right] \otimes \hat{\mathbf{1}}_I = \left[\hat{S}_i, \hat{S}_j\right], \tag{2.57}$$

$$\left[2\hat{S}_i\hat{I}_j, 2\hat{S}_i\hat{I}_k\right] = 4\hat{S}_i^2 \otimes \left[\hat{I}_j, \hat{I}_k\right] = \hat{\mathbf{1}}_S \otimes \left[\hat{I}_j, \hat{I}_k\right] = \left[\hat{I}_j, \hat{I}_k\right]. \tag{2.58}$$

Note that $\hat{I}_k^2 = \hat{S}_i^2 = \hat{\mathbf{1}}/4$ only for spin-1/2 objects.

2.3.2.2 Selective pulses

The excitation pulses which induce coherence or polarization transfer only between two particular density matrix elements are called selective. The product-operators representing selective pulses are composed of the Cartesian basis and their matrix representation contains only those non-zero elements which connect the target states. Consequently, the matrix form of the unitary operator generated by a selective pulse has the form of rotation. To show it, we start with the Pauli matrices

$$\sigma_x = \begin{pmatrix} 0 & 1 \\ 1 & 0 \end{pmatrix}, \qquad \sigma_y = \begin{pmatrix} 0 & -i \\ i & 0 \end{pmatrix}, \qquad \sigma_z = \begin{pmatrix} 1 & 0 \\ 0 & -1 \end{pmatrix}. \tag{2.59}$$

The exponentiation of these matrices gives

$$\begin{aligned} \exp\{\mathrm{i}\theta\sigma_i\} &= \mathbf{1} + \mathrm{i}\theta\sigma_i - \frac{\theta^2}{2!}\mathbf{1} - i\frac{\theta^3}{3!}\sigma_i + \frac{\theta^4}{4!}\mathbf{1} + \mathrm{i}\frac{\theta^5}{5!}\sigma_i - \ldots = \\ &= \left(1 - \frac{\theta^2}{2!} + \frac{\theta^4}{4!} - \ldots\right)\cdot\mathbf{1} + \mathrm{i}\left(\theta - \frac{\theta^3}{3!} + \frac{\theta^5}{5!} - \ldots\right)\cdot\sigma_i = \\ &= \cos(\theta)\cdot\mathbf{1} + i\sin(\theta)\cdot\sigma_i, \end{aligned} \tag{2.60}$$

in particular

$$e^{i\theta\sigma_x} = \begin{pmatrix} \cos(\theta) & i\sin(\theta) \\ i\sin(\theta) & \cos(\theta) \end{pmatrix}, \quad e^{i\theta\sigma_y} = \begin{pmatrix} \cos(\theta) & \sin(\theta) \\ -\sin(\theta) & \cos(\theta) \end{pmatrix}, \quad e^{i\theta\sigma_z} = \begin{pmatrix} e^{i\theta} & 0 \\ 0 & e^{-i\theta} \end{pmatrix}. \tag{2.61}$$

Thus, the propagators of the pulses along three orthogonal axes are

$$e^{\pm\mathrm{i}\theta\hat{S}_x} = \exp\left\{\pm\mathrm{i}\frac{\theta}{2}\sigma_x\right\} = \begin{pmatrix} \cos\left(\frac{\theta}{2}\right) & \pm\mathrm{i}\sin\left(\frac{\theta}{2}\right) \\ \pm\mathrm{i}\sin\left(\frac{\theta}{2}\right) & \cos\left(\frac{\theta}{2}\right) \end{pmatrix}, \tag{2.62a}$$

$$e^{\pm i\theta\hat{S}_y} = \exp\left\{\pm i\frac{\theta}{2}\sigma_y\right\} = \begin{pmatrix} \cos\left(\frac{\theta}{2}\right) & \pm\sin\left(\frac{\theta}{2}\right) \\ \mp\sin\left(\frac{\theta}{2}\right) & \cos\left(\frac{\theta}{2}\right) \end{pmatrix}, \tag{2.62b}$$

$$e^{\pm i\theta\hat{S}_z} = \exp\left\{\pm i\frac{\theta}{2}\sigma_z\right\} = \begin{pmatrix} e^{\pm i\frac{\theta}{2}} & 0 \\ 0 & e^{\mp i\frac{\theta}{2}} \end{pmatrix}. \tag{2.62c}$$

2.4 Effect of the RF and MW pulses

In this work, only selective pulses have been used: pulses that affect a single particular transition. The $\pi/2$ and π pulses are of utmost significance. In order to understand their effect, consider a four-level system with electron spin $S = 1/2$ and the same nuclear spin $I = 1/2$. To simplify the description, we construct a formal Hamiltonian which includes isotropic electron and nuclear Zeeman terms and a secular hyperfine term:

$$\hat{\mathcal{H}} = \mu_B g B_0 \hat{S}_z - \mu_N g_N B_0 \hat{I}_z + A\hat{S}_z\hat{I}_z \tag{2.63}$$

The schematic energy diagram corresponding to this Hamiltonian is shown in Figure 2.2. The levels are labelled both in the $|m_S, m_I\rangle$ and in a simple numerical notation. We will use the latter notation henceforth so that, for instance, a reference to transition $(1,3)$ will mean the transition $|-1/2,-1/2\rangle \leftrightarrow |+1/2,-1/2\rangle$. It is useful to remember that the levels which are located on the same vertical floor but at different horizontal displacement have the same m_S but different m_I – they represent nuclear sub-levels in the same electron manifold. In its turn, the levels on the same vertical line have different m_S but the same m_I – they are electron sub-levels in the same nuclear manifold. The filled rectangles in the diagram indicate an excess population while the hollow rectangles correspond to a deficit population.

Diagrams like that described will significantly facilitate understanding of complex pulse sequences, especially those explored in Chapter 6. The building blocks of any pulse sequence are MW or RF pulses, so in this section, I elucidate how different pulses affect the state of the spin-system and how it is reflected in its energy diagrams. We start with the system in thermal equilibrium at which the levels

with $m_S = -1/2$ (lower) are more populated and the state is described by density operator $\rho(0) = -\hat{S}_z\hat{\mathbf{1}}_\mathrm{n}$ (see Figure 2.2(a)).

2.4.1 Polarisation

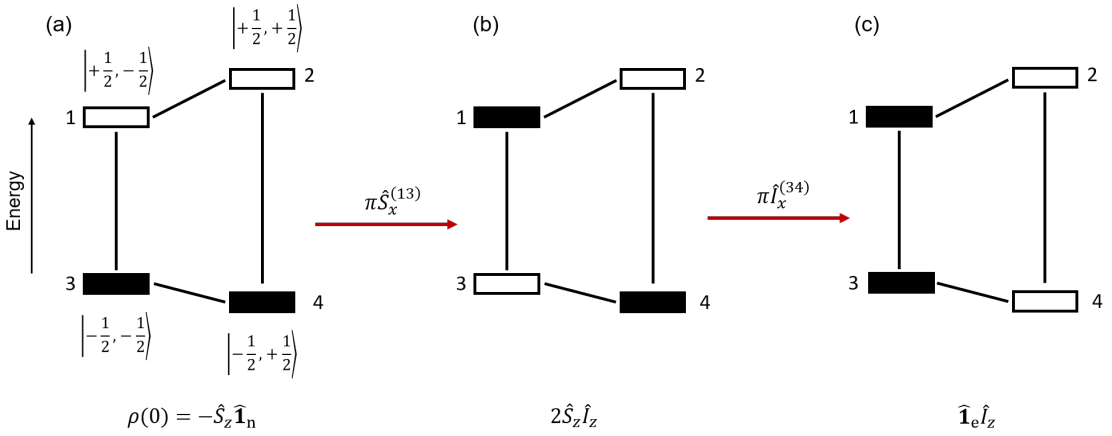

Figure 2.2: Energy-level diagram of a four-level system of two coupled spins $S = 1/2$ and $I = 1/2$. (a) At thermal equilibrium; (b) after application of a MW π-pulse on electron transition $(1, 3)$; (c) after application of an RF π-pulse on nuclear transition $(3, 4)$.

A selective MW pulse resonant with transition $(1, 3)$ inverts the polarization of the involved electron sub-levels and creates the electron-nuclear two-spin order (see Figure 2.2(b)). The spin-operator representation of this inversion is

$$\rho(0) = -\hat{S}_z\hat{\mathbf{1}}_\mathrm{n} \xrightarrow{\pi\hat{S}_x^{(13)}=\frac{\pi}{2}(\hat{S}_x+2\hat{S}_x\hat{I}_z)} 2\hat{S}_z\hat{I}_z. \tag{2.64}$$

For the pulse to be selective, it is required that its length t_p is larger than the reciprocal of A/h, which defines the separation of nuclear sub-levels in the same electron manifold. In the literature, this condition is known as hyperfine contrast selectivity [90].

In the same way, an RF pulse resonant with the nuclear transition $(3, 4)$ inverts the corresponding nuclear polarisation and equates the population on the electron sub-levels with equal m_I:

$$2\hat{S}_z\hat{I}_z \xrightarrow{\pi\hat{I}_x^{(34)}=\frac{\pi}{2}(\hat{I}_x-2\hat{S}_z\hat{I}_x)} \hat{\mathbf{1}}_\mathrm{e}\hat{I}_z. \tag{2.65}$$

The resulting energy diagram is shown in Figure 2.2(c).

2.4.2 Coherence

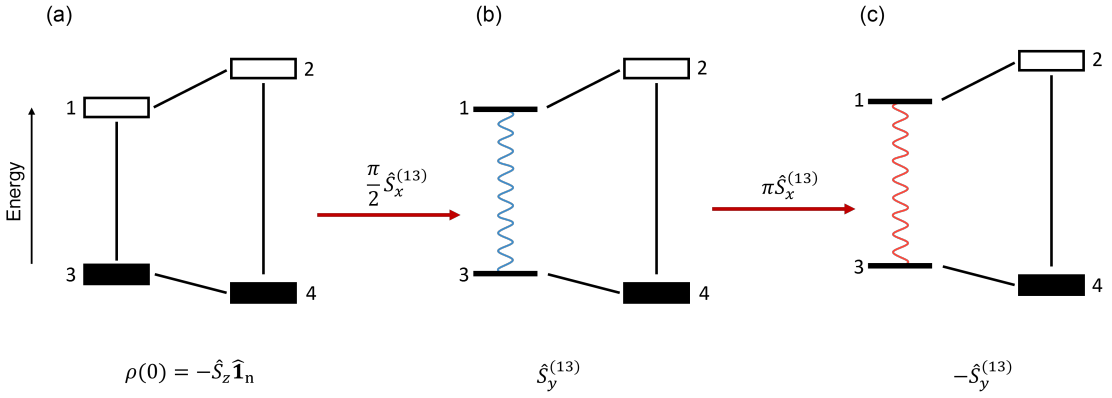

Figure 2.3: Energy diagrams reflecting the generation and inversion of spin coherence. (a) Initial thermal equilibrium; (b) generation of coherence by a MW $\pi/2$-pulse on electron transition $(1,3)$; (c) inversion (refocusing) of the evolution of coherence by applying a π-pulse on the same transition $(1,3)$.

Starting with the equilibrium state, the coherence can be generated by applying a selective $\pi/2$-pulse. Figure 2.3(a) and (b) demonstrate this process on transition $(1,3)$. It is conventional to denote coherence as a wavy line connecting the two levels. The spin-operator representation of this operation is a bit more convoluted:

$$-\hat{S}_z\hat{\mathbf{1}}_n \xrightarrow{\frac{\pi}{2}\hat{S}_x^{(13)}} \frac{1}{2}\left(2\hat{S}_z\hat{I}_z - \hat{S}_z\hat{\mathbf{1}}_n\right) + \frac{1}{2}\left[\hat{S}_y + 2\hat{S}_y\hat{I}_z\right] = \frac{1}{2}\left(2\hat{S}_z\hat{I}_z - \hat{S}_z\hat{\mathbf{1}}_n\right) + \hat{S}_y^{(13)}. \tag{2.66}$$

Only the terms in square brackets represent the actual coherence, whereas the terms in round brackets are responsible for the change in polarisation: the population on levels 1 and 3 have equalised, while that on levels 2 and 4 has been left unaffected. To shorten the notation we introduced the coherence operator $\hat{S}_y^{(13)} = \frac{1}{2}\left[\hat{S}_y + 2\hat{S}_y\hat{I}_z\right]$.

A subsequent π-pulse on the same transition inverts the evolution of the coherence

$$\frac{1}{2}\left(2\hat{S}_z\hat{I}_z - \hat{S}_z\hat{\mathbf{1}}_n\right) + \hat{S}_y^{(13)} \xrightarrow{\pi\hat{S}_x^{(13)}} \frac{1}{2}\left(2\hat{S}_z\hat{I}_z - \hat{S}_z\hat{\mathbf{1}}_n\right) - \hat{S}_y^{(13)}. \tag{2.67}$$

In Figure 2.3(c) the inversion of the coherence is shown with the wavy line being reflected and having a different colour. The two equations demonstrate that in experiments where only coherence is important, one could treat $\hat{S}_z$ as $\hat{S}_z^{(13)}$, thus considering just the $m_I = -1/2$ manifold, and ignore the nuclear spin-operators

and polarisation completely. Though the π-pulse seemingly does not do much with the coherence, it is a member of a family of tools used for refocusing the coherence. We will discuss how a π-pulse refocuses the coherence and why it is important in Section 2.4.3.

In the spin-operator equations above we considered the evolution of the spin system only under the action of a pulse while neglecting the static Hamiltonian 2.63. This corresponds to treating the pulses as infinitely short. This is normally a valid approximation in ESR and NMR when the excitation pulses are short and powerful, and the relaxation times of the spin species under study are much longer than the pulse duration. Nonetheless, in the pauses between pulses we must consider how coherence evolves under the action of the static Hamiltonian.

Having generated coherence, we might want to move it around between the levels. This is achievable with the use of π-pulses. Figure 2.4 demonstrates how the coherence on the electron transition $(1,3)$ can be transferred, first to the coherence on the forbidden and non-observable transition $(1,4)$ by an RF π-pulse which moves the tail of the wavy line from level 3 to level 4; then it is transformed into nuclear coherence on transition $(3,4)$ by a MW π-pulse moving another tail of the coherence curve from 1 to 3.

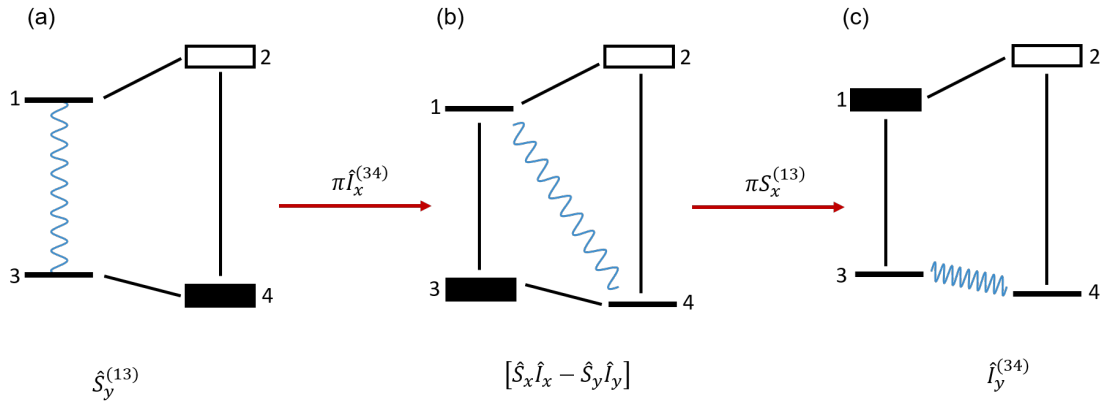

Figure 2.4: Energy diagrams reflecting the transfer of spin coherence (a) Initial coherence on transition $(1,3)$; (b) RF π-pulse transfers coherence to $(1,4)$; (c) MW π-pulse transfers coherence to $(3,4)$.

The spin-operator formulation reflects both the transfer of coherence and re-distribution of population between levels:

$$\frac{1}{2}\left(2\hat{S}_z\hat{I}_z-\hat{S}_z\right)+\hat{S}_y^{(13)}\xrightarrow{\pi\hat{I}_x^{(34)}=\frac{\pi}{2}(\hat{I}_x-2\hat{S}_z\hat{I}_x)}=\frac{1}{2}\left(\hat{I}_z-\hat{S}_z\right)+\frac{1}{2}\left[2\hat{S}_x\hat{I}_x-2\hat{S}_y\hat{I}_y\right], \quad (2.68)$$

$$\xrightarrow{\pi\hat{S}_x^{(13)}}-\frac{1}{2}\left(2\hat{S}_z\hat{I}_z+\hat{I}_z\right)+\frac{1}{2}\left[\hat{I}_y-2\hat{S}_z\hat{I}_y\right]=-\frac{1}{2}\left(2\hat{S}_z\hat{I}_z+\hat{I}_z\right)+\hat{I}_y^{(34)}. \quad (2.69)$$

As before, the coherence is represented by the terms in square brackets. The operator $\hat{I}_y^{(34)}=\frac{1}{2}\left[\hat{I}_y-2\hat{S}_z\hat{I}_y\right]$ denotes the nuclear coherence in manifold $m_S=-1/2$.

Apart from π- and $\pi/2$-pulses, one can apply pulses of arbitrary flip angle and phase. Their effect can still be approximated by Equation 2.45, or by performing a computer simulation of the density matrix evolution given by Equation 2.27.

In order to be measured, nuclear coherence has to be transferred back to electron coherences. Coherent electron spins form the transverse magnetisation $\left\langle\hat{S}_x\right\rangle$ and $\left\langle\hat{S}_y\right\rangle$ which are measured in an ESR spectrometer as the in-phase and quadrature components of a complex signal. It can be detected directly after a MW pulse as a free induction decay (FID), however this scheme is challenging to realise from an engineering point of view due to spectrometer's dead-time t_d (see Section 3.2). This issue can be solved by using the spin-echo sequence in which the system response can be delayed until after the dead-time is over.

2.4.3 Spin echo (or Hahn echo) sequence

It is difficult to overstate the importance of the spin echo sequence for ESR and NMR. It has become a standard tool for detecting both coherence and polarisation [90, 95]. It consists of just two pulses (see Figure 2.5): the $\pi/2$-pulse generates coherence between spins, and the π-pulse refocuses the coherence for it to be measured at a later time as a spin-echo. The pulse spacing and the period between the π-pulse and echo are denoted τ and are called the free-evolution periods, meaning that during them the system evolves only under the static Hamiltonian. The centre of the echo appears at $2\tau+t_e$, where t_e depends on the profile of the pulses and on their duration $t_{\mathrm{p}1}$ and $t_{\mathrm{p}2}$. Thus, if we use rectangular pulses of equal length, then $t_e=1.1t_{\mathrm{p}1}$, however if $t_{\mathrm{p}2}=2t_{\mathrm{p}1}$, $t_e=1.7t_{\mathrm{p}1}$ [90, 102]. Formally, the window during

which the echo is detected and recorded is also included in the sequence, whose overall length theoretically does not exceed $2(\tau + t_{\mathrm{p2}})$ [103, 104].

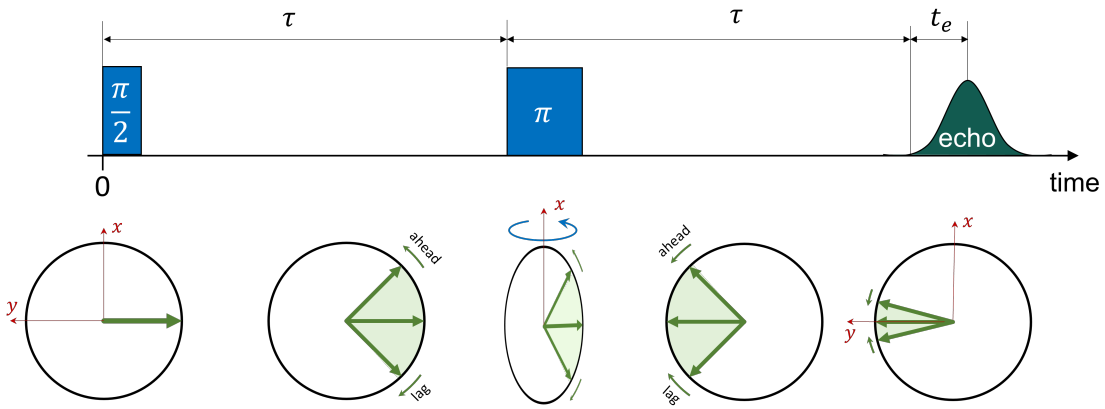

Figure 2.5: The spin echo pulse sequence and the schematic representation of the spin evolution.

To understand the echo phenomenon, consider a distribution of the spin packets over their resonance frequency ω_S due to, for instance, inhomogeneity in the static field $\boldsymbol{B}_0$. We will denote the offset of the Larmor frequency of a particular spin packet from the MW frequency of the excitation pulses as $\Omega_S = \omega_S - \omega_{\mathrm{MW}}$. Treating the pulses as instantaneous, the evolution of the spin system during the spin-echo sequence is expressed in the rotating frame in terms of the spin-operators as

$$\hat{\rho}_{\mathrm{eq}} = -\hat{S}_z \xrightarrow{\frac{\pi}{2}\hat{S}_x} \hat{S}_y \tag{2.70}$$

$$\xrightarrow{\Omega_S \tau \hat{S}_z} \hat{S}_y \cos(\Omega_S \tau) - \hat{S}_x \sin(\Omega_S \tau) \tag{2.71}$$

$$\xrightarrow{\pi \hat{S}_x} -\hat{S}_y \cos(\Omega_S \tau) - \hat{S}_x \sin(\Omega_S \tau) \tag{2.72}$$

$$\xrightarrow{\Omega_S t \hat{S}_z} -\hat{S}_y \cos(\Omega_S(\tau - t)) + \hat{S}_x \sin(\Omega_S(\tau - t)) \tag{2.73}$$

The sum of the final contributions with different Ω_S is non-zero only when $t = \tau$, so that the measured signal $\mathrm{Tr}(\rho S_y)$ is maximal at time 2τ after the start of the sequence. The evolution of the spin system under these equations can be visualised in the rotating frame by magnetisation vector pictures (see the lower panel of Figure 2.5).

Initially, the spin system was at its thermal equilibrium described by the density operator $-\hat{S}_z$, which corresponds to the macroscopic magnetisation lying along the

z-axis and perpendicular to the plane of the figure. The $\pi/2$-pulse rotates the spins into the transverse plane and aligns them with the negative direction of the y-axis. Since the spin packets have different resonance frequency, the magnetisation vectors of each spin packet start to fan out during the first period of free evolution.[3] In the figure, the fast spins rotate anticlockwise, while the slow spins rotate clockwise. After time τ, the π-pulse turns all the magnetisation vectors by 180° about the x-axis. Since the direction of the static magnetic field has not changed, the fast and slow spins continue rotating in their previous directions. As a result, the fan of the magnetisation vectors start collapsing and gives rise to a non-zero y-projection of the net magnetisation (refocusing). This resulting transverse magnetisation is called a *spin echo*. The y-projection reaches its maximum at approximately 2τ and then the separate vectors start to fan out again generating the falling slope of the echo.

The orientation of the y- and x-axes in the rotating frame can be chosen arbitrarily. In any case, a general spin echo signal will consist of two components corresponding to two projections of the net transverse magnetisation on the two orthogonal axes. Conventionally, one component is called the 'in-phase' signal, and the second one is known as the 'quadrature' component (see also Section 3.2.3).

The spin echo sequence is used as a detection scheme in many measurements [90]. Two common measurements are those for obtaining the EPR spectra and those which measure the relaxation times.

2.4.3.1 Echo-detected field sweep (EDFS)

An echo detected field sweep is performed by measuring the signal produced by the spin echo sequence at constant time intervals but at different values of the static field $\boldsymbol{B}_0$ (the field is swept). An example of a spectrum obtained by this technique is shown in Figure 2.6. Both the in-phase and quadrature components are read-out and the final spectrum is taken as the magnitude of the two-dimensional echo signal at each value of $\boldsymbol{B}_0$.

[3] This process is also known as inhomogeneous broadening.

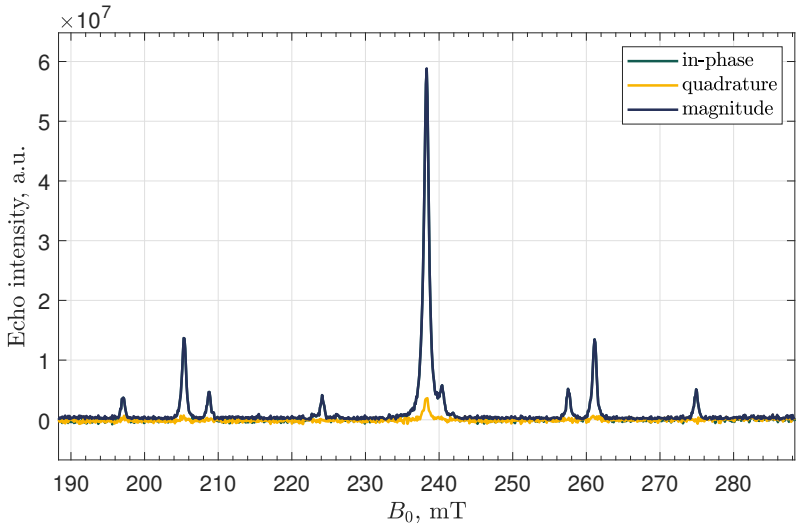

Figure 2.6: The EDFS of an [Yb (trensal)] sample at 9.79 GHz

The EDFS yields the EPR transition fields (spectrum), from which, in conjunction with other information, the spin-structure can be deduced [89–91]. The values of the parameters of the corresponding Hamiltonian are normally obtained by fitting the experimental spectra with simulation results. In my work, I have used either a home-written code or EasySpin [105] – an extensive library for simulating ESR data in MATLAB.

The example spectrum demonstrated in Figure 2.6 was measured on a single crystal of [Yb (trensal)] compound with its three-fold axis oriented perpendicularly to the $\boldsymbol{B}_0$ field. We knew that the source of the paramagnetic signal was the single unpaired electron of the ions of Yb. In the figure, we see three groups of peaks: one large central peak, two side peaks and six small peaks, one of which is located on the slope of the central feature. It could be assumed that the peaks were produced by three different isotopes with the nuclear spins $I = 0$, $I = 1/2$ and $I = 5/2$ [89–91]. And indeed, there are exactly three groups of isotopes of Yb with those values of I. Further details of how we used the obtained EDFS spectrum for studying [Yb (trensal)] are presented in Chapter 5.

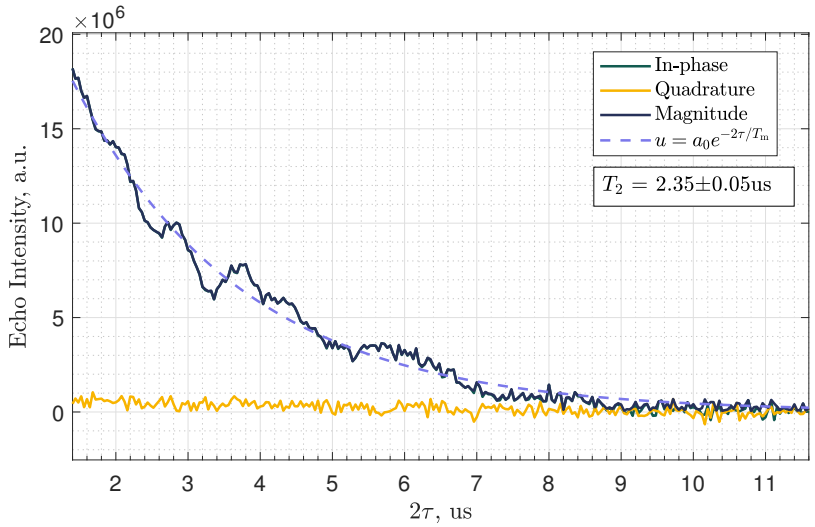

Figure 2.7: An example off the ESEEM measurement on [Yb (trensal)] at 261.1 mT

2.4.3.2 Measurement of relaxation times

The spin echo sequence with variable duration of the free-evolution period τ is used for obtaining the electron spin echo envelope modulation (ESEEM) data. An example graph obtained on an [Yb (trensal)] sample by sweeping τ at 261.1 mT is shown in Figure 2.7. The data consist approximately of an exponential decay with superimposed periodic oscillation. The latter can be used for studying the hyperfine and nuclear quadrupole interactions (see also ENDOR in Section 2.4.4), while the former provides an estimate of the transverse relaxation time T_2 or the phase memory time T_m [90]. The value of T_2 is found by fitting an exponential decay function

$$u(\tau) = a_0 e^{-\frac{2\tau}{T_2}} \tag{2.74}$$

to the experimental data. In this formula, 2τ is the total amount of time passed between the generation of coherence (transverse magnetisation) by the first $\pi/2$-pulse and the generation of the echo. The echo intensity decays exponentially with time 2τ with the characteristic time T_2 describing the relaxation of the electron coherence (see also Section 2.2.5). If a single exponential function fails to fit the data, a stretched exponential can be used to obtain the phase memory time [33]:

$$u(\tau, x) = a_0 \exp\left(-\left[\frac{2\tau}{T_\mathrm{m}}\right]^x\right), \tag{2.75}$$

where x here is known as the 'stretch parameter'. The value of x is determined by the mechanism of phase memory decay [97]. The oscillatory behaviour of the ESEEM is modelled phenomenologically as a sum of decaying oscillations as

$$u(\tau) = \sum_i a_i \cos(2\pi f_i \cdot 2\tau + \varphi_i) \exp\left(-\left[\frac{2\tau}{T_{\mathrm{m}i}}\right]^{x_i}\right), \tag{2.76}$$

where f_i and φ_i are the frequency and phase of the i-th ESE modulation component [90].

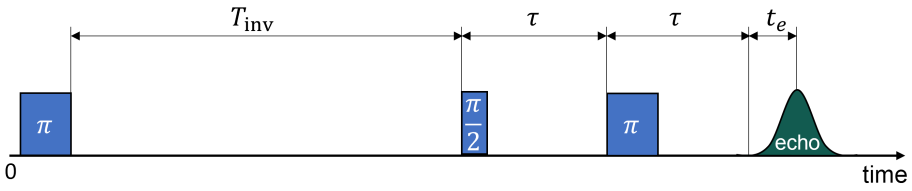

Figure 2.8: Inversion recovery sequence.

The longitudinal relaxation time is typically measured by means of the inversion-recovery sequence shown in Figure 2.8. The first π-pulse inverts the polarisation, after which we wait for time T_{inv} for the polarisation to recover back to equilibrium. The recovery is expected to follow an exponential law with the characteristic time T_1:

$$u(T_{\mathrm{inv}}) = a_0 \left(1 - 2e^{-\frac{T_{\mathrm{inv}}}{T_1}}\right) \tag{2.77}$$

However, when several processes contribute to the recovery process, a single exponential function is not able to describe the experiment. In those cases, a double-exponential function can help.

An example of this type of measurements together with the fit is demonstrated in Figure 2.9. There, the rotated spectrum is that where all signal was put into the in-phase component at the post-processing stage. In contrast to the echo magnitude, the rotated spectrum does not lose the sign of the magnetisation.

Another way of estimating the longitudinal relaxation time is to sweep the shot repetition time[4] while performing the spin echo sequence with all the other parameters unchanged. In this scenario, the echo magnitude follows a similar saturation graph but starts from 0 instead of from a negative value.

[4]The pause between separate spin echo sequences.

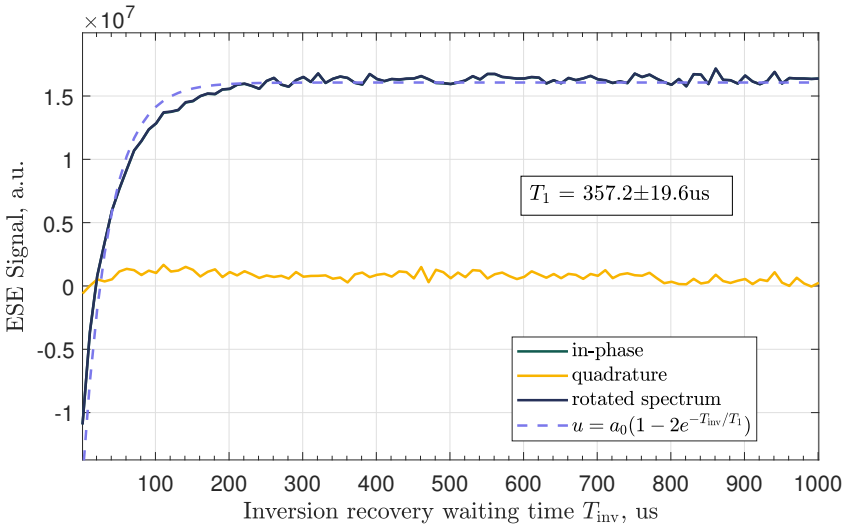

Figure 2.9: An example off the inversion-recovery measurement on [Yb (trensal)] at 261.1 mT

2.4.4 Davies ENDOR

Electron-nuclear double resonance (ENDOR) is a technique for measuring nuclear transition frequencies of paramagnetic compounds [90, 106]. Direct measurement of nuclear spins requires very high concentration of paramagnetic centres which significantly compromises the coherence time of the electron spins owing to dipolar interaction. The ENDOR experiment overcomes this issue by measuring the nuclear spins indirectly via the electron spin echoes. The two standard types of sequences, Davies [107] and Mims [108] ENDOR, are used for compounds with strong and weak hyperfine interactions, respectively. The strong interaction is that which allows us to use selective pulses to excite separate electron transitions. For instance, the manganese ions we are going to discuss in Chapters 4 and 6 posses $A/h \approx 200$ MHz. This hyperfine constant provides a good spectral addressability of $\Delta m_S = \pm 1$ ESR transitions for different m_I projections using pulses longer than 5 ns, and thus falls into the strong-interaction category.

The pulse sequence of Davies ENDOR is shown in Figure 2.10. The energy diagram of a two-spin system at different stages of the pulse sequence is shown in Figure 2.11. First, the MW π-pulse $\pi\hat{S}_x^{(13)}$ generates a two-spin order $2\hat{S}_z\hat{I}_z$. Next, the RF π-pulse attempts to swap the polarisation of levels on either of the nuclear

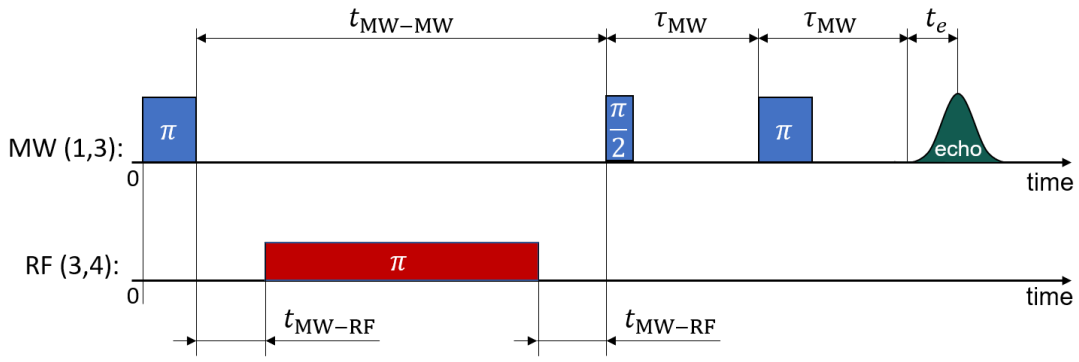

Figure 2.10: Pulse sequence of the Davies ENDOR experiment

transitions $(1, 2)$ or $(3, 4)$ – the success of this attempt depends on the frequency of the pulse f_{RF}. Finally, the last two MW pulses constitute the spin-echo sequence which converts the polarisation difference between 1 and 3 into electron coherence.

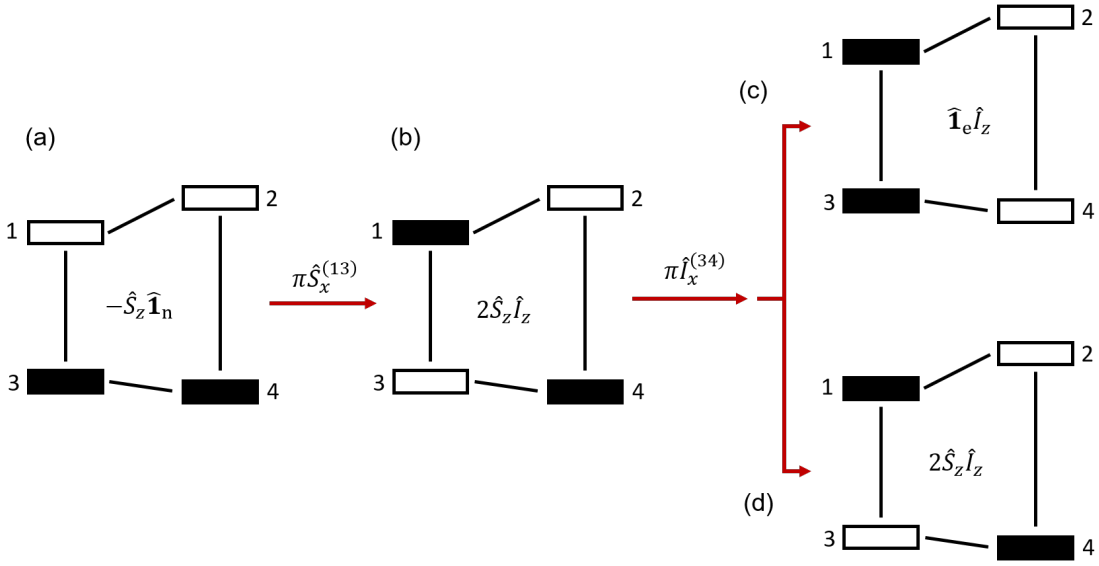

Figure 2.11: Evolution of the energy-level diagram for a two-spin system during Davies ENDOR experiment. Branch (c) does not produce a spin echo, whereas branch (d) does produce an echo signal.

During the experiment, one keeps the static field $\boldsymbol{B}_0$ constant but sweeps the frequency of the RF pulse. If f_{RF} matches the resonance frequency of, for instance, transition $(3, 4)$, the energy diagram evolves from (b) along the branch (c). In this case, levels 1 and 3 obtain roughly equal population and the spin-echo sequence does not generate echo. If, on the contrary, the bandwidth of the RF pulse does not cover the required resonance frequency, the energy diagram does not change and remains

in the two-spin order (branch (d)). In this case, the echo generated by the spin-echo sequence is at its strongest. Normally, the second scenario happens overwhelmingly more often during a frequency sweep, and the resulting dependence of the echo intensity on f_{RF} contains just several sharp dips representing the nuclear resonance. An example of a Davies ENDOR spectrum can be found in Figure 6.2(b).

The practical aspects of performing the Davies ENDOR measurement include choosing the right power/duration ratio of the pulses, and the delays between them. The pulses must achieve the required flip-angles. The time after inverting the polarisation by the first pulse and up until the $\pi/2$-pulse $t_{\mathrm{MW-MW}}$ should be shorter than the electron longitudinal relaxation time. For the same reason, the spacing between the MW and RF pulses $t_{\mathrm{MW-RF}}$ should also be kept short but not zero to allow for any ringdown effects and avoid spurious signals [109].

2.4.5 Electron-nuclear coherence transfer (ENCT-1)

This next pulse sequence allows one to test the possibility of transfer of coherence between the electronic and nuclear degrees of freedom [110–112]. A successful transformation of the electron coherence into the nuclear coherence and back can confirm that quantum information can be generated, encoded, and read out in an electron-nuclear coupled system. This will be an invaluable testing device in Chapter 6 where I discuss a quantum error-correction protocol exploiting nuclear spin degrees of freedom.

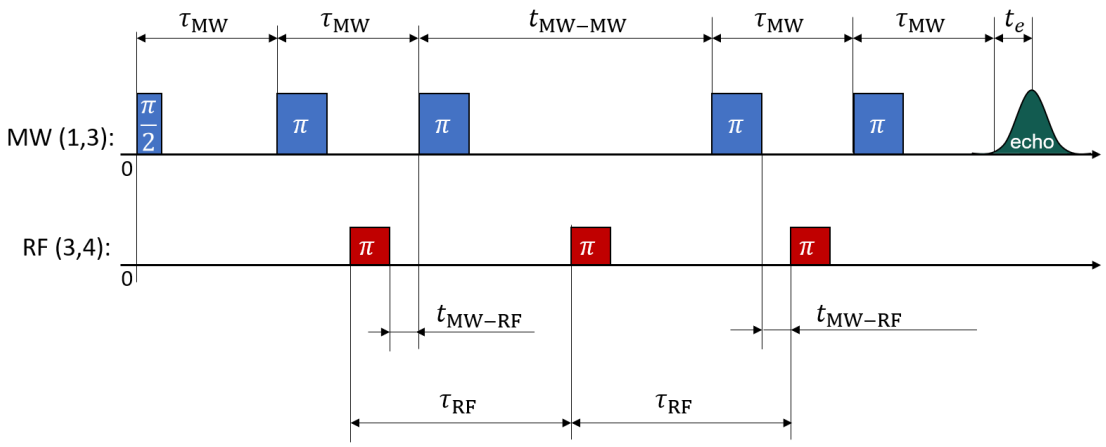

Figure 2.12: ENCT-1 pulse sequence.

The pulse sequence is shown in Figure 2.12. It was designed with the intention of dealing with inhomogeneous distribution of spins in mind; therefore, it contains several refocusing pulses. This sequence will serve as a basis for more complex sequences discussed in Chapter 6, so here I explain the action of each pulse in detail. In describing the evolution of the spin system, I will be referring to its states shown in the energy-level diagram in Figure 2.13.

As usual, we start with thermal equilibrium $\rho(0) = -\hat{S}_z$. The first MW $\pi/2$-pulse generates coherence on electron transition $(1,3)$ (states (a) and (b)). During the first delay τ_{MW} the coherence evolves under the static Hamiltonian $\hat{\mathcal{H}}_0$. In terms of macroscopic magnetisation, similar to that which we discussed in the context of spin-echo sequence, the magnetisation vectors fan out thus decreasing the amplitude of the net transverse magnetisation (cf. Figure 2.5). The second MW pulse refocuses the coherence (state (c)) and forces the spin-vectors to synchronise at approximately $2\tau_{\mathrm{MW}}$. At around that time, the first RF π-pulse transfers one tail of the coherence from level 3 to level 4 (state (d)). The subsequent MW π-pulse transfers the other tail of coherence to level 3 thus completing the transformation of the electron coherence on transition $(1,3)$ to the nuclear coherence on transition $(3,4)$ (state (e)).

The relaxation process of nuclear spins are normally slower than those of electron spins. Consequently, the nuclear coherence can be stored on transition $(3,4)$ for longer periods τ_{RF}, during which the nuclear spin packets with different Larmor frequencies are refocused using an RF π-pulse (see Section 2.4.6). In particular, the second RF π-pulse inverts the evolution of spin packets (state (f)) so that the nuclear coherence refocuses approximately at time $2\tau_{\mathrm{RF}}$ after its generation. At this moment the nuclear coherence can be transformed back to the electron coherence in order to be measured. For that, the MW π-pulse moves one tail of the wavy line from level 3 to level 1 (state (g)), and then the last RF π-pulse moves the other tail from level 4 to level 3 (state (h)). At this moment the coherence is back on transition $(1,3)$. It is refocused by the last MW π-pulse (state (i)) and measured as electron spin echo at time τ_{MW} after the last pulse.

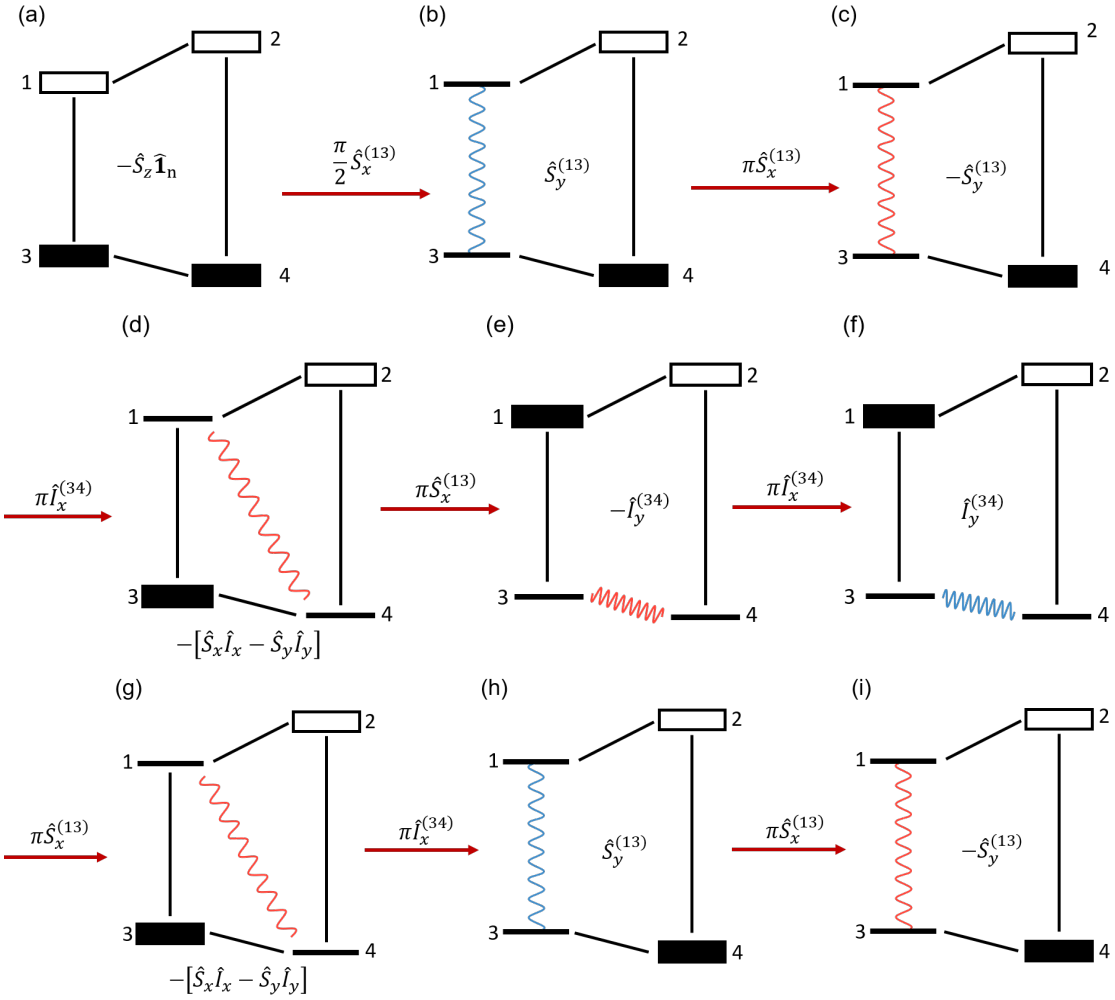

Figure 2.13: Evolution of the two-spin system during the ENCT-1 pulse sequence.

With an increase in τ_{RF}, the intensity of the ESE goes down, normally following a decaying exponential function. By measuring ESE at different τ_{RF} we can estimate the nuclear phase relaxation time – see, for instance, Figure 6.8.

For the sequence to work as expected, the RF and MW pulses should be selective. The frequency of the MW excitation must match the electron resonance $(1,3)$, while the frequency of the RF pulses must be that of the nuclear resonance $(3,4)$. The time τ_{MW-RF} separating the RF and MW pulses should be sufficient to prevent the RF and MW pulses from overlapping with one another. From a practical point of view, it is determined by the delays with which the pulses reach the resonator after generation, and by ringing of the RF coil. At the same time, it should be kept sufficiently short to bring the pulses close to the moment when the coherence is refocused.

From an experimental perspective, the final echo can have various undesired contributions, including the stimulated electron spin echo (which decays on the timescale of T_{1e}), electron echo/free induction decay due to the last two MW π-pulses, and detector's DC offset. To eliminate these contributions we implement a four-step phase cycling of the initial MW $\pi/2$ and the refocusing RF π-pulses (Table 2.1). This ensures that the measured echo signal is purely due to the transfer of the initial electron coherence via the nuclear spins.

Step number	MW $\pi/2$-pulse	RF π-pulse	Detection
1	$+x$	$+x$	$+$
2	$-x$	$+x$	$-$
3	$+x$	$+y$	$-$
4	$-x$	$+y$	$+$

Table 2.1: The phase cycling sequence and the signal for the ENCT-1 scheme.

The refocusing pulses do not have to be exclusively $\hat{J}_x$-pulses, but can have an arbitrary phase θ. This, however, affects the phase of the refocused coherence. We can examine this effect by varying the phase of the second nuclear pulse. Right before the pulse is applied, the system is in state (e) depicted in Figure 2.13 and its density operator is

$$\rho(c) = \frac{1}{2}\left(2\hat{S}_z\hat{I}_z + \hat{I}_z\right) - \frac{1}{2}\left[\hat{I}_y - 2\hat{S}_z\hat{I}_y\right]. \tag{2.78}$$

The selective refocusing π-pulse bearing an arbitrary phase θ changes the state

$$\rho(c) \xrightarrow{\pi\hat{I}_\theta^{(34)}} = \xrightarrow{-\theta\hat{I}_z^{(34)}} \xrightarrow{\pi\hat{I}_x^{(34)}} \xrightarrow{\theta\hat{I}_z^{(34)}} =$$
$$\frac{1}{2}\left(2\hat{S}_z\hat{I}_z + \hat{I}_z\right) + \frac{1}{2}\left[\hat{I}_y - 2\hat{S}_z\hat{I}_y\right]\cos(2\theta) - \frac{1}{2}\left[\hat{I}_x - 2\hat{S}_z\hat{I}_x\right]\sin(2\theta), \tag{2.79}$$

so that the resulting coherence acquires an additional phase of 2θ. As expected, the polarisation is left untouched.

2.4.6 Refocusing of the nuclear coherence

After its generation, the nuclear coherence $-\hat{I}_y^{(34)}$ (stage (e) in Figure 2.13) evolves under the static Hamiltonian 2.63, which in the doubly-rotating frame is given by

$$\hat{\mathcal{H}}_0'/\hbar = \Omega_S\hat{S}_z - \Omega_I\hat{I}_z + A'\hat{S}_z\hat{I}_z, \tag{2.80}$$

where Ω_S and Ω_I are the offset resonance frequencies of the electron and nuclear spin packets, respectively, and $A' = A/\hbar$. Thus, the evolution of coherence after time τ_{RF} is

$$-\hat{I}_y^{(34)} \xrightarrow{\tau\hat{\mathcal{H}}_0'/\hbar} -\hat{I}_y^{(34)} \cos\left(\left[\Omega_I + \frac{A'}{2}\right]\tau_{\mathrm{RF}}\right) - \hat{I}_x^{(34)} \sin\left(\left[\Omega_I + \frac{A'}{2}\right]\tau_{\mathrm{RF}}\right). \tag{2.81}$$

The refocusing π-pulse along the x-axis inverts the sign of the y-coherence but leaves the x-component unchanged:

$$\xrightarrow{\pi\hat{I}_x^{(34)}} \hat{I}_y^{(34)} \cos\left(\left[\Omega_I + \frac{A'}{2}\right]\tau_{\mathrm{RF}}\right) - \hat{I}_x^{(34)} \sin\left(\left[\Omega_I + \frac{A'}{2}\right]\tau_{\mathrm{RF}}\right). \tag{2.82}$$

After that, the coherence evolves freely again and in time t after the last pulse is

$$\xrightarrow{t\hat{\mathcal{H}}_0'/\hbar} \hat{I}_y^{(34)} \cos\left(\left[\Omega_I + \frac{A'}{2}\right]\tau_{\mathrm{RF}} - \left[\Omega_I + \frac{A'}{2}\right]t\right) - \\ - \hat{I}_x^{(34)} \sin\left(\left[\Omega_I + \frac{A'}{2}\right]\tau_{\mathrm{RF}} - \left[\Omega_I + \frac{A'}{2}\right]t\right). \tag{2.83}$$

The intensity of the y-component is maximal when $t = \tau_{\mathrm{RF}}$. This is the moment when the magnetisation vectors of individual refocused spin packets gather together and produce the maximal net magnetisation – the spin echo.

2.5 Electric-field effect

Chapters 4 and 5 focus on the investigation of electric field (E-field) effects in two distinct classes of compounds: the first comprising transition metal ions of manganese, and the second incorporating rare-earth ions of ytterbium. These compounds exhibit markedly different responses to the applied electric field, the specific characteristics of which are examined in detail within the respective chapters. This section provides a general overview of the theoretical aspects of the E-field effect and the methodology employed for its measurement. The experimental details of the measurement can be found in Section 3.4.

2.5.1 Change in the spin-Hamiltonian

We start our discussion of the E-field effect in solids by further simplifying the spin Hamiltonian given in Equation 2.5. In particular, we are going to neglect the nuclear Zeeman term due to its small energy scale. Here, the spin Hamiltonian takes the following form:

$$\hat{\mathcal{H}}_0 = \mu_\mathrm{B} \boldsymbol{B}_0^\mathrm{T} \mathbf{g} \hat{\boldsymbol{J}} + \hat{\boldsymbol{J}}^\mathrm{T} \boldsymbol{A} \hat{\boldsymbol{I}} + \sum_k \sum_{q=-k}^{k} B_k^q \hat{O}_k^q(\hat{\boldsymbol{J}}), \tag{2.84}$$

where as before, the first term is the Zeeman interaction of the unpaired electrons with the static magnetic field $\boldsymbol{B}_0$, the second term is the hyperfine interaction between the electrons and nucleus of the paramagnetic centre, and the last term is the multipole expansion of the crystal field (all the samples discussed in this thesis are crystals). We take into account only the nucleus of the paramagnetic centre itself and ignore all the nuclear interactions apart from the hyperfine one.

When an external electric field $\boldsymbol{E}$ is applied, it can affect the crystal environment of the paramagnetic centre by moving the ions and deforming the lattice, or it can modify the electron orbitals and, consequently, change the overall electron density distribution (i.e., polarising the wave functions). One of the examples of how the electric field can interact with a molecule is via the electric dipole of the latter: a bond between two ions with different electronegativity will either be stretched or shrunk when it is subject to $\boldsymbol{E}$. Mathematically, these changes appear as a modulation of the spin Hamiltonian parameters. Those are the $\mathbf{g}$-tensor, the hyperfine tensor $\boldsymbol{A}$, and all the coefficients B_k^q of the extended Stevens operators. In general, any of these parameters can be affected by $\boldsymbol{E}$ [53], however the symmetry of the spin system can significantly simplify the analysis by either eliminating certain terms in the Hamiltonian 2.84 directly, or by forbidding changes in some of the components of the mentioned parameters.

The terms modulated by the electric field will be some functions of $\boldsymbol{E}$. Even though in general those functions can take any form, here, we will be discussing only such changes of $\mathbf{g}$, $\mathbf{A}$ and B_k^q which are linear with respect to $\boldsymbol{E}$ (hence the name 'linear E-field effect') [53].

Any changes in the Hamiltonian will be rendered into a shift of its eigenvalues and modification of its eigenstates. In order to quantify the E-field effect, we use the ratio of these energy shifts expressed in frequency units to the magnitude of the electric field. We call the resulting quantity spin-electric coupling (SEC). The pulse ESR allows us to measure SEC with high sensitivity by employing a phase-sensitive detection (PSD) technique.

2.5.2 Measurement using PSD

In our experiments, the SEC is measured by incorporating an electric field pulse (E-field pulse) into the MW spin-echo sequence and by measuring the phase of the resulting electron spin echo (ESE) signal [113]. Both the original and modified spin-echo sequences are shown in Figure 2.14 together with a schematic representation of the motion of the magnetisation vectors. The time steps of both sequences are synchronised with respect to the location of the MW pulses and the echo response. The x- and y-axes are given in the rotating frame. Recall that the in-phase component of the echo is the projection of the net magnetisation vector onto the y-axis, whereas the quadrature component is the projection onto the x-axis.

As was demonstrated in Section 2.4.3, the application of only the microwave $\pi/2$ and π pulses, separated by τ_{MW} nanoseconds and with the oscillating magnetic field $\boldsymbol{B}_1$ directed along the x-axis, produces a spin echo signal after approximately $2\tau_{\mathrm{MW}}$ consisting purely of the in-phase component (see Figure 2.14(a)).

The modified spin-echo sequence is composed of the same MW pulses but has an additional E-field pulse applied right after the $\pi/2$-pulse (see Figure 2.14(b)). Because of that additional pulse, now it is not guaranteed that the echo signal will consist of the in-phase part only. The application of the E-field-pulse causes a shift in the eigenfrequencies of the Hamiltonian 2.84, detectable as an additional phase φ_{E} of the ESE:

$$\varphi_{\mathrm{E}} = 2\pi \cdot t_{\mathrm{E}} \cdot \delta f, \tag{2.85}$$

where t_{E} is the duration of the E-field pulse and δf is the shift in the resonant frequency. The value of the SEC is taken as the ratio $\delta f / E$ and measured in Hz/(V/m).

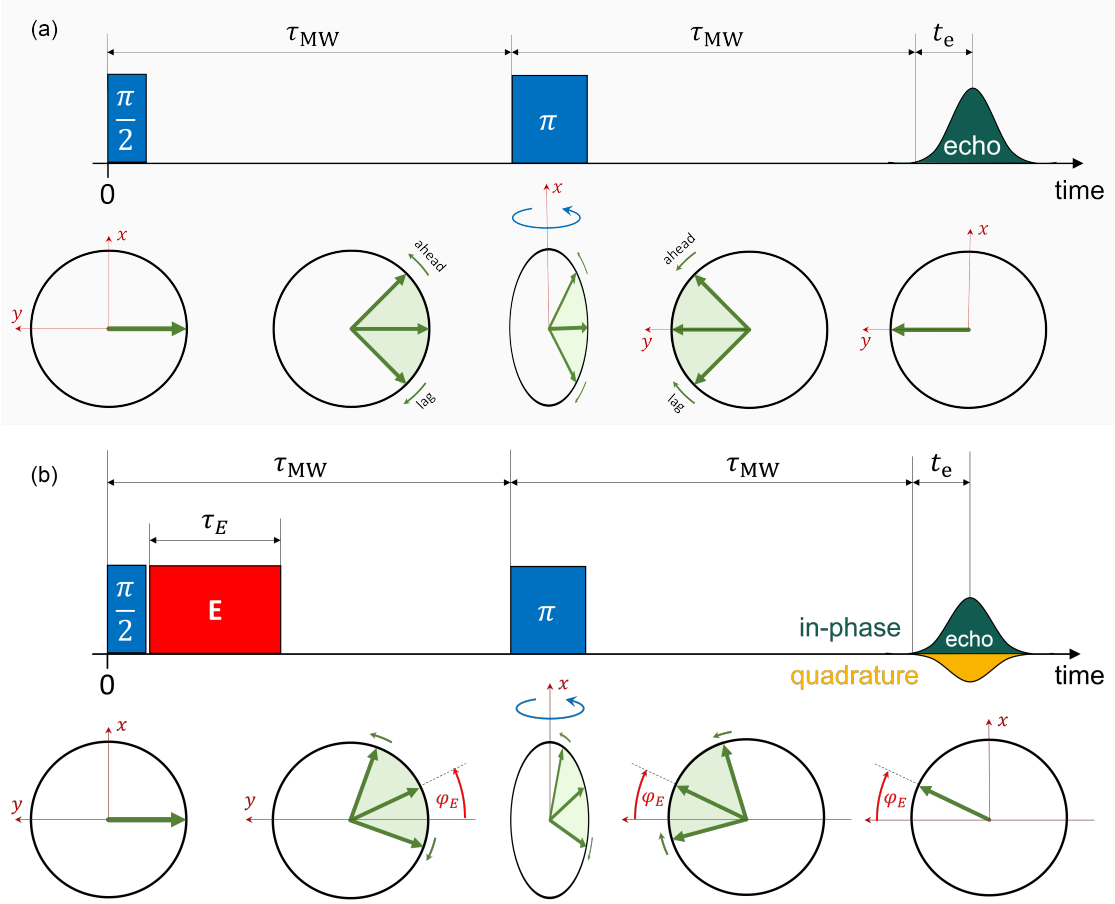

Figure 2.14: (a) The original spin-echo sequence and (b) the spin-echo sequence with an additional E-field pulse.

The set of the magnetisation vectors, which initially were along the z-axis, evolve during the pulse sequence in the following way. As in the original spin-echo sequence, the magnetisation is first rotated by $\pi/2$ into the xy transverse plane. During the first τ_{MW} period the vectors dephase from each other owing to inhomogeneities. Strictly speaking, it would be incorrect to call this period 'free evolution' because the system is subject to the additional electric field during an interval t_{E} inside that period, but we will do so colloquially. The E-field pulse speeds up or slows down all the spins equally and simultaneously, and shifts the centre of the fan of the magnetisation vectors to an angle φ_{E}, which is the phase shift acquired by the spins. The refocusing π-pulse inverts all the spins so that they start to gather into one single net-magnetisation vector again – its maximal magnitude will correspond to the maximal intensity of the ESE. The gathering process is the same as in the

original sequence, however, now the net magnetisation is at angle φ_E with respect to the y-axis. The y-projection of the net vector will be proportional to $\cos(\varphi_E)$, whereas the x-projection is proportional to $\sin(\varphi_E)$

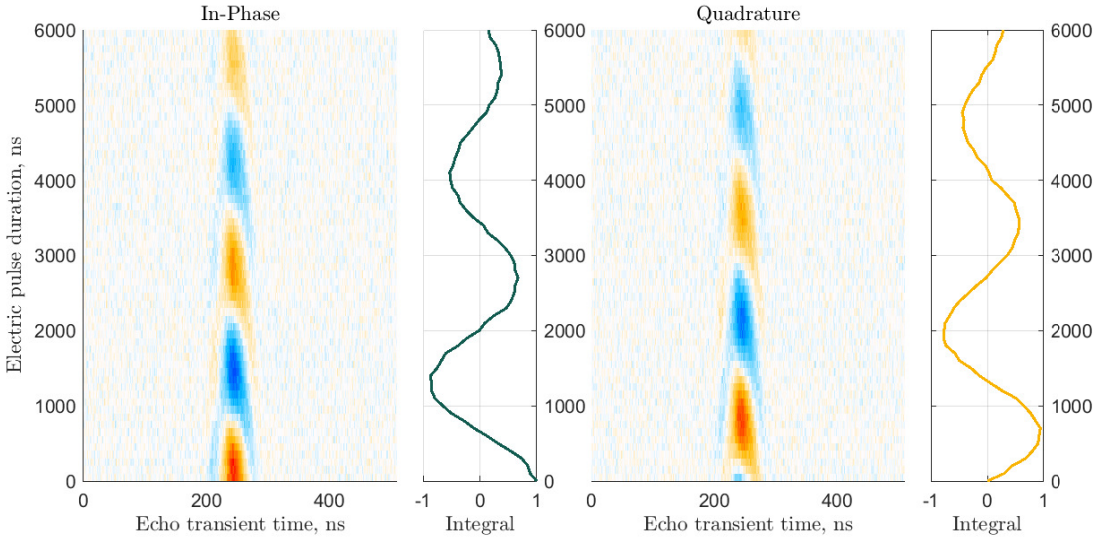

Figure 2.15: The phase-sensitive detection (PSD) of the spin-electric coupling (SEC). Sample: bipyramidal complex (**1**) (see Chapter 4), $\pi_{MW} = 32$ ns, $E \approx 240$ kV/m.

An example of the data acquired during a PSD measurement is shown in Figure 2.15. The 2D graphs demonstrate how the in-phase and quadrature components of the echo signal are changing with t_E. Each horizontal slice of these graphs represents the top-view of the echo signal: the horizontal axis corresponds to the time axis of the spectrometers' oscilloscope, and the colour represents both the intensity and the sign of the signal. The duration of the E-field pulse t_E is swept during the experiment and its values form the vertical axis of the 2D graphs. By moving from bottom to top we can track the evolution of the phase of the echo signal and observe how the signal transforms from the in-phase component to the quadrature component and back.

The side panels located next to the 2D graphs contain the integrated echo signal: this signal is proportional to $\cos(\varphi_E)$ and $\sin(\varphi_E)$ for the in-phase and quadrature components, respectively. In accordance with Equation 2.85, the Fourier transform

of the integrated echo yields the value of the frequency change δf due to the application of the E-field pulses of particular amplitude E.

The apparent decay of the ESE as t_{E} grows is typically caused by the spatial inhomogeneity in $\boldsymbol{E}$ (or in the SEC itself): different spin packets experience slightly different electric fields and with time the net magnetisation decreases (inhomogeneous broadening). This process is similar to that in the original spin echo sequence (see Section 2.4.3) and is reversible: the phase acquired during the first period of free evolution can be eliminated by applying the E-field pulse during the second free-evolution period. Examples of such phase recovery phenomena will be discussed in Sections 4.4.1 and 5.2.2.

2.5.3 A note on 'ligand field' and 'crystal field'

The distinction between the terms 'ligand field' and 'crystal field' remains ambiguously defined in much of the literature I have reviewed. Here, I use the explanation of their differences provided in References [91] and [114].

In the solid-state systems considered in this thesis, each paramagnetic ion is embedded within a crystal lattice composed of diamagnetic ions. The ions in closest proximity to the paramagnetic centre – whether or not they are chemically bonded to it – are referred to as 'ligands'. In organic chemistry, a ligand may also denote an entire functional group that coordinates with the central paramagnetic atom, forming a coordination complex. These ligand ions, typically charged, interact strongly with the paramagnetic ion, generating a significant electrostatic field known as the ligand field.

In crystal field theory, ligand ions and their associated orbitals are idealized as point charges. These are considered to establish an additional electrostatic potential – the crystal potential or crystal (electric) field – that embodies the symmetry of the coordination environment and its immediate surroundings. Magnetic electrons, which are localized on the central ion and subject to this potential, undergo a Stark splitting of their orbital energy levels. The lowest-energy orbitals are those in

which the negatively charged electrons are most effective at avoiding the negatively charged ligand ions, thereby minimizing electrostatic repulsion [91].

An advancement over the crystal field approximation is ligand field theory, which can be viewed as an extension of molecular orbital theory. This approach emphasizes the role of the central ion's d-orbitals and their overlap with orbitals of the surrounding ligands, offering a more nuanced and quantum-mechanically accurate depiction of the bonding and electronic structure in coordination complexes. [91, 114]

In other words, it seems that 'crystal field' is the most generic term used for denoting the field generated by the ions surrounding the paramagnetic centre of interest. The term 'ligand field' is used in this context when the authors would like to highlight the importance of the ligands coordinated with the central metal ion (for instance, in Reference [91]). The distinction between the crystal and ligand fields becomes important when one juxtaposes the corresponding two theories.

In this thesis, the notions of the crystal field and crystal-field parameters will be used in connection with the zero-field term in Hamiltonian 2.5 expressed via the extended Stevens operators:

$$\hat{\mathcal{H}}_{\mathrm{ZFS}} = \sum_{k} \sum_{q=-k}^{k} B_k^q \hat{O}_k^q(\hat{\boldsymbol{J}}). \tag{2.86}$$

Apart from the crystal field potential, this term also incorporates the electron spin-spin interaction and a pertinent part of the spin-orbit coupling [89].

2.6 Conclusions

This chapter establishes the general theoretical framework for the rest of the thesis. It introduces the basic concepts of nuclear and electron magnetic resonances and provides the mathematical tools required for describing quantum-physical phenomena and experiments. Two major tools are employed to examine and describe the states of spin ensembles and their evolution during experiments: the density operator formalism and the spin-operator formalism. Using these concepts, the chapter further explores how the control over a spin system can be achieved by using different MW and RF pulses. Building on this foundation, several measurement

techniques widely used in ESR are discussed. The details of our experimental setup are explained in Chapter 3.

The ENCT-1 sequence covered in Section 2.4.5 is the bulding block for the sequences we developed for the quantum error correction protocol presented in Chapter 6. The E-field effect introduced in Section 2.5 is the major topic of Chapter 4 and Chapter 5.

Chapter 3
Experimental setup

Contents

The projects presented in this thesis were performed either on the commercial Bruker spectrometers in the CAESR facility located in the Inorganic Chemistry Laboratory or on our custom-built spectrometer at the Department of Physics. This chapter is mostly devoted to the latter: I present the general scheme of our spectrometer and discuss the most important aspects of the ESR measurements.

The spectrometer description consists of the pulse and CW sections, with the former being the most used in our projects and the latter added here for the fullness of the narrative. I assembled, tested, and prepared our spectrometer under the guidance and supervision of Dr Junjie Liu and Prof Arzhang Ardavan.

3.1 Introduction: ESR spectrometer

Utilising magnetic resonance techniques, in particular ESR and NMR, is the method of choice when working with spins. An experimental setup which allows one to investigate magnetic resonance phenomena is conventionally called a *spectrometer*. The name assumes that one type of the output data of such a machine is a distribution of intensity of the resonance effect as a function of field and/or frequency. This, however, is not its only function: in general, the range of a spectrometer's capabilities will depend on its particular implementation, and each laboratory can assemble a device and maximise its performance for their specific tasks. Apart from custom-build devices, there are, of course, also commercially available spectrometers which are designed to serve as a set of user-friendly universal tools for performing all sorts of standard magnetic-resonance measurements.

In Oxford, the CAESR facility has several Bruker spectrometers which allow one to conduct a wide range of ESR measurements in X, Q, and W frequency bands (typically 9.7, 34 and 94 GHz, respectively). Commercial spectrometers are robust machines and we use them regularly to perform standard ESR experiments rapidly. However, they are rather rigid in terms of integrating with third-party devices, and it is rarely possible to modify the existing equipment to conduct new and non-standard experiments.

In order to have greater flexibility in designing and conducting state-of-the-art experiments, our group decided to set up a new customizable ESR spectrometer which would operate in X and Q bands.

There are two major branches of the ESR technique. Historically, the first one was the continuous wave (CW) ESR during which a sample is subject to EM radiation of a fixed frequency f_{MW} and relatively low and constant power while

its absorption (and/or dispersion) is measured as a function of $\boldsymbol{B}_0$ [115]. The second branch is the high-power pulse ESR in which EM pulses enable coherent manipulation of spins, thus allowing one to measure dynamic properties of spin systems [90]. Almost all experiments in this thesis were performed in the pulse mode, so we will discuss it first.

I begin by presenting the scheme of our spectrometer and then give a short description of a general measurement process. Subsequent sections provide deeper insight into particular technical details.

3.2 Pulse mode

The scheme of our spectrometer in its default configuration for performing pulse measurements is shown in Figure 3.1. In this configuration, the setup was used for implementing the quantum error correction protocol which I will present in Chapter 6.

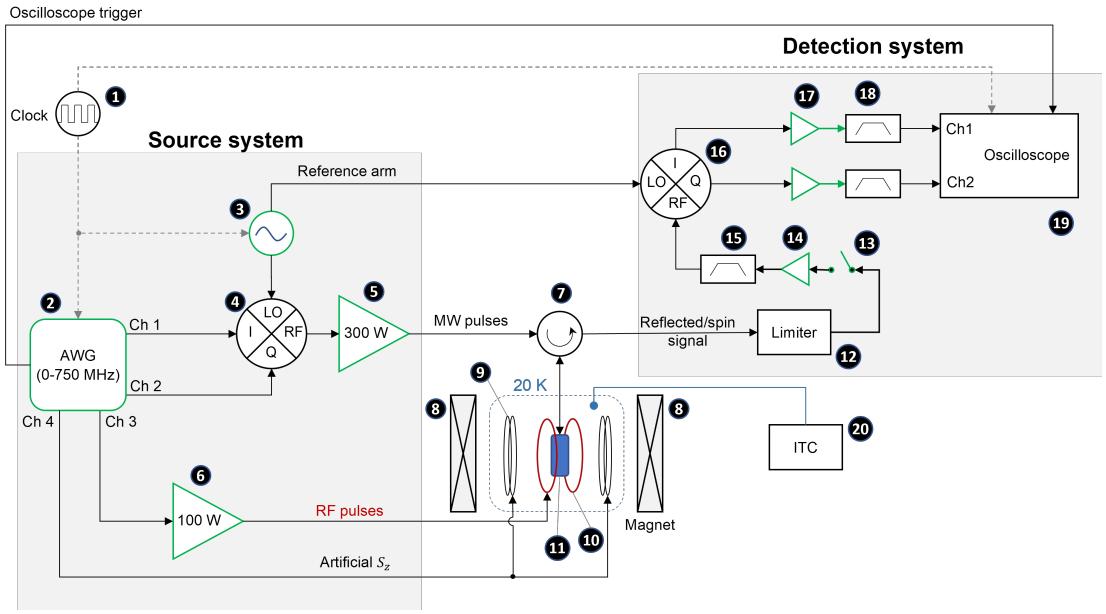

Figure 3.1: The schematic representation of the pulse ESR spectrometer we assembled at the Department of Physics.

The number-notation of the devices is as follows

1. Clock, 10MHz TTL-reference: Sandford Research Systems FS725

2. Arbitrary waveform generator (AWG): Zurich instruments, HDAWG 750 MHz, 4 ports
3. Microwave (MW) source: Keysight EE8257D PSG Signal Generator
4. IQ-mixer for up-conversion: MLIQ-0416, 4-16 GHz
5. MW Amplifier: ERZIA ERZ-HPA-0850-0980-55, 8.5-9.8 GHz, 60 dB, 300 W
6. RF Amplifier: Mini-Circuits ZHL-100W-52-S+, 50-500 MHz, 52 dB, 100 W
7. Microwave X-band circulator
8. Resistive magnet. Max field: 970 mT

9-11 : Bruker EN 4118X-MD4-W1 resonator inserted into an Oxford Instruments cryostat

9. Modulation coils
10. RF ENDOR coils
11. MW cavity, sample location

12. Limiter: Narda LIM 201, 1-18 GHz, max 1 us at 150W
13. Protection switch: SP213DHTS-80, 70 dB isolation
14. Cascade of low-noise MW amplifiers: Narda-MITEQ LNA-40-08001200-09-10P, unspecified 30 dB LNA, and Mini-Circuits ZX60-05113LN+
15. Cavity bandpass filter: Mini-Circuits ZVBP-9750-S+, 9.5-10 GHz
16. IQ-mixer for down-conversion: MLIQ-0416, 4-16 GHz (the same as 2)
17. Preamplifier: Sandford Research Systems SR445A, 350 MHz, 13dB, 10 W
18. Bandpass filter: Mini-Circuits BBP-100+, 87-117 MHz
19. Oscilloscope: Tektronix DPO7254 with FastFrame option
20. Intelligent temperature controller: ITC503

The AWG (2) and the power supply of magnet (8) are connected to the computer controlling the spectrometer via Ethernet, whereas MW source (3), oscilloscope (19) and the temperature controller (20) are connected via the GPIB interface. The MW signal is guided exclusively via the SMA coaxial cables, but for the RF signal we use both the SMA and BNC cables. The cryogenic temperatures are maintained by means of cryostat ESR CF935 (schematically denoted by the label '20 K'), gas flow controller VC41 (not shown), and temperature controller (20).

3.2.1 Short description of the measurement process

During measurements, a sample is located in the MW cavity of the Bruker EN 4118X-MD4-W1 (MD4) resonator (11), the static magnetic field $\boldsymbol{B}_0$ is generated by the resistive magnet (8), and the reference 10-MHz signal is provided by the frequency standard (1).

Pulse sequences are programmed in Python on an external computer and are uploaded onto the AWG (2) via an Ethernet interface. The external computer programmatically triggers the AWG (2) making it produce a required number of identical pulse-sequences (shots). At the end of each sequence, the AWG (2) sends a TTL trigger signal to the oscilloscope (19). The TTL pulse is synchronised with the RF and MW pulses.

The RF pulses are generated by the AWG (2) and get directly amplified at (6) before they are fed to the RF coil of the Bruker MD4 resonator (10). As for MW pulses, the AWG (2) first generates the envelopes of future MW pulses at 100MHz and sends them to the IQ-mixer (4), where they get mixed with the 9.8 GHz signal from the MW-source (3) and undergo up-conversion to about 9.7 GHz. After that, the MW pulses are amplified at (5) and enter the MW cavity of the MD4 resonator (11) directed by the circulator (7). A proper alignment of the MD4 resonator allows one to ensure that MW-field $\boldsymbol{B}_1$, RF-field $\boldsymbol{B}_2$ and the static field $\boldsymbol{B}_0$ are mutually perpendicular.

The MW excitation pulses reflected from the resonator cavity and the useful signal generated by the spin system are directed by the circulator (7) towards the detection circuit of the spectrometer. The excitation pulses are prevented from entering and damaging the detection system by the limiter (12) and protection switch (13). The opening time of the switch defines the dead-time of the spectrometer.

After the switch is closed, the signal produced by the spin-system can proceed to the cascade of low-noise amplifiers (14), band-pass filter (15), and to the IQ-mixer (16) where it gets down-converted to 100 MHz using the reference arm going from the MW-source (3). The use of the IQ-mixer (16) allows us to perform quadrature detection and obtain both the in-phase and quadrature components of the signal.

Both down-converted signals are amplified at (17), pass the band-pass filters (18), and reach the oscilloscope (19). The echoes resulting from separate shots of identical pulse-sequences are captured by the oscilloscope (19).

Finally, the external computer downloads the average signal from the oscilloscope for further data-processing.

Modification for the QEC project: The simulation of the $\hat{S}_z$-error for the quantum error correction protocol (see Section 6.5.2) was implemented using the modulation coils of the MD4 resonator (9). The corresponding pulses were incorporated into the pulse sequences uploaded to the AWG (2), whose output was fed to the modulation coils (9).

3.2.2 Bandwidth and filtering

All signals propagating in the spectrometer are subject to the filtering effect of the bandwidth of separate hardware components. Such filtering can be intentional as in filters (15) and (18), but most often it is caused by the general specifications of the devices.

While filters (15) and (18) are optional, there is one crucial component of the spectrometer with relatively narrow bandwidth which we cannot avoid: the MW cavity (11). Its frequency response in terms of B_1 field is shown in Figure 3.2. From it, we can estimate the resonator bandwidth as approximately 400 MHz. The bandwidth determines which MW frequencies survive in the cavity and consequently interact with the spin system in the most efficient way. It also limits the frequency content of the signal produced by the spins – the frequencies outside the bandwidth are quickly attenuated.

In case of a wide inhomogeneous broadening, the actual distribution of the resonance frequencies of spin packets in a sample can be wider than the resonator bandwidth. Since the ESR spectra are normally measured via a field sweep, it is convenient to express the bandwidth in the field units. Conventionally it is

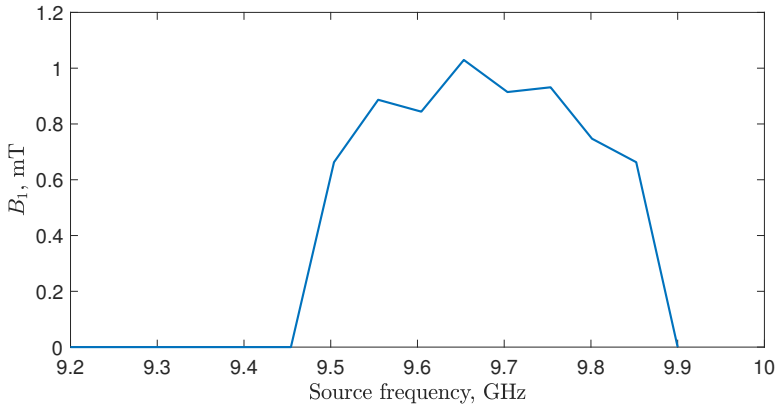

Figure 3.2: The bandwidth of a fully-overcoupled MD4 resonator. This was performed by Bruker in CAESR on the acceptance test in 2014. Adapted from the figure provided by Dr William Myers.

accomplished by using the Zeeman energy formula for spin-1/2 and the free-electron g-factor:

$$B_{\mathrm{f}} = \frac{h}{\mu_{\mathrm{B}} g_{\mathrm{e}}} f_{\mathrm{B}}, \tag{3.1}$$

where the subscripts in B_{f} and f_{B} are used to highlight the fact of the transformation of units. This approach gives approximately 28 MHz per 1 mT. Thus, in the fields units, the resonator bandwidth is about 14.3 mT. The signal generated by those samples whose linewidth is narrower than this value will not be noticeably affected by the resonator frequency profile.

The broad linewidth is a property of a sample and generally cannot be changed; we can, however, control which spins we excite by choosing the right excitation pulses. The excitation bandwidth of a square DC pulse with duration t_{p} can be extracted from its Fourier transform which is the sinc function. The full width of its central peak at half maximum (f.w.h.m.) is given by

$$\Delta f_{\mathrm{p}} = \frac{1.207}{t_{\mathrm{p}}}. \tag{3.2}$$

For the MD4 resonator, a pulse which would excite all spins in the MW cavity must have a bandwidth shorter than 3 ns. Any pulses longer than that value will excite a narrower spin packet. At full power of our MW amplifier (5), the shortest π-pulse we were able to generate was 10 ns with a bandwidth of 120 MHz.

Consequently, we do not expect that the signal generated by excited spins gets significantly affected by the resonator frequency profile, unless the signal is close to either 9.45 or 9.9 GHz. Moreover, in the widely used spin-echo sequence (see Section 2.4.3) the excitation bandwidth is determined by the π-pulse which has either the same or twice narrower bandwidth than the $\pi/2$-pulse depending on whether we are using different power or different duration for those pulses.

In summary, the bandwidth of the signal produced by the excited spins will be determined at the output of the resonator by the narrowest of the three: the resonator bandwidth, the spectral linewidth or the excitation bandwidth. This is true in the first approximation, wherein we do not consider the precise shape of the frequency characteristics.

As long as the components in the detection system of our setup do not have a bandwidth narrower than that of the useful signal[1], we can expect the latter to propagate without a significant distortion. To guide the signal between the separate components of the spectrometer we use coaxial cables with a wide bandwidth: 18 GHz for the SMA cables. The splitter cut-off frequency is equal to 14.8 GHz, while that of the circulator is 16.0 GHz. The bandwidths of the limiter and the protection switch are 1-18 GHz and 2-18 GHz, respectively.

The 500 MHz-wide cavity bandpass filter (15) clears the signal from most of the thermal noise introduced by the circuit components at room temperature and amplified by the cascade (14). After that, the signal gets mixed with the reference arm at mixer (16) which down-converts it to an RF signal in the range 0-3.5 GHz (the bandwidth of ports I and Q). At this point, the I and Q channels of the mixer can be directly connected to the oscilloscope (19). The bandwidth of the latter is 2.5 GHz and with the maximal sampling rate of 10^{10} samples per second it can faithfully read out the frequency content of any useful signal which has left the resonator. However, the signal can be increased further by an RF amplifier and cleared from the RF noise by an additional filter. Our video amplifier (17) has a bandwidth 0-300 MHz, while the bandpass filters (18) leave only the signal in the range 87-117 MHz.

[1]The 'useful signal' is whatever we would like to detect.

Even though the bandwidth of filters (18) is significantly lower than that of the resonator, they can still be used when the spectral linewidth or the excitation bandwidth are sufficiently narrow. For instance, the linewidth of the Mn spectrum in ZnO is 0.04 mT corresponding to just 1.1 MHz (see Chapter 6); while in the [Yb (trensal)] project we used 200 ns-long excitation pulses whose bandwidth was approximately 6 MHz (see Chapter 5). Both signals could be passed through the filters (18) which reduce the noise at the final stage of the measurement without losing the information.

3.2.3 Up-conversion and down-conversion

One of the major technical differences of our spectrometer from typical commercial devices is that it generates MW pulses via the up-conversion process at an IQ-mixer instead of cutting continuous MW radiation using PIN diodes.

Mixing: The excitation pulses are produced via the heterodyne process at mixer (4), while the detected signal is the result of an analogous process at mixer (16). Inside, the major components of the mixers are diodes whose non-linear response generates the sum and difference of the input frequencies [116, 117]. Mathematically, this mixing process is expressed as the trigonometric relation

$$\cos(\omega_1)\cos(\omega_2) = \frac{1}{2}\left[\cos(\omega_1+\omega_2)+\cos(\omega_1-\omega_2)\right], \tag{3.3}$$

where the physical meaning of the two frequencies will depend on the mode in which the mixer works.

Normally, we would like to have control over the bandwidth of our signal and choose only one required sideband (either the sum or difference). A standard 3-port mixer produces both of these signals at its output. A straightforward way of eliminating one of the sidebands would be using an image rejection filter, however when the two frequencies differ by several orders of magnitude, the rejection requires an expensive filter with a very sharp cut-off characteristic. If $\omega_1 \approx \omega_2$ and they are both close to the bandwidth of the mixer, the sum of these frequencies will be outside

the bandwidth and will be naturally rejected by the mixer itself. Another solution would be a single sideband upconverter with a built-in function of intentional cancellation of one of the signal components. This type of a mixer, however, rejects one of the sidebands unconditionally, thus limiting our control over the signal. With one addition port, an IQ mixer introduces a flexible control over the phase, amplitude, and frequency of the output signal. It allows us to suppress one of the sidebands and enhance the other through the manipulation of the input signal phase [118].

When only the sum of the frequencies survives in Equation 3.3, the process is called 'up-conversion', whereas the difference of the frequencies corresponds to 'down-conversion'. The functions of the 4 ports of our IQ mixers, and the meaning of frequencies ω_1 and ω_2 vary depending on whether the mixer is in the source system and performs up-conversion or it is in the detection system and performs down-conversion.

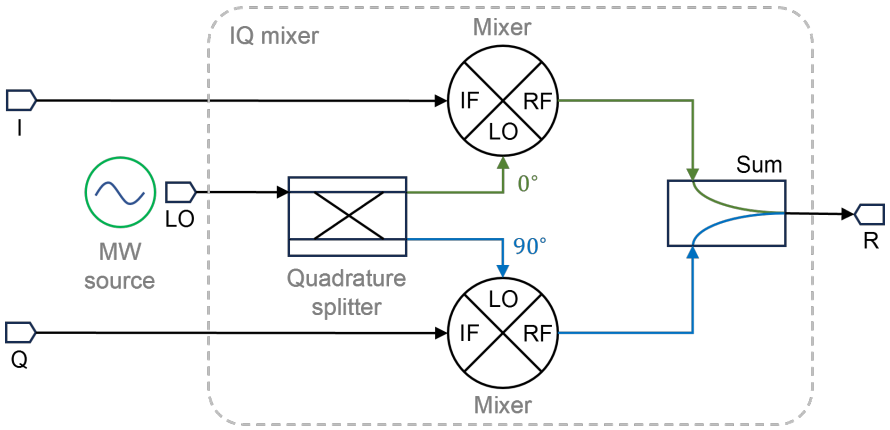

Figure 3.3: The operational diagram of an IQ-mixer (adapted from Reference [118]).

Up-conversion: The IQ-mixer (4) is responsible for forming the excitation pulses. Its inner operation can be represented by a diagram involving two traditional mixers – see Figure 3.3. The IQ-mixer first splits the input LO signal into two branches leaving one part unchanged and shifting the phase of the other part by 90° [118]. Represented mathematically, let the LO signal be

$$u_{\mathrm{LO}} = U_{\mathrm{LO}} \sin(\omega_0 t + \varphi_0), \tag{3.4}$$

where U_{LO}, ω_0, and φ_0 are the amplitude, angular frequency, and the phase of the signal, respectively. The same signal shifted by 90° is then

$$u_{\mathrm{LO}}^{90^\circ} = U_{\mathrm{LO}} \sin(\omega_0 t + \varphi_0 + \pi/2) = U_{\mathrm{LO}} \cos(\omega_0 t + \varphi_0). \tag{3.5}$$

During the mixing stage, the IQ-mixer multiplies the direct LO signal with whatever is fed into the I port, and multiplies the LO signal rotated by 90° with the input at port Q. Finally, it combines the power of the two branches and outputs the resulting signal at port RF[2]:

$$u_{\mathrm{RF}} = u_{\mathrm{I}} \cdot u_{\mathrm{LO}} + u_{\mathrm{Q}} \cdot u_{\mathrm{LO}}^{90^\circ}. \tag{3.6}$$

Note that the mixer yields a non-zero u_{RF} only when there is a non-zero signal on either port I or port Q.

The LO input in our spectrometer is always the MW signal generated by the MW source (3). If the input signals u_{I} and u_{Q} are trivial rectangular pulses, the output of the mixer (4) are pulses of the carrier frequency ω_0 with rectangular enveloping shapes.

Now consider the situation when u_{I} and u_{Q} are themselves pulses with a non-zero carrier frequency ω_{IF} given by

$$u_{\mathrm{I}} = U_{\mathrm{I}} \sin(\omega_{\mathrm{IF}} t), \tag{3.7a}$$

$$u_{\mathrm{Q}} = U_{\mathrm{Q}} \sin(\omega_{\mathrm{IF}} t + \varphi_{\mathrm{IF}}), \tag{3.7b}$$

where φ_{IF} is their relative phase difference. From Equations 3.3 and 3.5 it follows that u_{RF} will consist of the two harmonics with frequencies $(\omega_0 + \omega_{\mathrm{IF}})$ and $(\omega_0 - \omega_{\mathrm{IF}})$:

$$\begin{aligned} u_{\mathrm{RF}} = {} & \frac{U_{\mathrm{I}} U_{\mathrm{LO}}}{2} \left[\cos((\omega_0 - \omega_{\mathrm{IF}})t + \varphi_0) - \cos((\omega_0 + \omega_{\mathrm{IF}})t + \varphi_0)\right] + \\ + & \frac{U_{\mathrm{Q}} U_{\mathrm{LO}}}{2} \left[\cos\left((\omega_0 - \omega_{\mathrm{IF}})t + \varphi_0 + \frac{\pi}{2} - \varphi_{\mathrm{IF}}\right) - \cos\left((\omega_0 + \omega_{\mathrm{IF}})t + \varphi_0 + \frac{\pi}{2} + \varphi_{\mathrm{IF}}\right)\right]. \end{aligned} \tag{3.8}$$

[2]Here, RF is the conventional notation of one of the ports of a mixer. Depending on what function a mixer accomplishes in our spectrometer, the RF port can operate with either radio or microwave frequencies.

Thus, if $U_I = U_Q$ and $\varphi_{IF} = -\pi/2$, only the sum of the two frequencies survives, whereas if $\varphi_{IF} = +\pi/2$ then the output signal oscillates at their difference. Both approaches are equivalent: in our measurements we used the difference of the two signals.

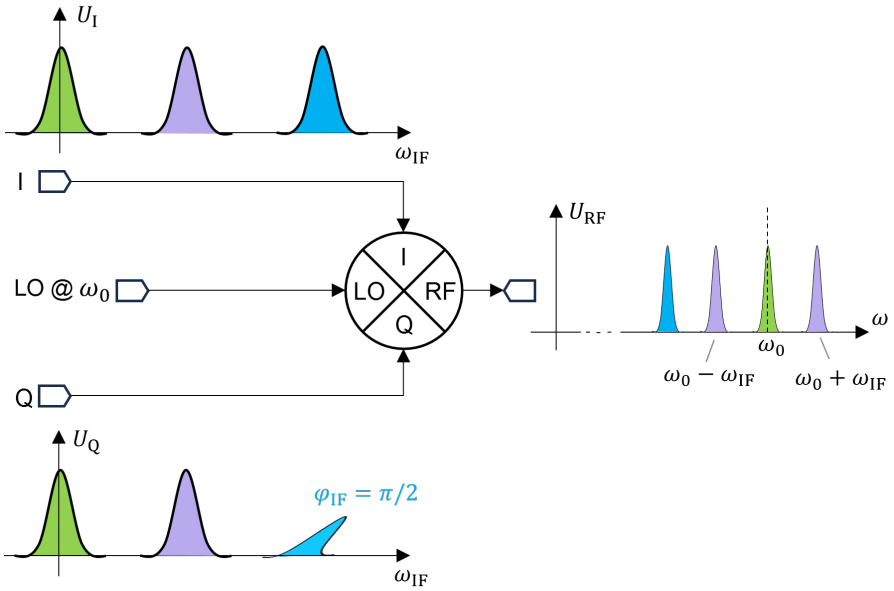

Figure 3.4: Mixing of signals in an IQ-mixer for three different frequency content of the IF channels. *Green*: square DC pulses, the RF signal is centred at ω_0; *lilac*: the I and Q channels at a non-zero ω_{IF}, the RF signal consists of both sum and difference of the input frequencies; *blue*: I and Q are at the same frequency but at $\varphi_{IF} = \pi/2$ phase difference, RF signal is centred at $\omega_0 - \omega_{IF}$.

In general, the shape and the frequency of the output pulses are determined by the input signals u_I and u_Q. The process of mixing signals is depicted in Figure 3.4 (frequency domain) and in Figure 3.5 (time domain) for different I and Q input signals. By design, the bandwidth of ports I and Q is in the RF range (they are also called the IF, intermediate frequency, ports). Therefore, one can think of the signals sent to these ports as low-frequency templates for the actual MW excitation pulses which will be sent to the resonator. We generate these templates using the arbitrary waveform generator (2) which, as the name implies, equips us with the full control over the shape, phase, and even the carrier frequency of the pulses (within the limits of its bandwidth).

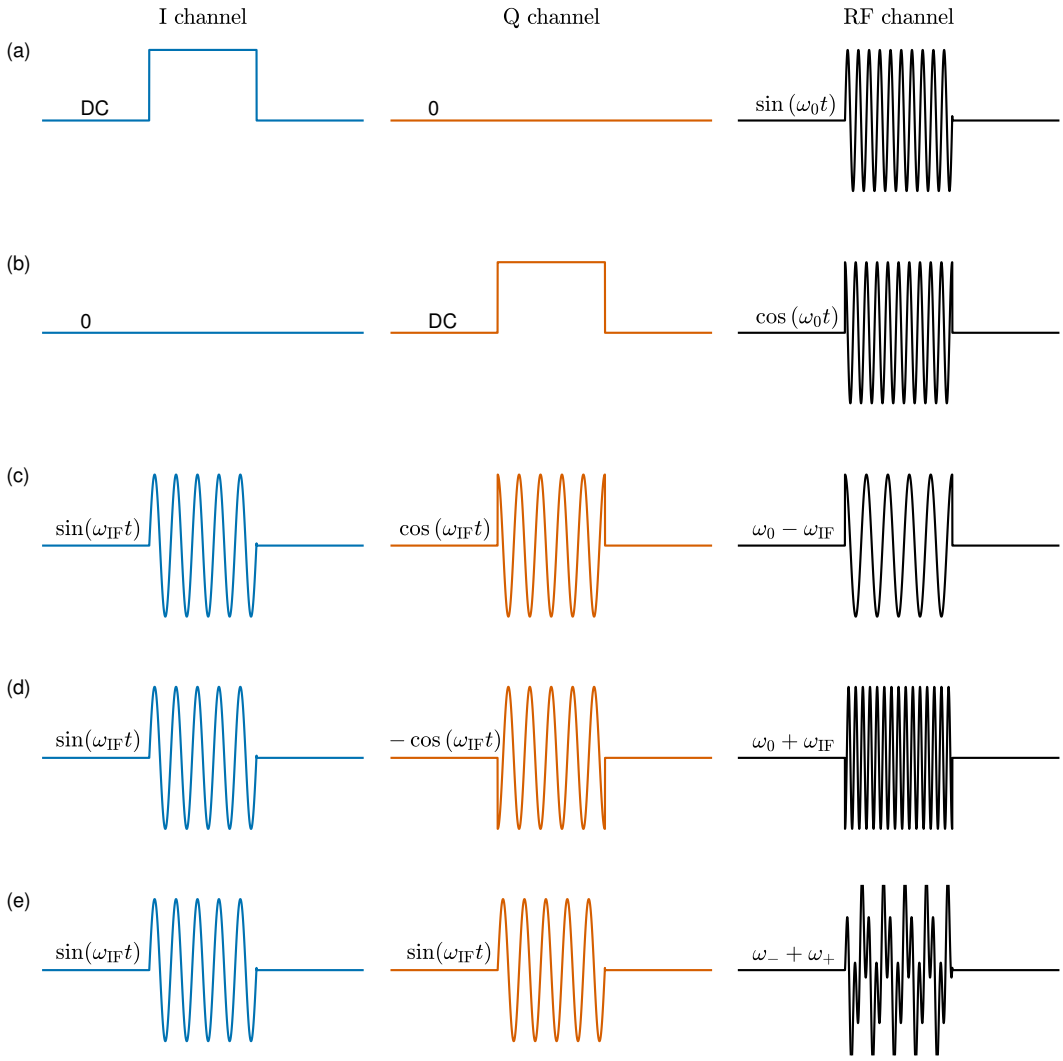

Figure 3.5: Simulation of signal mixing in an IQ-mixer in the time domain. The input signals are I, Q, and LO with $\omega_0 = 2\omega_{\mathrm{IF}}$. The output is RF. (a) and (b): square DC pulses in I or Q channel only produce sine or cosine pulses at the LO carrier frequency ω_0; (c) and (d): square pulses with carrier frequency ω_{IF} produce either the difference (c) or sum (d) of the two frequencies depending on the relative phase between the input I and Q signals; (e): similar I and Q pulses with an arbitrary phase (here $\varphi_{\mathrm{IF}} = 0$) produce a mixture of the sum (ω_+) and difference (ω_-) of ω_0 and ω_{IF}.

Our standard configuration employs square RF pulses u_{I} and u_{Q} oscillating at the carrier frequency of 100 MHz and the MW LO signal at 9.8 GHz. The frequency of the resulting excitation pulses corresponds to the resonance frequency of the MD4 resonator (11). We decided to work at a non-zero carrier frequency of the template

pulses in order to reduce the noise generated by lower frequencies[3] and keep the up-converted and down-converted side bands well apart from each other in case one of them is not fully eliminated by the phase difference between I and Q channels.

Down-conversion: The useful signal generated by the precessing spins is in the MW range, around the resonance frequency of the MW cavity (11). In the case of the MD4 or MD5 (4118X-MD5-W1) resonators, this means ≈ 9.7 GHz. The analog-to-digital converter (19) which we used in our setup has a bandwidth of only 2.5 GHz and thus is unable to record the direct signal faithfully. To circumvent this obstacle, we first down-convert the MW signal back to the RF frequency of the excitation template pulses. This is accomplished in the IQ-mixer of the detection system (16).

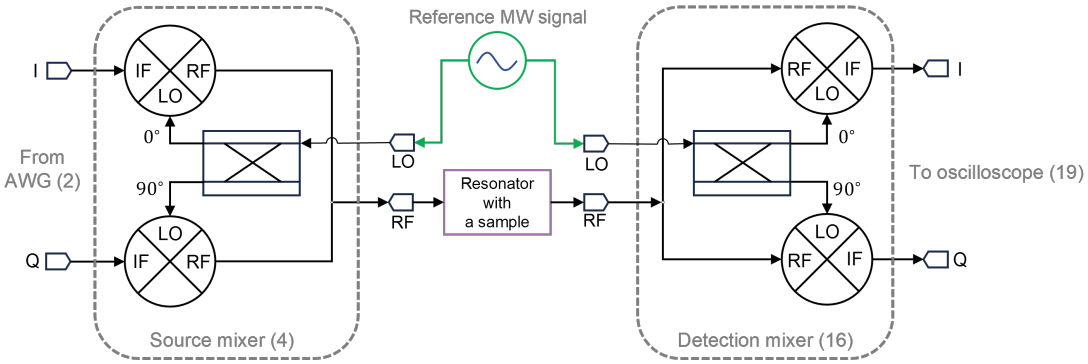

Figure 3.6: A simplified diagram for connecting two synchronised IQ-mixers to perform up- and down-conversion.

The schematic connection of the two synchronised mixers (4) and (16) is shown in Figure 3.6. As was mentioned before, the LO port of mixer (16) receives exactly the same signal as the LO port of the up-conversion mixer (4), though now it plays the role of a reference signal (reference arm). The roles of the IF and RF ports are swapped: the signal reflected from the resonator is fed as an input into the RF port of mixer (16) while its ports I and Q act as the output channels.

In approximate theoretical calculations, it is assumed that the spins precess at the exact frequency of the MW excitation pulses; that is, $(\omega_0 - \omega_{\mathrm{IF}})$. In reality,

[3]Detecting a signal in the vicinity of a particular frequency helps to increase the SNR in the presence of almost any kind of noise. Our system suffers mostly from the noise that decreases as frequency increases.

however, a spin system consists of spin packets each with their own resonance frequency slightly shifted from the expected value by $\delta\omega_e$. We can expect that the amplitude of the useful signal changes with time but does so significantly slower than the oscillation of the carrier frequency:

$$u_e = U_e(t)\sin\Big((\omega_0 - \omega_{IF} + \delta\omega_e)t + \theta\Big), \tag{3.9}$$

where θ incorporates the phase difference between the RF and LO ports, and, more importantly, also the phase shift acquired by the spin system due to our manipulation with it. If the lengths of the paths for the reference arm and the path between the RF output of the up-conversion mixer (4) and the RF input port of the down-conversion mixer (16) do not change, we can ignore the former component of θ and work with the latter which bears valuable information about the spin system.

Analogously to the up-conversion case, the output signal at port I is again the sum and difference of the input frequencies, which in this case are both in the MW range:

$$\begin{aligned} &u_I(t) = u_{LO}(t)\cdot u_e(t) = \\ &\frac{1}{2}U_{LO}U_e(t)\left[\cos((\omega_0 - \omega_0 + \omega_{IF} - \delta\omega_e)t - \theta) - \cos((\omega_0 + \omega_0 - \omega_{IF} + \delta\omega_e)t + \theta)\right]. \end{aligned} \tag{3.10}$$

The component with higher frequency is rejected by the mixer itself due to its MW bandwidth (4-16 GHz). The lower component has frequency $\omega_{IF} - \delta\omega_e$ and is centred around the carrier frequency of the excitation pulse templates. Similarly, the signal at port Q is

$$u_Q(t) = u_{LO}^{90^\circ}(t)\cdot u_e(t) \approx -\frac{1}{2}U_{LO}U_e(t)\left[\sin((\omega_{IF} - \delta\omega_e)t - \theta)\right]. \tag{3.11}$$

The I and Q components are shifted by 90° with respect to each other. The technique of simultaneously measuring both these signals is called 'quadrature detection scheme' or 'measurement in quadratures'. The output signal at port I is the 'in-phase' component, whereas the output at port Q is called the 'quadrature component'. The signal arriving to our oscilloscope (19) oscillates at $\omega_{IF} - \delta\omega_e$ (see example in Figure 3.7(a)).

3.2.4 Down-conversion during post-processing

The bandwidth of the useful signal leaving the IF ports of mixer (16) is centred around the carrier frequency ω_{IF} of the pulse patterns generated by the AWG. The use of $\omega_{\mathrm{IF}} \neq 0$ is not mandatory: commercial Bruker spectrometers by default use square DC pulse patterns, however a non-zero carrier frequency allows us to achieve a higher SNR by avoiding the noise coming from other frequencies.

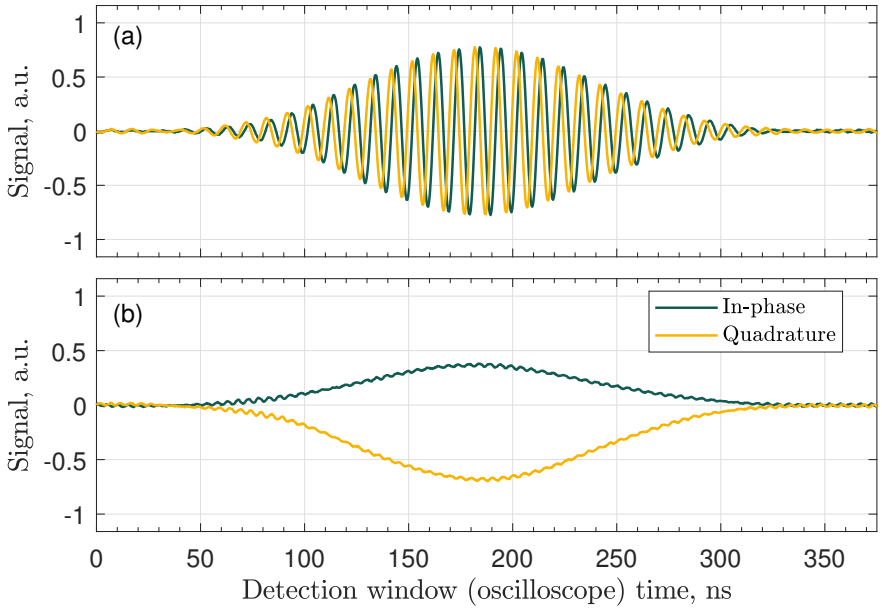

Figure 3.7: Example of the software down-conversion of a BDPA echo signal at RT. (a) Echo signal oscillating at the carrier frequency; (b) the same signal but after down-conversion.

An example of an echo signal obtained on a sample of BDPA at $\omega_{\mathrm{IF}}/2\pi = 100$ MHz is shown in Figure 3.7(a). We can down-convert this signal by programmatically mixing it with sine and cosine waves at ω_{IF}, so that

$$u_{0\mathrm{I}}(t) = u_{\mathrm{I}}(t) \cdot \cos(\omega_{\mathrm{IF}} t) - u_{\mathrm{Q}}(t) \cdot \sin(\omega_{\mathrm{IF}} t), \tag{3.12a}$$

$$u_{0\mathrm{Q}}(t) = u_{\mathrm{I}}(t) \cdot \sin(\omega_{\mathrm{IF}} t) + u_{\mathrm{Q}}(t) \cdot \cos(\omega_{\mathrm{IF}} t). \tag{3.12b}$$

The final result of this mixing will consist of the DC part only. Frame (b) in Figure 3.7 contains an example of down-converting the echo signal shown in frame (a). The ratio between the quadrature and in-phase component magnitudes defines the tangent

of the signal phase θ. The small high-frequency oscillations in the down-converted signal are due to the parasitic side-band which left the up-converting mixer at $\omega_0+\omega_{\mathrm{IF}}$. Its down-converted frequency is $2\omega_{\mathrm{IF}}$. This parasitic component can be minimised by slightly adjusting the phases of the original template pulses (see Section 3.2.5).

When post-processing the experimental data, we can choose whether we want to work with the down-converted signal, or to apply Fourier analysis to the original data directly. If one is interested in the signal intensity only, in principle, both approaches are equivalent, but the second approach yields a higher SNR if we are only interested in the signal in a particular frequency range, say in the vicinity of ω_{IF} (thus ignoring the parasitic component). Besides, Fourier analysis is preferable when the knowledge of the frequency content of the signal and its phase is what we need.

3.2.5 Mixer calibration

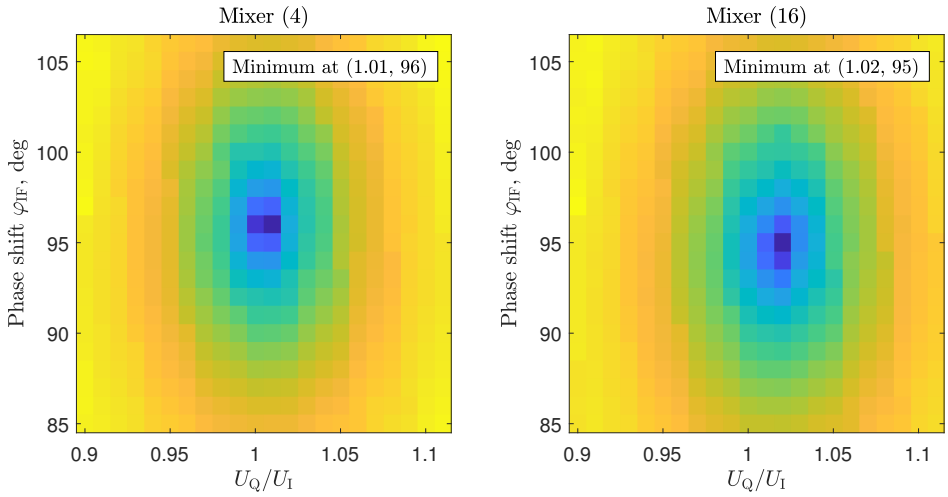

Figure 3.8: Calibration of the side-band rejection at 9.7 GHz. The colour shows the intensity of the side-band magnitude growing from blue to yellow.

According to the formulae derived in Section 3.2.3, the perfect rejection of the side-band oscillating at the sum of the input frequencies $\omega_0 + \omega_{\mathrm{IF}}$ is achieved when the amplitude of channel Q is the same as that of channel I, and their phase difference is exactly $\varphi_{\mathrm{IF}} = +90°$. Our tests showed that real mixers, however, generate the upper-frequency side-band even if the parameters of the signal are set as required. In order to find the optimal values of the parameters, we calibrated our

mixers by sweeping the relative amplitude U_Q/U_I and the phase φ_{IF} in the vicinity of the expected values. The results of the calibration at $\omega_0/2\pi = 9.7$ GHz[4] are shown in Figure 3.8. The intensity of the side-band at the up-converting mixer (4) is minimised when we use $U_Q/U_I = 1.01$ and $\varphi_{IF} = 96°$.

3.2.6 AWG and programming pulse sequences

The shaping of the excitation pulses is accomplished by sending pertinent voltage waveforms to the I and Q ports of the up-converting mixer (4) as described in Section 3.2.3. We generate these waveforms using the Zurich Instruments arbitrary waveform generator (AWG) – see number (2) in Figure 3.1. In addition to the excitation pulses themselves, the AWG also generates a pulse for closing the protection switch (13), a pulse opening the gate of the high-power MW amplifier (5), and it finalises each sequence with a pulse which triggers the oscilloscope (19). In the E-field experiment, the AWG is also responsible for triggering the electric-pulse generator. In this way, the AWG plays the role of a master-clock that synchronises the excitation of the spin system and the read-out of its response.

The spectrometer as a whole is controlled by a separate computer which initialises separate devices, uploads the pulse sequence onto the AWG, and triggers the latter when the user presses the 'run experiment' button. All the scripts and drivers have been written in Python, while post processing scripts are mostly implemented in MATLAB.

3.2.6.1 Structure of a generic script

The general flow of an experiment programmed as a script is depicted in Figure 3.9. It is structured into four distinct phases: initialisation, execution, error handling, and finalisation.

Initially, the script performs parameter compilation by translating user-defined high-level inputs into device-specific configurations. A validation step follows to

[4]The nominal resonance frequency of the EN 4118X-MD4-W1 and ER 4118X-MD5 resonators.

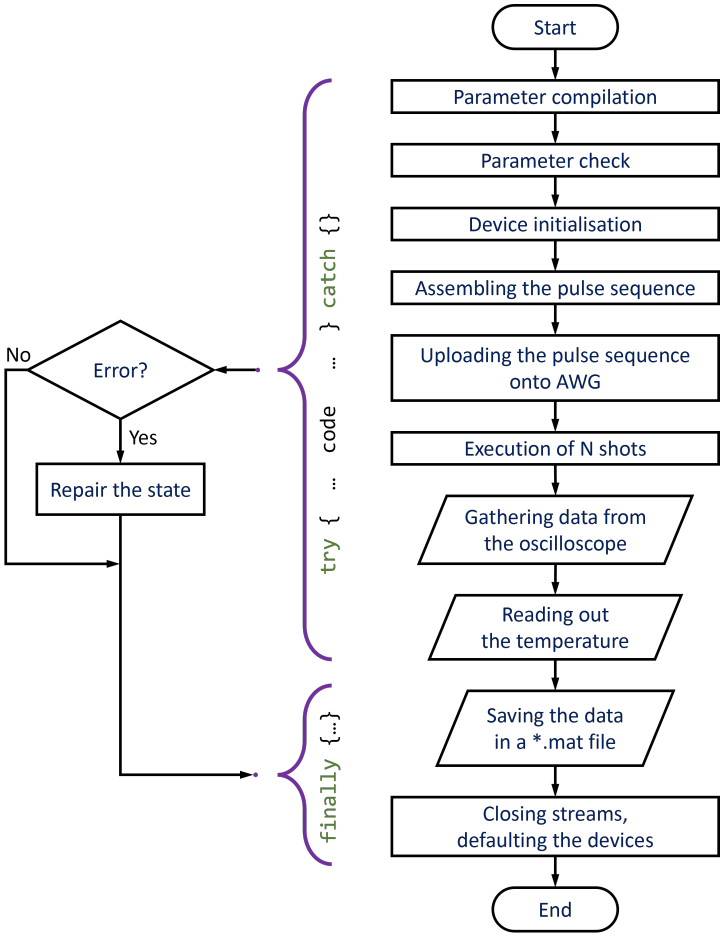

Figure 3.9: Block-diagram of an experiment programmed for execution on our spectrometer.

ensure that the parameters are physically consistent and free from common user errors, such as a too short repetition time or invalid range of a sweep.

Upon successful validation, the system proceeds with device initialization, after which it constructs the pulse sequence for the experiment. This sequence is then uploaded to the AWG, which performs internal consistency checks prior to execution. The script then triggers the AWG for a predefined number of shots, corresponding to repeated experimental runs under identical conditions.

Following data acquisition, the script retrieves measurement waveforms from the oscilloscope and records temperature data from the ITC. All relevant data, along with the initial configuration parameters, are serialized and stored in a MATLAB-compatible .mat file on our data server.

In the event of an error during any stage of the execution phase, control is transferred to a recovery routine that attempts to restore the system to a consistent state, thereby preventing resource locks or hardware faults. It will also attempt to save whatever data points have been measured by the moment when the exception was raised.

Regardless of whether the experiment completes successfully or is interrupted by an error, a finalization routine is executed. This routine closes all data streams, releases temporary resources, and returns all instruments to a safe standby mode, ensuring reproducibility and readiness for subsequent runs.

Over the course of my DPhil we have changed several components which have necessitated updating the existing code. Two such updates were the acquisition of a new AWG and the replacement of the digital pulse generator, which was our master clock at the early stage of the assembling process. In order to integrate the new devices and arrange the operation of the spectrometer around the new AWG, I had to significantly rewrite the programming library several times. The upside of these changes was that I have separated the high-level design of the pulse sequences and the low-level assembling and compilation of the waveforms for the AWG. In addition, all the drivers for separate stand-alone devices are stored in separate class-files which can be used in other projects straight away.

An example of a high-level script for running the spin-echo sequence is shown in Listing 3.1. There are only two entities here: the `experiment` and its `parameters`, with the latter being initialised first. Most of the fields have self-explanatory names. All the time intervals are normally measured in nanoseconds. Frequency fields use hertz apart from `mw_frequency_in_resonator` – its units are conventionally GHz. The power is given in fractions with the maximal value of 1.0. Fields `data_start` and `data_end` are measured in samples (integer numbers) and define the part of the oscilloscope waveform to be transferred and saved in the final data file. The oscilloscope can record waveforms from four channels – those which should be saved after measurement are given by the array in `channels_to_record`.

```
parameters = SpinEchoParameters()
parameters.pulse_generator_type = (
PulseGeneratorTypes.HdAwgOnlyPrecise)
parameters.mw_frequency_in_resonator = 9.70  # GHz
parameters.pi_by_two_pulse_duration = 20
parameters.pulse_frequency = 100e6
parameters.sequence_offset = 900.0
parameters.tau = 400.0  # ns
parameters.center_field = 3340.0
parameters.shots_per_point = 512
parameters.data_start = 1
parameters.data_end = 10000
parameters.pause_between_pulse_sequences = 1e6
parameters.mw_pulse_amplitude = 0.6
parameters.channels_to_record = [1, 2]
parameters.measurement_or_sample_name = "test_" + \
str(parameters.center_field).replace('.', 'p') + "G"

experiment = SpinEcho(parameters)
experiment.run()
experiment.save_to_matlab_file()
```

Listing 3.1: The script for performing a single spin-echo measurement

3.2.6.2 Efficient vs. precise implementation

Currently, there are two major classes responsible for assembling the pulse sequences in two different ways: `PulseSequenceBuilderHdAwgOnlyEfficient` and `PulseSequenceBuilderHdAwgOnlyPrecise`. Both classes are inherited from a more general `PulseSequenceBuilderHdAwgOnly` and contain methods which convert user-friendly parameters of a measurement into the code sequences written in the inner programming language of the AWG. The long names of the two classes are the result of several code updates. They reflect the fact that we are using AWG as a master clock instead of a digital pulse generator. The `Efficient` and `Precise` versions differ in how they treat delays between pulses: the former uses the special `wait()` procedure which does not require AWG memory apart from storing the function call itself, whereas the latter explicitly encodes the delays as a zero-voltage output of the AWG channels at every time step throughout the duration of delay.

In its implementation, the `Efficient` version requires the knowledge of the AWG's inner programming language and the understanding of how it reads waveforms from the memory. The `Precise` version, though inefficient in its memory usage, is significantly easier to use. Each pulse sequence can be assembled by simply staking pulses one after another. An example of instantiating a pulse in `PulseSequenceBuilderHdAwgOnlyPrecise` is shown in Listing 3.2. One needs to tell the script which AWG core to use for generating the pulse: MW or RF; the axis of the pulse ($\pm X$, $\pm Y$); the pulse amplitude; the offset of the pulse from the start of the waveform; the duration of the pulse; its down-converted frequency (100 MHz by default); and, finally, the phase of the pulse.

```
self.add_sine_excitation_pulse(
    HdAwgCores.MW,
    PulseAxes.PLUS_X,
    pi_pulse_amplitude / 2.0,
    pulse_offset_in_ns,
    pi_by_two_pulse_duration_in_ns,
    frequency_in_hz,
    pulse_phase)
```

Listing 3.2: Setting up an excitation pulse.

In Listing 3.1, the choice between the two implementations of the pulse-sequence builder is performed by selecting the corresponding `pulse_generator_type` in the `parameters` entity.

3.2.6.3 Amplifier gate pulse and protection pulse

```
amp_left_margin = 400  # ns
amp_right_margin = 100  # ns
amp_minimum_open_gate_time = 1000  # ns
minimum_shot_repetition_time_for_closing_amp = 20e3

time_to_travel_from_awg_to_switch = 200  # ns
switch_left_margin = 100  # ns
switch_right_margin = 500  # ns

protection_pulse_marker = 0b01
amp_gate_pulse_marker = 0b10
e_pulse_generator_trigger_marker = 0b10
```

Listing 3.3: Fields of `PulseSequenceBuilderHdAwgOnly`

The parent class `PulseSequenceBuilderHdAwgOnly` contains several crucial parameters important for the spectrometer's operation – they are shown in Listing 3.3. Among these parameters are those that deal with the pulse opening the gate of the high-power MW amplifier (5) and the pulse controlling the protection switch (13) that does not allow the powerful excitation pulses to go to the detection system (number-notation is given in Figure 3.1).

Figure 3.10 depicts the meaning of the time parameters in terms of the location of the MW sequence, the MW amplifier gate pulse, and the protection pulse. There, the MW sequence rectangle denotes the beginning of the first MW pulse and the end of the last MW pulse. According to the specifications, the gate of amplifier (5) must not be open for times shorter than 1000 ns. Moreover, it should be open 400 ns before the first MW pulse (`amp_left_margin`, t_{alm}) and must be kept open for at least 100 ns after the last MW pulse (`amp_right_margin`, t_{arm}). While the gate is open, the amplifier increases the magnitude of any incoming signal by about 55 dB – this amplification can be dangerous for the components of the detection system (see Figure 3.1). Therefore, the detection system gets disconnected from the resonator by the protection switch (13). To allow for any pulse misalignment and cavity ring-down effects, the protection pulse controlling the switch is extended before and after the gate pulse (`switch_left_margin`, t_{slm} and `switch_right_margin`, t_{srm}, respectively).

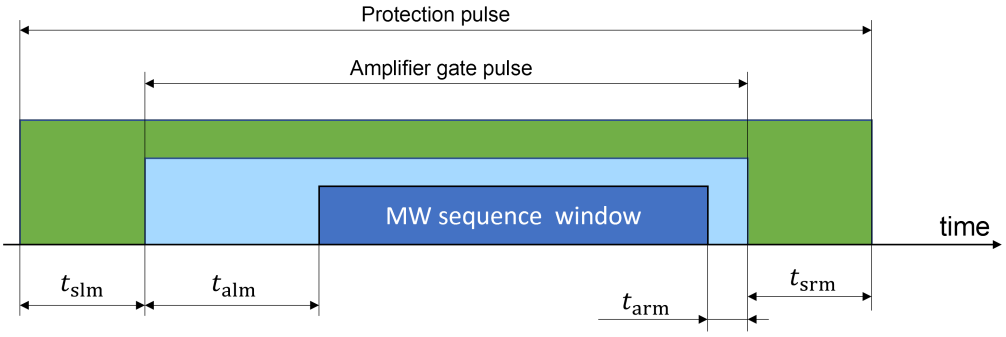

Figure 3.10: Relative location of the MW sequence, amplifier gate pulse, and the protection pulse. The pulses of the sequence can be placed anywhere in the MW sequence window.

Times t_{arm} and t_{srm} together form the so-called spectrometer dead-time t_{d} during which any useful signal coming from the resonator will not be detected. To make this time minimal, the actual MW sequence is shifted as close as possible to the right end of the amplifier gate pulse leaving space only for t_{arm}.

All the parameters in Listing 3.3 are not available to the end-user of any high-level experimental scripts and should therefore be changed directly in the code of `PulseSequenceBuilderHdAwgOnly`. This should be done with caution and by an experienced user of the spectrometer only. While it is common to adjust the duration of the protection pulse for decreasing dead-time t_{d} and achieving a greater SNR in case of fast-relaxing samples, one should change only `switch_right_margin` using small steps of approximately 10 ns and performing the ringing check after each adjustment!

3.2.7 Synchronisation and phase noise

Many of our experiments concern the measurement of the spin phase coherence. To that end, the active elements of the spectrometer, namely MW source (3), AWG (2) and oscilloscope (19) have to be properly synchronised, and the overall phase noise generated in the spectrometer should be minimised where possible.

In our setup, the synchronisation is realised by the rubidium frequency standard (1) which generates a 10 MHz reference signal with the phase noise of less than -130 dBc/Hz at 10 Hz. Slightly larger noise is produced by the MW source (3). According to its specifications, the absolute phase noise it generates for signals between 3-10 GHz is -37 dBc/Hz (at 1 Hz), -81 dBc/Hz (at 100 Hz) and -110 dBc/Hz (at 10 kHz).

We expected that a possible source of a more significant phase noise would be the cascade of three MW low-noise amplifiers (LNA) (14) collectively providing 90 dB amplification. In order to minimise the noise generated by the cascade as a whole, we had to connect the LNAs in ascending order of the noise they produce separately. To do this, we have measured the transmission characteristic S_{21} of the separate LNAs using a virtual network analyser (VNA) Rohde&Schwarz ZVA50. The details

of these measurements are provided in Appendix A.2.1. After we obtained the data for separate amplifies, we assembled the cascade in its optimal configuration and measured the overall phase noise it produced. At 9.7 GHz and room temperature the numbers were the following: −28 dBc/Hz (at 10 Hz), −49 dBc/Hz (at 100 Hz), −50 dBc/Hz (at 1 kHz), −51 dBc/Hz (at 10 kHz).

The estimates of noise mentioned in this section are limited by the available devices and can be useful in calculating the SNR, however, its precise value is not important for further discussion. Practically, a higher SNR is preferable because it reduces the number of shots required to obtain a single data point, and, therefore, the overall duration of a measurement. The acceptable level of the SNR varies from measurement to measurement. Qualitatively, the SNR can be estimated by comparing the echo signal intensity with the baseline of the measured waveform.

3.3 CW mode

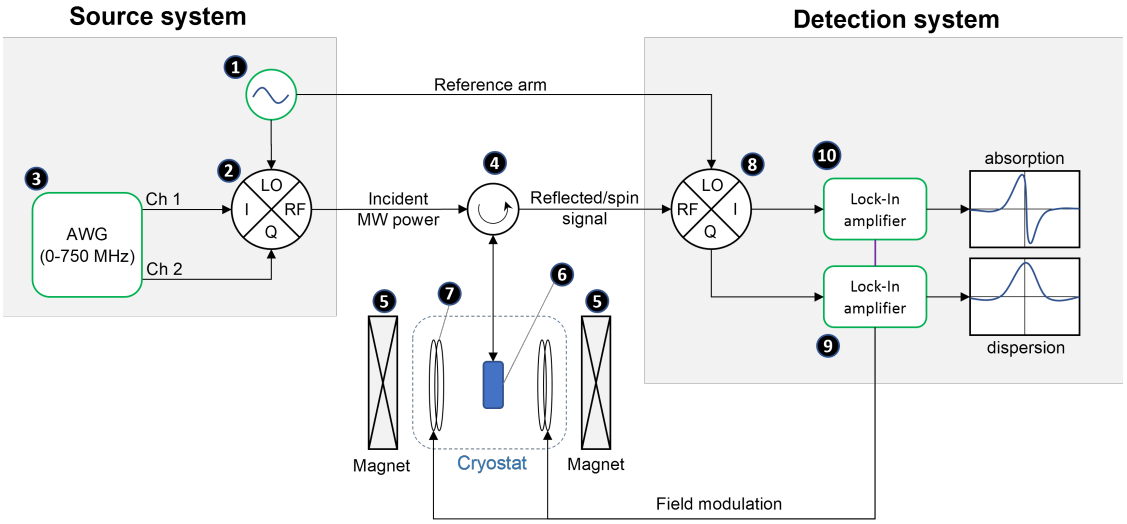

Figure 3.11: Schematic representation of the ESR spectrometer in CW mode. Green colour denotes active elements.
The number-notation of the constituent components is as follows:
1 - microwave source; 2 - IQ mixer for up-conversion and power attenuation; 3 - arbitrary waveform generator (provides the DC voltage for attenuating power output at mixer 2); 4 - circulator; 5 - magnet; 6 - resonator (with probe); 7 - field modulation coils; 8 - down-converting mixer of the detection system; 9 - lock-in amplifier generating the field modulation signal and amplifying the signal form the Q channel of mixer 8; 10 - lock-in amplifier synchronised with 9 and amplifying the signal from the I channel of mixer 8.

Figure 3.11 illustrates the arrangement of the main parts of the spectrometer in CW mode.

The microwave radiation of frequency f_0 lying in the X-band is produced by an Agilent E8257D signal generator (1) and is immediately split into two parts. The first part is attenuated to the required level by the IQ-mixer of the source system (2) via applying corresponding DC voltage to the I and Q channels and then is directed to the resonator (6). The circulator (4) ensures that only the signal reflected from the resonator is sent to the detection system, while simultaneously preventing it from returning back to the mixer and source. Between the devices, the microwave radiation is transmitted by means of waveguides, e.g., coaxial cables or hollow metal tubes. The magnetic field $\boldsymbol{B}_0$ necessary for any ESR measurement is generated in the area between the cones of the resistive magnet core (5) and can be considered to be uniform at the location of the resonator. The distance between the magnet core edges cannot be changed in the current set-up, so the magnitude of $\boldsymbol{B}_0$ is limited to a maximum of 0.97 T.

Before any CW measurement, the frequency of the source and the coupling between the resonator and the waveguide itself are tuned in such a way that no microwave radiation is reflected from the resonator. More precisely, this means that the reflection coefficient, which depends on the radiation frequency, the impedances of the transmission line and of the resonator, is equal to zero. The frequency at which this happens is called the resonant frequency f_{res}. Since the sample inserted into the resonator contributes to the impedance of the resonator, any disturbance in its properties, e.g., due to the ESR phenomenon, will change the reflection coefficient. In turn, this will affect the amplitude and the phase of the radiation reflected from the resonator. Therefore, it is important to tune the frequency of the microwaves to its resonance value and to tune the coupling between the resonator and the waveguide, while ensuring that the reflected power in the absence of spin resonance is close to zero.

3.3.1 Magnetic resonance in CW mode

The ESR phenomenon is closely connected with the AC susceptibility $\chi = \chi' - \mathrm{i}\chi''$ of a material under study. Assuming a linear medium, the AC magnetic flux density $b(t)$ inside a sample subject to a magnetic field $h(t)$ is

$$b(t) = \mu_0 (1 + \chi) h(t) = \mu_0 (1 + \chi' - \mathrm{i}\chi'') h(t), \tag{3.13}$$

where μ_0 is the vacuum permeability and t stands for time.
The dissipated power can be found as $P = h(t)\frac{\mathrm{d}b(t)}{\mathrm{d}t}$ [119]. Given $h(t) = h_0 e^{\mathrm{i}\omega t}$, the average rate of energy loss $\langle P \rangle$ is calculated from the real part of P such that

$$\langle P \rangle = \frac{1}{2}\mu_0 \chi'' \omega h_0^2, \tag{3.14}$$

where ω is the angular frequency of the magnetic field h.

In light of Equation 3.14, the energy dissipated in the sample depends only on the imaginary part of the sample susceptibility; the real part of χ is responsible for the delay of $b(t)$ relative to $h(t)$. Consequently, χ'' and χ' are known as absorptive and dispersive parts of the susceptibility, respectively.

The connection between the AC susceptibility of a sample and its ESR spectrum can be understood by considering the resonator as a series RLC-circuit. The reflection coefficient can be expressed in terms of the impedance values of the transmission line and of the resonator as

$$\Gamma = \frac{Z_0 - Z}{Z + Z_0}, \tag{3.15}$$

where Z is the resonator impedance and Z_0 is the characteristic impedance of the cable connected to it [120].

When the resonator is critically coupled with the transmission line, $\Gamma = 0$ and $Z_0 = Z$. In this case, the impedance of the resonator is

$$Z = Z_0 = -\frac{\mathrm{i}}{\omega_{\mathrm{res}} C} + \mathrm{i}\omega_{\mathrm{res}}(1 + \chi)L + R, \tag{3.16}$$

where R, L, and C are the effective resistance, inductance, and capacitance of an empty resonator and $\omega_{\mathrm{res}} = 2\pi f_{\mathrm{res}}$. The insertion of a sample into the

resonator cavity modifies the magnetic flux flowing through the inductance via χ (see Equation 3.13).

Any small perturbation in the susceptibility $\delta\chi = \delta\chi' - \mathrm{i}\delta\chi''$ of the sample placed inside the cavity will cause a change in the resonator impedance, δZ, and a corresponding change in Γ according to

$$\delta Z = \omega_{\mathrm{res}} L \delta\chi'' + \mathrm{i}\omega_{\mathrm{res}} L \delta\chi', \tag{3.17}$$

$$\delta\Gamma = \frac{Z_0 - (Z_0 + \delta Z)}{(Z_0 + \delta Z) + Z_0} \approx -\frac{1}{2}\frac{\delta Z}{Z_0} = \mathrm{Re}\{\delta\Gamma\} + \mathrm{iIm}\{\delta\Gamma\}, \tag{3.18}$$

where we assume that $\delta Z << Z_0$.

In the case of a lossless resonator and sample, we can further exclude the real part from Z_0; that is, there is no dissipation of energy in the absence of spin resonance. Then, the real and imaginary parts of $\delta\Gamma$ are

$$\mathrm{Re}\{\delta\Gamma\} = -\frac{1}{2}\frac{\omega_{\mathrm{res}}^2 LC}{(\omega_{\mathrm{res}}^2(1+\chi')LC - 1)}\delta\chi', \tag{3.19}$$

$$\mathrm{Im}\{\delta\Gamma\} = \frac{1}{2}\frac{\omega_{\mathrm{res}}^2 LC}{(\omega_{\mathrm{res}}^2(1+\chi')LC - 1)}\delta\chi''. \tag{3.20}$$

Since the incident u_{i} and reflected u_{r} signals are related via the reflection coefficient by $u_{\mathrm{r}} = \delta\Gamma u_{\mathrm{i}}$, the quadrature part of u_{r} carries information about the amount of energy absorbed by the sample, whereas the in-phase component reflects the shift in the resonant frequency of the cavity containing the sample. Thus, it is natural to decompose the experimental ESR spectra into absorptive and dispersive parts, proportional to χ'' and χ', respectively.

3.3.2 Down-conversion and de-modulation

The microwave signal reflected from the resonator is down-converted by the IQ-mixer (8) of the detection system which uses the second part of the microwave generated by the source as the local oscillator (LO) signal (also known as the reference arm). As a result, the DC voltage at the I and Q channels of the mixer are the amplitudes of the in-phase and quadrature components of the reflected microwave with respect to the reference arm. Both signals are mixtures of the absorptive and dispersive parts

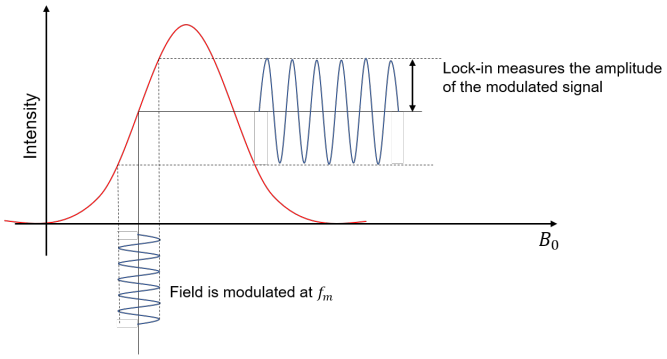

Figure 3.12: Modulation of the ESR signal.

of the ESR spectrum, which can be separated if the initial phase difference between the reference arm and the microwave reflected from the resonator φ_0 is known.

Unfortunately, it is not unusual that the I and Q signals are weak and contaminated with a lot of noise. In order to increase the signal-to-noise ratio (SNR), the static field $\boldsymbol{B}_0$ is modulated by one of the two SR830 DSP lock-in amplifiers (9) at frequency f_m via modulation coils (7), and, consequently after the down-convertion at the mixer (8), the I and Q signals oscillate at f_m (see Figure 3.12). The amplitude of the modulated signals is separated from the noise by the synchronised lock-in amplifiers (9 and 10). The demodulation process is similar to that which takes place in the mixers (see Section 3.2.3 and Reference [117]). Each of the lock-ins measures the amplitude of the in-phase and the quadrature components of the modulated oscillating signal with respect to the reference of the modulation, thus effectively producing the derivatives of the I and Q signals (with respect to $\boldsymbol{B}_0$) which would be measured without the field modulation.

Since I and Q signals are demodulated by separate lock-ins, each output data point corresponding to a certain value of $\boldsymbol{B}_0$ generated by the spectrometer consists of four components: I_x, I_y, Q_x and Q_y, where the subscript x denotes the demodulated in-phase component and y stands for the quadrature component. If the phase difference φ_m between the modulated signal and the reference arm of the modulation does not change, the data points measured by a separate lock-in form a straight line (see Figure 3.13), which can be found using linear regression. By simply rotating the coordinate system at the angle between that line and the x-axis, which is

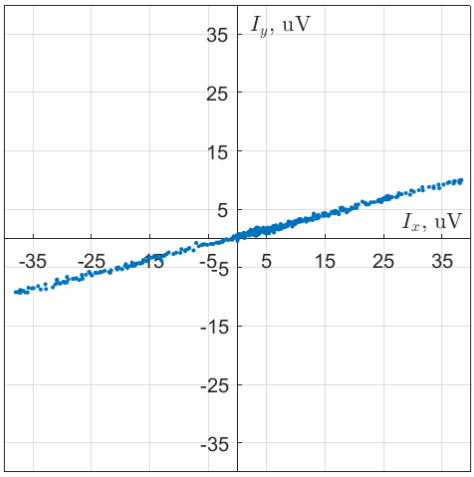

Figure 3.13: I_x and I_y components of the demodulated signal measured by one of the lock-ins as functions of B_0.

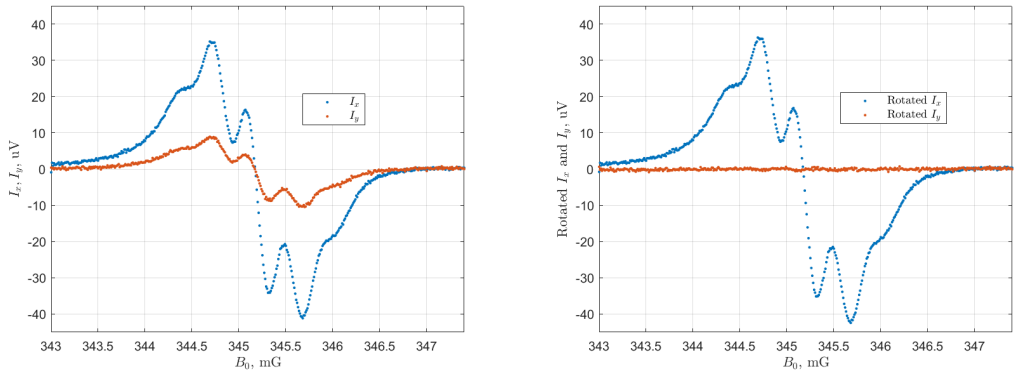

(a) Initial measured signals **(b)** Components after rotation

Figure 3.14: Rotation of the measured in-phase and quadrature demodulated signals I_x and I_y for the purpose of eliminating one of the components.

approximately equal to φ_{m}, it is possible to transfer the entire signal to the x component. Figure 3.14(a) shows the measured I_x and I_y signals, and Figure 3.14(b) demonstrates the result of the appropriate rotational transformation. The phase difference φ_{m} depends on the path that the modulated signal undertakes on its way from the lock-in (9), through all the cables, the resonator cavity containing a sample (6), mixer (8), and back to the lock-in amplifiers (9, 10). This path varies from experiment to experiment, hence, the proposed rotation of the I_x, I_y and Q_x, Q_y signals is a necessary step of every measurement and it provides the calibration of the modulation reference arm.

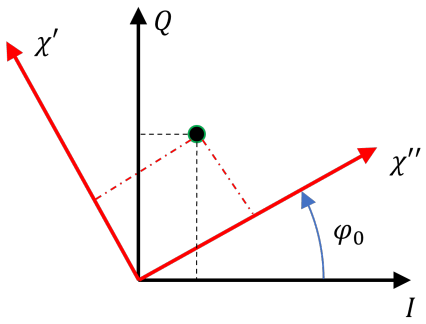

Figure 3.15: The signal (the dot) is measured by the lock-ins in terms of I and Q channels of the detection mixer, but at the same time, it can be decomposed into χ'' and χ' components. The transformation from one coordinate system to another one is a simple rotation, but angle φ_0 must be known.

The quality of the separation of the absorptive and dispersive signals depends on the precision with which the phase φ_0 between the signal reflected from the resonator and the reference arm in the absence of the field can be determined. If, in the absence of spin resonance, the microwave signal reflected from the resonator arrives in the detection mixer (8) completely in phase with the reference arm, the demodulated I and Q signals will represent the derivatives of the pure dispersive and absorptive components, respectively [121, 122]. Otherwise, each signal will be a mixture of the two components, which can be separated via rotating the I-Q signal at angle φ_0 (see Figure 3.15), similarly to how it was done for the signal demodulation. The main difficulty preventing one from successfully measuring φ_0 is that at the beginning of measurement, the resonator is tuned in such a way that there is no or a minuscule amount of radiation coming from it, therefore the I and Q signals are extremely small and noisy. The development of other methods of separating pure dispersive and absorptive components from the I and Q signals is one of the possible directions to improve the spectrometer.

Despite the difficulty of extracting the pure absorptive and dispersive signals, the CW mode allows one to find the location of the ESR signal on the B_0 axis. Additional information about the samples under study, like the expected symmetry of the spectra, can constrain the phase difference φ_0 and guide the required rotational transformation. Moreover, by measuring simultaneously the in-phase and quadrature

components of the reflected signal, our spectrometer allows one to obtain more information than a standard commercial device where the quadrature component is accessible only via Hilbert transform under the assumption of the signal analyticity. For instance, the availability of both I and Q channels of the signal allows one to conduct sophisticated 2D experiments with field and frequency sweeps [123, 124].

3.3.3 Operation and automatisation scripts

To conduct measurements in an automatic way, I wrote a class library and a set of scripts in Python for both CW and pulse modes. The devices are managed via the GPIB or Ethernet physical interfaces and Visa library.

The CW library consists of scripts for tuning the coupling of the resonator with the transfer line, for determining the resonant frequency and the quality factor of the resonator, for calibrating the mixers, for measuring the frequency response of different components, as well as for running the field swept spectra. The syntax of the scripts running a CW experiment is similar to that shown in Listing 3.1.

3.4 E-field effect measurements

The measurement of the E-field effect which I discuss in Chapters 4 and 5, requires the implementation of an electric field pulse in addition to the standard π and $\pi/2$ pulses of the spin echo sequence (see Section 2.5).

3.4.1 Generation of the E-field

For these experiments, our group designed a new probe-head which is compatible with the standard Bruker resonators and allows one to measure orientational dependencies of the SEC (see Figure 3.16).

The E-field pulses are fed into the probe-head via an SMA connector attached to a rigid coaxial cable. At the other end, the outer layer and the copper core of the cable are soldered to two separate gold-plated PCB plates. The metalisation of the plates was done by the thermal evaporation of 10 nm chromium followed with 100 nm of gold (see also Section 3.4.3). The electric field $\boldsymbol{E}$ which acts on

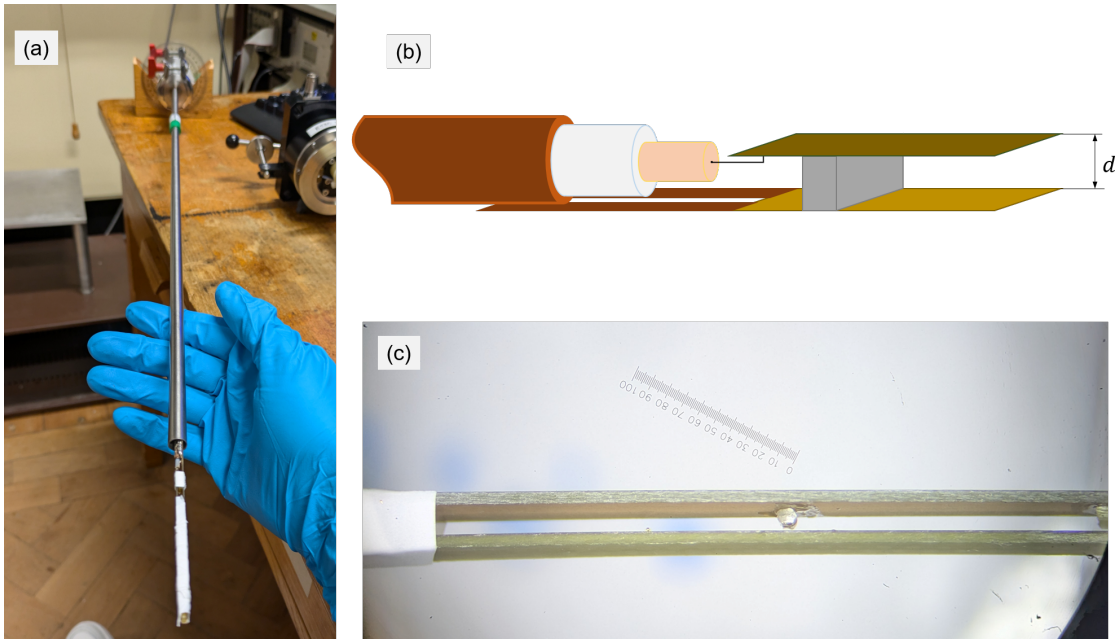

Figure 3.16: (a) An assembled probe-head for the E-field measurements. (b) Diagram of the connection between the coaxial cable and the gold-plated PCB plates. The outer layer of the cable is soldered to the copper-covered extensions of the ground plate. (c) A sample ([Yb (trensal)]) mounted on one of the PCB plates.

the sample is generated between those two plates, therefore, the sample must be located between them. The separation of the plates d was kept constant during a measurement by using a stack of short non-conducting pieces of PCB. For different measurements we used different probes, so that the value of d varied between 1 and 2 mm depending on the particular configuration and experiment.

The E-field pulses were produced by the Avtech AVR-4-B voltage pulse generator. To prevent the reflection of the pulses from the probe-head, a 50 Ohm termination was connected at the input of the probe-head using a parallel T-connector. In our spectrometer, the generator was initialised by an external computer and triggered by the AWG. The maximum available voltage for pulse generation was 400 V which allowed us to use electric fields of $200 - 400$ kV/m, depending on the plate separation d.

3.4.2 General details and sample mounting

All pulsed ESR experiments discussed in Chapter 4 and the X- vs Q-band E-field measurements presented in Section 5.2.3 were conducted on a Bruker E580 CW/pulsed spectrometer in the CAESR facility. An Oxford Instruments continuous flow ESR CF935 cryostat and ITC 503 system were used for temperature control. The orientational dependences of the E-field measurements in Chapter 5 were performed on our home-built spectrometer in the Department of Physics.

The pulse measurements in X-band, and the PSD experiment in particular (see Section 2.5.2), were carried out using a standard Bruker ER 4118X-MD5-W1 pulsed/CW (MD5) resonator: in comparison with the MD4 resonator, MD5 has a larger space for inserting samples, equivalent to a 4.8 mm quartz tube. The static magnetic field $\boldsymbol{B}_0$ was applied horizontally – its direction defines the laboratory z-axis. Inside, the MD5 resonator contains a dielectric ring (cylinder) which ensures the spatial isolation of the MW electric and magnetic fields: the electric component is localised mostly inside the ring, whereas the magnetic $\boldsymbol{B}_1$ component has the highest intensity in the hole of the ring and oscillates along the vertical x-axis of the laboratory frame. Figure 3.17 contains a schematic representation of the experimental arrangement inside the resonator and the mutual orientation of the sample and the applied fields.

At Q-band ($\approx$ 34 GHz), the experiment was conducted using a Bruker ER 5106 QT-W pulsed/CW Bruker resonator with the maximal allowed quartz tube diameter of 3 mm. The design of this probe does not include a dielectric ring, so the separation of the electric and magnetic MW fields is achieved by simply confining the MW radiation in the cavity. Further details of how the E-field measurements were performed are applicable to both resonators.

For E-field measurements at a static orientation, that is, when the orientation of vector $\boldsymbol{E}$ was fixed with respect to the crystal axes, the sample was mounted directly onto one of the PCB plates using a touch of vacuum grease (see frame (c) in Figure 3.16). For measuring the orientational dependences of the E-field effect, that is, when the angle between $\boldsymbol{E}$ and one of the crystal axes, e.g. C_3-axis, has to be

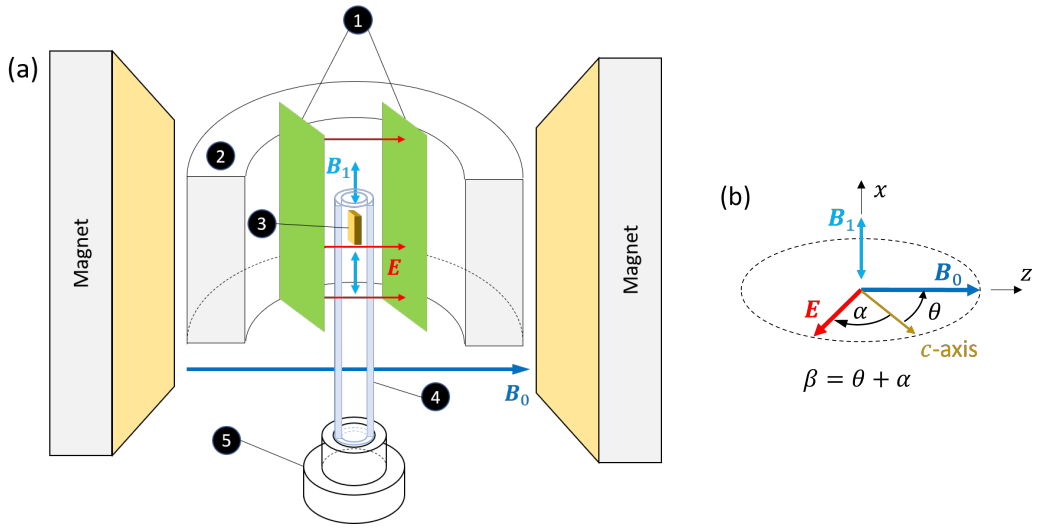

Figure 3.17: (a) Schematic representation of the sample position inside an MD5 resonator: 1 – the gold-plated PCB plates, 2 – dielectric ring, 3 – sample, 4 – 1.6 mm quartz tube for mounting the sample from the bottom of the resonator, 5 – PTFE pedestal. (b) Orientation of the magnetic and electric fields with respect to sample's crystal axis. Both angles θ and α can be changed in our experiment.

gradually changed, the sample was first mounted on the edge of or inside a Q-band quartz tube with outer diameter 1.6 mm. After that, the tube with the sample was inserted into the resonator from the bottom and fixed by means of a pedestal made of PTFE (see (a) in Figure 3.17). In this arrangement, the E-field could be freely rotated around the sample while staying in the yz-plane of the laboratory frame by rotating the probe-head, whereas the orientation of the sample itself could be changed by rotating the resonator – this is schematically shown in Figure 3.17(b). To prevent the plates from moving with respect to each other and the tube from exiting the region between the plates, we connected the plates by non-conducting pieces of PCB – in this way the quartz tube was always coaxial with the laboratory x-axis.

3.4.3 Metallisation of the capacitor plates

MW radiation decays extremely quickly in good conductors, so we need to make sure that the metallisation of the PCB plates does not significantly impede the propagation of the MW radiation.

The attenuation of a signal by a layer of metal is proportional to

$$\exp\left(-\frac{d_{\mathrm{Me}}}{\delta_{\mathrm{Me}}}\right), \tag{3.21}$$

where d_{Me} denotes the thickness of the layer and δ_{Me} is the skin depth of the metal given by

$$\frac{1}{\delta_{\mathrm{Me}}} = \omega\sqrt{\frac{\epsilon\mu}{2}}\left[\sqrt{1+\left(\frac{\sigma}{\epsilon\omega}\right)^2}-1\right]^{1/2}, \tag{3.22}$$

where ϵ is permittivity and μ is permeability of the material: for our estimation, these can be set to those of a vacuum; σ is the conductivity of the metal [125].

Given the conductivity of gold and chromium are $4.55 \cdot 10^7$ and $0.78 \cdot 10^7 (\mathrm{Ohm} \cdot \mathrm{meter})^{-1}$, respectively, the plates made of 10 nm of chromium and 100 nm of gold will attenuate the amplitude of the MW wave at 9.7 GHz by approximately 13%. In terms of pulse measurements, this results in a proportional increase in the pulse duration for the same flip angle.

3.5 Conclusions

We have assembled a fully-functioning X-band pulse spectrometer with full access to its settings and properties which enables us to perform state-of-the-art experiments as well as to test new samples in a robust and reproducible manner. Some technical specifications of the set-up are presented in Table 3.1

In conjunction with standard resonators, our spectrometer allows us to implement pulse sequences containing both MW and RF pulses of arbitrary shape, frequency, and phase. The static and orientational E-field measurements are done by means of a probe-head of our own design. The spectrometer's capabilities can be extended by replacing any of the components: for instance, we can replace the MW amplifier to obtain a wider amplification bandwidth.

All the measurements presented in Chapter 6 and the majority of experiments discussed in Chapter 5 were performed on our spectrometer.

Magnetic field	
Max B_0	0.97 T
Resolution	0.02 mT
MW amplification	
Bandwidth	$8.7 - 9.8$ GHz
MW output power	300 W or 55 dBm
Shortest MW π-pulse	10 ns
Rise time	2 ns
Fall time	9 ns
Minimal open gate time	1000 ns
Maximal open gate time	Unlimited
Minimal dead-time t_d	100 ns
RF amplifiers	
Bandwidth	$0.3 - 35$ MHz
RF output power	300 W
Bandwidth	$0.1 - 200$ MHz
RF output power	30 W
Bandwidth	$50 - 500$ MHz
RF output power	100 W
Operation mode	Pulse or CW
AWG	
Shortest pulse sequence	14 ns
Longest pulse sequence	$\sim$ 2.5ms
Min. waveform length	32 samples
Rise time	0.3 ns
Sample rate	2.4 GS/s
Electric field	
Max amplitude	400 V
Shortest pulse	80 ns
Longest pulse	100 μs
Rise & fall times	$\leq$ 15 ns

Table 3.1: Specifications of the spectrometer we assembled.

Chapter 4

Mn(II) trigonal bipyramidal complexes

Contents

This chapter presents our original research into the SEC in the Mn(II) trigonal bipyramidal complexes. The project was completed in collaboration with Dr Junjie Liu; the molecules were synthesised by Dr François Lambert, Dr Christian Herrero, Dr Règis Guillot, and Prof Talal Mallah – they also provided the X-ray diffraction data; high-frequency CW ESR analysis was performed by Dr Anne-Laure Barra; and the DFT theoretical calculations were provided by Dr Nicolas Suaud, Dr Benjamin

Cahier, and Prof Nathalie Guihéry. The results of the research were assembled into a paper which was recently published in Nature Chemistry [126]. This chapter is largely a reproduction of that paper with some additional data and insights.

4.1 Introduction

In this chapter we discuss the possibility of using pulses of static electric fields in order to coherently control qudits implemented on molecular magnets. In particular, we consider three trigonal bipyramidal Mn(II) complexes where a single electropositive Mn ion with $S = 5/2$ and $L = 0$ is juxtaposed to one of three different electronegative halogens (I, Br or Cl). Each of these molecules lacks inversion symmetry and possesses a spontaneous electric dipolar moment together with uniaxial magnetic anisotropy. Those properties allow us to demonstrate significant coupling of the complexes with the E-field (see Section 4.4). An attractive feature of these compounds is the ability to change the halogen ion relatively easily: this allows one to fine-tune the molecular electric dipole moment and, consequently, the E-field coupling without modifying the Mn ion valence. It also presents an opportunity to study how the quantum properties and relaxation times of the molecules vary when just a single ion is replaced.

4.1.1 Molecular and crystal structure

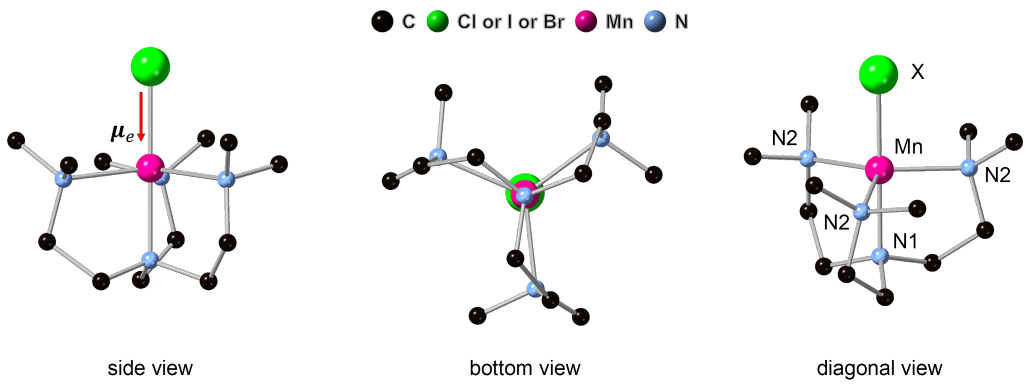

Figure 4.1: The molecule of the Mn(II) trigonal bipyramidal complexes. The protons are hidden for clarity.

Here we investigate three molecules in which a single ion of manganese (II) is positioned in the pentacoordinate environment provided by the organic ligands of Tris[2-(dimethylamino)ethyl]amine (Me_6tren, for short). Figure 4.1 contains the ball-and-stick representation of the molecules: Mn(II) is surrounded by one axial (N1) and three equatorial (N2) nitrogen ions. The environment of Mn is additionally tuned by attaching a halogen ion X of either chlorine, bromine, or iodine ($X \in \{Cl, Br, I\}$). Each molecule possesses a three-fold symmetry axis passing through the halogen, manganese, and the axial nitrogen ions (X-Mn-N1). Due to the different electronegativity of these three ions, it was anticipated and later confirmed by DFT that their arrangement generates a spontaneous electric dipole $\boldsymbol{\mu}_e$. As we will see later, this dipole moment provides a significant coupling between an external electric field and the spin-state of the manganese ion.

In all three molecules, the distances between the manganese and nitrogen ions, and the N1-Mn-N2 angles vary by less than one percent, whereas the length of the Mn-X bond differs significantly: it is 2.3458(3) Å, 2.5026(18) Å and 2.7133(6) Å for X = Cl, Br and I, respectively. As expected, the Mn-X distance affects the value of the molecular electric dipole; a careful choice of the halogen ion enables one to tune the SEC of these compounds.

With the addition of a tetrahedral perchlorate ClO_4^- counterion, the Cl derivative (**1**) crystallises in the $R3c$ trigonal space group [127–129]. Analogously, the Br derivative (**2**) crystallises into the $R3m$ trigonal space group with PF_6^- as a counter anion. Finally, the I derivative (**3**) crystallises in the cubic $P2_13$ space group with the help of an additional ion of I^-. Together with the crystallisation agents, the formal chemical formula of the compounds is [Mn(Me_6tren)X]Y (where X = Cl, Y = ClO_4 for (**1**), X = Br, Y = PF_6 for (**2**), and X = I, Y = I for (**3**)). The desired concentration of 0.1% or 1.0% of paramagnetic molecules was achieved by diluting them in isostructural diamagnetic hosts with Zn(II) instead of Mn(II). In (**1**) and (**2**) the C_3-axis coincides with the c-axis of the crystals, whereas in (**3**) the C_3-axis is one of the diagonals of the cubic unit cell.

4.1.2 Spin Hamiltonian

Given the spin-quantisation z-axis along the molecular C_3-axis, the low-energy states of the Mn(II) ions are well described by the approximate phenomenological spin Hamiltonian

$$\hat{\mathcal{H}}_0 = \mu_{\mathrm{B}} g \boldsymbol{B}_0^{\mathrm{T}} \hat{\boldsymbol{S}} + A \hat{\boldsymbol{I}}^{\mathrm{T}} \hat{\boldsymbol{S}} + D \hat{S}_z^2, \tag{4.1}$$

were μ_{B} is the Bohr magneton, $\boldsymbol{B}_0$ is the static magnetic field, and g and A are the isotropic g-factor and hyperfine coupling constant, respectively. The last term describes the magnetic anisotropy of the system with D being the axial ZFS parameter – it corresponds to the B_2^0 term in the sum of the extended Stevens operators in Equation 2.84.

4.2 CW characterisation

In order to determine the magnitude and sign of the crystal-field parameter D, and the magnitude of the hyperfine constant A, our colleague, Dr Anne-Laure Barra, performed high-frequency CW measurements of the *powder* spectra for all three compound derivatives at the concentration of paramagnetic molecules of 1%. The CW spectra have been measured at 255.36 GHz and at two temperatures of 5 and 15 K. The results are shown in Figure 4.2.

The values of the spin-Hamiltonian parameters have been obtained by fitting the experimental data with simulated spectra – results are presented in Table 4.1. During simulation, no evidence of transverse anisotropy was found. Compound (**1**) possesses an easy axis of magnetization ($D < 0$), whereas (**2**) and (**3**) exhibit the easy-plane type of anisotropy ($D > 0$). The values of D, though significant, allow the ESR transitions of these molecules to be accessible by the X- and Q-band ESR spectrometers. The hyperfine coupling constant was found to be more or less the same for all three derivative compounds.

The difference in the sign of D between (**1**) and both (**2**) and (**3**) can be deduced by inspecting the spectra. Indeed, for (**1**) the intensity of the peaks at low fields

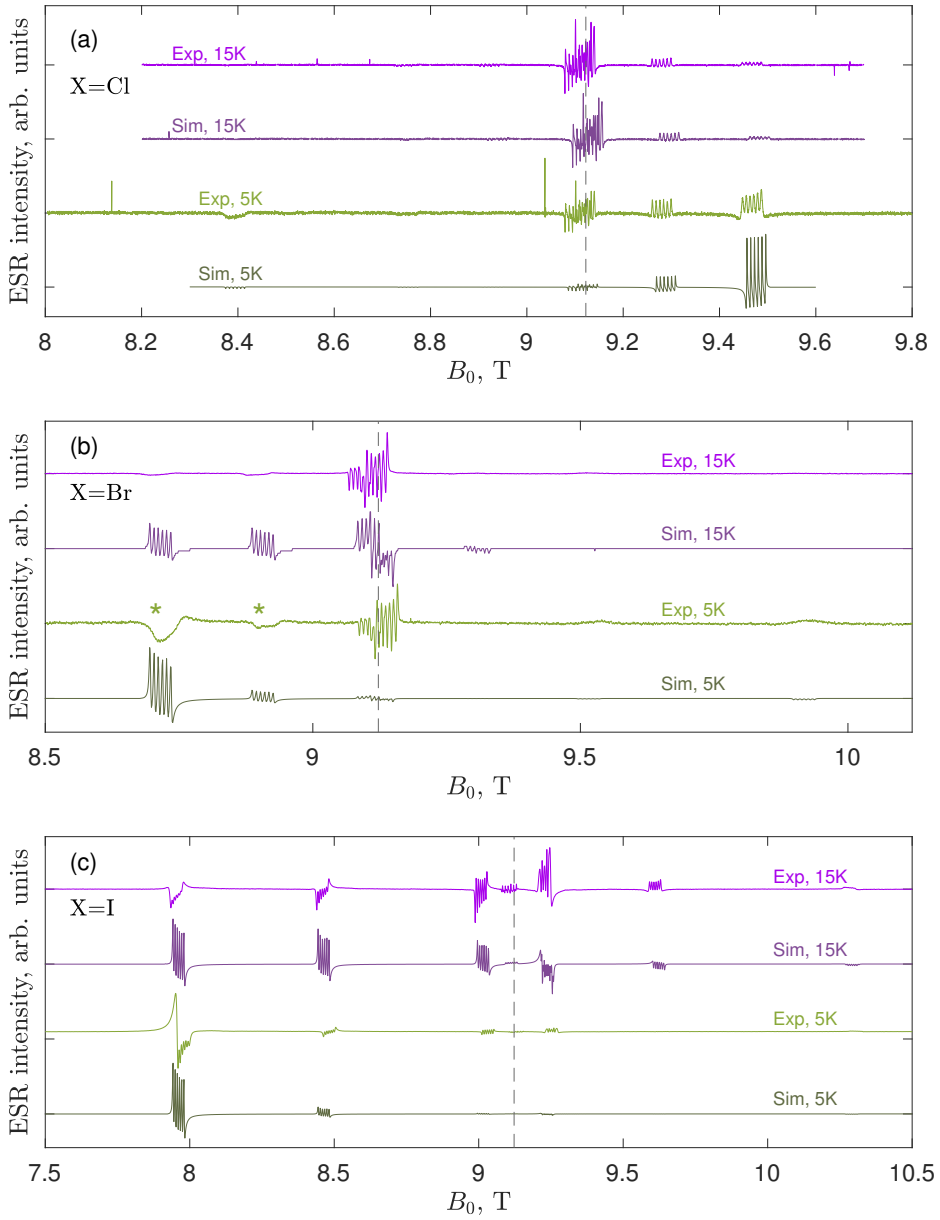

Figure 4.2: (a), (b) and (c): powder CW experimental and simulated spectra at 255.36 GHz for (**1**), (**2**) and (**3**) respectively. The resonance field for g = 2 of an isotropic spin-5/2 system is indicated by the vertical dashed lines. The simulation was performed using the SIM library [130].

(on the left from the line $g = 2$) is significantly lower than the intensity of the peaks at higher fields (on the right from $g = 2$). In fact, the resonance of (**1**) is almost undetectable at fields below 9 T. The situation is the opposite for (**2**) and (**3**), with the peaks at lower fields possessing higher intensity than that of the peaks at higher fields. This opposite behaviour indicates the difference in the

Molecule	(**1**)	(**2**)	(**3**)
Experiment			
g	1.98	1.99	2, 06
$\lvert A\rvert$, MHz	220	210	210
D, GHz	−5.04	5.64	16.5
$\max\left(\frac{\delta D}{\mathrm{d}E}\right)$, Hz/(V/m)	−0.42	−1.20	−1.70
Theory: values of D at $\boldsymbol{E} = 0$			
$D_{\mathrm{X-Ray}}$, GHz	−5.16	−1.71	2.94
D_{DFT}, GHz	−3.90	0.15	5.22
Theory: μ_{e}, debye, at $\lvert E\rvert = 1.0284 \cdot 10^9$ V/m			
initial μ_{e}	7.787	9.861	11.933
$\mu_{\mathrm{e}}^{\uparrow}$, when $\boldsymbol{E}$ is along N1-Mn-X	6.755	8.764	10.700
$\mu_{\mathrm{e}}^{\downarrow}$, when $\boldsymbol{E}$ is along X-Mn-N1	8.818	10.958	13.165
$\Delta\mu_{\mathrm{e}} = \mu_{\mathrm{e}}^{\downarrow} - \mu_{\mathrm{e}}^{\uparrow}$	2.063	2.194	2.465
Theory: $\max\left(\frac{\delta D}{\mathrm{d}E}\right)$, Hz/(V/m)			
(a) displacement of electronic density only	−0.043	−0.112	−0.239
(b) change in geometry due to $\boldsymbol{E}$ only	−0.192	−0.278	−0.498
(c) both effects	−0.234	−0.390	−0.735

Table 4.1: Measured values of the spin-Hamiltonian parameters, and results of theoretical *ab initio* calculations. The theoretical results for the zero-E-field D values are calculated using both the X-ray structure (DXR) and the structure optimised using DFT (DDFT). $\frac{\delta D}{\mathrm{d}E}$ and μ_{e} are calculated using three different scenarios as described in Section 4.5.1.

sign of D between different compounds.

It is worth noting that the spectra for (**2**) exhibit two broad features due to unresolved hyperfine structure, as indicated by symbols * in Figure 4.2(b), whereas all hyperfine features are clearly resolved in the spectra of (**1**) and (**3**). This can only be explained by including a substantially larger D-strain parameter for (**2**). Increasing the overall linewidth, A-strain or g-strain in the simulation lead to unresolved hyperfine features for all transitions, which is inconsistent with the data. This is in agreement with the pulsed ESR data for (**2**) (see Figure 4.3(b)), where

only the inter-Kramers transitions show unresolved hyperfine features and all the nuclear spin states can still be clearly identified for the intra-Kramers transitions.

4.3 Pulse characterisation

4.3.1 EDFS

The pulse EDFS spectra and energy level diagrams for the situation where the static magnetic field is applied close to the C_3-axis are shown in Figure 4.3.

The spectra of (**1**) and (**2**) obtained at the Q-band contain both inter-Kramers ($m_S : \pm 5/2 \leftrightarrow \pm 3/2$ and $m_S : \pm 3/2 \leftrightarrow \pm 1/2$) and intra-Kramers ($m_S : -1/2 \leftrightarrow +1/2$) transitions. Some of the groups of electron transitions $\Delta m_S = 1$ have a fine structure of peaks due to the hyperfine interaction. As in the CW case, the hyperfine structure of the compound with Br is unresolved for the transitions $m_s : +1/2 \leftrightarrow +3/2$ and $m_s : +3/2 \leftrightarrow +5/2$ but is clearly visible for $m_s : -1/2 \leftrightarrow +1/2$; this signals the presence of the strain (distribution) in the crystal field parameter D. The corresponding ZFS term in the Hamiltonian 4.1 shifts the $m_s = -1/2$ and $m_s = +1/2$ levels by the same amount, so that its effect is not spectroscopically detectable at the ESR transition between these levels, but is visible at other transitions. The accessibility of different ESR transitions together with resolved hyperfine structure (in case of (**2**) at least in the intra-Kramers group) allows one to investigate the SEC of all the spin-Hamiltonian parameters separately.

Though the Q-band offers higher sensitivity, the spectrum of (**3**) was measured at the X-band, and the reason for that is as follows. The cubic unit cell of (**3**) contains four distinct sites which give four different orientations of the molecules. Together, those sites produce a forest of peaks at the Q-band, making the process of choosing a peak for a desired transition unfeasible. In addition, the high value of D makes some of the transitions simply inaccessible while using a resistive magnet.

Moreover, while aligning the crystal so that one of its C_3 axes is precisely parallel to $\boldsymbol{B}_0$, we did not manage to obtain spectra containing distinguishable and observable inter-Kramers transitions. Therefore, we oriented the crystal in such a way that the C_3-axis of one of its molecular subpopulations was slightly tilted away

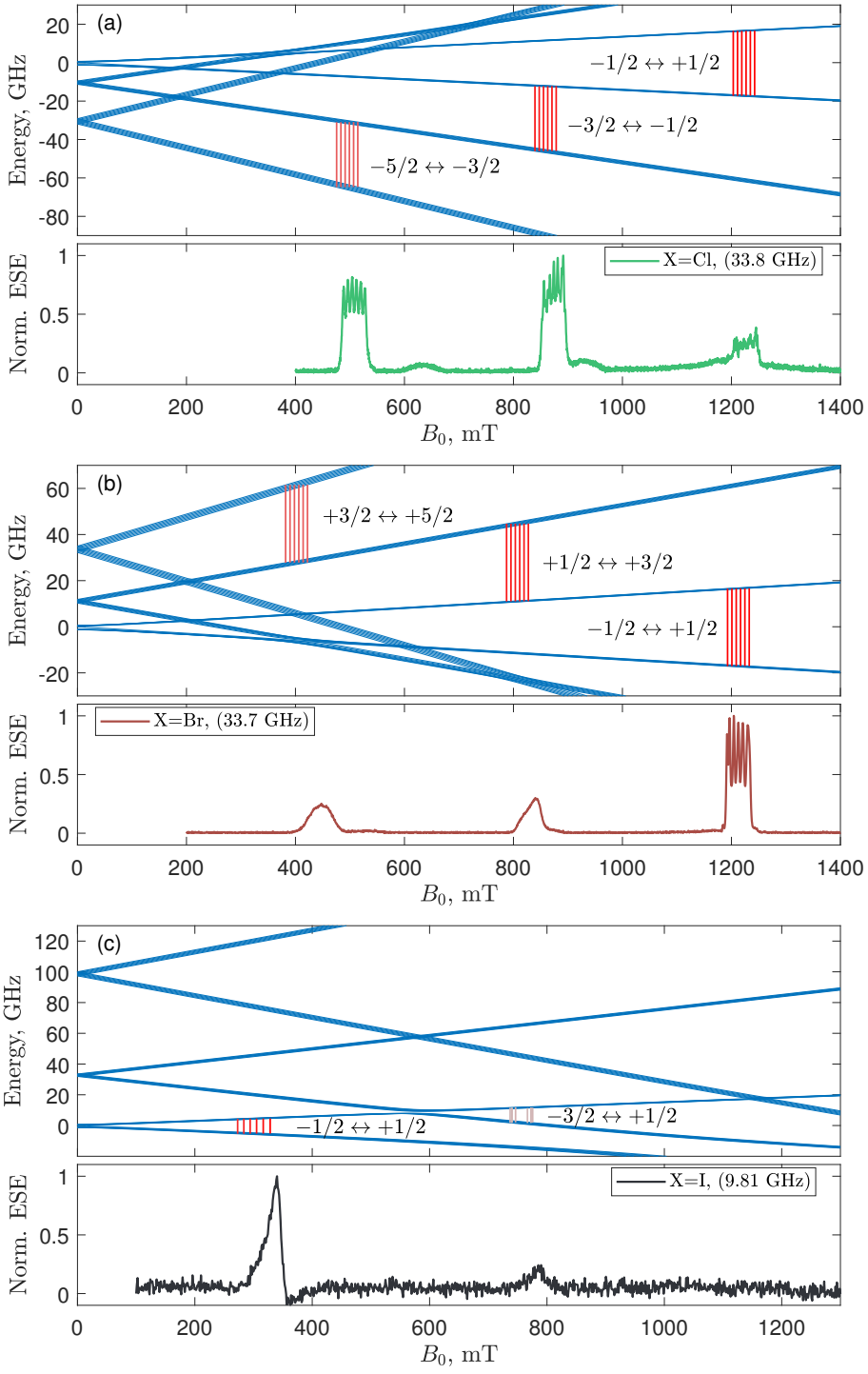

Figure 4.3: (a), (b) and (c): The energy level diagrams showing resonance transitions (model) and the corresponding EDFS spectra (experiment) for (**1**), (**2**) and (**3**) respectively.

from $\boldsymbol{B}_0$ (at $\approx 10°$). This small tilt mixes states with different m_S, thus making a nominally forbidden transition (m_S : $-3/2 \leftrightarrow +1/2$, $\Delta m_S = 2$) visible in the ESR experiment, as indicated by the label in the top panel of Figure 4.3(c). Both

the numerical simulations and the experimental data show that this transition is only observable within a small range of tilting angles, approximately between 7° and 13°. Outside this range, the resonance either becomes too broad (for large tilt) or the transition probability vanishes (for small tilt), making the resonance indistinguishable from the spectrum baseline. Importantly, only one molecular subpopulation will contribute to this resonance, while the X-band transitions for the other three subpopulations only appear at much lower fields, contributing to the large feature centred around 0.3 T. Hence, this experimental configuration allowed us to select one molecular subpopulation and investigate the correlation between the SEC and its structure for (**3**).

4.3.2 Relaxation times

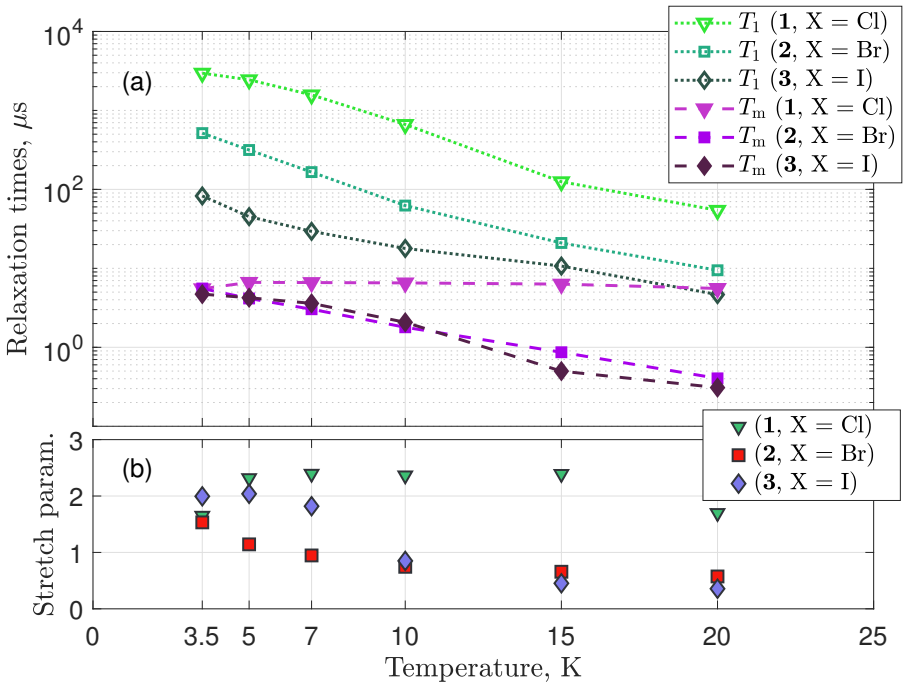

Figure 4.4: (a) Relaxation times and (b) the stretch parameters for fitting the T_m data.

The dependence of both the longitudinal relaxation time T_1 and the phase memory time T_m on temperature has been measured at the Q-band for all three derivatives and is shown in Figure 4.4(a). For (**1**) and (**2**), the relaxation times were measured at $m_s : -5/2 \leftrightarrow -3/2$ and $m_s : +3/2 \leftrightarrow +5/2$ transitions, respectively.

It was not possible to determine the transition of (**3**) unambiguously due to a complex structure of its spectrum at the Q-band.

Spin-lattice relaxation time T_1 grows monotonically with a decrease in temperature. The acceleration of the T_1-relaxation processes as we go from (**1**) to (**2**) and then to (**3**) can be explained by the increase in the distance between the manganese and halogen ions down the group Mn-Cl → Mn-Br → Mn-I: the vibrations of atomic chains with a longer lattice constant are more easily excited at a given temperature due to weaker inter-atomic bonds. This is also consistent with the unresolved hyperfine structure in the EDFS of (**2**) and the assumption of the strain in its parameter D.

The values of the phase memory times T_m were obtained by fitting the experimental data with a stretched exponential of the form $\exp[-(2\tau_\mathrm{MW}/T_\mathrm{m})^x]$ (see Section 2.4.3.2). The dependence of the stretch parameter x on temperature is shown in Figure 4.4(b). The fact that at lower temperatures the stretch parameter is close to 2 suggests that the dominant mechanism of electron decoherence is the interaction with the nuclear spin bath surrounding the paramagnetic Mn centres (nuclear spin diffusion) [33, 97].

In the context of measuring the SEC, the relaxation times bear the following practical meaning. The spin-lattice relaxation time defines how long one has to wait between running repetitive measurements of the same data-point. Theoretically, the spin system will reset itself thermally to 95% of its initial state after $5T_1$ – any time longer than this value can safely be chosen as the shot repetition time for applying identical pulse sequences. The phase-memory time defines the maximal length of τ_MW and of the electric pulse duration one can use while maintaining a sufficient SNR level and a reasonable overall duration of the experiment (see Section 2.5.2).

4.4 Electric-field effect

The general details of our experimental set-up are presented in Section 3.4; the algorithm of acquiring the value of SEC is discussed in Section 2.5.2. Here I present the results of our measurements on the Mn(II) bipyramidal complexes.

4.4.1 Phase recovery during coherent electric control

The first step after preparing and tuning the experimental set-up for measuring the E-field effect is to test whether a sample responds to the application of the electric field at all. If the answer to this question is positive, then the next step is to determine whether we can manipulate the spins coherently by applying E-field pulses.

A quick test which can answer both those questions is to perform the measurement of the E-field spin echo sequence in quadrature (see Section 2.5.2) while allowing the E-field pulse to extend from right after the first MW $\pi/2$-pulse to up to the moment where the echo is expected to appear $t_E \approx 2\tau_{MW}$. The application of an E-field pulse in the first free-evolution period of the spin-echo sequence causes the accumulation of a positive phase shift. By contrast, in the second free-evolution period, the phase shift will be negative due to the inversion of the spin evolution by the refocusing π-pulse. The progressive recovery of the initial phase and magnitude of the echo after the refocusing pulse as a function of t_E will confirm that the application of the E-field pulse empowers one with coherent control over the spin system using the electric degree of freedom [51].

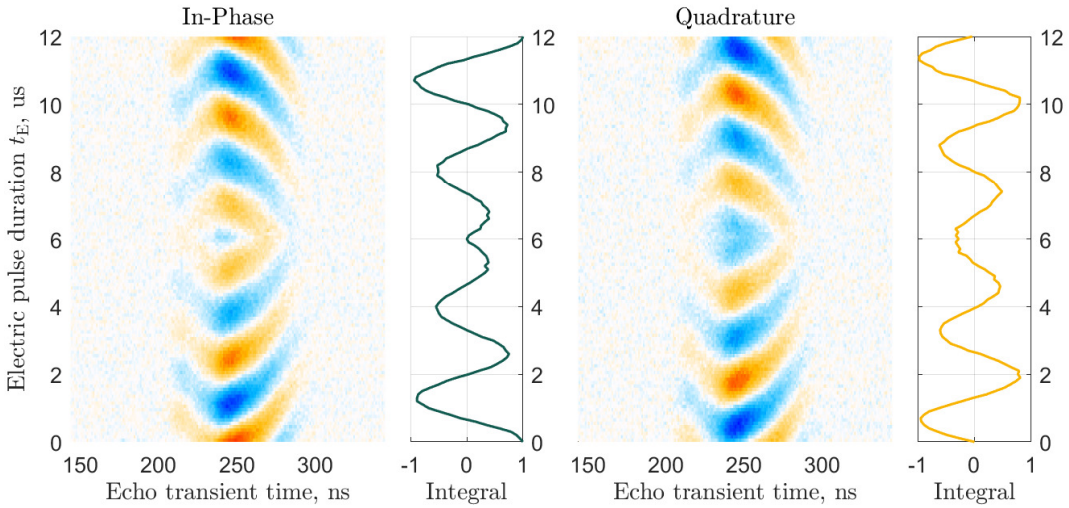

Figure 4.5: Phase-recovery measurement for the Cl derivative (**1**). Note that at the beginning of the experiment ($t_E = 0$ ns) we always put all the signal into the in-phase component.

An example of the phase-recovery measurement for (**1**) is shown in Figure 4.5.

The duration of the MW pulses were $t_{p1} = 16$ ns, $t_{p2} = 32$ ns and $\tau_{MW} = 6000$ ns. Since the excitation pulses were much shorter than the maximal duration of the E-field pulse $t_E = 12000$ ns, one can observe at $t_E = \tau_{MW}$ a clear border acting as a mirror plane between almost identical top and bottom parts of the echo evolution with respect to t_E. This result proves that we can coherently control spins using the E-field pulses.

4.4.2 Modulation of the Hamiltonian by the E-field

The Hamiltonian 4.1 contains three parameters: g, A and D. Theoretically, any of these can be modulated by an applied electric field. We can use the properties of the zero-field term $D\hat{S}_z^2$ in order to separate the effects of modulating g and A from those of modulating D.

Any change δD in the crystal field parameter shifts the eigenvalues of the Zeeman Hamiltonian by the value of the corresponding diagonal matrix elements

$$\delta\epsilon = \langle m_s|\delta D \cdot \hat{S}_z^2|m_s\rangle\,. \tag{4.2}$$

For $S = 5/2$ and $m_s \in \left\{-\frac{5}{2}, -\frac{3}{2}, -\frac{1}{2}, +\frac{1}{2}, +\frac{3}{2}, +\frac{5}{2}\right\}$, the vector representing the shifts of the eigenlevels will be $\delta\epsilon = (\delta D/4)\cdot(25, 9, 1, 1, 9, 25)^{\mathrm{T}}$. Thus, the energy levels of $m_s = -1/2$ and $m_s = +1/2$ are shifted by the same amount and the ESR transition $m_s : -1/2 \leftrightarrow +1/2$ occurs at the same frequency and field. In its turn, the resonant frequency of the inter-Kramers transitions do change: for $m_s : +1/2 \leftrightarrow +3/2$ the change is equal to $2\delta D/h$, and that for $m_s : +3/2 \leftrightarrow +5/2$ is $4\delta D/h$. Note that we did not say anything about the nature of change in D, so it does not matter what caused δD as long as all the other parameters of the Hamiltonian remain unchanged. It also follows that if one detects a frequency shift for $m_s : -1/2 \leftrightarrow +1/2$ transition, it must be caused by a change in either g or A, but not in D.

The evolution of the integrated echo signal as a function of the E-field pulse duration at different ESR transitions of (**2**) is shown in Figure 4.6. The signal exhibits clear oscillations for transitions $m_s : +1/2 \leftrightarrow +3/2$ and $m_s : +3/2 \leftrightarrow +5/2$, with the frequency of the latter being about twice as large as the frequency of

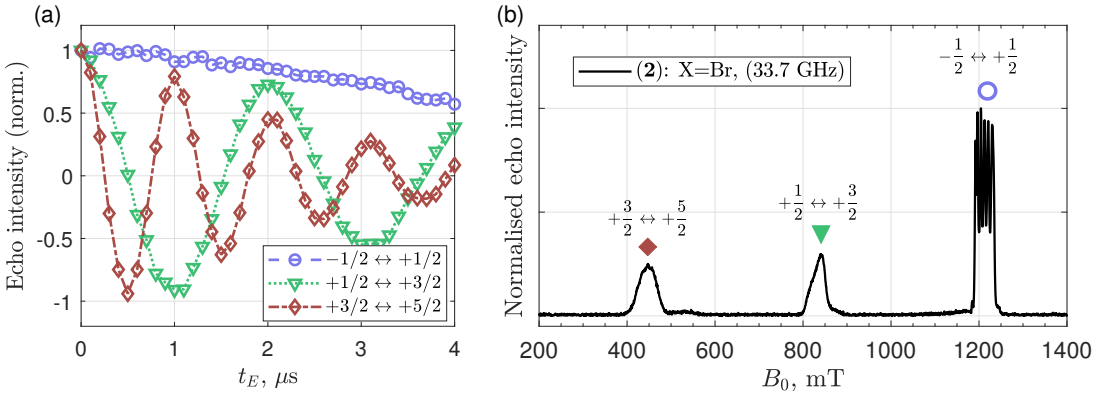

Figure 4.6: (a) The integrated in-phase component of the echo signal for the Br derivative at the three ESR transitions whose location is shown on the EDFS in sub-figure (b).

the former. In comparison with those, the signal of $m_s : -1/2 \leftrightarrow +1/2$ transition demonstrates just a weak SEC. It is not absent though: the weak change in the echo's phase is most probably due to an imperfect alignment of the crystal, so that $\boldsymbol{B}_0$ is not precisely directed along the C_3 axis, and the response at this transition is caused by the admixing of other eigenstates of $\hat{S}_z$. From these data we conclude that the change in the Hamiltonian 4.1 caused by the E-field pulse is predominantly due to the change in the crystal field parameter D.

As was mentioned in Section 4.1.1, each molecule of the Mn(II) bipyramidal compounds possesses a non-zero electric dipole moment along its three-fold axis, that is along the X-Mn-N1 bond. All the molecules in the crystals of (**1**) and (**2**), and molecules of the same subpopulation in the crystal of (**3**) are ordered in such a way that their X-Mn-N1 bonds are oriented in the same direction – that is, the molecules do not have inversion images[1]. Depending on its direction, an external electric field can either stretch or shrink those bonds leading to two different responses in the electric field effect. For the integrated echo signal, it will mean that there will be a π-radian shift in the phase of the oscillation of the quadrature component at any given magnitude of $\boldsymbol{E}$. The in-phase component of the echo will not change when the direction of $\boldsymbol{E}$ is switched due to the algorithm of our measurement technique: at $t_{\mathrm{E}} = 0$ we maximise the in-phase component and it can only decrease from

[1]Two molecules would be called 'inversion images' of each other if their X-Mn-N1 bonds, and consequently $\boldsymbol{\mu}_{\mathrm{e}}$, were collinear but pointed in opposite directions [53].

there producing a cosine-like oscillation, whilst the quadrature component starts oscillating from the origin and has a sine-like shape (see Section 2.5.2).

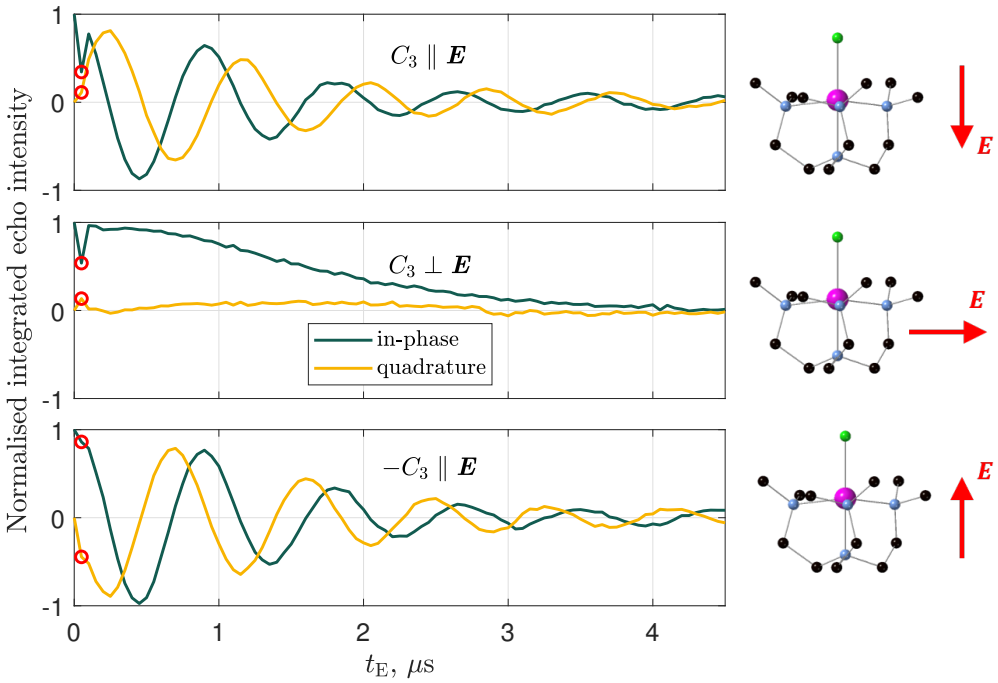

Figure 4.7: Dependence of the in-phase and quadrature components of the echo signal of (**2**) at transition $m_s : +3/2 \leftrightarrow +5/2$ at three orientations of $\boldsymbol{E}$ with respect to the X-Mn-N1 bond. The phase of the quadrature component changes by π when the direction of $\boldsymbol{E}$ is inverted. The highlighted point is a measurement artefact (see Appendix A.3.1).

Figure 4.7 demonstrates the effect of reversing the direction of the electric field in (**2**). It contains the dependence of the integrated echo components on the duration of the E-field pulse at three different arrangements of the C_3-axis and vector $\boldsymbol{E}$ while keeping the three-fold axis aligned with $\boldsymbol{B}_0$. In all sub-figures, the in-phase component follows the cosine trend, while the quadrature component changes its behaviour depending on the direction of vector $\boldsymbol{E}$.

The described behaviour is allowed for any odd order of the E-field effect; that is, when change δD is proportional to $E^{(2n+1)}, n \in Z$. The graph in Figure 4.8 demonstrates that the SEC effect in the Mn bipyramidal complexes is linear. The frequency change due to a linear E-field effect is $\delta f = \alpha E$, and the change of the sign in quadrature component follows directly from its proportionality to $\sin(2\pi\alpha E t_E)$. In our spectrometer, when the frequency shift is positive, the quadrature component

behaves like minus-sine, whereas if the frequency shift is negative, the quadrature component is akin to a normal plus-sine function.

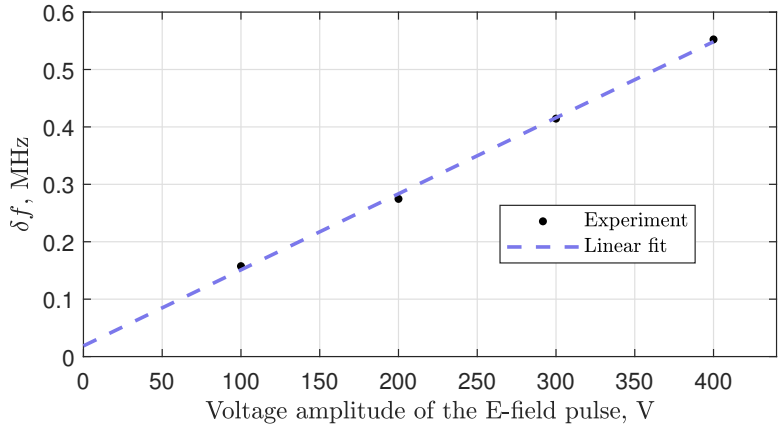

Figure 4.8: Linear dependence of the SEC on the E-pulse voltage for (**2**).

4.4.3 Polarity of the SEC

In this Section, by the polarity of the SEC, we understand the dependence of the sign of δD on the orientation of field $\boldsymbol{E}$ with respect to the direction defined by the X-Mn-N1 bond.

By tracking the direction of the electric field $\boldsymbol{E}$ we applied to the crystals of (**1**), (**2**) and (**3**) in our SEC experiments, and by performing the X-ray diffraction measurements on the same crystals, we were able to unambiguously tell how the E-field was oriented relative to the X-Mn-N1 bonds. Next, from the behaviour of the quadrature component of the echo we were able to determine the sign of δf. A positive δf means that the separation between energy levels participating in the ESR transitions increases, whereas a negative δf means the opposite. By consulting the energy diagrams in Figure 4.3 and the spin Hamiltonian 4.1 while taking into account the sign of initial D, we were able to deduce the sign of δD.

Consider the SEC measurements shown in Figure 4.9 – it demonstrates the connection between the behaviour of the echo and the direction of the electric field with respect to the molecular C_3-axes. To simplify the discussion, I have chosen the cases in which the quadrature components behaved as the minus-sine

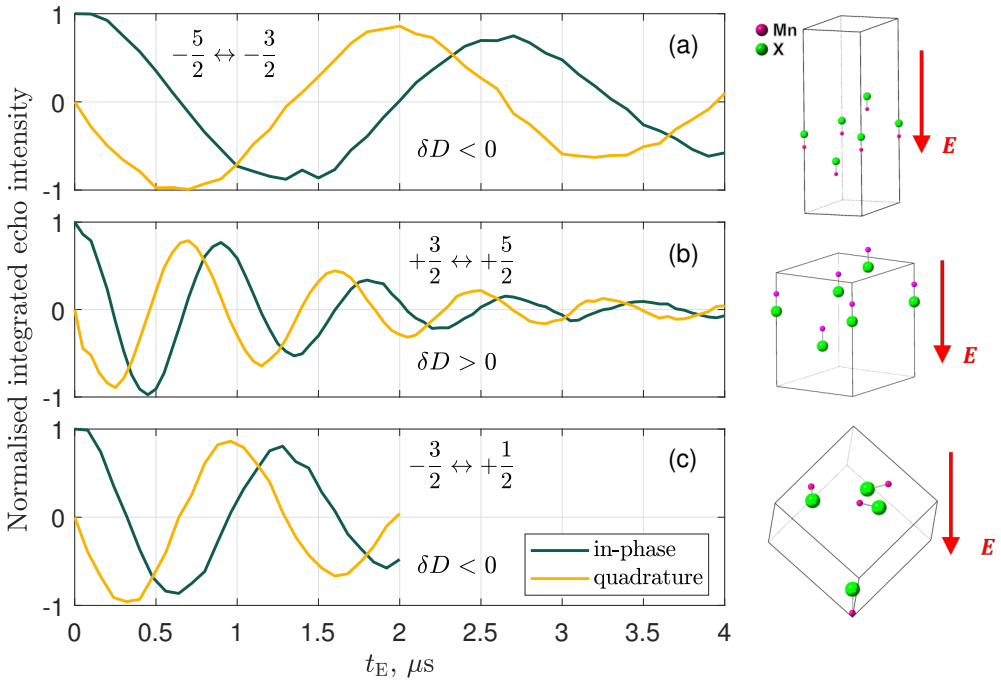

Figure 4.9: Dependence of the in-phase and quadrature components of the echo signal for (a) (**1**) at $m_S : -5/2 \leftrightarrow -3/2$, (b) (**2**) at $m_S : +3/2 \leftrightarrow +5/2$, (c) (**3**) at $m_S : -3/2 \leftrightarrow +1/2$. The side figures show the orientation of the E-field relative to the unit-cells of the crystals: only the X-Mn bonds are shown for clarity.

function corresponding to positive δf, and the direction of $\boldsymbol{E}$ was the same in each measurement. Taking into account the transitions at which the measurements were performed, the sign of δD is determined by the following calculations.

For (**1**), neglecting hyperfine interaction, the resonance frequency of transition $m_S : -5/2 \leftrightarrow -3/2$ when the E-field is applied is roughly $|-\mu_B g B_0 + 4D + 4\delta D|/h$, $(D < 0)$ or approximately $|-13.7 - 20.1 + 4\delta D/h|$ GHz – since $\delta f > 0$, we find that the change in D must be negative, that is $\delta D < 0$, so the magnitude of D increased (it became 'more negative').

For (**2**), the transition frequency of $m_S : +3/2 \leftrightarrow +5/2$ is $|\mu_B g B_0 + 4D + 4\delta D|/h$ but $(D > 0)$, so it is $|12.8 + 22.6 + 4\delta D/h|$ GHz since $\delta f > 0$, we find that $\delta D > 0$ – the magnitude of D increased.

Finally, for (**3**), the resonance frequency of transition $m_S : -3/2 \leftrightarrow +1/2$ is $|-2\mu_B g B_0 + 2D + 2\delta D|/h$ or $|-44.0 + 33.0 + 2\delta D/h|$ GHz – for $\delta f > 0$, therefore we find that $\delta D < 0$.

By checking the orientation of molecules in Figure 4.9, we conclude that δD is negative when $\boldsymbol{E}$ is applied in the direction from the halogen to the manganese ion ($\boldsymbol{E} \parallel$ X-Mn-N1), for all three compounds (**1**), (**2**) and (**3**).

4.4.4 Orientational behaviour of the SEC

The importance of the molecular electric dipole along the X-Mn-N1 bond can be further understood by studying the orientational dependence of the SEC. To do so, we conducted a set of measurements on all three derivatives of the Mn(II) bipyramidal compounds. The crystals were in the same orientation as described in Section 4.3.1 where we discussed their EDFS spectra – the X-Mn-N1 bonds were closely aligned with the static magnetic field $\boldsymbol{B}_0$. After that we measured the SEC at different orientations of the electric field $\boldsymbol{E}$ with respect to the X-Mn-N1 bond while keeping the sample in the same position. The result of these measurements is the dependence of the shift δD on the angle between $\boldsymbol{E}$ and the direction of the C_3-axis defined by moving from X to Mn and then to N1 along the X-Mn-N1 bond (i.e. the angle between $\boldsymbol{E}$ and the dipole). The three dependences for the three compounds with Cl, Br, and I are presented in Figure 4.10.

For all three compounds, the maximal E-field effect was observed when the electric field was collinear with the C_3-axis. Almost no effect was observed when the electric field was perpendicular to the X-Mn-N1 bond. The overall orientational dependence of the SEC in all the derivatives exhibits a cosine-like behaviour thus highlighting the significance of the molecular dipole along the X-Mn-N1 bond.

The maximal achieved effect in (**3**) can theoretically provide a frequency shift of $4\delta D/E > 6$ Hz/(V/m)[2] for transition $m_s : +3/2 \leftrightarrow +5/2$. This effect is significant, especially considering that Mn(II) ions are typically associated with weak spin orbit interaction due to their half-filled $3d^5$ outer shell. The effect is larger than that reported for other nanomagnets with Mn(II) (≈ 0.68 Hz/(V/m)) [131], and is comparable with the SEC obtained on the complexes containing lanthanides ($\approx$ 11 Hz/(V/m)) [55].

[2]Strictly speaking, the LHS should be divided by h, but here I follow the convention.

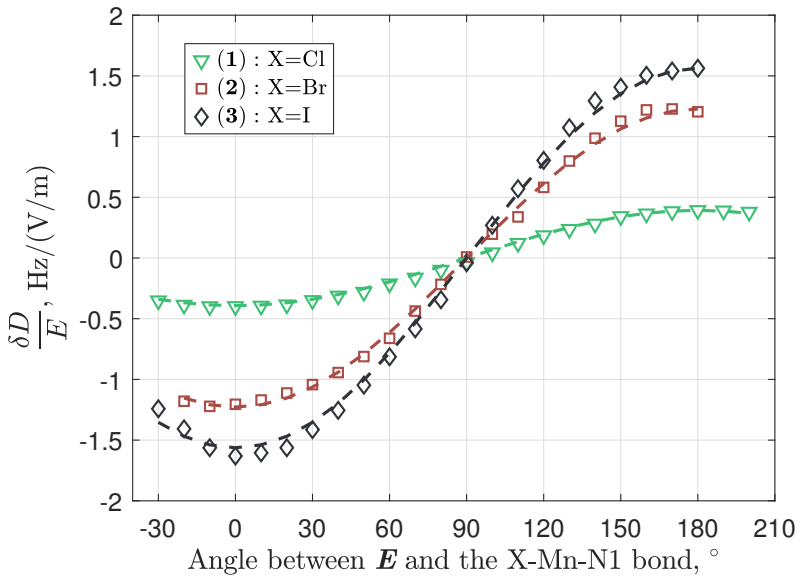

Figure 4.10: Dependence of the SEC for all three compounds of the Mn(II) bipyramidal complexes on the angle between $\boldsymbol{E}$ and the X-Mn-N1 bond. The markers represent the measured data, and the dashed lines are the cosine fit giving zero SEC at the right angle between $\boldsymbol{E}$ and the C_3-axis. The uncertainties are smaller than the marker size.

The E-field effect on the ZFS parameter itself, $|\delta D/E| = 1.7$ Hz/(V/m) for (**3**), is also comparable to those found for Mn^{2+} spins doped in inorganic crystals: 1.26, 2.25, 1.33 and 3.3 Hz/(V/m) for CaWO4 [132], SrWO4 [133], PbMoO4 [134] and ZnO [43], respectively. For the scheelite lattices [132–134], the SEC is largely attributed to the displacement of the spin-carrying ion in the applied electric field. In ZnO [43], the SEC is associated with the piezoelectric nature of the host lattice which allows a significant E-field-induced distortion of the lattice geometry.

These previous studies are consistent with our findings: a strong SEC is likely due to the significant molecular electric dipole and the fact that it is directly correlated to the molecular magnetic anisotropy. An E-field distorts the geometry of the molecule, modulating the ZFS of the Mn^{2+} spins.

4.5 DFT Simulation

Our colleagues from the group of Prof Nathalie Guihéry have performed wavefunction-based *ab initio* calculations of the crystal-field parameter D and have simulated the

change δD caused by an applied electric field $\boldsymbol{E}$. The purpose of this simulation was to find the main mechanism of SEC in all three molecules, and to investigate the dependence of SEC on the choice of the halogen atom X.

4.5.1 Calculation of D

The axial ZFS parameters D for all three molecules in the absence of an external electric field have been calculated using two geometries: one being the structure obtained by X-Ray diffraction, and the other being the molecular geometry optimised by density functional theory (DFT) while preserving the C_3 symmetry point group. Both calculations reproduce the trend of D observed in the ESR measurements – the ZFS shifts from the easy-axis type ($D < 0$) to the easy-plane type ($D > 0$) as the halogen atom varies from Cl to I (see Table 4.1). Some details of the calculation are given in Appendix A.3.2. Here we focus on the results obtained using DFT-optimised geometry since it allows us to investigate the E-field induced distortions.

4.5.2 E-field effect calculation

There are two major effects of the application of an electric field to the Mn(II) bipyramidal complexes which result in a change in D. The first is the distortion of the electron density by the direct interaction of the electric field and the electronic charge. The second is the geometrical deformation of the molecule caused by the interaction of $\boldsymbol{E}$ and the molecular electric dipoles μ_e: the electric field can either stretch or shrink the bonds in the X-Mn-N1 chain. These two effects not only act together but can contribute to each other. For instance, a change in the location of nuclei in a molecule will inevitably cause redistribution of the electron density. By employing DFT methods the two effects can be studied both separately and in conjunction.

N.G. calculated the values of D for (**1**), (**2**) and (**3**) in three different scenarios: (a) the E-field only modifies the electron density, with the molecular geometry kept unperturbed; (b) the E-field distorts the geometry of the molecule, leading to a new electron density (not affected by $\boldsymbol{E}$ directly); (c) the E-field distorts the molecular geometry and the resulting electron density is optimised while taking into

account its direct interaction with the E-field. To reduce numerical errors in the computation, N.G. used a strong electric field of approximately 10^9 V/m (this is significantly larger than the field applied in the experiment, which was $\approx 10^5$ V/m). To obtain the maximal value of the SEC, the field was applied along the molecular C_3-axes. The calculations produce linear E-field dependence of D, allowing us to make a direct comparison between the calculation and experiment.

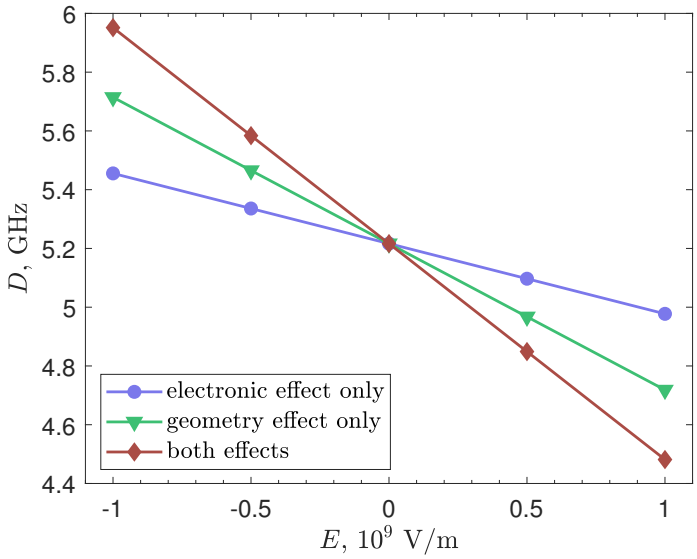

Figure 4.11: Dependence of D on $\boldsymbol{E}$ for three scenarios of simulation on (**3**). The E-field was applied along the C_3-axes of the molecule with positive direction being along the X-Mn-N1 chain, and the negative direction being the opposite.

All three compounds have demonstrated similar behaviour: the representative example of D as a function of applied field $\boldsymbol{E}$ is shown in Figure 4.11 for the three scenarios performed on (**3**). The calculation confirmed a linear electric-field effect. The slopes of the lines $\delta D/\mathrm{d}E$ are presented in Table 4.1. The contributions from scenarios (a) and (b) perfectly sum up to produce results of both effects (c). Note that the geometric effect is more than twice larger than the purely electronic one – this confirms that the electric dipole moment of molecules μ_e plays an important role in the SEC mechanism.

The comparison of the slopes $\delta D/\mathrm{d}E$ reproduces the trend observed in the experiment showing that the SEC grows as the halogen atom is varied from chlorine to iodine. Interestingly, the calculations showed that although the overall SOC is

greater for (**1**), the variations due to the E-field are much smaller. This is because the ion of chlorine Cl^- is less polarisable than I^-, inducing weaker distortions, hence a smaller variation of the SOC magnitude. The dipole moment (Table 4.1) is larger in the iodine complex and its variation with the field is greater – this is in agreement with the more significant changes in geometry under the effect of the field.

Finally, it is worth noting that the optimisation of the structures used in the calculations was performed on a single molecule in vacuum, therefore any packing and deformation effects that may be present in the crystals were neglected. This is one explanation for the discrepancy between the calculated and measured $\delta D/\mathrm{d}E$ slopes. Compare its experimental -0.42, -1.20, -1.70 Hz/(V/m) vs calculated -0.234, -0.390, -0.735 Hz/(V/m) values for (**1**), (**2**) and (**3**), respectively. Nevertheless, the theoretical results are in reasonable agreement with the experimental data.

4.6 Conclusions

The discussion of Mn(II) bipyramidal complexes presented in this chapter has demonstrated how properties of qubits based on molecular magnets can be tuned by replacing a single atom[3] in the molecule. The central manganese(II) ion situated in the pentacoordinate environment of Me_6tren ligands possesses high electron and nuclear spins which can serve as a physical implementation of a qudit. The existence of stable crystals at cryogenic and room temperatures is convenient for experiments establishing the fundamentals. The ESR transitions are accessible in the conventional X- and Q-band of the MW frequencies. This is partly a consequence of the low spin-orbit coupling of Mn: it produces relatively low values of the ZFS, which vary depending on the choice of halogen atom to be additionally attached to Mn.

We have demonstrated that the ZFS of the molecules can be tuned further by subjecting them to an external electric field. All three compounds exhibit high SEC which can lead to a 1.4 MHz shift in the resonance ESR frequency in reasonable electric fields of about 200 kV/m.

[3]The halide ligand.

One of the major results of this chapter is that the SEC of Mn(II) bipyramidal complexes stems not from high SOC, but is due to a large molecular electric dipole moment generated by the chain of atoms X-Mn-N1. The possibility to tune D by using rational chemical design and application of an electric field, presents a prospect of synthesising a molecule with switchable magnetic anisotropy (voltage-controlled magnetic anisotropy) and of implementing qudits with frequency-selective control.

Chapter 5

Ytterbium-trensal complexes

Contents

This chapter presents an investigation of the E-field effect in a chemical compound [Yb(trensal)] which contains a lanthanide ion of ytterbium. The samples were prepared by our colleagues from the group of Prof Stergios Piligkos. All the measurements and simulations were performed by me. These were complemented by insightful discussions with Dr Junjie Liu, Dr Sumin Lim, and Prof Arzhang Ardavan. Comparative X- and Q-band experiments were conducted in the CAESR facility, while all the orientational dependences were acquired using our spectrometer at the Department of Physics.

5.1 Introduction

In Chapter 4, we discussed the bipyramidal complexes with Mn, whose main advantages were (i) the accessibility of the m_S-sublevels of the ground electronic state of Mn via X- and Q-band ESR spectroscopy, and (ii) a significant SEC even in the absence of strong SOC due to the intrinsic electric dipole moment of the molecules. Unlike those bipyramidal complexes, the molecule of [Yb (trensal)] that we are going to discuss in this chapter contains a rare-earth ion of ytterbium (Yb); unlike manganese, ytterbium has one unpaired electron in a $4f$-orbital and exhibits a strong SOC leading to the separation between the ground and first excited states of [Yb (trensal)] by approximately 14 THz [135]. At first glance, such an energy scale will prevent us from using conventional ESR spectroscopy. It turns out, however, that the behaviour of [Yb (trensal)] is not that straightforward and gets even more exciting when we start investigating its spin-electric coupling.

5.1.1 The molecule and the crystal

[Yb (trensal)] is a threefold symmetric coordination complex consisting of a central Yb(III) ion and a tripodal ligand H_3trensal[1] (see Figure 5.1) [135, 137–139]. Similar to the Mn bipyramidal complexes, [Yb (trensal)] molecules lack inversion symmetry, their threefold axis passes through the apical amine and the metal, and the arrangement of these atoms suggests the existence of a spontaneous electric dipole moment. These properties on their own promise a noticeable SEC in [Yb (trensal)]. In addition, like most lanthanides, Yb(III) exhibits a large SOC which has been mentioned as one of the key components for achieving high values of SEC [51, 55].

To investigate the SEC effect using ESR spectroscopy, [Yb (trensal)] was doped into an isostructural diamagnetic host [Lu (trensal)] at concentration 0.01%. The compound crystallizes in a space group $P\bar{3}c1$, Z4 [136] with its C_3-axis coinciding with the threefold axis of the molecule. The molecules in the crystal are organised into alternating enantiomeric coaxial chains, with adjacent chains running in opposite directions parallel to the crystal c-axis [136]. Each unit cell contains four distinct

[1] Also known as 2,2′,2″-tris(salicylideneimino)triethylamine [136].

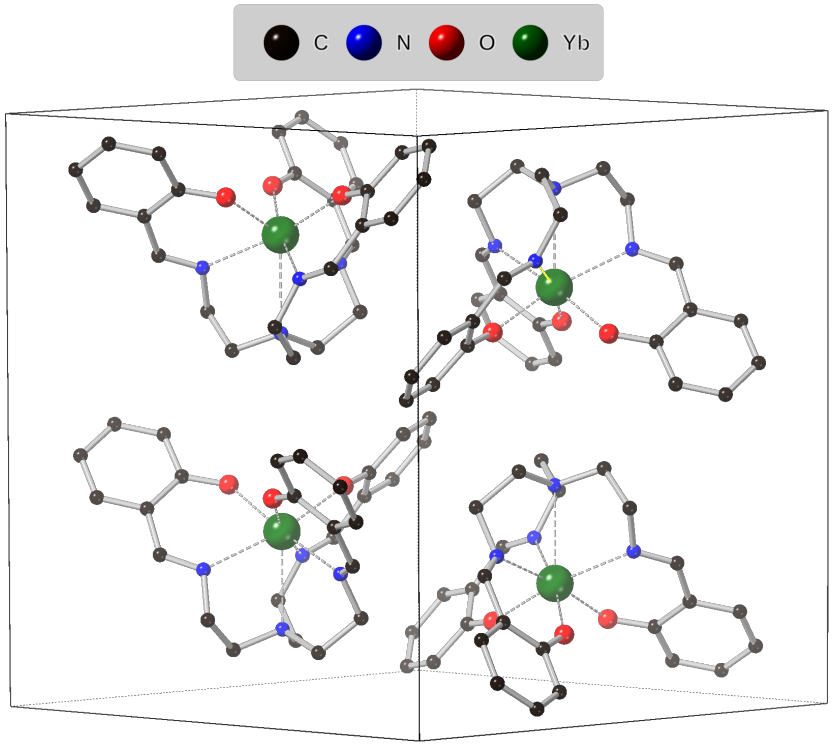

Figure 5.1: Unit cell diagram showing coaxial arrangement of enantiomeric pairs in the [Yb (trensal)] crystals (protons are hidden for clarity).

sites as shown in Figure 5.1, where two sites of one chain are inversion images of the other chain. This makes [Yb (trensal)] particularly interesting for quantum information: it has been proposed [139, 140] that molecules related by the inversion symmetry of a crystal (dimers) can be used to generate high-fidelity entangled states mediated by the dipole-dipole interaction between the spins of different molecules. One of the requirements for implementing this proposal is the ability to manipulate the states of individual molecules in the dimer. A previous study conducted in our group demonstrated that molecular magnets with holmium can be addressed by the MW radiation individually by employing their SEC and separating their resonance frequencies using modest E-field pulses of the order of 10^2 kV/m [55]. The same technique could be used on [Yb (trensal)] if its SEC were sufficiently large.

Taking into account all the structural similarities between [Yb (trensal)] and the Mn bipyramidal complexes, we might expect their SEC to have similar ori-

entational behaviour too: with the maximal effect when $\boldsymbol{E} \parallel C_3$ and no effect when $\boldsymbol{E} \perp C_3$. As we will see in Section 5.2.5, [Yb(trensal)] exhibits different and rather surprising behaviour.

5.1.2 Spin Hamiltonians and EDFS

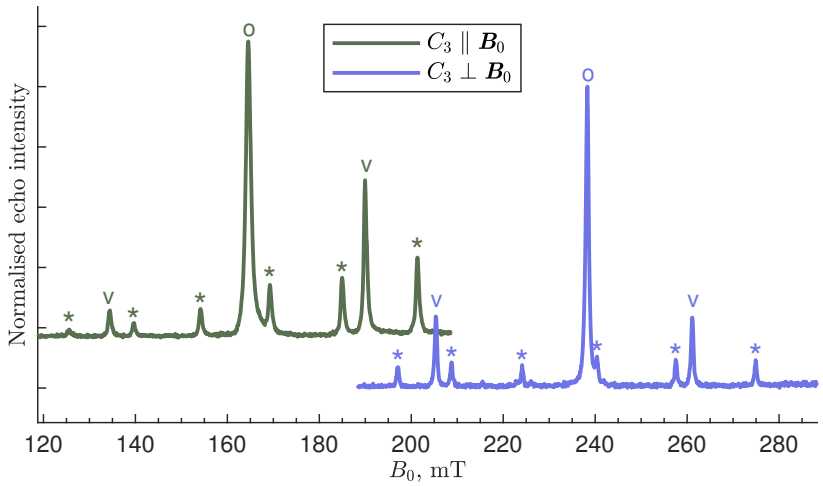

(a) X-band

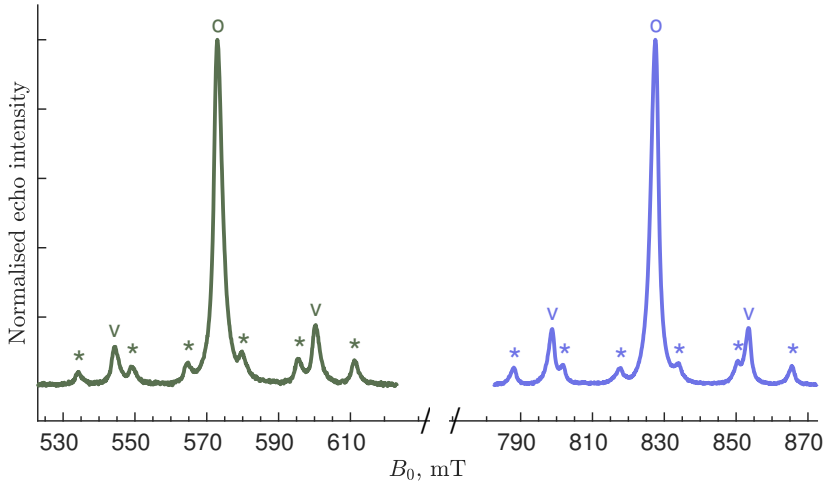

(b) Q-band

Figure 5.2: EDFS of [Yb(trensal)] at 9.7 GHz in two orientations: $C_3 \parallel \boldsymbol{B}_0$ – lower fields (green), $C_3 \perp \boldsymbol{B}_0$ – higher fields (blue). Markers above the peaks denote the corresponding nuclear spins; (o): $I = 0$, (v): $I = 1/2$ and (*): $I = 5/2$.

The electronic structure of Yb^{3+} is $[Xe]4f^{13}$ with one unpaired electron in a $4f$ orbital. According to Hund's rules, this results in the lower-energy level $^2F_{7/2}$

with $S = 1/2$, $L = 3$, and $J = 7/2$. In [Yb (trensal)], this level is well separated by ~ 300 THz from the next excited state $^2F_{5/2}$ thanks to the spin-orbit coupling [135]. Consequently, in first approximation J can be taken as a good quantum number, and at cryogenic temperatures the magnetic properties of [Yb(trensal)] pertinent for this study can be described by the Hamiltonian

$$\hat{\mathcal{H}} = \mu_B g_J \mathbf{B}_0^T \hat{\boldsymbol{J}} + A_J \hat{\boldsymbol{J}}^T \hat{\boldsymbol{I}} + \sum_{k=2,4,6} \sum_{q=-k}^{k} B_k^q \hat{O}_k^q(\hat{\boldsymbol{J}}). \tag{5.1}$$

The first term in the Hamiltonian is the Zeeman interaction between the total electronic angular momentum $\hat{\boldsymbol{J}}$ and the external magnetic field $\mathbf{B}_0$ where μ_B is the Bohr magneton and g_J stands for the non-dimensional gyroscopic ratio (Landé g-factor).

The second term represents the isotropic hyperfine interaction between $\hat{\boldsymbol{J}}$ and nuclear spin $\hat{\boldsymbol{I}}$. The isotropic hyperfine parameter A_J takes different values for the two groups of Yb isotopes possessing a non-zero nuclear spin: $A_J^{I=1/2} = 775.7$ and $A_J^{I=5/2} = -223.1$ MHz for $I = 1/2$ and $I = 5/2$, respectively [135].

Finally, the third term describes the ligand crystal field in terms of a series of the extended Stevens operators $\hat{O}_k^q$ with coefficients B_k^q [141]. This term is responsible for the anisotropic behaviour of the sample. The maximal order of the operator which should be included is given by $2J$, while the precise composition of the sum is determined by the symmetry. Thus, the only operators allowed by the space group of the crystal are those with $k = 2, 4, 6$ and q being either 0, ± 3 or ± 6.[2] The values for the corresponding coefficients B_k^q were found by Pedersen et al. [135] by fitting experimental data for [Yb (trensal)] diluted in [Y (trensal)] and are given here in Table 5.1.

B_k^q, GHz								
B_2^2	B_2^0	B_4^3	B_4^0	B_6^6	B_6^3	B_6^0	B_6^{-3}	B_6^{-6}
0	−334(2)	−267(1)	−4.59(9)	1.02(6)	1.80(9)	0.213(6)	−2.1(9)	3.0(2)

Table 5.1: The ESO coefficients obtained by means of near-infrared spectroscopy by Pedersen et al. [135].

[2] Spin operators of odd k are excluded because they are not invariant under time reversal [91].

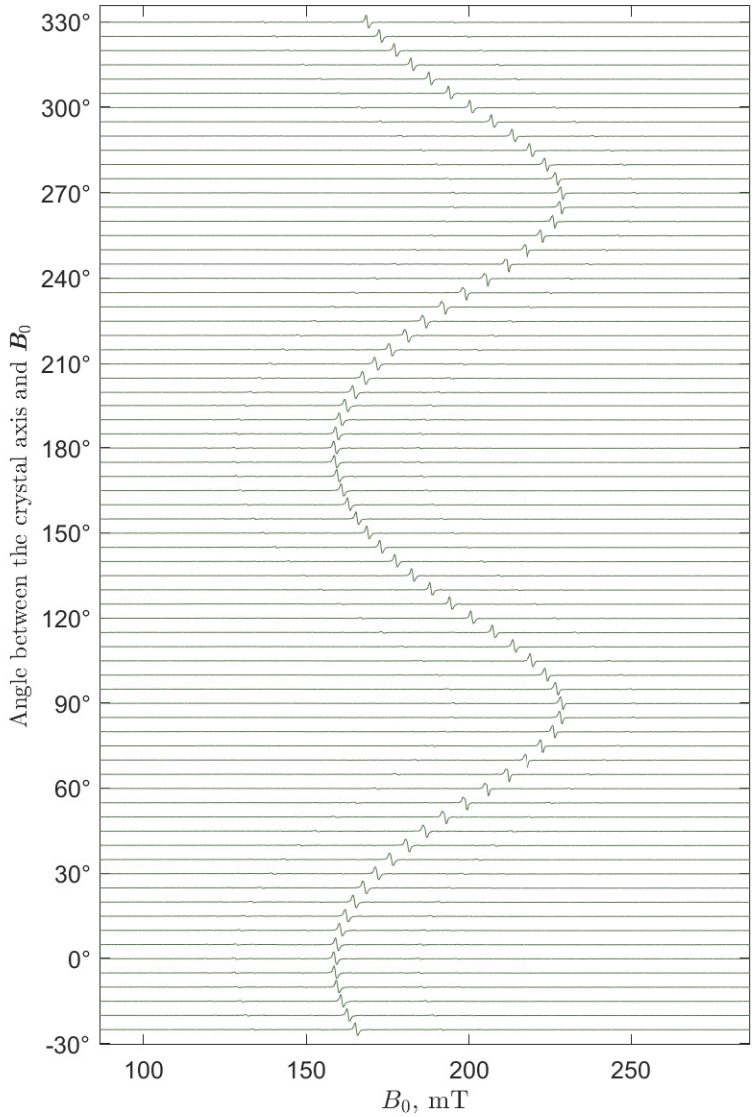

Figure 5.3: Rotational dependence of the CW spectra of [Yb (trensal)] on the angle between the static magnetic field $\boldsymbol{B}_0$ and the crystal C_3-axis. The spectra are normalised for 9.7 GHz. The figure demonstrates the presence of an anisotropy axis.

Nuclear Zeeman and quadrupole terms have also been detected [139, 142, 143], but they are small and not relevant for the present discussion.

The symmetry of the crystal suggests uniaxial anisotropy and, indeed, its ESR response strongly depends on the orientation of the samples. Figure 5.2 shows the EDFS of a sample with its C_3 axis parallel and then perpendicular to the static magnetic field $\mathbf{B}_0$ at two MW bands. The number of the peaks and their intensity is given by the natural content of the ytterbium isotopes in the sample. Several isotopes

with three different nuclear spins are known: ^{168,170,172,174,176}Yb, I = 0, (70%); ^{171}Yb, I = 1/2, (14%); and ^{173}Yb, I = 5/2, (16%), where their natural abundance is given in the brackets. Note that the central peak is produced by the most abundant isotopes: as a result it has the highest intensity but its relaxation times may be deteriorated by the spin-spin interaction between neighbouring resonant ions. A 360-degree rotational dependence of CW spectra is given in Figure 5.3.

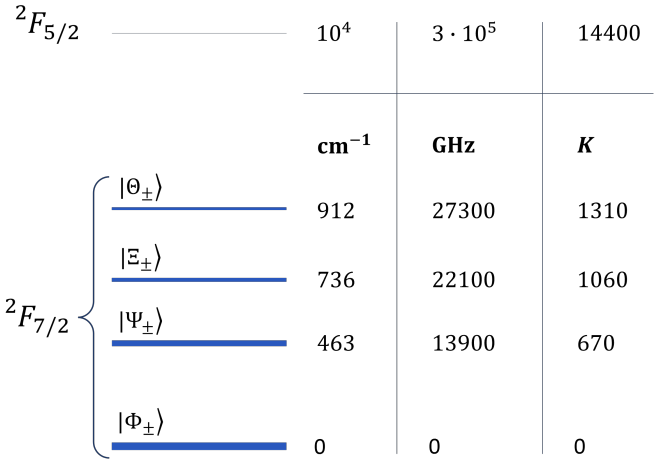

Figure 5.4: Schematic representation of the lowest energy levels of [Yb (trensal)]. $|\Phi_\pm\rangle$, $|\Psi_\pm\rangle$, $|\Xi_\pm\rangle$, and $|\Theta_\pm\rangle$ denote the doublets produced by the crystal field term of Hamiltonian 5.1.

While measuring ESR, the dominant effect on the energy levels of [Yb (trensal)] is the spin orbit coupling (≈ 300 THz), next in order of importance comes the crystal field effect (≈ 3 THz), then the interaction with an external magnetic field (≈ 10 GHz), and lastly the hyperfine interaction (≈ 1 GHz). To appreciate the energy scale, see Figure 5.4. The ligand field of the trensal lifts the degeneracy of the energy levels corresponding to different values of $|m_J|$ and mixes the eigenstates of operator $\hat{J}_z$. Yb^{3+} $(4f^{13})$ is a Kramers ion, which means that four doublets are guaranteed under the crystal electric field [91, 114, 119]. Thus the ground doublet is given by

$$|\Phi_\pm\rangle = 0.764 \left|\pm\frac{7}{2}\right\rangle + 0.345 \left|\mp\frac{5}{2}\right\rangle + 0.545 \left|\pm\frac{1}{2}\right\rangle \tag{5.2}$$

where the probability amplitudes were obtained by diagonalising the crystal field Hamiltonian (only the third term in Equation 5.1) in EasySpin [105].

Due to the crystal field, the next Kramers doublet $|\Psi_{\pm}\rangle$ is separated from $|\Phi_{\pm}\rangle$ by approximately 13.9 THz. This makes $|\Phi_{\pm}\rangle$ resemble a spin-1/2 system, and thus renders it accessible using the conventional ESR technique and frequencies. Neglecting the purely nuclear terms, the effective spin Hamiltonian for $S = 1/2$ employed in the literature [139, 143, 144] for this context is then

$$\hat{\mathcal{H}}^{S=1/2} = \mu_{\mathrm{B}} \boldsymbol{B}_0^{\mathrm{T}} \boldsymbol{g} \hat{\boldsymbol{S}} + \hat{\boldsymbol{S}}^{\mathrm{T}} \boldsymbol{A} \hat{\boldsymbol{I}}, \tag{5.3}$$

where the axial tensors $\boldsymbol{g}$ and $\boldsymbol{A}$ have corresponding components $g_{\parallel} = 4.29$, $g_{\perp} = 2.90$, $A_{\parallel}^{I=5/2} = -936.25$ MHz, $A_{\perp}^{I=5/2} = -672.14$ MHz, $A_{\parallel}^{I=1/2} = 3370.6$ MHz, and $A_{\perp}^{I=1/2} = 2220.6$ MHz [135].

5.1.3 Relaxation times

The spin-lattice relaxation time T_1 and the phase-memory time T_{m} of [Yb (trensal)] have been extensively studied before, although at higher concentrations of the paramagnetic molecules than our 0.01%; see, for instance, References [135, 138, 139]. Those studies showed that the spin dynamics in [Yb (trensal)] is determined by the Raman-like processes, and that the relaxation times are essentially isotope-independent. Above 3 K, time T_1 obeys a power law with respect to temperature and is proportional to T^{-6}. At X-band, 5 K and 7% doping, the T_1 time was reported to be around 500 μs [138]. The phase memory time T_{m} also did not exhibit any obvious dependence on the hyperfine interaction, and was only weakly temperature-dependent – it reached the saturation level of 0.5 μs at 5 K .

The results of our measurements at 5 K are shown in Table 5.2 and Table 5.3.

	T_1, μs			
	X		Q	
Orientation:	$C_3 \parallel \boldsymbol{B}_0$	$C_3 \perp \boldsymbol{B}_0$	$C_3 \parallel \boldsymbol{B}_0$	$C_3 \perp \boldsymbol{B}_0$
$I = 0$	244 ± 17	241 ± 19	123 ± 4	155 ± 2
$I = 1/2$	382 ± 16	440 ± 20	168 ± 6	183 ± 5
$I = 5/2$	400 ± 80	500 ± 40	126 ± 6	205 ± 10

Table 5.2: Spin-lattice relaxation time of samples with 0.01% [Yb (trensal)] at 5K.

	T_2, μs			
	X		Q	
Orientation:	$C_3 \parallel \boldsymbol{B}_0$	$C_3 \perp \boldsymbol{B}_0$	$C_3 \parallel \boldsymbol{B}_0$	$C_3 \perp \boldsymbol{B}_0$
$I = 0$	1.57 ± 0.01	1.45 ± 0.01	1.99 ± 0.03	2.91 ± 0.04
$I = 1/2$	2.47 ± 0.02	2.41 ± 0.02	2.69 ± 0.01	3.27 ± 0.05
$I = 5/2$	2.68 ± 0.06	2.85 ± 0.06	2.71 ± 0.01	3.18 ± 0.04

Table 5.3: The spin-spin relaxation time of samples with 0.01% [Yb (trensal)] at 5K.

At X-band, the spin-lattice relaxation time is about 240 μs for $I = 0$ and varies between 380 and 500 μs for other isotopes. Interestingly, at Q-band, the T_1 times are slightly shorter varying between 123 μs and 205 μs. Based on the upper limit of T_1, we chose the pause between consecutive measurements (shot repetition time) of the E-field sequences to be 5 ms.

The measurement of the spin-spin relaxation time T_2 was complicated by the electron spin echo envelope modulation (ESEEM) which manifests itself in the variation of the echo intensity as a function of τ_{MW} (see Figure 5.5(a)). The ESEEM of [Yb (trensal)] strongly depends on B_0 and is more pronounced when $C_3 \parallel \boldsymbol{B}_0$: the consequence of this effect is the different intensities of the ESR peaks in Figure 5.2(a) (during EDFS, τ_{MW} is kept constant but the ESEEM profile changes). When short excitation pulses are used, the echo amplitude fluctuates rapidly with time τ_{MW} due to the presence of the spin-carrying isotopes of ytterbium and to many other nuclei in the trensal ligand.

We partially solved the problem by using longer excitation pulses: the plot in Figure 5.5(b) demonstrates that this approach allowed us to filter out fast oscillations [90]. Nonetheless, we did not manage to eliminate entirely the effect of ESEEM for every transition. In comparison to a single decaying exponential, the decaying oscillation model (see Section 2.4.3.2) fits the data significantly better. All values given in Table 5.3 were obtained using Equation 2.76 with the stretch parameter $x = 1$, two oscillating components and one pure decaying exponential.

The lowest spin-spin relaxation time was observed for the central peak: this transition corresponds to the most abundant group of ytterbium isotopes with

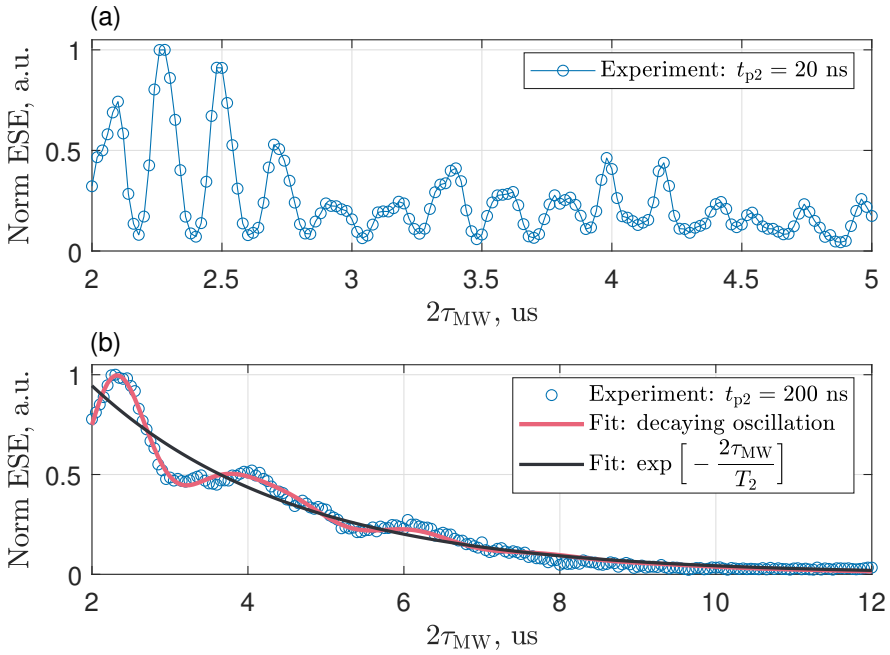

Figure 5.5: The intensity of the electron spin echo as function of τ_{MW}. The effect of ESEEM at different durations of the MW π-pulses: (a) 20 ns and (b) 200 ns.

$I = 0$, so that the high concentration of spins and their mutual interaction increase relaxation rates. Similar behaviour was observed in [Gd (trensal)] [145]. At X-band, time T_2 of [Yb (trensal)] varies between 1.45 and 2.85 μs without significant difference between orientations $C_3 \parallel \boldsymbol{B}_0$ and $C_3 \perp \boldsymbol{B}_0$. Similar vales of T_2 were observed at Q-band for the case $C_3 \parallel \boldsymbol{B}_0$, whereas at $C_3 \perp \boldsymbol{B}_0$ (higher resonance fields) the spin-spin relaxation time was higher and varied between 2.91 μs at $I = 0$ and 3.18 μs at $I = 5/2$.

The T_2 measurements at every ESR transition allowed us to choose the optimal value of τ_{MW} (which determines maximal t_E) for the E-field spin-echo sequences (see Section 2.5.2). Note that during the SEC measurements, only the duration/amplitude of the E-field pulse is varied, while the delay between the microwave pulses (τ_{MW}) remains unchanged. As a result, the measurement of the SEC is essentially not affected by the ESEEM effects

5.2 E-field effect in [Yb (trensal)]

5.2.1 Sample orientation

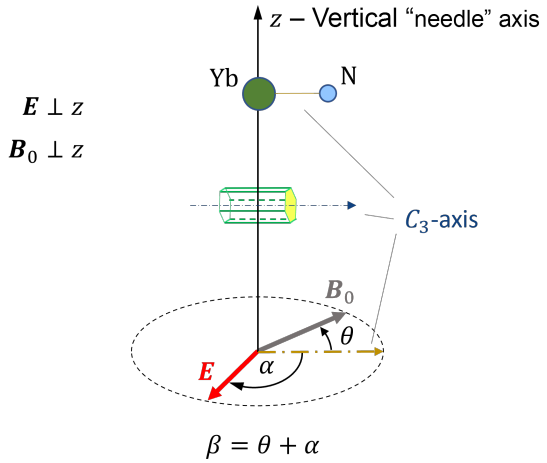

Figure 5.6: Schematic representation of the mutual orientation of the C_3-axis, electric field $\boldsymbol{E}$ and magnetic field $\boldsymbol{B}_0$. The arrows show the positive direction for counting the angles.

In this section, we will discuss the results of the single-crystal measurements of SEC in [Yb (trensal)]. The general technique of measuring the SEC is described in Sections 2.5 and 3.4. We have conducted several experiments with different orientations of the crystal, including those in which we rotated either the E-field or the sample itself. Figure 5.6 shows schematically the notation I will use to describe the orientation of the crystal, the fields used in the experiment, and the mutual orientation of the sample and the fields with respect to each other. The z-axis (sometimes called the 'needle axis') defined the vertical orientation in both static and rotating frames of reference. The angle between $\boldsymbol{B}_0$ and $\boldsymbol{E}$ could be varied but both vectors always lied in the horizontal plane perpendicular to the z-axis (see also Figure 3.17).

The first four particular arrangements are depicted in Figure 5.7. The orientation of the sample is given by the orientation of its C_3-axis, which can make an arbitrary angle θ with the static magnetic field $\boldsymbol{B}_0$. In the static setups (a) and (b) the orientation of the crystal was fixed in the laboratory frame at $C_3 \parallel \boldsymbol{B}_0$ and $C_3 \perp \boldsymbol{B}_0$, respectively, while the electric field was fixed in both cases along the crystal C_3-axis

($C_3 \parallel \boldsymbol{E}$). The setups (c) and (d) were used to measure the orientational dependence of the SEC: again, the C_3-axis of the crystal was fixed either in the parallel (c) or perpendicular (d) orientation with respect to $\boldsymbol{B}_0$, whereas the electric field was rotated in the plane perpendicular to the z-axis. The precise orientation of the electric field was given by angle α between $\boldsymbol{E}$ and the C_3-axis, so that the SEC was measured as a function of α. Two more setups will be presented later in the text.

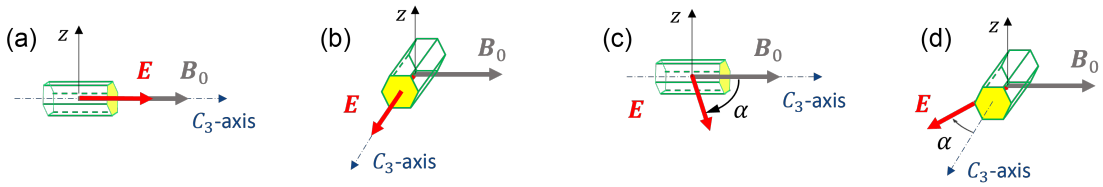

(a)	(b)	(c)	(d)
$\boldsymbol{E} \perp z$	$\boldsymbol{E} \perp z$	$\boldsymbol{E} \perp z$	$\boldsymbol{E} \perp z$
$\boldsymbol{B}_0 \perp z$	$\boldsymbol{B}_0 \perp z$	$\boldsymbol{B}_0 \perp z$	$\boldsymbol{B}_0 \perp z$
$C_3 \parallel \boldsymbol{B}_0$	$C_3 \perp \boldsymbol{B}_0$	$C_3 \parallel \boldsymbol{B}_0$	β is varied
$C_3 \parallel \boldsymbol{E}$	$C_3 \parallel \boldsymbol{E}$		
$\theta = 0°$	$\theta = 90°$	$\theta = 0°$	$\theta = 90°$
$\alpha = 0°$	$\alpha = 0°$	α is varied	α is varied
$\beta = 0°$	$\beta = 90°$	$\beta = \alpha$	$\beta = 90° + \alpha$

Figure 5.7: Different orientations of the sample and fields used in our experiments.

5.2.2 Phase recovery during coherent electric control

For our first test measurements we oriented the sample as demonstrated by diagram (b) in Figure 5.7, because that orientation provided a greater ESR signal. Analogously to Section 4.4.1, we first checked whether the sample responds to the application of an E-field at all. We then tested whether the effect is reversed when the E-field pulse starts in the first free-evolution period of the spin-echo sequence, propagates throughout the MW π-pulse and ends in the second free-evolution period.

The results of the measurements are summarised in Figure 5.8 which shows how the echo signal changes with the duration of the E-field pulse t_{E}. This dependence attests to the presence of the SEC in [Yb (trensal)]. We used $t_{\mathrm{p1}} = 16$ ns, $t_{\mathrm{p2}} = 32$ ns, $\tau_{\mathrm{MW}} = 3720$ ns, and the E-field pulse was delayed by 220 ns so that its maximal duration was 6970 ns. While the E-field pulse was applied only during the first

free-evolution period ($t_E < \tau_{MW}$), the echo intensity was gradually reduced with t_E due to the inhomogeneity of the applied E-field (and/or SEC): it introduced different phase shifts to different spin packets making them go out of phase with each other. After t_E overcame 3480 ns, the echo phase began to recover: the part of the E-field pulse which was applied after the MW π-pulse reduced the phase shift induced by the part applied before the π-pulse (see Section 2.5.2). The successful recovery of the phase of the echo at about $t_E = 7000$ ns proved that we can manipulate the spin coherence electrically. The sample demonstrated a similar phase-recovery behaviour when it was oriented at $C_3 \parallel \boldsymbol{B}_0$ as depicted in Figure 5.7(a).

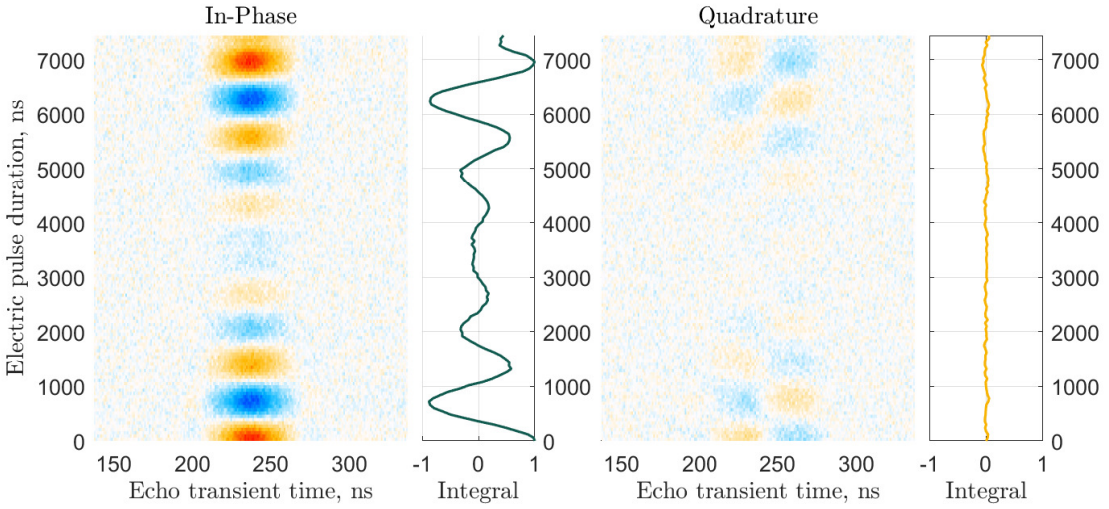

Figure 5.8: Phase recovery of the [Yb(trensal)] crystal subject to the E-field spin-echo sequence at $C_3 \parallel \boldsymbol{E}$ and $C_3 \perp \boldsymbol{B}_0$ (Figure 5.7(b)). The data were obtained at Q-band, 400 V and $d = 0.84$ mm. The Fourier transform of the integrated signal produces the SEC coefficient.

Note that unlike the similar dependence of the Mn bipyramidal complexes demonstrated in Figure 4.5, here, it is almost exclusively the in-phase component that fluctuates with t_E. This is the consequence of the fact that the unit cell of [Yb (trensal)] contains an equal number of inversion-image sites which experience identical but opposite-sign phase shift φ_E [53]. The small leak of the signal into the quadrature component is caused by slightly off-resonance conditions (the field was not precisely equal to the position of the top of the peak). The (near) absence

of the quadrature component also hints at the odd power of the SEC effect, that is when the frequency shift δf is proportional to E^{2k+1}, $k \in \mathbb{Z}$.

Checking the order of the SEC effect is pretty straightforward: we simply need to measure the SEC as a function of the magnitude of $\boldsymbol{E}$ while keeping all the other parameters of the experiment unchanged. The linear graph in Figure 5.9 confirms the linearity of the E-field effect in [Yb (trensal)].

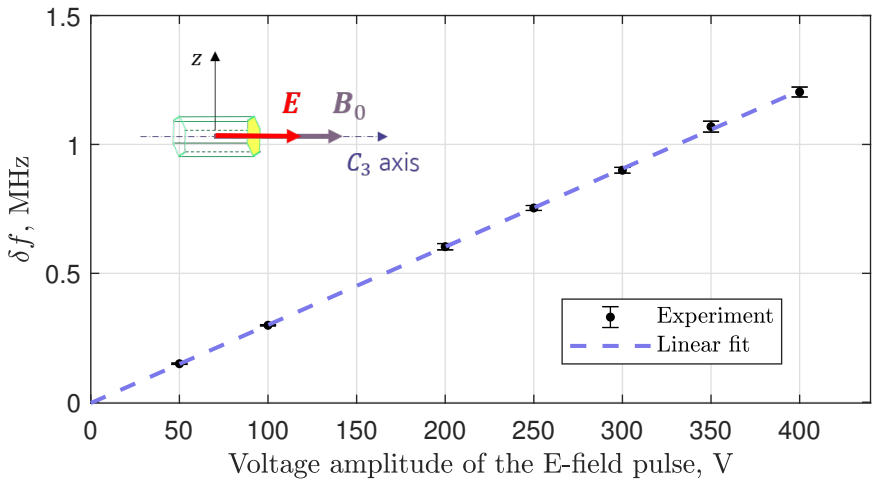

Figure 5.9: Linear dependence of the SEC on the E-pulse voltage for $I = 0$ at Q-band, $C_3 \parallel \boldsymbol{E}$ and $C_3 \parallel \boldsymbol{B}_0$

However, to describe the nature of this effect in full, we have to determine which terms in the Hamiltonian 5.1 are affected by the electric field.

5.2.3 Measurements at different frequency bands

We will start by testing the parameters of the effective Hamiltonian 5.3 which represents [Yb (trensal)] as an effective spin-1/2 system. The Hamiltonian contains just two parameters: the $\boldsymbol{g}$-tensor and the hyperfine tensor $\boldsymbol{A}$. If the E-field modulates the $\boldsymbol{g}$-tensor, the SEC must be proportional to the static field $\boldsymbol{B}_0$. If the E-field affects $\boldsymbol{A}$, the SEC will be different when measured at ESR peaks corresponding to different projections of the nuclear spin m_I. It can also happen that the E-field affects both parameters. Note that exactly the same logic can be applied when considering the effect of the E-field on the Zeeman and hyperfine terms of the J-Hamiltonian 5.1.

To simultaneously test whether either $\boldsymbol{g}$ or $\boldsymbol{A}$ is modulated by $\boldsymbol{E}$, we measured the SEC at every ESR peak shown in Figure 5.2. The measurements were conducted at two MW frequency bands (X and Q), and two orientations of the samples, namely with $C_3 \parallel \boldsymbol{B}_0$ and $C_3 \perp \boldsymbol{B}_0$, while keeping $C_3 \parallel \boldsymbol{E}$ (these correspond to orientations (a) and (b) in Figure 5.7, respectively). The obtained values of SEC are summarised in Table 5.4, Table 5.5, and Figure 5.10.

	X-band (9.77 GHz)			
	$C_3 \parallel \boldsymbol{B}_0$		$C_3 \perp \boldsymbol{B}_0$	
Nuclear spin	Field mT	SEC Hz/(V/m)	Field mT	SEC Hz/(V/m)
0	164.6	0.71±0.03	238.3	0.44±0.01
1/2	134.0	0.70±0.02	205.3	0.40±0.02
1/2	190.6	0.69±0.01	261.1	0.40±0.02
5/2	125.2	0.71±0.04	197.1	0.41±0.03
5/2	139.3	0.69±0.03	208.1	0.38±0.02
5/2	154.1	0.69±0.03	224.1	0.39±0.02
5/2	169.5	0.68±0.03	239.8	0.42±0.02
5/2	185.5	0.68±0.02	257.0	0.43±0.02
5/2	202.2	0.69±0.01	274.9	0.42±0.03

Table 5.4: The SEC values for $C_3 \parallel \boldsymbol{E}$ at X-band and two orientations of the crystal relative to the static field $\boldsymbol{B}_0$.

We find that the SEC depends on both the orientation of the sample and the MW band at which the experiment was conducted. Furthermore, the values of the SEC are proportional to the resonance field[3] of the central peaks: for the same orientation of the sample, the data-points for $I = 0$ at X and Q bands in Figure 5.10 lie on a line originating approximately at the origin. The slope of each line depends on the angle between C_3 and $\boldsymbol{B}_0$, so that at an arbitrary orientation of the sample, the SEC data points are expected to be on a line located between the solid and dashed lines shown in Figure 5.10. Given the line equation $\text{SEC} = a_0 + a_1 B_0$, the fitting produced $a_0^{\parallel} = -0.040$ Hz/(V/m), $a_1^{\parallel} = 4.5$ [Hz/(V/m)]/T for $C_3 \parallel \boldsymbol{B}_0$, and $a_0^{\perp} = -0.025$ Hz/(V/m), $a_1^{\perp} = 1.9$ [Hz/(V/m)]/T for $C_3 \perp \boldsymbol{B}_0$.

[3]Or the resonance frequency of the central peak obtained using Equation 3.1.

	Q-band (33 GHz)			
	$C_3 \parallel \boldsymbol{B}_0$		$C_3 \perp \boldsymbol{B}_0$	
Nuclear spin	Field mT	SEC Hz/(V/m)	Field mT	SEC Hz/(V/m)
0	572.9	2.56±0.02	827.5	1.58±0.02
1/2	544.5	2.55±0.02	798.8	1.59±0.02
1/2	600.4	2.54±0.02	853.5	1.56±0.02
5/2	534.3	2.58±0.02	788.1	1.56±0.02
5/2	549.4	2.54±0.02	801.7	1.56±0.02
5/2	564.6	2.53±0.02	817.7	1.56±0.02
5/2	579.9	2.56±0.02	834.0	1.58±0.03
5/2	595.6	2.56±0.02	850.4	1.55±0.03
5/2	611.3	2.57±0.02	865.6	1.56±0.02

Table 5.5: The SEC values for $C_3 \parallel \boldsymbol{E}$ at Q-band and two orientations of the crystal relative to the static field $\boldsymbol{B}_0$.

The proportionality of the SEC to the resonance field looks like evidence that it is the Zeeman term of Hamiltonian 5.3 which gets modulated by $\boldsymbol{E}$. However, consider the set of measurements at X-band when the C_3-axis was parallel to $\boldsymbol{B}_0$ (dark blue): the resonance field grows by 62% between 125.2 and 202.2 mT, whereas the SEC just barely fluctuates around the average of 0.69 Hz/(V/m). The same can be said about the other sets of measurements, though the change in field there is not as drastic. This compels us to conclude that the electric field does not modulate the Zeeman term.

We further notice that the approximately horizontal rows of markers of the same colour in Figure 5.10 show that the SEC does not depend on the value of the nuclear spin magnetic number m_I and is essentially the same for all three groups of the ytterbium isotopes. Therefore, we conclude that the electric field does not modulate the hyperfine interaction either.

The static measurements discussed in this subsection demonstrated that the SEC in [Yb(trensal)] is neither due to the Zeeman nor the hyperfine terms, so that the modulation of any of the parameters in the effective Hamiltonian 5.3 cannot explain it. Consequently, we need to investigate the modulation of the

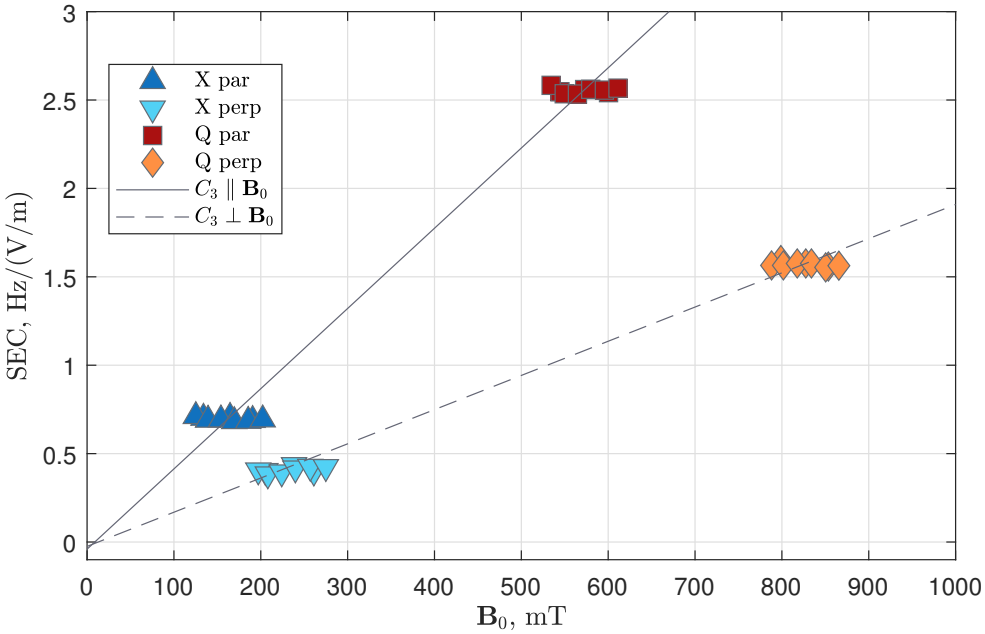

Figure 5.10: The SEC values for $C_3 \parallel \boldsymbol{E}$ at two frequency bands and two orientations of the crystal relative to the static field $\boldsymbol{B}_0$. The solid and dashed lines demonstrate proportionality of the effect with respect to the resonance field of the $I = 0$ peak.

ESO (ligand field) term in the full J-Hamiltonian 5.1.

5.2.4 Modulation of the ESO coefficients

The only term left in the Hamiltonian 5.1 which we have not yet inspected for the influence of the electric field is the sum of the extended Stevens operators representing the interaction present even in the absence of the static field $\boldsymbol{B}_0$.

We will study the effect of modulating coefficients B_k^q by fitting the experimental SEC data with the simulation using the EasySpin library [105]. The values of the SEC were obtained by finding the difference between the separation of the eigenvalues of the spin Hamiltonian, which are calculated first with original and then with modified coefficients B_k^q. The eigenvalues were extracted using the function `levels`. This function requires the orientation of the magnetic field with respect to the molecular axis to be specified via a polar and azimuthal angles. The polar angle corresponds to the angle θ introduced in Figure 5.6, while the azimuthal angle was treated as one of the fitting parameters which we will call φ_3.

A single Hamiltonian describes only one of the four molecules in the unit cell of [Yb (trensal)] (see Figure 5.1). In general, in order to calculate the net SEC we would need to consider the response from each of these molecules separately. However, the symmetry of the crystal simplifies the task if we are interested only in the magnitude of SEC [53]. Indeed, all four molecules have their 3-fold axes parallel to the crystal C_3-axis, and because space group $P\bar{3}c1$ contains an inversion centre each molecule comes with its inversion image. These factors enable us to assume that the response of all four molecules to an applied electric field will produce a SEC of the same magnitude, and that we can use the Hamiltonian of only one paramagnetic centre.

A satisfying match between the experimental EDFS spectra and simulation was reached using the Landé g-factor $g_J = 8/7$ for $J = 7/2$, the isotropic hyperfine parameters $A_J^{I=1/2} = 887.2$ MHz and $A_J^{I=5/2} = -243.3$ MHz [91], and the set of values for the coefficients B_k^q obtained by means of near-infrared spectroscopy by Pedersen et al. [135] (see Table 5.1). We used these parameters as a starting point for our models.

5.2.5 Orientational behaviour of the SEC

5.2.5.1 Horizontal orientation

In order to get more insight into the anisotropic nature of the E-field effect in [Yb (trensal)], we conducted a set of measurements revealing the orientational dependence of the SEC on the angle between the C_3-axis and the electric field $\boldsymbol{E}$. The data presented in this section were gathered for all three isotopes of ytterbium, and the results were identical for all of them. Therefore, the figures will show the data for the ESR peak of $I = 0$ only.

The first two sets of measurements were performed on a crystal of [Yb (trensal)] oriented horizontally with its 3-fold axis first parallel and then perpendicular to the static magnetic field (arrangements (c) and (d) in Figure 5.7, respectively). At each of these two orientations, the plates generating the electric field were rotated about the vertical z-axis with a 10-degree step, and the SEC was measured at every orientation of $\boldsymbol{E}$. The results of the measurement are presented in Figure 5.11.

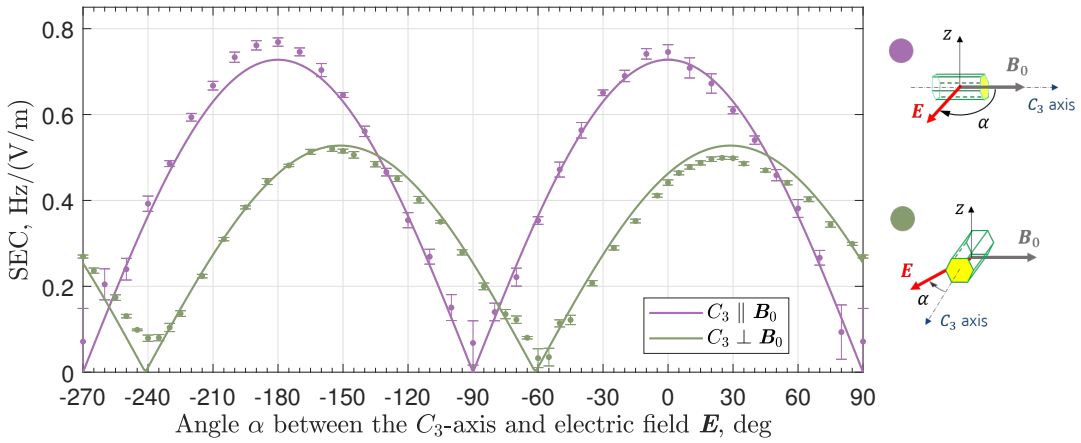

Figure 5.11: Rotation of the electric field $\boldsymbol{E}$ about the vertical axis for the two orientations of the crystal: $C_3 \parallel \boldsymbol{B}_0$ and $C_3 \perp \boldsymbol{B}_0$. Solid lines are the fitting of Equations 5.4 to the data represented by the markers with error bars.

For fitting we have used a model involving only two coefficients B_2^0 and B_2^2 corresponding to operators $\hat{O}_2^0 = 3\hat{J}_z^2 - J(J+1)\hat{\boldsymbol{I}}$ and $\hat{O}_2^2 = (\hat{J}_+^2 + \hat{J}_-^2)/2$. These operators represent the crystal field potential along the *molecular* z-axis and in the transverse xy-plane, respectively. One, therefore, expects a sinusoidal dependence of their coefficients with respect to the angle α between the C_3-axis and the electric field, with the maximal effect when vector $\boldsymbol{E}$ is either along the z-axis for B_2^0, or in the xy-plane for B_2^2:

$$\begin{aligned} B_2^0(E) &= B_2^0(0) + \kappa_{20} \cdot \cos(\alpha) \cdot E, \\ B_2^2(E) &= B_2^2(0) + \kappa_{22} \cdot \sin(\alpha) \cdot E, \end{aligned} \tag{5.4}$$

where the notation $B_2^0(E)$ and $B_2^2(E)$ is used to highlight the fact that these coefficients are functions of the magnitude of the electric field. The fitting parameters κ_{20} and κ_{22} were found to be equal to 42.9 and -126 Hz/(V/m), respectively, with the azimuthal angle $\varphi_3 = -30°$.

5.2.5.2 Horizontal orientation: frequency dependence of the SEC

In Section 5.2.3, it was mentioned that the SEC exhibits clear dependence on the resonance field of the *central* peaks with $I = 0$. A slightly different view on the situation is offered by using the effective Hamiltonian 5.3 and considering the resonance MW frequency at which the SEC was observed. This frequency can

		SEC, Hz/(V/m)	
Frequency, GHz		$C_3 \parallel \boldsymbol{B}_0$	$C_3 \perp \boldsymbol{B}_0$
9.77	Experiment:	0.71±0.03	0.44±0.01
	Model:	0.73	0.46
34.0	Experiment:	2.56±0.02	1.58±0.02
	Model:	2.55	1.62

Table 5.6: The comparison of the measured and modelled values of the SEC for the case when $C_3 \parallel \boldsymbol{E}$ ($\alpha = 0°$) at two different MW bands and two orientations of the crystal (arrangements (a) and (b) in Figure 5.7).

be taken directly from the parameters of our experiments, or it can be calculated using the expression for the Zeeman energy as

$$f^{S=1/2} = \frac{\mu_B g}{h} B_0 \tag{5.5}$$

with g taking the pertinent values for $C_3 \parallel \boldsymbol{B}_0$ and $C_3 \perp \boldsymbol{B}_0$. This equation shows that if the SEC of the central peak is linear with respect to the resonance field, it must also be linear with respect to $f^{S=1/2}$, if the orientation of the sample does not change. The dependence of the SEC at $I = 0$ on the MW frequency would produce linear graphs similar to those depicted in Figure 5.10.

This behaviour can be replicated by the same model (Equations 5.4) that we used to describe the orientational dependence of the SEC, in conjunction with the J-Hamiltonian 5.1. Table 5.6 contains the results of comparing the experiment with the model: all four values for two orientations of the sample and two frequency bands are in a good agreement. It is interesting that the dependence of the SEC on the MW frequency stems not from the Zeeman interaction but from the ZFS term of the Hamiltonian.

5.2.5.3 Vertical orientation

The graph for the perpendicular orientation of the crystal in Figure 5.11 exhibits counter-intuitive behaviour: there is a SEC effect even when $\boldsymbol{E}$ is perpendicular to the C_3-axis. To investigate this phenomenon further, we oriented the sample vertically, so that the C_3-axis was always perpendicular to both $\boldsymbol{B}_0$ and $\boldsymbol{E}$. The

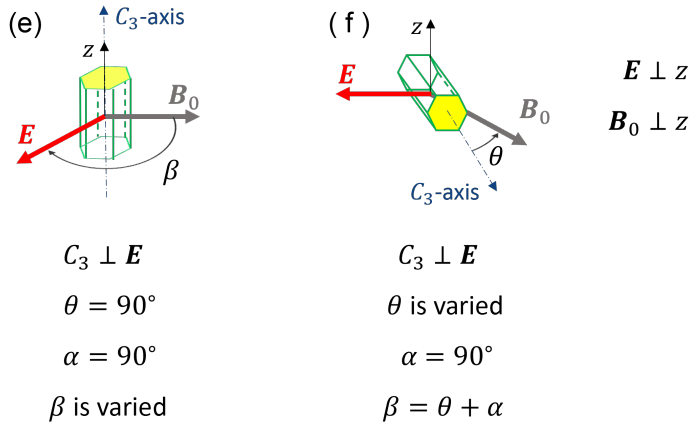

Figure 5.12: Two additional orientations used for testing the SEC effect when $C_3 \perp \boldsymbol{E}$. The single-letter notation continues that of Figure 5.7.

electric field was then rotated about the z-axis while always staying in the laboratory xy-plane. Arrangement (e) in Figure 5.12 depicts the orientation of the crystal and fields in more detail. To denote the orientation of the electric field in this arrangement, we employ angle β between $\boldsymbol{B}_0$ and $\boldsymbol{E}$.

The dependence of the SEC on β is shown in Figure 5.13, where it is juxtaposed with the graph for the perpendicular (but horizontal) orientation from Figure 5.11. The measurement did not reveal any significant dependence of SEC on the orientation of $\boldsymbol{E}$. Note that the two graphs intersect at β equal to about -180, 0 and +180 degrees, which corresponds to the electric field $\boldsymbol{E}$ being perpendicular to the C_3-axis in both horizontal and vertical orientations simultaneously. The other two intersections are due to the symmetry of the crystal. The dependence of the SEC on the amplitude of the E-field pulse shown in Figure 5.14 confirms that this perpendicular effect is also linear.

The simulation of the SEC behaviour at $C_3 \perp \boldsymbol{E}$ and $C_3 \perp \boldsymbol{B}_0$ turned out to be challenging. If we just use the model described by Equations 5.4 and take into account that the change in B_2^2 rotates together with $\boldsymbol{E}$, the simulation generates a clear dependence of SEC on the orientation of $\boldsymbol{E}$ repeating the symmetry of $\hat{O}_2^2$. My attempts to use other simple models where only one of the ESO coefficients is changed have not been fruitful either. One of the possible solutions could be taking into account the chirality and different orientations of the molecules in the

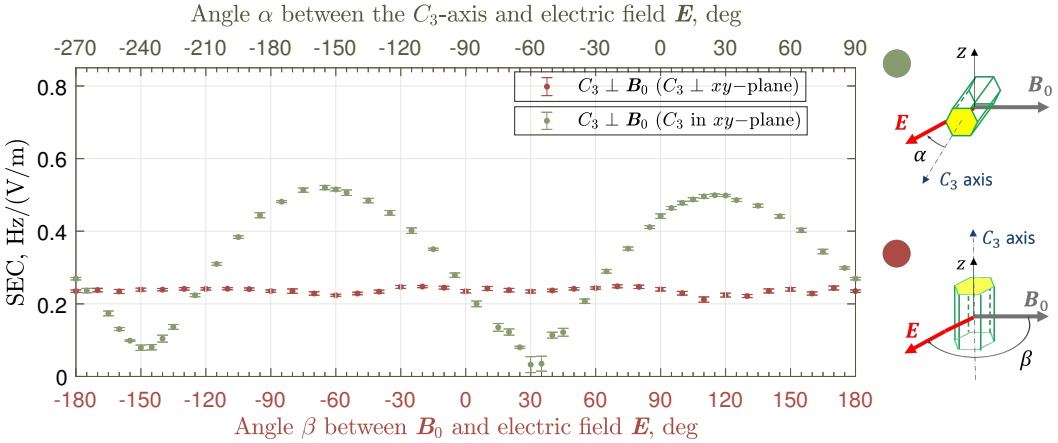

Figure 5.13: Rotation of the electric field $\boldsymbol{E}$ about the vertical axis when $C_3 \perp \boldsymbol{B}_0$ for the two orientations of the crystal: with the C_3-axis being in the horizontal xy-plane (the same as in Figure 5.11); and C_3 with the C_3-axis lying along the vertical z-axis.

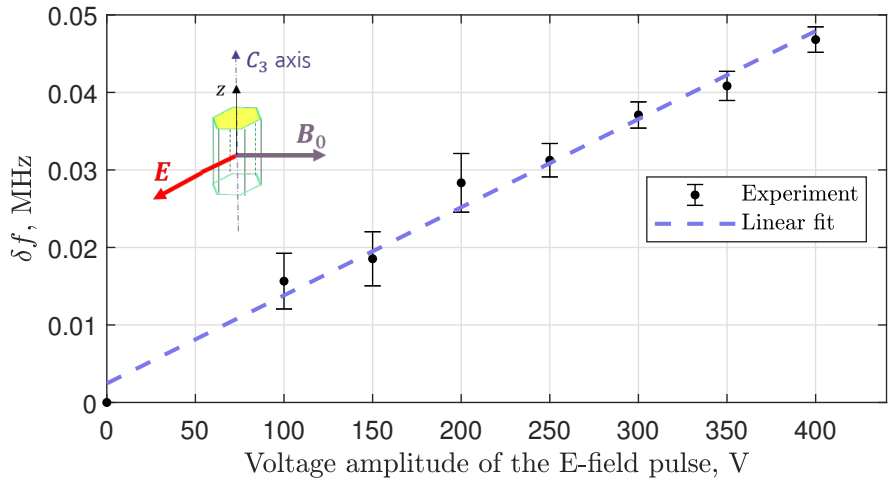

Figure 5.14: Linear dependence of the SEC on the E-pulse voltage for $I = 0$ at X-band, when $C_3 \perp \boldsymbol{E}$ and $C_3 \perp \boldsymbol{B}_0$.

unit cell of the crystal. We assumed that the single-molecule Hamiltonian would be enough, but probably the space group of the crystal introduces new and not obvious nuances to the behaviour of the SEC in [Yb(trensal)]. The results presented in Reference [146] could potentially help us elucidate the effect in the future.

5.2.5.4 Rotation of the sample while keeping $C_3 \perp \boldsymbol{E}$

It is interesting to investigate how the SEC changes if we keep the orientation of the electric field constant, $C_3 \perp \boldsymbol{E}$, but change the angle between the C_3-axis

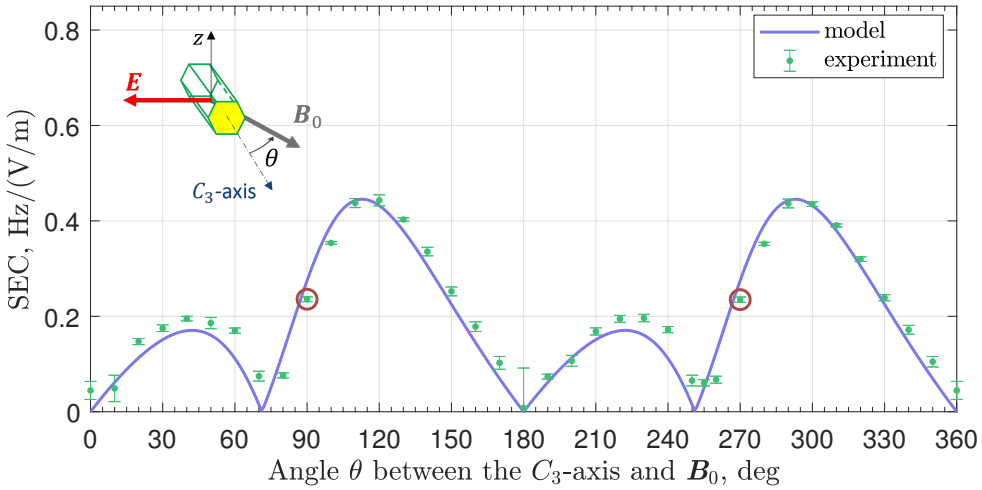

Figure 5.15: Dependence of the SEC values of the angle between the C_3-axis and $\boldsymbol{B}_0$ while preserving $C_3 \perp \boldsymbol{E}$. The circle markers highlight the orientation at which $C_3 \perp \boldsymbol{B}_0$ and $\boldsymbol{E} \perp \boldsymbol{B}_0$; these correspond to the points with β equals 0° and 180° in Figure 5.13.

and the static magnetic field $\boldsymbol{B}_0$ (arrangement (f) in Figure 5.12). Figure 5.15 demonstrates the result of such a measurement. The behaviour of the SEC values can be described by using only one ESO coefficient, namely B_2^2, since for $C_3 \perp \boldsymbol{E}$ the coefficient B_2^0 is not affected by the electric field (see Equations 5.4). The result of the simulation strongly depends on angle φ_3 denoting rotation about the crystal C_3-axis. The blue modelled graph was built with exactly the same value $\kappa_{22} = 126$ Hz/(V/m) and $\varphi_3 = -30°$ as the graphs in Figure 5.11.

The symmetry of the crystal requires coefficient $B_2^2(0)$ to be zero [135], however the results presented in Figures 5.11 and 5.15 require B_2^2 to be modified by the E-field. This suggests that the E-field breaks the axial symmetry of the crystal, thus causing the unique behaviour of [Yb (trensal)] manifesting in the presence of the SEC when the E-field is perpendicular to the C_3-axis.

5.3 Conclusions

The [Yb (trensal)] compound is an attractive candidate for the physical implementation of electrically controlled qudits. Despite its high SOC, its ground-state ESR fits the specifications of the conventional X- and Q-band spectrometers, so that

the control of the qudits can be achieved using existing MW and RF technology. Mathematically, this means that its standard low-temperature ESR properties are well described by an effective spin-1/2 Hamiltonian. Previous investigations demonstrated that spin-1/2 systems possess little to no SEC [51]. However, thanks to its high SOC and the ligand-field interaction, [Yb (trensal)] exhibits significant values of SEC which can lead to an about 1 MHz frequency shift at Q-band in an E-field of the order of 400 kV/m (which is what was used in our setup).

The unique property of [Yb (trensal)] is that it demonstrates linear SEC even when the E-field is oriented perpendicularly to the C_3-axis of the molecule, and that this *perpendicular* SEC is of the same order of magnitude as the *parallel* effect. However, the lack of any angular dependence for the vertical orientation of the sample in Figure 5.13 is not understood yet.

From an ESR perspective, [Yb (trensal)] is a rare example of an apparent spin-1/2 system with significant SEC.

The existence of isotopes with nuclear spin $I = 1/2$ and $I = 5/2$ makes [Yb (trensal)] molecules good candidates for realisation of qudits and implementation of quantum error-correction protocols (see Section 6.2 and [37, 86]) as well as testing the proofs of concepts of quantum simulation [144].

Chapter 6
Quantum Error Correction

Contents

This chapter outlines our original research focused on the implementation of a quantum error correction (QEC) protocol, as first proposed in Reference [86]. The work was conducted in collaboration with Dr Sumin Lim, Dr Junjie Liu, and

Prof Arzhang Ardavan. The outcomes of this research were consolidated into a paper that has recently appeared in Physical Review Letters [147]. This chapter serves as a largely faithful reproduction of that paper, with additional data and new insights.

6.1 Introduction

6.1.1 Quantum computing using ESR and NMR

NMR and ESR are recognised as technology for possible implementation of quantum computing techniques [13, 26, 27]. This is mostly due to the fact that electron and nuclear spins are natural candidates for units of quantum information – qubits (and qudits in general). The theoretical framework of the physics of spins is presented in Chapter 2.

Quantum computation is performed by applying unitary transformations which implement some desired logic operations on qubits. These unitary operations are known as quantum logic gates [148]. In NMR and ESR, separate spin-based qubits are manipulated via the application of RF and MW pulses (see Section 2.4). The corresponding formulae are particularly simple in the rotating frame of reference (see Section 2.1.3).

For instance, X-gate (NOT-gate) can be realised as a π-pulse about the x-axis:

$$X = \pi_x = \xrightarrow{\pi \hat{J}_x} = e^{-\mathrm{i}\pi \hat{J}_x} = -\mathrm{i}\begin{pmatrix} 0 & 1 \\ 1 & 0 \end{pmatrix}. \tag{6.1}$$

Here the gate is represented in five equivalent notations: the one which is conventional in quantum information literature, as an angle and axis of rotation, as a product operator, as a propagator, and as a matrix (Equations 2.62). The global phase $-\mathrm{i}$ is not measurable and is often ignored.

Similarly, the Y-gate would be equal to a π-pulse about the y-axis given by

$$Y = \pi_y = \xrightarrow{\pi \hat{J}_y} = e^{-\mathrm{i}\pi \hat{J}_y} = -\mathrm{i}\begin{pmatrix} 0 & -\mathrm{i} \\ \mathrm{i} & 0 \end{pmatrix}. \tag{6.2}$$

The Z-gate is somewhat special: it can be realised virtually as a rotation of the coordinate frame about the z-axis by adjusting the phase of all consecutive pulses [13]. The other way to implement this gate is by putting the system into a

slightly off-resonance state thus making it undergo rotations about the z-axis in the rotating frame. This can be done by a π-pulse of magnetic field parallel to $\boldsymbol{B}_0$:

$$Z = \pi_z = \xrightarrow{\pi \hat{J}_z} = e^{-\mathrm{i}\pi \hat{J}_z} = -\mathrm{i}\begin{pmatrix} 1 & 0 \\ 0 & -1 \end{pmatrix}. \tag{6.3}$$

A rotation at angle θ about an arbitrary axis which lies in the xy-plane is most easily implemented by tuning the phase of the excitation pulse φ. The other approach is to use composite pulses (see Section 2.3.1.1). Thus, a rotation about an axis making azimuthal angle φ with the x-axis is equal to

$$\theta_\varphi = \xrightarrow{-\varphi \hat{J}_z} \xrightarrow{\theta \hat{J}_x} \xrightarrow{\varphi \hat{J}_z} = e^{-\mathrm{i}\varphi \hat{J}_z} e^{-\mathrm{i}\theta \hat{J}_x} e^{\mathrm{i}\varphi \hat{J}_z}. \tag{6.4}$$

A rotation about the z-axis can be implemented via composite x- and y-pulses analogously as

$$\theta_z = \xrightarrow{-\frac{\pi}{2} \hat{J}_x} \xrightarrow{\theta \hat{J}_y} \xrightarrow{\frac{\pi}{2} \pi \hat{J}_x} = \xrightarrow{\frac{\pi}{2} \hat{J}_y} \xrightarrow{\theta \hat{J}_x} \xrightarrow{-\frac{\pi}{2} \pi \hat{J}_y}. \tag{6.5}$$

The Hadamard gate would be

$$H = \xrightarrow{\pi \hat{J}_z} \xrightarrow{\frac{\pi}{2} \hat{J}_y} = \xrightarrow{-\frac{\pi}{2} \hat{J}_y} \xrightarrow{-\pi \hat{J}_x} = e^{\mathrm{i}\pi \hat{J}_x} e^{\mathrm{i}\frac{\pi}{2} \hat{J}_y} = -\mathrm{i}\frac{\sqrt{2}}{2}\begin{pmatrix} 1 & 1 \\ 1 & -1 \end{pmatrix}. \tag{6.6}$$

While single-qubit gates are implemented via the Zeeman coupling, the multiple-qubit gates are implemented by taking advantage of coupling terms in the Hamiltonian describing the system [13, 26, 27]. The use of hyperfine interaction was proposed in one of the first designs of quantum computers [44].

The quantum gates are intentional operations and require application of MW and RF pulses of certain duration, frequency, phase, and amplitude. However, the spin system is also subject to EM noise which can cause transformations with random axes and flip angles, and, consequently, introduce error into information stored in qubits. The effect of the EM noise is divided into roughly two groups in the literature [26, 27]: (i) discrete quantum errors like flip-bit (X-gate error) and phase-flip (Z-gate error), and (ii) continuous quantum noise like depolarising channel, amplitude, and phase damping. The QEC protocol which we will discuss in this chapter is related to the phase damping. The protocol was developed to

deal with rotations about the z-axis at a random angle θ (phase kick). One can say that the phase-flip error is a particular case of a phase kick with $\theta = \pi$.

The standard approach in the theory of both classical and quantum computing is to use redundancy as a means of protecting information. In ordinary computers this is done by copying bits of information so that if one is corrupted, the others will preserve the information. The similar approach is forbidden in quantum computing due to the no-cloning theorem. In our QEC protocol, we encode a logical qubit in the states of a physical qudit and protect information by employing the idea somewhat similar to that of the 'decoherence-free subspaces'.

6.1.2 Decoherence-free subspaces

In quantum error correction, it is normally assumed that errors happening to different qubits are independent and uncorrelated. This is, however, rarely true: qubits interact with one another and their broader environment such that there is always some sort of coupling between them, thus making errors correlated. This is especially true for qubits located physically close to each other: the noise in the EM fields will cause their errors to be quite similar.

This situation requires a special attention, and we can use the fact that the errors are correlated to our advantage. Instead of actively detecting and correcting errors, we can try to prevent the error from happening in the first place. The collection of qubits on which such error *prevention* can be implemented are called decoherence-free subspaces [27, 149].

The idea for a protecting algorithm entails the use of code words which will be resilient to error in the first instance. If it is possible to find such code words, they can be used further as logical basis states $|0_{\mathrm{L}}\rangle$ and $|1_{\mathrm{L}}\rangle$. The following example is adapted from Reference [27]. Consider the situation when qubits are subject to the phase-flip error Z. If we choose the code words to be two Bell states

$$|0_{\mathrm{L}}\rangle = \frac{(|01\rangle + |10\rangle)}{2}, \quad |1_{\mathrm{L}}\rangle = \frac{(|01\rangle - |10\rangle)}{2}, \tag{6.7}$$

it turns out that any linear combination of these states will be insensitive to the error:

$$\alpha\frac{(|01\rangle+|10\rangle)}{2}+\beta\frac{(|01\rangle-|10\rangle)}{2}\xrightarrow{Z\otimes Z}-\left(\alpha\frac{(|01\rangle+|10\rangle)}{2}+\beta\frac{(|01\rangle-|10\rangle)}{2}\right) \quad (6.8)$$

Again, this is true only when the two entangled qubits experience the same type and intensity of error simultaneously. In the context of EM noise, it means that the qubits must be very close to each other, which is impossible to achieve for all qubits in a system. The solution to this can be encoding logical qu**b**its using qu**d**its – physical entities with more than two eigenstates – this guarantees the condition of physical proximity. A natural example of a qudit would be an atom with non-zero electron and nuclear spins.

Further, I present our investigation on the possibility of implementing an error *correction* protocol on a spin qudit that protects information not from discrete phase-flip error but against random small rotations about the z-axis.

6.2 Our QEC

6.2.1 Summary

Here we discuss a particularly simple proposal that employs an electron spin $S = 1/2$ hyperfine-coupled to a nuclear spin $I = 3/2$ to encode logical qubit states. These states are protected against fluctuations of the magnetic field ΔB_0 along the quantisation axis, represented by operator

$$\hat{O}_{\text{fluct.}} = \left(\gamma_S \hat{S}_z + \gamma_I \hat{I}_z\right)\Delta B_0, \quad (6.9)$$

where γ_S and γ_I are the electron and nuclear spin gyromagnetic ratios, respectively.

The protocol can be summarised as follows. We prepare information on the qubit in the fast electron manifold and then encode that information in the four levels of the slow-relaxing nuclear manifold in a particular way. The encoding procedure ensures that the uncorrupted and corrupted information gets separated into orthogonal qudit subspaces. After the qudit state is decoded back to the electron manifold, a projective measurement will be able to tell us if an error occurred and the initial information will be recovered in any case.

6.2.2 Details

A qubit state $|\psi\rangle$ encoded on the electron spin with a particular projection of the nuclear spin $m_I = -1/2$ can be represented in the notation $|m_S\rangle \otimes |m_I\rangle$ as

$$|\psi\rangle = \left[\alpha \left|+\frac{1}{2}\right\rangle + \beta \left|-\frac{1}{2}\right\rangle\right] \otimes \left|-\frac{1}{2}\right\rangle, \tag{6.10}$$

where α and β are, in general, complex numbers representing information we aim to protect. This state is transformed by rotation into a protected 'encoded' state

$$|\psi_{\mathrm{L}}\rangle = \alpha\,|0_{\mathrm{L}}\rangle + \beta\,|1_{\mathrm{L}}\rangle \tag{6.11}$$

with

$$|0_{\mathrm{L}}\rangle = \left|-\frac{1}{2}\right\rangle \otimes \left[\frac{1}{2}\left|+\frac{3}{2}\right\rangle - \frac{\sqrt{3}}{2}\left|-\frac{1}{2}\right\rangle\right], \tag{6.12a}$$

$$|1_{\mathrm{L}}\rangle = \left|-\frac{1}{2}\right\rangle \otimes \left[\frac{\sqrt{3}}{2}\left|+\frac{1}{2}\right\rangle - \frac{1}{2}\left|-\frac{3}{2}\right\rangle\right] \tag{6.12b}$$

The result of the magnetic field fluctuation acting for time δt on the logical qubit state is found using the TDSE:

$$|\psi_{\mathrm{L}}, t+\delta t\rangle = \exp\left\{-\frac{\mathrm{i}}{\hbar}\hat{O}_{\text{fluct.}}\delta t\right\}|\psi_{\mathrm{L}}, t\rangle\,. \tag{6.13}$$

The two terms comprising $\hat{O}_{\text{fluct.}}$ commute with each other since $\hat{S}_z$ and $\hat{I}_z$ act on different spins. Because γ_S is generally larger than γ_I, encoding the qubit in the nuclear degrees of freedom already provides an element of protection against magnetic field fluctuations [110]. The electron spin part of $|0_{\mathrm{L}}\rangle$ and $|1_{\mathrm{L}}\rangle$ are eigenstates of $\hat{S}_z$ with the same $m_S = -1/2$:

$$\mathrm{i}\hbar\frac{\partial\,|m_S\rangle}{\partial t} = \gamma_S \delta B_0 \hat{S}_z\,|m_S\rangle = \gamma_S \delta B_0 m_S\,|m_S\rangle\,. \tag{6.14}$$

Its evolution introduces a global phase $\exp\{\mathrm{i}\omega_S\delta t/2\}$ with $\omega_S = \gamma_S \Delta B_0/\hbar$, thus the general Equation 6.13 converts to

$$|\psi_{\mathrm{L}}, t+\delta t\rangle = \exp\left\{\mathrm{i}\frac{\omega_S}{2}\delta t\right\} \cdot \exp\left\{-\mathrm{i}\theta\hat{I}_z\right\}|\psi_{\mathrm{L}}, t\rangle\,, \tag{6.15}$$

where $\theta = \gamma_I \Delta B_0 \delta t/\hbar$. The global phase is undetectable for this system in isolation, and we shall neglect it in what follows. Expanding the second factor as

$$\exp\left\{-\mathrm{i}\theta\hat{I}_z\right\}|\psi_\mathrm{L}\rangle = \sum_{n=0} A_n \frac{(-\mathrm{i}\theta)^n}{n!}\hat{I}_z^n\,|\psi_\mathrm{L}\rangle \approx A_0\,|\psi_\mathrm{L}\rangle - \mathrm{i}A_1\theta\hat{I}_z\,|\psi_\mathrm{L}\rangle\,, \tag{6.16}$$

where the approximation holds for a weak perturbation $\theta\hat{I}_z$, i.e. a small ΔB_0 acting for a short time δt. Here, $A_n = 1$ for all n if the dynamics of the system is as we expect; we shall later use A_n to parameterise our experimental results. The effect of the perturbation is to shift amplitude from the logical qubit subspace into the "error" subspace spanned by

$$\hat{I}_z\,|0_\mathrm{L}\rangle = \frac{\sqrt{3}}{2}\left|-\frac{1}{2}\right\rangle \otimes \left[\frac{\sqrt{3}}{2}\left|+\frac{3}{2}\right\rangle + \frac{1}{2}\left|-\frac{1}{2}\right\rangle\right], \tag{6.17a}$$

$$\hat{I}_z\,|1_\mathrm{L}\rangle = \frac{\sqrt{3}}{2}\left|-\frac{1}{2}\right\rangle \otimes \left[\frac{1}{2}\left|+\frac{1}{2}\right\rangle + \frac{\sqrt{3}}{2}\left|-\frac{3}{2}\right\rangle\right], \tag{6.17b}$$

where the coefficients in front of the states are left here for completeness but are usually removed during normalisation. The uncorrupted information has amplitude proportional to A_0, whereas the amplitude of the part corrupted by the phase error is proportional to $A_1\theta$.

Note that the logical states $|0_\mathrm{L}\rangle$ and $|1_\mathrm{L}\rangle$ into which we initially encoded the information and the error states $\hat{I}_z\,|0_\mathrm{L}\rangle$ and $\hat{I}_z\,|1_\mathrm{L}\rangle$ are mutually orthogonal. Equation 6.16 tells us that the effect of the perturbation is to shift part of the signal from the logical qubit subspace into the orthogonal error subspace. The fact that the uncorrupted component (the first term in the RHS of 6.16) is orthogonal to the corrupted component (the second term) allows us to identify a unitary transformation (see Appendix A.4.1) which "decodes" [86] this state to

$$\begin{aligned} A_0\left|-\frac{1}{2}\right\rangle \otimes \left[\alpha\left|-\frac{1}{2}\right\rangle + \beta\left|+\frac{1}{2}\right\rangle\right] \\ -\mathrm{i}\theta A_1\left|+\frac{1}{2}\right\rangle \otimes \left[\alpha\left|-\frac{1}{2}\right\rangle + \beta\left|+\frac{1}{2}\right\rangle\right]. \end{aligned} \tag{6.18}$$

Thus, a projective measurement of the electron spin state m_S yields whether an error occurred ($m_S = +1/2$) or not ($m_S = -1/2$); in either case, the error-corrected qubit state is recovered on the $m_I = \pm 1/2$ superposition.

There are certain requirements on a physical system on which this protocol is to be implemented. Fundamentally, we require: that $S \geq 1/2$ and $I \geq 3/2$; that all transitions are independently spectrally addressable; and the availability of projective measurement of the electron spin.

While a number of physical systems show promise in meeting these requirements [150–152], we have chosen to explore the implementation and spin dynamics of the protocol in a system offering experimental convenience and flexibility, at the cost of the availability of projective measurement.

6.3 Characterisation of the Mn(II) defects in ZnO

In our study we employed impurities of manganese (II) in single-crystal zinc oxide (ZnO) which crystallises in the P63mc space-group. The ions of Mn(II) have five unpaired electrons on five d-orbitals with total spin number $S = 5/2$ and similar nuclear spin $I = 5/2$. Together they form a 36-dimensional qudit.

6.3.1 Spin Hamiltonian and EDFS

When the static field $\boldsymbol{B}_0$ is aligned with the c-axis of the hexagonal crystal system of ZnO, the low-energy levels of the Mn(II) defects are well described by the Hamiltonian

$$\hat{\mathcal{H}}_0 = \left(\gamma_S \hat{S}_z + \gamma_I \hat{I}_z\right) B_0 + A\hat{\boldsymbol{S}}^{\mathrm{T}}\hat{\boldsymbol{I}} - D\hat{S}_z^2, \tag{6.19}$$

which comprises electron and nuclear spin Zeeman terms, an isotropic hyperfine coupling, and an electron spin zero field splitting. In units convenient for understanding the experiment, $\gamma_S/h \approx 28.02$ GHz/T, $\gamma_I/h \approx -10.96$ MHz/T, $A/h \approx -220.0$ MHz, and $D/h \approx 707.0$ MHz, yielding an energy level structure shown as a function of magnetic field in Figure 6.1(a). At the X-band MW frequency (≈ 9.7 GHz, corresponding to $B_0 \approx 0.35$ T) the electron Zeeman energy is the dominant term in the Hamiltonian 6.19, so that the high-field approximation is valid and both m_S and m_I can be treated as good quantum numbers. A convenient way of labelling the energy levels is, therefore, using quantum-state notation $|m_S, m_I\rangle$. The electron

spin zero field splitting (ZFS) ensures that the five groups of allowed ESR transitions (for which $\Delta m_S = \pm 1$, $\Delta m_I = 0$) are non-degenerate. The further subdivision of each group is due to the hyperfine interaction and six different values of m_I.

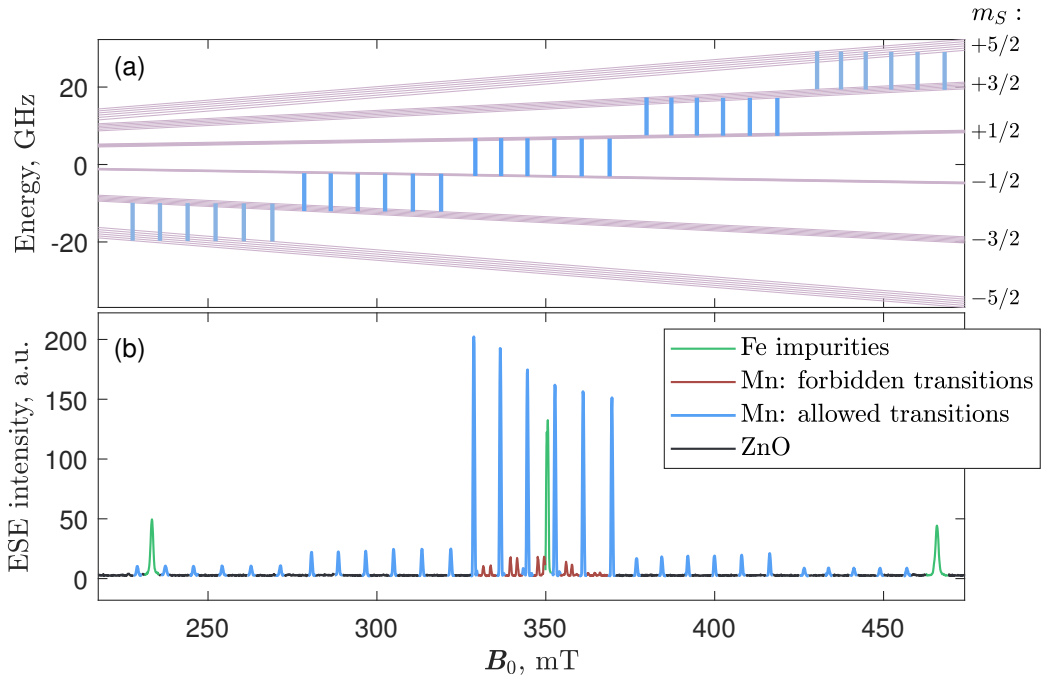

Figure 6.1: (a) Energy diagram of Mn(II) and (b) EDFS of a ZnO crystal, when $\boldsymbol{B}_0$ is parallel to the crystal c-axis.

All electron transitions are spectroscopically distinguishable as depicted in Figure 6.1(b) that shows the EDFS of a single crystal of ZnO. The intrinsic line-width of the peaks is about 0.04 mT but the apparent line-width is broader due to the convolution with the bandwidth of the excitation pulses (48 ns for the π-pulse). If the $\boldsymbol{B}_0$-field is not precisely aligned with the c-axis of the crystal, the spectrum becomes contaminated with forbidden transitions which appear between the allowed ones. Apart from Mn, the ZnO crystals might also contain other impurities among which is the ubiquitous Fe(III) – its peaks are highlighted with a different colour. In the first approximation, the intensity of the Mn peaks corresponding to transitions $(m_S \leftrightarrow m_S - 1)$ is proportional to $S(S+1) - m_S(m_S - 1)$ (see Section A.1.2). That is why the peak height goes down from the central transition group to the side ones. The D-strain and the associated inhomogeneous broadening can additionally contribute to decreasing the intensity of the transition with high m_S.

Apart from electronic $\Delta m_S = \pm 1$ transitions, we can also excite allowed nuclear transitions corresponding to $\Delta m_I = \pm 1$ by subjecting the sample to pulses of an RF frequency. The $A\hat{S}_x\hat{I}_x$ and $A\hat{S}_y\hat{I}_y$ terms in the isotropic hyperfine interaction lead to second-order shifts in the nuclear spin energy levels of the order of $A^2/\gamma_S B_0$, which in X-band lifts the degeneracy of the NMR transitions by about 4 MHz. By employing the Davies electron-nuclear double resonance technique (ENDOR, see Section 2.4.4) we found the precise frequencies of the NMR transitions: the representative results for $m_S = -1/2$ are shown in Figure 6.2.

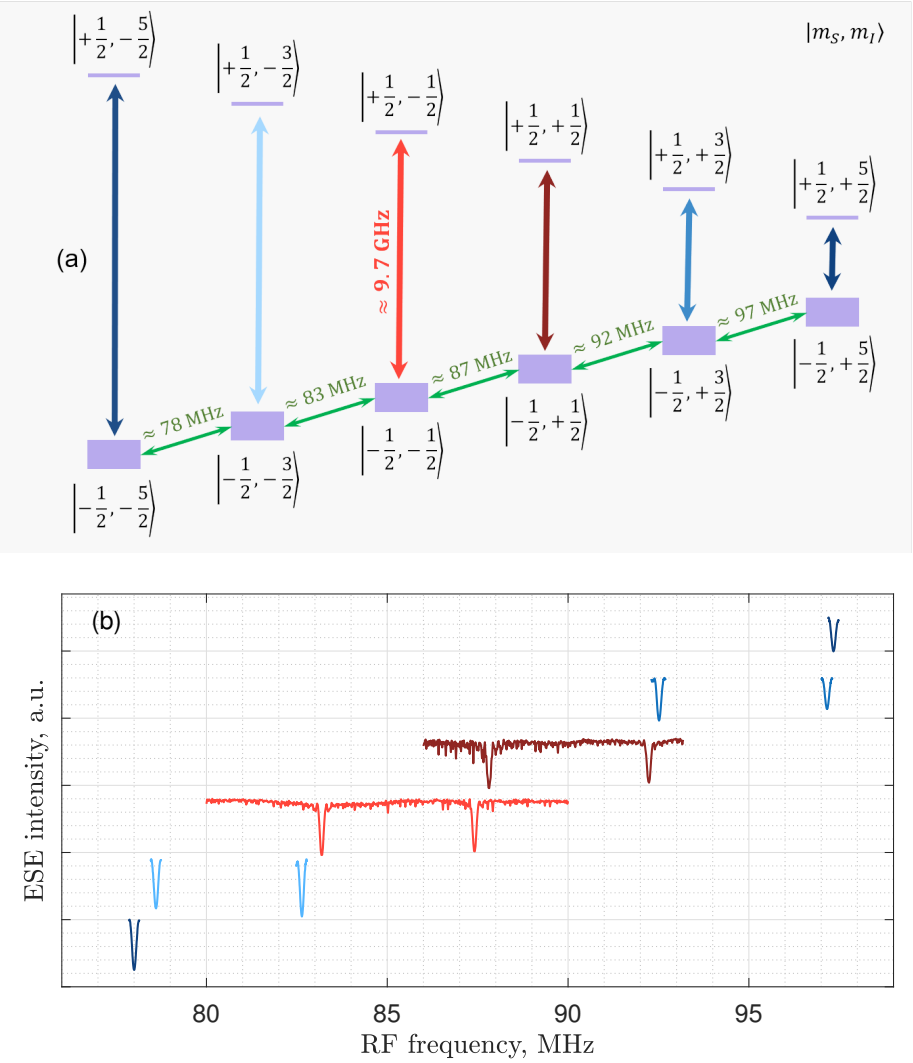

Figure 6.2: (a) Schematic representation of nuclear levels in the $m_S = \pm 1/2$ manifold (central group of the ESR transitions); (b) Davies ENDOR spectra for $m_S = -1/2$ with dips showing the resonance frequency of the nuclear transitions. $\boldsymbol{B}_0$ is parallel to the crystal c-axis.

The top panel of Figure 6.2 demonstrates how each group of electronic levels (for $m_S = -1/2$ or $m_S = +1/2$) is subdivided into six nuclear sub-levels (for different m_I). The allowed transitions observed in the experiment are shown by arrows: the vertical arrows correspond to the central group of the ESR peaks shown in Figure 6.1(b), while the tilted arrows are the nuclear transitions which are represented by the dips in the ENDOR spectra in the lower panel of Figure 6.2. As portrayed, allowed transitions connect each of the levels only with its closest neighbours; that is why, for instance, the ENDOR spectrum of $|-1/2, -1/2\rangle$ consists of two dips, whereas the spectra of $|-1/2, -5/2\rangle$ and $|-1/2, +5/2\rangle$ contain only one dip each. Dips that appear in two spectra, e.g., the resonance around 87 MHz, are shifted by approximately 1 MHz by the nuclear Zeeman interaction – different ENDOR sweeps were done at different resonance fields of the corresponding ESR peaks. We have performed wide sweeps only for $|-1/2, -1/2\rangle$ and $|-1/2, +1/2\rangle$ base levels because all the nuclear transitions occurred approximately where our simulation and previous reports [153, 154] predicted; moreover, these are the transitions that will be of interest later.

6.3.2 Accessing nuclear spin qudit subspace

When implementing the error-correction protocol we would like to be able to access different levels of the Mn(II) qudit in a single pulse sequence. In practice, this means choosing the right magnetic field $\boldsymbol{B}_0$ and the MW and RF frequencies for each pulse.

The nuclear transitions in the range 70-100 MHz in Figure 6.2(b) were measured using the same power-duration ratio of the RF pulses and did not demonstrate significant deterioration in intensity due to the bandwidth of our RF components. As for the MW pulses, in our experimental set-up, the bandwidth and the excitation mode of the MW resonator cavity does not allow us to excite electron transitions corresponding to different m_I without changing the field $\boldsymbol{B}_0$. At the same time $\boldsymbol{B}_0$ cannot be changed quickly enough between the application of the MW pulses: the required change in $\boldsymbol{B}_0$ is equal to the hyperfine splitting of the ESR peaks (≈ 8 mT), while the spacing of the MW pulses is about 4 μs; such pulses of $\boldsymbol{B}_0$

(≈ 2 kT/s) are unachievable on our resistive magnet. Consequently, during all the measurements presented here, we kept the $\boldsymbol{B}_0$ equal to the resonance field of the electron $m_S : -1/2 \leftrightarrow +1/2$, $m_I = -1/2$ (third peak in the central group) and the MW frequency at about 9.7 GHz. The access to different levels of the Mn(II) electron-nuclear qudit was implemented by RF pulses of different frequencies.

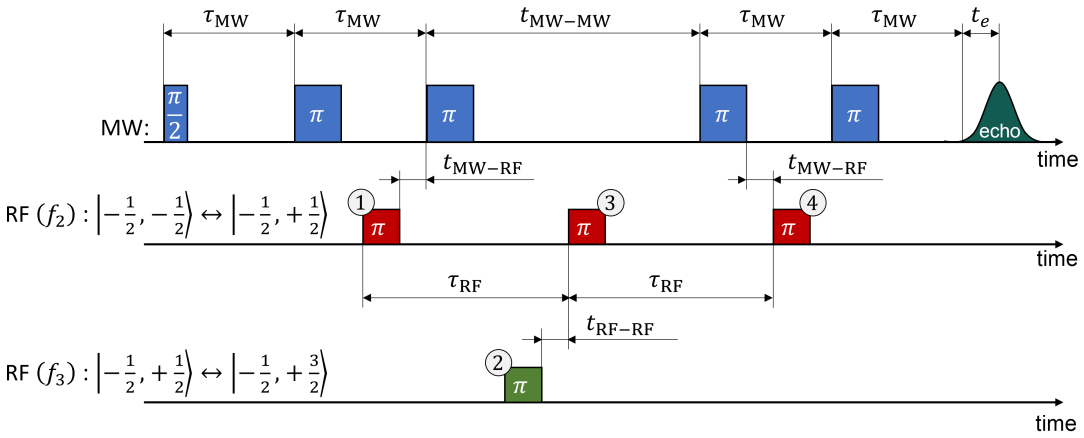

Figure 6.3: ENCT-2 sequence.

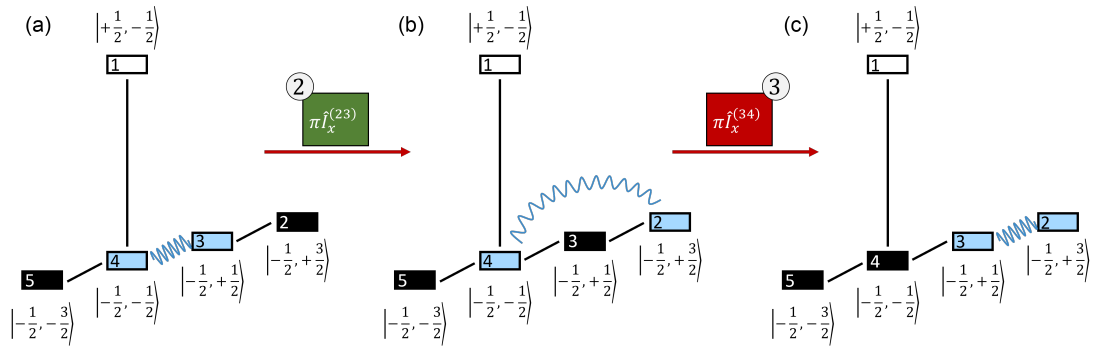

Figure 6.4: Evolution of the qubit spin system during application of the second and third RF pulses of the ENCT-2 sequence (counting all RF pulses together).

The standard ENDOR sequence allows us to measure only two nuclear resonance frequencies for a single level $|m_S, m_I\rangle$ directly. For the $m_I = -1/2$ transitions, the frequencies are $f_1 = 83$ MHz and $f_2 = 87.2$ MHz. Accessing other nuclear transitions without changing the static magnetic field requires a more advanced pulse sequence shown in Figure 6.3. It is largely identical to the coherence transfer scheme ENCT-1 discussed in Section 2.4.5 but contains an additional π-pulse of the third

RF frequency applied right before the refocussing $|-1/2,-1/2\rangle \leftrightarrow |-1/2,+1/2\rangle$ pulse. The purpose of the additional pule is to sabotage the normal flow of the ENCT-1 sequence and prevent the generation of echo.

For example, when the frequency of the additional π-pulse matches that for the $|-1/2,+1/2\rangle \leftrightarrow |-1/2,+3/2\rangle$ nuclear transition, the nuclear spin coherence is transferred to the superposition of the $|-1/2,-1/2\rangle$ and $|-1/2,+3/2\rangle$ states (Figure 6.4(a) and (b)). The subsequent refocussing π-pulse transfers the coherence to the $|-1/2,+1/2\rangle \leftrightarrow |-1/2,+3/2\rangle$ transition completely. Under this circumstance, the coherence cannot be transferred back to the electron spins by the rest of the pulses, which leads to a reduction of the electron spin echo. If, however, the frequency of the additional pulse does not match the resonance frequency of $|-1/2,+1/2\rangle \leftrightarrow |-1/2,+3/2\rangle$, the sequence behaves as normal ENCT-1 and restores the coherence back to the electron manifold producing an ESE of full amplitude. The spectrum obtained by ENCT-2 looks very similar to that of the ENDOR sequence, where sharp dips represent the nuclear resonance.

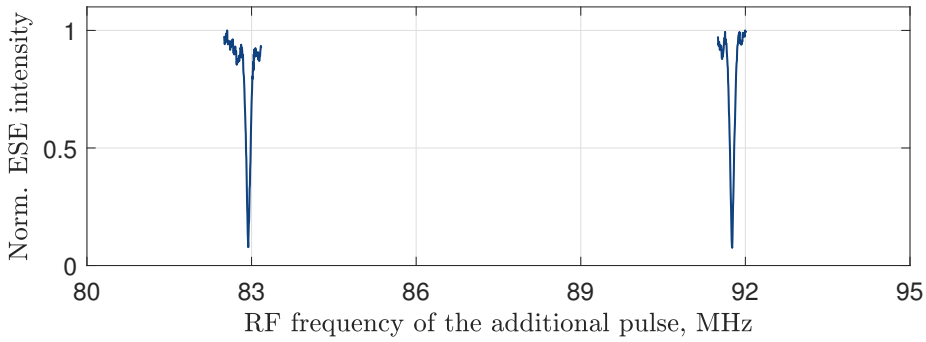

Figure 6.5: ENCT-2 spectrum with the dips corresponding to the resonance of $|-1/2,-1/2\rangle \leftrightarrow |-1/2,-3/2\rangle$ (frequency f_1) and the resonance of $|-1/2,+1/2\rangle \leftrightarrow |-1/2,+3/2\rangle$ transition (frequency f_3). $\boldsymbol{B}_0$ is parallel to the crystal c-axis.

An example of the ENCT-2 spectrum for finding f_3 is shown in Figure 6.5. During the measurement we kept the frequency f_2 constant at around 87.2 MHz and swept the frequency of the additional π-pulse. The resonance is observed not only when the frequency of the additional pulse matches the frequency of the nuclear transition $|-1/2,+1/2\rangle \leftrightarrow |-1/2,+3/2\rangle$ at around 92 MHz, but also at 83 MHz

which corresponds to the resonance frequency of $|-1/2, -3/2\rangle \leftrightarrow |-1/2, -1/2\rangle$. In the latter case the additional pulse moves one tail of the coherence from level $|-1/2, -1/2\rangle$ to level $|-1/2, -3/2\rangle$ so that it is never recovered back. As a result, the electron coherence between levels $|-1/2, -1/2\rangle \leftrightarrow |+1/2, -1/2\rangle$ is not restored and the echo is not generated. We assign f_3 the resonance frequency of transition $|-1/2, +1/2\rangle \leftrightarrow |-1/2, +3/2\rangle$ equal to 91.8 MHz.

The repetition time between shots of the same sequence is limited by the electron longitudinal relaxation T_{1e}, because it is the electron coherence which is generated and then transferred between the nuclear levels and back, or is just left on one of the nuclear transitions. The pause between the RF pulses t_{RF-RF} depends on the ringing of the RF coil in the resonator and in our case was chosen as one tenth of the RF π-pulse duration.

6.3.3 Relaxation times

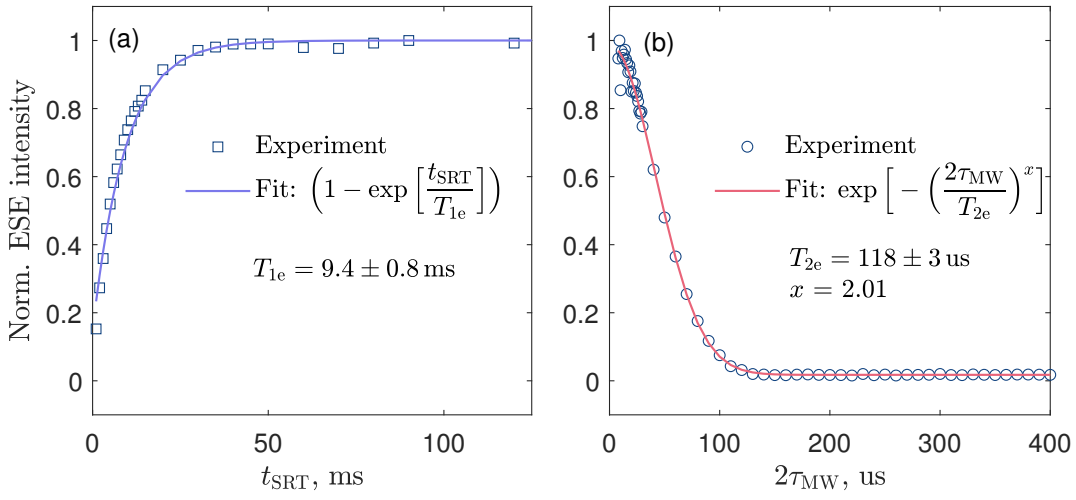

Figure 6.6: Estimation of the relaxation times at 20 K for $m_S : -1/2 \leftrightarrow +1/2$: (a) T_{1e} measured by echo saturation via fast repetition, (b) T_{2e} measured by primary echo decay fitted to a stretched exponential.

We measured the electron relaxation times using the standard spin-echo sequence where we varied the shot-repetition time (SRT) to estimate the spin-lattice relaxation time T_{1e}, and we varied the delay between the MW pulses τ_{MW} to estimate the phase-memory time T_{2e} (see Section 2.4.3.2 for details). At 20 K $T_{1e} = 9.4 \pm 0.8$ ms

and $T_{2e} = 118 \pm 3$ μs (see Figure 6.6). Both quantities did not show any significant variation with respect to the static field $\boldsymbol{B}_0$. Allowing for the difference in the impurity concentration, the results were consistent with the previously published temperature dependencies of the relaxation times [43]. As in the case of Mn(II) bipypramidal complexes, the stretch coefficient of the T_{2e}-fit is close to 2 which hints at the presence of multiple decoherence mechanisms.

Eventually, time T_{1e} defines how fast any non-equilibrium population of energy levels with different m_S is going to relax to the equilibrium state. Consequently, it determines the pause between applying the same sequence of pulses repeatedly to achieve a required level of the SNR. For sequences where only the polarisation of the energy levels was important, we chose 50 ms as the shot repetition time.

In order to estimate the nuclear longitudinal relaxation time T_{1n}, we conducted a series of the same ENDOR sequences at a single nuclear resonance frequency of interest while varying the shot repetition time. This approach is based on the definition of T_{1n} which determines the characteristic time at which the population of nuclear levels with the same m_S but different m_I relaxes to its equilibrium state.

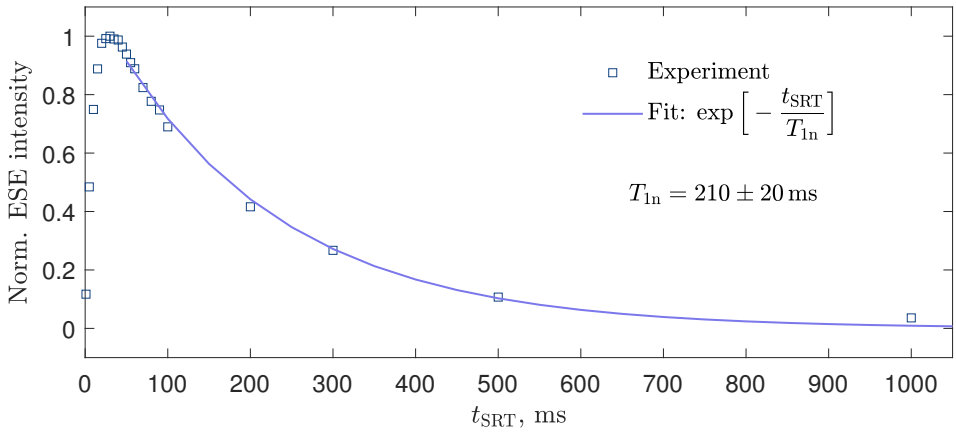

Figure 6.7: Estimation of the nuclear longitudinal relaxation time at 20 K for m_S : $-1/2 \leftrightarrow +1/2$ and m_I : $-3/2 \leftrightarrow -1/2$, 83 MHz measured by saturating ENDOR echo signal by fast repetition.

The result of the measurement is shown in Figure 6.7. In order to understand it, one should remember that the way we measure the signal in ENDOR is the two-pulse echo, and that at nuclear resonance the echo signal is minimal on account

of the successful transfer of population between the nuclear sub-levels. When $t_{\mathrm{SRT}} < 50$ ms, neither the electron nor nuclear population has enough time to restore, and the shape of the graph is similar to that of Figure 6.6(a). Right after t_{SRT} overcomes the value of 50 ms, we allow enough time for the electron sub-population to relax, but that is still not enough for the relaxation of nuclear sub-population: the RF-pulse in the ENDOR sequence does almost nothing, and the intensity of the read-out echo is at its highest. With growing t_{SRT}, the echo intensity decays and the RF-pulse becomes more and more efficient in inverting the population of the nuclear levels. By fitting the experimental data to a decaying exponential function, we obtain $T_{1\mathrm{n}} = 210 \pm 20$ ms.

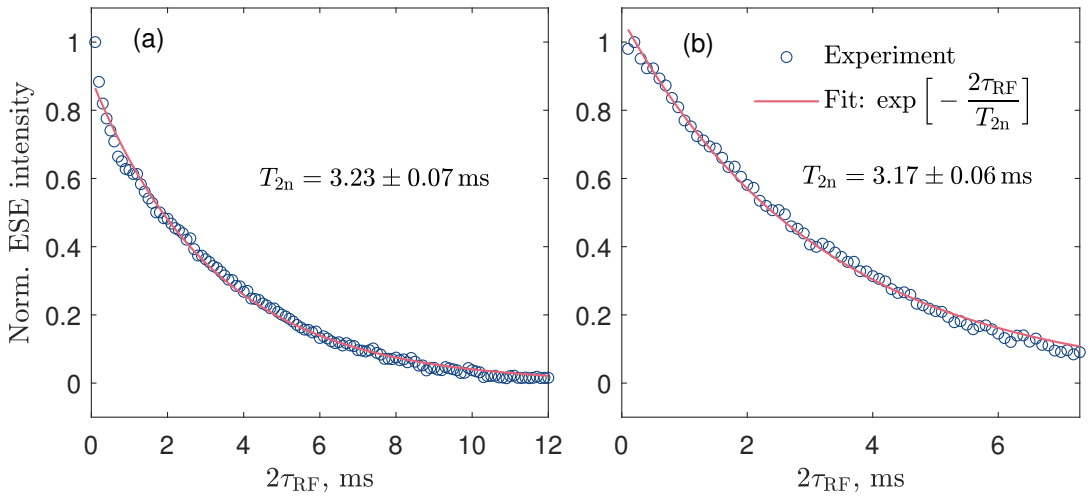

Figure 6.8: Estimation of the nuclear spin-spin relaxation time at 20 K for $m_S : -1/2 \leftrightarrow +1/2$ and (a) $m_I : -1/2 \leftrightarrow -1/2$, 87 MHz (b) $m_I : -3/2 \leftrightarrow -1/2$, 83 MHz measured by the ENCT-1 sequence.

Measurement of the nuclear spin-spin relaxation time $T_{2\mathrm{n}}$ was accomplished by the ENCT-1 sequence discussed in Section 2.4.5. The sequence generates coherence in the electron manifold, transfers it into the nuclear manifold and keeps it there for storage time $2\tau_{\mathrm{RF}}$; after which it returns the coherence back to the electron manifold for it to be read out as the electron spin echo. The intensity of the echo decays exponentially with $2\tau_{\mathrm{RF}}$ with the characteristic time $T_{2\mathrm{n}}$. An example of the data obtained by this sequence is demonstrated in Figure 6.8.

The fit of the measured data-points yields time $T_{2n} = 3.23 \pm 0.07$ ms for $m_I : -1/2 \leftrightarrow +1/2$ nuclear transition, which is the same as that of transition $m_I : -3/2 \leftrightarrow -1/2$ (within the range of uncertainty). This is close to the T_{1e} time for the $m_S : -1/2 \leftrightarrow +1/2$ electronic transition at the same temperature, suggesting that nuclear phase relaxation is dominated by electronic spin flips. It exceeds very significantly the electronic T_{2e} time of about 120 µs, demonstrating successful coherence transfer. Measurement of T_{2n} using the ENCT-3 sequence produced similar results (see Appendix A.4.2).

6.3.4 Conclusion to this section

In summary, owing to the final two terms in the Hamiltonian 6.19, all of the spin transitions occur at distinct frequencies and are spectrally addressable. This allows us to control the electron-nuclear coupled spin system of the Mn(II) defects using electron and nuclear pulsed magnetic resonance, and to detect ensemble electron spin coherences via Hahn echoes.

The coherence transfer experiments between the electronic and nuclear degrees of freedom and within the nuclear spin qudit subspace confirmed that it is possible to generate, encode, and read out quantum information in our system.

6.4 The qudit

Here, we exploit the addressability of the electronic and nuclear sub-levels of Mn(II) to select the subspace suitable for implementation of the fault-tolerant memory protocol described in Section 6.2. In fact, the encoding in Equations 6.10, 6.11 and 6.12 and the experiments described below involve only one level from the $m_S = +1/2$ subspace, $|+1/2\rangle \otimes |-1/2\rangle$, in addition to the four levels in the $m_S = -1/2$ subspace, $|-1/2\rangle \otimes |m_I\rangle$ with $m_I = -3/2, -1/2, +1/2, +3/2$ (see Figure 6.4). In $|m_S, m_I\rangle$ notation they are

$$\left\{\left|+\frac{1}{2},-\frac{1}{2}\right\rangle,\left|-\frac{1}{2},+\frac{3}{2}\right\rangle,\left|-\frac{1}{2},+\frac{1}{2}\right\rangle,\left|-\frac{1}{2},-\frac{1}{2}\right\rangle,\left|-\frac{1}{2},-\frac{3}{2}\right\rangle\right\}. \tag{6.20}$$

Figure 6.9(a) shows the 5 energy levels of this system. The numbering of the levels will correspond to the rows and columns of the density matrix and other operator matrices in the remainder, as schematically demonstrated in Figure 6.9(b).

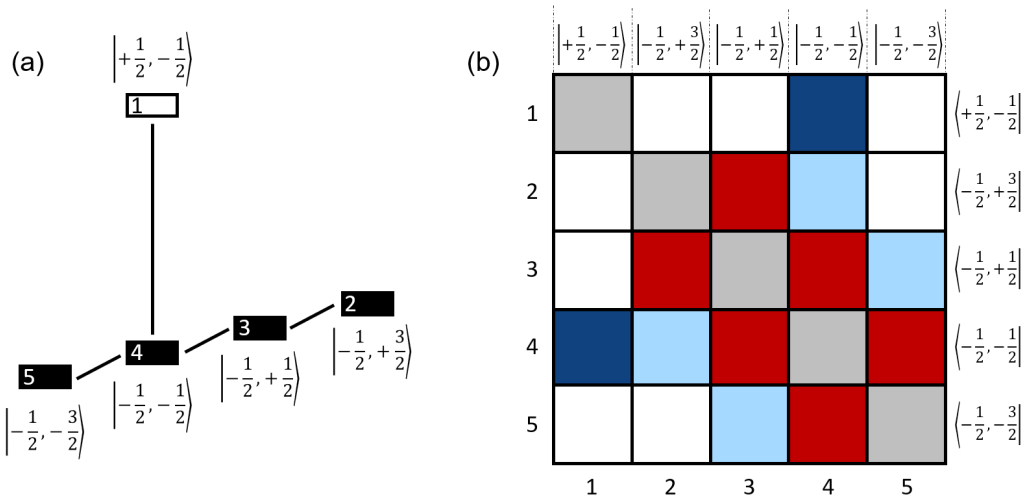

Figure 6.9: (a) The energy diagram of the states forming qudit 6.20. (b) Representation of the corresponding density matrix where the diagonal elements stand for the population, the dark blue and dark red squares stand for the MW and RF allowed transitions (single quantum coherences [90]), respectively, and the light blue squares denote the coherences forming the logical qudit states.

The measurements were conducted at 20 K and the field corresponding to the electron $|-1/2,-1/2\rangle \leftrightarrow |+1/2,-1/2\rangle$ transition (≈343.3 mT) excited by the X-band MW frequency (≈ 9.7 GHz). The frequencies for the three nuclear transitions were obtained as described in Section 6.3; they are $f_1 = 83.2$ MHz, $f_2 = 87.4$ MHz, and $f_3 = 92.6$ MHz for $|-1/2,-3/2\rangle \leftrightarrow |-1/2,-1/2\rangle$, $|-1/2,-1/2\rangle \leftrightarrow |-1/2,+1/2\rangle$ and $|-1/2,+1/2\rangle \leftrightarrow |-1/2,+3/2\rangle$ transitions, respectively (see also the diagram in Figure 6.2).

6.4.1 Initialization

The straightforward way to initialise a system of spins is to cool it down to the $m_S = -5/2$, $m_I = -5/2$ state. In the context of EPR, the goal temperature would

be significantly below 1.6 K and 0.5 K for the Q- and X-bands, respectively. For NMR, the temperature would be at least two orders of magnitude lower. While these temperatures are attainable, they make the T_{1e} and T_{1n} relaxation times grow to such an extent that the overall time of running an experiment becomes unreasonably long.

In order to work at 20 K and still be able to perform controlled manipulation of information, we must consider the thermal equilibrium population distribution in our spin ensemble, which represents the starting state for each experimental shot. As was discussed in Section 2.2.2.1, the initial state of an ensemble of electron and nuclear spins can be described by the density operator ρ given in Equation 2.23. In its matrix form for the full basis of m_S and m_I states, it contains 36 non-zero diagonal components. Conveniently, for our error correction protocol we need only five states 6.20.

The Zeeman energy at X-band (9 GHz) is by far the leading term in Hamiltonian 6.19, but is still significantly smaller than $k_B T$ (420 GHz in frequency units). Under this condition, the part of the full density matrix corresponding to the states 6.20 is approximately

$$\rho(0) = \frac{1}{(2S+1)(2I+1)} \left[\mathbf{1} - \frac{\gamma_S B_0}{k_B T} \begin{pmatrix} +\frac{1}{2} & 0 & 0 & 0 & 0 \\ 0 & -\frac{1}{2} & 0 & 0 & 0 \\ 0 & 0 & -\frac{1}{2} & 0 & 0 \\ 0 & 0 & 0 & -\frac{1}{2} & 0 \\ 0 & 0 & 0 & 0 & -\frac{1}{2} \end{pmatrix} \right]. \tag{6.21}$$

This can be rewritten as a pseudo-pure state of the form given in Equation 2.26 as

$$\rho(0) = \frac{1}{(2S+1)(2I+1)} \left[\left(1 + \frac{1}{2}\frac{\gamma_S B_0}{k_B T}\right)\mathbf{1} - \frac{\gamma_S B_0}{k_B T} \begin{pmatrix} 1 & 0 & 0 & 0 & 0 \\ 0 & 0 & 0 & 0 & 0 \\ 0 & 0 & 0 & 0 & 0 \\ 0 & 0 & 0 & 0 & 0 \\ 0 & 0 & 0 & 0 & 0 \end{pmatrix} \right]. \tag{6.22}$$

Note that this is sill the state of thermal equilibrium, meaning that our system does not require any additional active preparation to be put into a pseudo-pure state [72, 155, 156]. The identity part does not transform under unitary transformations

and the remainder is a pure state with a reduced intensity. In the above-mentioned basis this pure state is

$$|\psi, t = 0\rangle = \Big(\mathrm{i}, \quad 0, \quad 0, \quad 0, \quad 0,\Big). \tag{6.23}$$

In Section 6.5, I will show how we manipulate this initial state using MW and RF pulses in order to implement the logical qubit states. In Section 2.4, I mostly used the spin-operator formalism – this is still valid here, although direct consideration of the state components can provide deeper and clearer insight into the mechanics of the protocol. All pulses in our sequences are selective so that their action can be represented as a rotation between the two states involved in the resonant transition using Equations 2.62.

6.5 Main pulse sequence (ENCT-8)

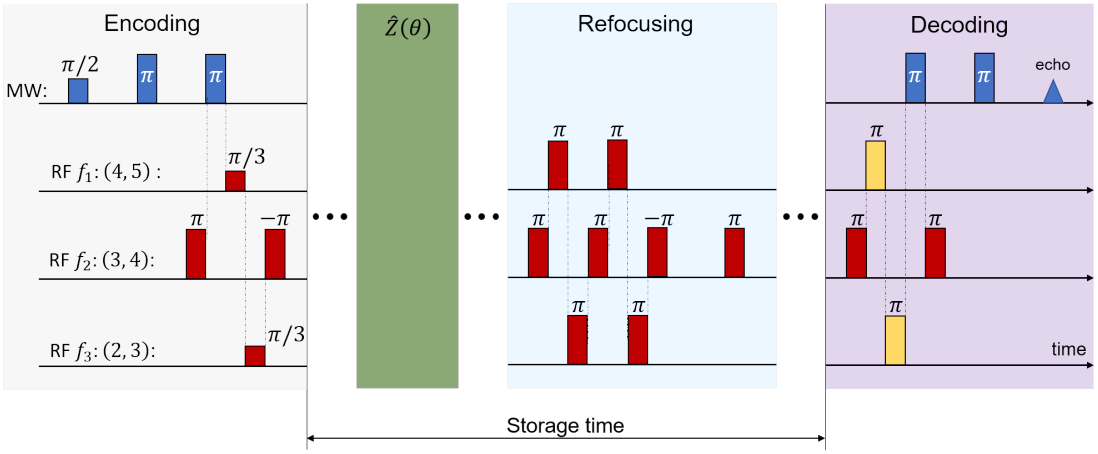

Figure 6.10: The pulse sequence comprising four stages. (1) the generation of a qubit state and its encoding in the logical-qubit subspace; (2) "$\hat{Z}(\theta)$", the controlled artificial perturbation; (3) refocussing of the inhomogeneities within the nuclear subspace; (4) decoding of the nuclear coherences back to the electron subspace: decoding of m_I : $-1/2 \leftrightarrow +1/2$ when the yellow pulses are absent, and decoding m_I : $-3/2 \leftrightarrow +3/2$ when the yellow pulses are present.

The coherence transfer experiments equip us to implement the encoding defined in Equations 6.11 and 6.12, and to explore the dynamics of the encoded state. Figure 6.10 shows the pulse sequence on which our investigation is based; it comprises four units.

6.5.1 Encoding

The first, the Encoding unit, generates an electron spin qubit state (chosen as $\alpha = \mathrm{i}\beta = \mathrm{i}/\sqrt{2}$, i.e. a σ_y eigenstate) by applying a MW $\pi/2$-pulse to the initial state 6.23 along the x-axis:

$$e^{-\mathrm{i}\frac{\pi}{2}S_x^{(14)}}\,|\psi, t=0\rangle = \begin{pmatrix} \cos\left(\frac{\pi}{4}\right) & 0 & 0 & -\mathrm{i}\sin\left(\frac{\pi}{4}\right) & 0 \\ 0 & 0 & 0 & 0 & 0 \\ 0 & 0 & 0 & 0 & 0 \\ -\mathrm{i}\sin\left(\frac{\pi}{4}\right) & 0 & 0 & \cos\left(\frac{\pi}{4}\right) & 0 \\ 0 & 0 & 0 & 0 & 0 \end{pmatrix} \begin{pmatrix} \mathrm{i} \\ 0 \\ 0 \\ 0 \\ 0 \end{pmatrix} = \frac{1}{\sqrt{2}} \begin{pmatrix} \mathrm{i} \\ 0 \\ 0 \\ 1 \\ 0 \end{pmatrix} = \begin{pmatrix} \alpha \\ 0 \\ 0 \\ \beta \\ 0 \end{pmatrix}. \tag{6.24}$$

The subsequent MW π-pulse refocuses coherence to $(-\mathrm{i}\beta, 0, 0, -\mathrm{i}\alpha, 0)^{\mathrm{T}}$ and then it is transferred to the nuclear transition $(3,4)$ by the RF and MW π-pulses in the same way as it is accomplished in the ENCT-1 sequence (see Section 2.4.5 and Appendix A.4.5). The state of the system right before the first RF $\pi/3$-pulse is $(0, 0, -\alpha, -\beta, 0)^{\mathrm{T}}$ – its energy diagram is shown in Figure 6.11(a).

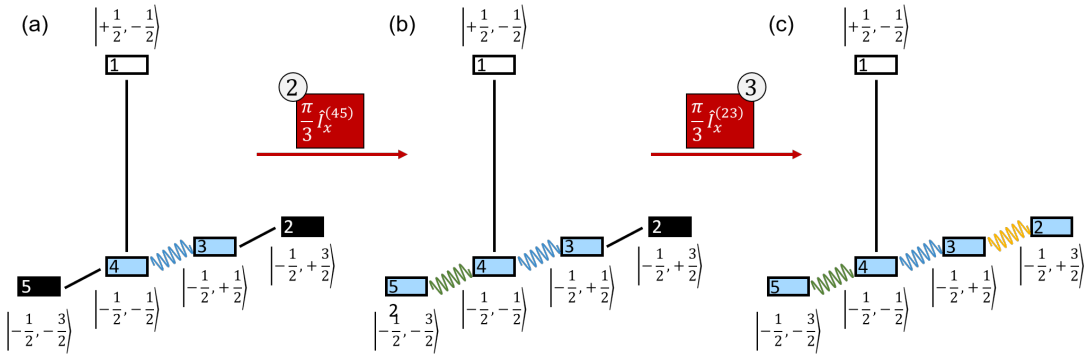

Figure 6.11: Evolution of the system under the RF $\pi/3$-pulses in ENCT-8.

The first RF $\pi/3$-pulse on transition $(4,5)$ divides the coherence between levels 4 and 5:

$$e^{\mathrm{i}\frac{\pi}{3}I_x^{(45)}}\,|\psi\rangle = \begin{pmatrix} 0 & 0 & 0 & 0 & 0 \\ 0 & 0 & 0 & 0 & 0 \\ 0 & 0 & 0 & 0 & 0 \\ 0 & 0 & 0 & \cos\left(\frac{\pi}{6}\right) & \mathrm{i}\sin\left(\frac{\pi}{6}\right) \\ 0 & 0 & 0 & \mathrm{i}\sin\left(\frac{\pi}{6}\right) & \cos\left(\frac{\pi}{6}\right) \end{pmatrix} \begin{pmatrix} 0 \\ 0 \\ \alpha \\ -\beta \\ 0 \end{pmatrix} = \begin{pmatrix} 0 \\ 0 \\ \alpha \\ -\beta\sqrt{3}/2 \\ -\mathrm{i}\beta/2 \end{pmatrix} \tag{6.25}$$

These examples demonstrate how the matrix notation should be understood when it represents selective pulses. A selective pulse affects only two transitions (in this case, 4 and 5), and we should leave those components of the state vector unchanged which correspond to empty lines in the rotation matrix. The resulting energy diagram is depicted in Figure 6.11(b).

The second RF $\pi/3$-pulse on transition $(2,3)$ divides the coherence even further:

$$e^{\mathrm{i}\frac{\pi}{3}I_x^{(23)}}|\psi\rangle = \begin{pmatrix} 0 & 0 & 0 & 0 & 0 \\ 0 & \cos\left(\frac{\pi}{6}\right) & \mathrm{i}\sin\left(\frac{\pi}{6}\right) & 0 & 0 \\ 0 & \mathrm{i}\sin\left(\frac{\pi}{6}\right) & \cos\left(\frac{\pi}{6}\right) & 0 & 0 \\ 0 & 0 & 0 & 0 & 0 \\ 0 & 0 & 0 & 0 & 0 \end{pmatrix} \begin{pmatrix} 0 \\ 0 \\ \alpha \\ -\beta\sqrt{3}/2 \\ -\mathrm{i}\beta/2 \end{pmatrix} = \begin{pmatrix} 0 \\ \mathrm{i}\alpha/2 \\ \alpha\sqrt{3}/2 \\ -\beta\sqrt{3}/2 \\ -\mathrm{i}\beta/2 \end{pmatrix} \tag{6.26}$$

The last RF $-\pi$-pulse in the encoding unit inverts the coherence on transition $(3,4)$ turning the state of the system into $\begin{pmatrix} 0 & \mathrm{i}\alpha/2 & \mathrm{i}\beta\sqrt{3}/2 & -\mathrm{i}\alpha\sqrt{3}/2 & -\mathrm{i}\beta/2 \end{pmatrix}^{\mathrm{T}}$ as shown in Figure 6.11(c). Ignoring the global phase its ket representation is

$$|\psi_{\mathrm{L}}\rangle = \alpha\left|-\frac{1}{2}\right\rangle \otimes \left[\frac{1}{2}\left|+\frac{3}{2}\right\rangle - \frac{\sqrt{3}}{2}\left|-\frac{1}{2}\right\rangle\right] + \beta\left|-\frac{1}{2}\right\rangle \otimes \left[\frac{\sqrt{3}}{2}\left|+\frac{1}{2}\right\rangle - \frac{1}{2}\left|-\frac{3}{2}\right\rangle\right] \tag{6.27}$$

$$|\psi_{\mathrm{L}}\rangle = \alpha\,|0_{\mathrm{L}}\rangle + \beta\,|1_{\mathrm{L}}\rangle \tag{6.28}$$

which exactly corresponds to the states defined in Equations 6.11 and 6.12.

6.5.2 Controlled perturbation $\hat{Z}(\theta)$

This is followed by a controlled application of the perturbation against which the encoding is designed to protect, a fluctuation of B_0, in a unit of the sequence labelled "$\hat{Z}(\theta)$". We achieve this by applying a current pulse of calibrated amplitude and duration to a pair of appropriately oriented Helmholz coils proximal to the sample (see Section 3.2). With small currents applied for short durations, the effect of the artificial perturbation is small and the approximation in Equation 6.16 holds. By increasing the current and the pulse duration, we have the scope to explore experimentally the regime beyond the small-perturbation limit; our apparatus allows us to apply pulses for which θ exceeds $\pm\pi/2$ radians. The calibration of the $\hat{Z}(\theta)$ apparatus is described in Appendix A.4.4.

According to the approximation of Equation 6.16, the evolution of the system eventually renders into each of the state vector components acquiring an additional factor which depends on particular m_I:

$$\Phi(m_I) = A_0 - \mathrm{i}A_1\theta m_I - A_2\frac{\theta^2}{2!}m_I^2 + \mathrm{i}A_3\frac{\theta^3}{3!}m_I^3 + A_4\frac{\theta^4}{4!}m_I^4 - \mathrm{i}A_5\frac{\theta^5}{5!}m_I^5 + \dots \quad (6.29)$$

To keep the formulae concise, I am going to neglect this factor in discussing the refocussing procedure, but will take it into account while calculating the final echo components.

6.5.3 Refocussing

Working with an ensemble introduces a requirement that we account for inhomogeneities. In the qubit case, where only two energy eigenstates are involved in a superposition, the effects of static inhomogeneities are refocused by a single π-pulse (see Section 2.4.3). In our qudit case, involving a superposition across four energy eigenstates, the situation is more subtle: it is not straightforward to implement an operation achieving full refocussing while preserving the system within the error-protected subspace. Approaches to refocussing arbitrary qudit states have been identified [157], but they lead to extended periods when the encoded state resides outside the logical qubit space, destroying the protection. Under this constraint it is only possible to guarantee refocussing within the $m_I = \pm 1/2$ and $m_I = \pm 3/2$ subspaces (states 2, 3, 4, and 5), but the relative phase between these subspaces is uncontrolled.

Between MW and RF pulses, the system evolves under the static Hamiltonian 6.19. Let a general system state expressed in the eigenbasis of the Hamiltonian be $(0, \xi, \zeta, \eta, \lambda)$. During the evolution, each of these components acquire an additional phase which oscillates with time at frequency proportional to the energy ϵ_i of the corresponding eigenstate:

$$\begin{pmatrix} 0 \\ \xi \\ \zeta \\ \eta \\ \lambda \end{pmatrix} \xrightarrow{\tau\hat{\mathcal{H}}} \begin{pmatrix} 0 \\ \xi e^{-\mathrm{i}\tau\epsilon_3/\hbar} \\ \zeta e^{-\mathrm{i}\tau\epsilon_2/\hbar} \\ \eta e^{-\mathrm{i}\tau\epsilon_1/\hbar} \\ \lambda e^{-\mathrm{i}\tau\epsilon_0/\hbar} \end{pmatrix} = e^{-\mathrm{i}\tau\epsilon_0/\hbar} \begin{pmatrix} 0 \\ \xi e^{-\mathrm{i}\tau(\epsilon_3-\epsilon_0)/\hbar} \\ \zeta e^{-\mathrm{i}\tau(\epsilon_2-\epsilon_0)/\hbar} \\ \eta e^{-\mathrm{i}\tau(\epsilon_1-\epsilon_0)/\hbar} \\ \lambda \end{pmatrix} = \begin{pmatrix} 0 \\ \xi e^{-\mathrm{i}\tau\Omega_3} \\ \zeta e^{-\mathrm{i}\tau\Omega_2} \\ \eta e^{-\mathrm{i}\tau\Omega_1} \\ \lambda \end{pmatrix} \quad (6.30)$$

In general, offset frequencies Ω_i are different for different nuclear spin packets and give rise to the inhomogeneous broadening. This produces different phase shifts for the coherences on three corresponding transitions – this shift cannot be eliminated using a single refocussing pulse. To refocus the coherence, we designed a composite refocussing sequence as schematically shown in Figure 6.10. The refocussing pulses act effectively as a single π-pulse over the four dimensional nuclear spin subspace of $m_I = +3/2,\ +1/2,\ -1/2$ and $-3/2$. The refocussing unit can be represented by the propagator

$$\hat{P}_{\text{refocus}} = \begin{pmatrix} 0 & 0 & 0 & 0 & 0 \\ 0 & 0 & 0 & 0 & -1 \\ 0 & 0 & 0 & \mp 1 & 0 \\ 0 & 0 & -1 & 0 & 0 \\ 0 & \mp 1 & 0 & 0 & 0 \end{pmatrix}, \tag{6.31}$$

where the $\mp$ sign accounts for the phase cycling (see Appendix A.4.5.4 and A.4.6). The refocussing pulses then swap the coherence within the subspace, allowing the nuclear spins to evolve for another period of τ under the same inhomogeneous shifts, as

$$\hat{P}_{\text{refocus}} |\psi\rangle (\tau) = \begin{pmatrix} 0 \\ -\lambda \\ \mp\eta e^{-\mathrm{i}\tau\Omega_1} \\ -\zeta e^{-\mathrm{i}\tau\Omega_2} \\ \mp\xi e^{-\mathrm{i}\tau\Omega_3} \end{pmatrix} \xrightarrow{\tau\hat{\mathcal{H}}} \begin{pmatrix} 0 \\ -\lambda e^{-\mathrm{i}\tau\Omega_3} \\ \mp\eta e^{-\mathrm{i}\tau(\Omega_1+\Omega_2)} \\ -\zeta e^{-\mathrm{i}\tau(\Omega_2+\Omega_1)} \\ \mp\xi e^{-\mathrm{i}\tau\Omega_3} \end{pmatrix} \tag{6.32}$$

When the initial state is an encoded logical qubit defined by Equation 6.11, this refocussing sequence retains the quantum information stored in α and β by using logical qubits throughout the storage time of 2τ.

Note the same additional phase at $m_I = \pm 1/2$ and $m_I = \pm 3/2$ states – the coherence stored on the corresponding transitions is refocussed for any type of inhomogeneity. The other coherences, those in the superpositions $|-1/2, +3/2\rangle \leftrightarrow |-1/2, +1/2\rangle$ and $|-1/2, -1/2\rangle \leftrightarrow |-1/2, -3/2\rangle$ (transitions $(2, 3)$ and $(4, 5)$) cannot be refocussed using our sequence. Nevertheless, the two recovered coherences allow us to extrapolate the information about the evolution of the encoded state using the measurement scheme described in Section 6.5.4.

Coming back to our original notation, the final qudit state is now

$$|\psi, 2\tau\rangle = \begin{pmatrix} 0 \\ [\beta/2]e^{-\mathrm{i}\tau\Omega_3} \\ \pm[\alpha\sqrt{3}/2]e^{-\mathrm{i}\tau(\Omega_1+\Omega_2)} \\ -[\beta\sqrt{3}/2]e^{-\mathrm{i}\tau(\Omega_2+\Omega_1)} \\ \mp[\alpha/2]e^{-\mathrm{i}\tau\Omega_3} \end{pmatrix} \tag{6.33}$$

It is ready to be decoded and transferred back to the electron spin for the read-out process.

6.5.4 Decoding

Depending on what coherence we want to measure, the decoding unit divides into two paths (for details see Appendix A.4.5.6). Essentially, the last RF π-pulse and two MW π-pulses transfer whichever coherence had been prepared on transition $(3,4)$, that is $|-1/2,-1/2\rangle \leftrightarrow |-1/2,+1/2\rangle$, to the electron coherence on transition $(1,4)$ or $|-1/2,-1/2\rangle \leftrightarrow |+1/2,-1/2\rangle$.

If the yellow pulses in Figure 6.10 are not applied, the echo is composed of the coherences proportional to $\sqrt{3}/2$:

$$\begin{pmatrix} -\mathrm{i}\Phi(+\frac{1}{2})[\beta\sqrt{3}/2]e^{-\mathrm{i}\tau(\Omega_2+\Omega_1)} \\ \mp\mathrm{i}\Phi(-\frac{1}{2})[\alpha\sqrt{3}/2]e^{-\mathrm{i}\tau(\Omega_1+\Omega_2)} \end{pmatrix} \rightarrow \frac{\sqrt{3}}{2}\begin{pmatrix} \Phi\left(+\frac{1}{2}\right)\beta \\ \pm\Phi\left(-\frac{1}{2}\right)\alpha \end{pmatrix}. \tag{6.34}$$

The corresponding echo amplitudes $I_{\pm\frac{1}{2},x}$ and $I_{\pm\frac{1}{2},y}$ can be calculated as the expectation values of operators $\hat{S}_x$ and $\hat{S}_y$ according to Equations 2.39, but now coefficients in Equation 6.29 must also be considered. For $\alpha = \mathrm{i}\beta = \mathrm{i}/\sqrt{2}$ (eigenstate of $\hat{S}_y$), the echo components for the $m_I = \pm 1/2$ coherence are proportional to

$$I_{\pm\frac{1}{2},x} = -\frac{3\theta}{8}A_0A_1 + \frac{\theta^3}{64}\left(3A_1A_2 + A_0A_3\right) + O\left(\theta^5\right), \tag{6.35a}$$

$$I_{\pm\frac{1}{2},y} = \frac{3}{8}A_0^2 - \frac{3\theta^2}{32}\left(A_1^2 + A_0A_2\right) + O\left(\theta^4\right). \tag{6.35b}$$

If, on the contrary, the additional yellow RF π-pulses are applied, they move the coherence from transitions $(2,3)$ and $(4,5)$ to $(3,4)$, and we measure the $m_I = \pm 3/2$ coherence given by

$$\begin{pmatrix} \mathrm{i}\Phi(-\frac{3}{2})[\beta/2]e^{-\mathrm{i}\tau\Omega_3} \\ \pm\mathrm{i}\Phi(+\frac{3}{2})[\alpha/2]e^{-\mathrm{i}\tau\Omega_3} \end{pmatrix} \rightarrow \frac{1}{2}\begin{pmatrix} \Phi\left(-\frac{3}{2}\right)\beta \\ \pm\Phi\left(+\frac{3}{2}\right)\alpha \end{pmatrix}. \tag{6.36}$$

In this case, the echo components are proportional to the following quantities:

$$I_{\pm\frac{3}{2},x} = -\frac{3\theta}{8}A_0A_1 + \frac{9\theta^3}{64}\left(3A_1A_2 + A_0A_3\right) + O\left(\theta^5\right), \tag{6.37a}$$

$$I_{\pm\frac{3}{2},y} = \frac{1}{8}A_0^2 - \frac{9\theta^2}{32}\left(A_1^2 + A_0A_2\right) + O\left(\theta^4\right). \tag{6.37b}$$

Note that in our paper we chose an eigenstate of $\hat{S}_x$ for the initial state of the qubit, consequently, all the quantities presented here are shifted by $\pi/2$ with respect to those reported in the paper (i.e. x and y should be swapped). I used an eigenstate of $\hat{S}_y$ here, in order to check all the formulae once again.

6.5.5 Conclusion to this section

This section has described the ENCT-8 sequence of MW and RF pulses which was designed for demonstrating our implementation of the error correction protocol. The sequence yields, as a function of the artificially applied error angle θ, four echoes: the in-phase (x) and quadrature (y) components of echoes arising from the coherences on transitions $m_I : -1/2 \leftrightarrow +1/2$ (obtained without the yellow pulses in Figure 6.10 absent) and $m_I : -3/2 \leftrightarrow +3/2$ (obtained with the yellow pulses present). We label the four echo amplitudes $I_{\pm\frac{1}{2},x}$, $I_{\pm\frac{1}{2},y}$, $I_{\pm\frac{3}{2},x}$, $I_{\pm\frac{3}{2},y}$. The results of the measurements are discussed in Section 6.6.

6.6 Demonstration of the qudit dynamics

The four echo components $I_{\pm\frac{1}{2},x}$, $I_{\pm\frac{1}{2},y}$, $I_{\pm\frac{3}{2},x}$, $I_{\pm\frac{3}{2},y}$ measured for a fixed storage time of 0.2 ms are plotted in Figure 6.12 as functions of θ. The experimental results are accompanied by a global fit to a model based on a truncation of the series in Equation 6.16 with free parameters A_n, $n = 0, ..., 5$ (solid lines). Also shown are the amplitudes expected under the exact theoretical ($A_n = 1$) evolution with θ (dashed lines). The values of the fit parameters are given in Table 6.1 normalised to A_0, accounting for the overall echo signal gain in the experiment. The proximity of A_n/A_0 (with $n > 0$) to 1 is indicative of how close the evolution of the system is to the exact theoretical evolution.

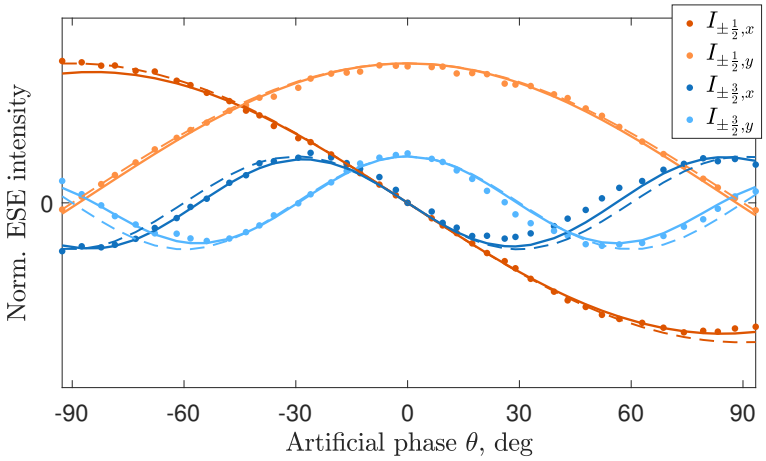

Figure 6.12: The evolution of the four detectable echoes at the end of the sequence as a function of the applied perturbation angle θ with a fixed storage time of 0.2 ms.

A_0	A_1/A_0	A_2/A_0	A_3/A_0	A_4/A_0	A_5/A_0
20.10	1.00	1.12	1.13	1.03	1.22
$\pm$0.007	$\pm$0.015	$\pm$0.04	$\pm$0.11	$\pm$0.09	$\pm$0.37

Table 6.1: Values of the fit parameters A_n. They are normalised to A_0, which defines the overall vertical scale in Figure 6.12. Quoted errors are $\pm 1\sigma/A_0$ bounds.

Given that we cannot achieve full refocussing and that our detection of the properties of the system state is via spin echoes of electron coherences, the question arises: what features of the protected state can we observe as a function of the perturbation $\hat{Z}(\theta)$? The echo amplitudes in terms of A_n are given in Equations 6.35 and 6.37.

Our principal experimental objective is to monitor the evolution of state amplitude from the logical qubit subspace into the orthogonal "error" subspace defined immediately following Equation 6.16 under the action of the perturbation, i.e. to monitor the amplitudes A_0 and $A_1\theta$ as functions of θ. We can access these quantities from the available echo data. The linear combination

$$3I_{\pm\frac{1}{2},y} - I_{\pm\frac{3}{2},y} = A_0^2 + O(\theta^4) \tag{6.38}$$

gives access to the square of the uncorrupted amplitude, and is plotted in Figure 6.13(a) as a function of θ (points), along with the model fit (solid line) and the predicted exact evolution (dashed line). The remarkably flat behaviour over

a wide range around $\theta = 0$ is a direct reflection of the fact that the perturbation is moving amplitude from the logical qubit subspace into an orthogonal subspace, thus preserving it. We may obtain the amplitude of the corrupted state directly from a scaling of the in-phase echoes

$$-\frac{8}{3} I_{\pm\frac{1}{2},x} = A_0 A_1 \theta + O(\theta^3) \tag{6.39a}$$

and

$$-\frac{8}{3} I_{\pm\frac{3}{2},x} = A_0 A_1 \theta + O(\theta^3) \tag{6.39b}$$

as plotted in Figure 6.13(b). Over a significant range around $\theta = 0$, both quantities are coincident with a line of gradient 1 through the origin, confirming that they faithfully report the corrupted amplitude.

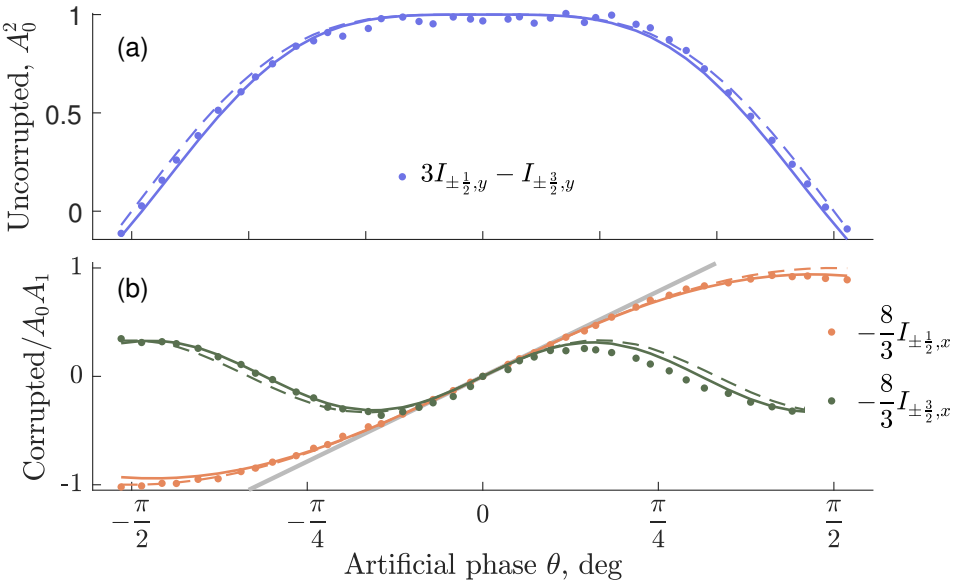

Figure 6.13: (a) A linear combination of the echoes yielding, for small θ, the squared amplitude of the uncorrupted component A_0^2. (b) Rescaled appropriately, the out of phase echoes yield the amplitude of the corrupted component for small θ. The grey line has gradient 1 and passes through the origin.

6.7 Conclusion

The results presented in Figures 6.13 offer strong evidence that (*i*) we can implement the logical qubit encoding presented in Equation 6.12, and (*ii*) the dynamics of

this qubit under the perturbation that the qubit is designed to protect against are as expected. We conclude that the deployment of hyperfine-coupled nuclear qudits can indeed serve as a valuable resource for implementing fault-tolerant quantum memories [37, 86, 158].

The potential of this approach provides a fresh impetus for developing single-spin, single-shot projective measurement for condensed matter based electron spin qubits, including broadening the scope of applicability of demonstrated methods [57, 150] as well as exploring new approaches. The important question of the potential performance of a quantum memory of the kind described here is explored elsewhere [86], but we note that it will depend critically on the fidelities of both the encoding and measurement protocols.

It is worth noting that though we used only five levels of the Mn ions, the other states can be used for something else – for storing another logical qubit, for instance.

Appendices

Appendix A

Thesis Appendices

Contents

A.1 Mathematics

A.1.1 Properties of the Kronecker product

If A, B, C and D are square $m \times m$ matrices, then

$$(A \otimes B)(C \otimes D) = (AC) \otimes (BD). \tag{A.1}$$

The trace of a Kronecker matrix is equal to the product of the traces:

$$\mathrm{Tr}(A \otimes B) = \mathrm{Tr}(A)\,\mathrm{Tr}(B) \tag{A.2}$$

A.1.1.1 Ensemble average of an extensive quantity

Let us calculate the expectation value of an extensive quantity measured on an ensemble of n identical spins. The composite operator acting on the entire system is given by

$$\hat{Q}^{(\mathrm{composite})} = \sum_{i=1}^{n} \hat{\mathbf{1}}^{(1)} \otimes \hat{\mathbf{1}}^{(2)} \otimes \cdots \otimes \hat{\mathbf{1}}^{(i-1)} \otimes \hat{Q}^{(i)} \otimes \hat{\mathbf{1}}^{(i+1)} \otimes \cdots \otimes \hat{\mathbf{1}}^{(n)}, \tag{A.3}$$

and, similarly, the composite density operator is

$$\hat{\rho}^{\mathrm{composite}} = \hat{\rho}^{(1)} \otimes \hat{\rho}^{(2)} \otimes \cdots \otimes \hat{\rho}^{(n)}, \tag{A.4}$$

where all $\hat{\mathbf{1}}^{(i)}$, $\hat{Q}^{(i)}$ and $\hat{\rho}^{(i)}$ are the same for any i.

Then the expectation value is

$$\begin{aligned}
\left\langle \hat{Q}^{(\mathrm{composite})} \right\rangle &= \mathrm{Tr}\left(\rho^{(\mathrm{composite})} Q^{(\mathrm{composite})}\right) = \\
\mathrm{Tr}\left(\left(\rho^{(1)} \otimes \rho^{(2)} \otimes \cdots \otimes \rho^{(n)}\right)\left(\sum_{i=1}^{n} \mathbf{1}^{(1)} \otimes \mathbf{1}^{(2)} \otimes \cdots \otimes \mathbf{1}^{(i-1)} \otimes \hat{Q}^{(i)} \otimes \mathbf{1}^{(i+1)} \otimes \cdots \otimes \mathbf{1}^{(n)}\right)\right) &= \\
\mathrm{Tr}\left(\sum_{i=1}^{n} \left\{\left(\rho^{(1)}\mathbf{1}^{(1)}\right) \otimes \cdots \otimes \left(\rho^{(i)}Q^{(i)}\right) \otimes \cdots \otimes \left(\rho^{(n)}\mathbf{1}^{(n)}\right)\right\}\right) &= \\
\sum_{i=1}^{n} \left\{\mathrm{Tr}\left(\left(\rho^{(1)}\mathbf{1}^{(1)}\right) \otimes \cdots \otimes \left(\rho^{(i)}Q^{(i)}\right) \otimes \cdots \otimes \left(\rho^{(n)}\mathbf{1}^{(n)}\right)\right)\right\} &= \\
\sum_{i=1}^{n} \left\{\mathrm{Tr}\left(\rho^{(1)}\mathbf{1}^{(1)}\right) \times \cdots \times \mathrm{Tr}\left(\rho^{(i)}Q^{(i)}\right) \times \cdots \times \mathrm{Tr}\left(\rho^{(n)}\mathbf{1}^{(n)}\right)\right\} &= \\
\sum_{i=1}^{n} \mathrm{Tr}\left(\rho^{(i)}Q^{(i)}\right), &
\end{aligned} \tag{A.5}$$

and finally

$$\left\langle \hat{Q}^{(\text{composite})} \right\rangle = n \,\text{Tr}(\rho Q), \tag{A.6}$$

where ρ and Q are the matrices corresponding to a single spin.

A.1.2 Time-dependent perturbation

If the perturbation is given by Hamiltonian

$$\hat{\mathcal{H}}_{\text{MW}} = \mu_{\text{B}} g B_1 \hat{S}_x, \tag{A.7}$$

the intensity of EPR transitions to the linear high-field approximation (with dominant Zeeman interaction) is going to be proportional to the matrix elements

$$\langle m_S | \, \hat{S}_x \, | m_S + 1 \rangle = \frac{1}{2} \left[S(S+1) - m_S(m_S+1) \right]^{1/2}, \tag{A.8}$$

where $|m_S\rangle$ is an eigenstate of operator $\hat{S}_z$ [91].

A.2 Experimental set-up

A.2.1 Measurement of phase noise

To faithfully measure phase noise, it was crucial to provide the VNA with the same reference signal as the other active devices. The other important setting is the measurement bandwidth of the VNA's IF filter: for high precision it can be set up to tenths of Hz (the time of measurements is inversely proportional to the bandwidth).

While measuring the phase noise, I used the following procedure:

1. Measure the carrier power P_{c} in dBm
2. Move to a given offset (10 Hz, 100 Hz, 1 kH 10 kHz)
3. Measure the phase noise power P_{n} over 1 Hz IF filter bandwidth (dBm/Hz)
4. Subtract the power levels ($P_{\text{n}} - P_{\text{c}}$)

The result is the phase noise in dBc/Hz at the given offset.

A.3 Mn(II) bipyramidal complexes

A.3.1 E-field measurement artefact

The measurement artefact in Figure 4.7 is due to a bug in the script which was running the E-field measurement. After each sweep of the E-field pulse duration t_{E}, the output of the E-field generator was switched off. In this way, the first point of each consecutive sweep was measured without application of the E-field pulses. The second point in the data corresponds to $t_{\mathrm{E}} = 50$ ns, which is smaller than the minimal value of the pulse width allowed by our generator (80 ns), therefore it did not change the pulse duration and kept the very last value from the previous sweep, namely 4.5 μs. However, since the duration of the pulse was non-zero, the script turned the output of the generator on.

As a result, the second point of all the sweeps starting with the second one was measured with a 4.5 μs-long E-field pulse (instead of 50 ns). The averaging of the sweeps together with the first one produced a value different from that at true $t_{\mathrm{E}} = 4.5$ μs.

A.3.2 The ZFS parameter for the bipyramidal complexes

The calculations presented in this section were performed by our colleagues from the group of Prof Nathalie Guihéry. The detailed analysis was carried out on (**1**) and (**3**) to substantiate the trends observed experimentally.

In the high spin Mn(II) ($S = 5/2$, $L = 0$) ground state, all five d-orbitals are singly occupied, leading to a sextuplet ^6A. As a result, the ZFS can only emerge due to interactions between the electronic ground state and the excited quadruplet states, $^4Y^i$, via spin-orbit coupling (SOC), where superscript i denotes a particular excited term (the notation is imposed by the C_3 symmetry). In most of the determinants of the quadruplet states considered, one of the d-orbitals is doubly occupied and another one is empty (leaving three orbitals being singly occupied).

The contributions of the m_{sl} components of each i-th excited quadruplet state $^4Y^i$ with the excitation energy $\varepsilon\,(^4Y^i)$ relative to the ground level ^6A can be analysed by means of the second-order perturbation theory using the following expression:

$$C(D)\left[^4Y^i_{m_{sl}}\right] = \sum_k \frac{\left|\left\langle {}^6A_{m_s}\middle|\zeta_k[(\hat{L}_+\hat{S}_- + \hat{L}_-\hat{S}_+)/2 + \hat{L}_z\hat{S}_z]\middle|{}^4Y^i_{m_{sl}}\right\rangle\right|^2}{\varepsilon(^4Y^i)}, \qquad \text{(A.9)}$$

where the sum over k runs through 5 electrons in the d-orbitals, ζ_k is the SOC constant that depends on the two orbitals involved in the excitation $^4Y^i$. In order to obtain the ZFS term, one needs to sum all the contributions $C(D)\left[^4Y^i_{m_{sl}}\right]$ over the excited terms (index i), and over the magnetic quantum numbers m_s and m_{sl}. For the ground state $^6A_{m_s}$, m_s runs through $\{\pm 5/2, \pm 3/2, \pm 1/2\}$, whereas for an excited state $^4Y^i_{m_{sl}}$ the values $m_{sl} \in \{\pm 3/2, \pm 1/2\}$.

N.G.'s calculations show that the main contributions to D arise from (i) four doubly degenerate states E^i, ($i = 1$ to 4) that couple to the ground state through $\left(\hat{L}_+\hat{S}_- + \hat{L}_-\hat{S}_+\right)/2$ and lead to negative contributions to D, and (ii) two non-degenerate states A^i ($i = 1$ to 2) that couple to the ground state through $\hat{L}_z\hat{S}_z$ and lead to positive contributions to D [159]. In other words, $C(D)\,[^4E^i] < 0$ and $C(D)\,[^4A^j] > 0$, for $i = 1$ to 4 and $j = 1$ to 2. The interplay of these contributions defines the overall sign of D and the type of magnetic anisotropy. It is worth noting that the spin-spin contribution to D which was considered in the calculations is very small [160].

Each term $C(D)\left[^4Y^i_{m_{sl}}\right]$ in Equation A.9 is proportional to the SOC magnitude and inversely proportional to the excitation energies $\varepsilon\,(^4Y^i)$. While for many series of complexes, the excitation energies govern the magnitude and nature of D, it turned out that for the Mn(II) bipyramidal complexes the variation of the SOCs plays the most important role. The variation in SOCs can have two origins: either the coefficient on the $^4Y^i$ state determinants involved in the coupling varies between (**1**) and (**3**), or the spin-orbit constants ζ_k vary. In general, both variations need to be considered; however, in our case, the dominant effect concerns the spin-orbit constants. The values of the mean spin-orbit constant extracted from the *ab initio*

ligand field method implemented in ORCA are 9.31 THz and 9.04 THz for (**1**) and (**3**), respectively. The constant ζ_k is weaker for the iodine-containing complex than for the chlorine-containing complex due to the relativistic nephelauxetic effect. The nature of this effect is expressed in reduced values of the SOC constants of ions when they constitute part of a ligand in comparison with those of free ions [161].

The result of the calculations is that the negative contributions to D brought about by the doubly degenerate states E^i decrease (less negative) when going from the chlorine to the iodine derivatives, while the positive contributions brought by the non-degenerate states A^i increases (more positive). The two effects are complementary and produce an increase in the values of D when moving from the chlorine to the iodine derivative – that is exactly what is observed experimentally. The numerical results are summarised in Table 4.1.

When an electric field is applied in the direction from X to Mn, it stretches the X-Mn bond and shrinks the Mn-N1 bond. This perturbs the d-orbitals, decreases the positive SOC contribution from the excited states A^i, increases the negative SOC contribution from states E^i, therefore generating an overall negative change in D.

A.4 QEC

A.4.1 Operations encoding and decoding the logical qubit

A.4.1.1 Encoding and decoding within the $m_S = -1/2$ subspace

At the heart of the protocol is a unitary transformation within the $m_S = -1/2$ subspace,

$$\begin{aligned}\hat{U}_{\text{enc}} = &|0_{\text{L}}\rangle \left\langle -\frac{1}{2}, -\frac{1}{2}\right| \\ &+ |1_{\text{L}}\rangle \left\langle -\frac{1}{2}, +\frac{1}{2}\right| \\ &+ \frac{2}{\sqrt{3}} \hat{I}_z \, |0_{\text{L}}\rangle \left\langle -\frac{1}{2}, -\frac{3}{2}\right| \\ &+ \frac{2}{\sqrt{3}} \hat{I}_z \, |1_{\text{L}}\rangle \left\langle -\frac{1}{2}, +\frac{3}{2}\right|,\end{aligned} \tag{A.10}$$

where $|m_S, m_I\rangle = |m_S\rangle \otimes |m_I\rangle$, whereas $|0_\mathrm{L}\rangle$ and $|1_\mathrm{L}\rangle$ are defined in Equation 6.12, but I repeat it here for convenience:

$$|0_\mathrm{L}\rangle = \left|-\frac{1}{2}\right\rangle \otimes \left[\frac{1}{2}\left|+\frac{3}{2}\right\rangle - \frac{\sqrt{3}}{2}\left|-\frac{1}{2}\right\rangle\right], \tag{A.11a}$$

$$|1_\mathrm{L}\rangle = \left|-\frac{1}{2}\right\rangle \otimes \left[\frac{\sqrt{3}}{2}\left|+\frac{1}{2}\right\rangle - \frac{1}{2}\left|-\frac{3}{2}\right\rangle\right]. \tag{A.11b}$$

We start with an electron qubit

$$|\psi\rangle = \left[\alpha\left|+\frac{1}{2}\right\rangle + \beta\left|-\frac{1}{2}\right\rangle\right] \otimes \left|-\frac{1}{2}\right\rangle. \tag{A.12}$$

Then, we transform this into a nuclear spin qubit

$$\alpha\left|-\frac{1}{2}, -\frac{1}{2}\right\rangle + \beta\left|-\frac{1}{2}, +\frac{1}{2}\right\rangle. \tag{A.13}$$

After that, operator $\hat{U}_\mathrm{enc}$ encodes the nuclear qubit to the state $|\psi_\mathrm{L}\rangle$ (Equation 6.11):

$$\begin{aligned} &|\psi_\mathrm{L}\rangle = \alpha\,|0_\mathrm{L}\rangle + \beta\,|1_\mathrm{L}\rangle = \\ &= \alpha\left|-\frac{1}{2}\right\rangle \otimes \left[\frac{1}{2}\left|+\frac{3}{2}\right\rangle - \frac{\sqrt{3}}{2}\left|-\frac{1}{2}\right\rangle\right] + \beta\left|-\frac{1}{2}\right\rangle \otimes \left[\frac{\sqrt{3}}{2}\left|+\frac{1}{2}\right\rangle - \frac{1}{2}\left|-\frac{3}{2}\right\rangle\right]. \end{aligned} \tag{A.14}$$

Under the action of the perturbation, $|0_\mathrm{L}\rangle$ and $|1_\mathrm{L}\rangle$ are mixed with $\frac{2}{\sqrt{3}}\hat{I}_z\,|0_\mathrm{L}\rangle$ and $\frac{2}{\sqrt{3}}\hat{I}_z\,|1_\mathrm{L}\rangle$, respectively.

The inverse transformation, $\hat{U}^\dagger_\mathrm{enc}$, decodes from the protected basis so that the uncorrupted component is restored to the state in Equation A.13, and the error component arrives on the superposition

$$\epsilon\left(\alpha\left|-\frac{1}{2}, -\frac{3}{2}\right\rangle + \beta\left|-\frac{1}{2}, +\frac{3}{2}\right\rangle\right), \tag{A.15}$$

where, comparing with Equations 6.16 and 6.18, $\epsilon = -\mathrm{i}\theta$.

The practical implementation of $\hat{U}_\mathrm{enc}$ depends on the operations that are available in the specific physical system on which the protocol is to be implemented. For a system in which $\Delta m = \pm 1, \pm 2$ transitions are available, an efficient operation yielding $\hat{U}_\mathrm{enc}$ is provided by the sequence of pulses represented by rotation operators

$$R_{\left|-\frac{1}{2}\right\rangle \leftrightarrow \left|+\frac{3}{2}\right\rangle, \frac{\pi}{3}} \cdot R_{\left|-\frac{3}{2}\right\rangle \leftrightarrow \left|+\frac{1}{2}\right\rangle, \frac{5\pi}{3}} \cdot R_{\left|+\frac{1}{2}\right\rangle \leftrightarrow \left|-\frac{1}{2}\right\rangle, -\pi} \tag{A.16}$$

The decoding pulse sequence implementing $\hat{U}_{\text{enc}}^{\dagger}$ is generated by reversing the sequence of pulses and replacing θ with $-\theta$ for each.

In physical systems for which only $\Delta m = \pm 1$ transitions are available, alternative equivalently functional encodings within this space can be identified (see Section 6.5.1).

A.4.1.2 Swapping between electron and nuclear spin states

The encoding between Equations A.12 and A.14 requires a step before the operation described in Section A.4.1.1, transferring the electron qubit state in Equation A.12 onto the nuclear qubit in Equation A.13. This operation can be achieved using a sequence of one nuclear π-pulse and one electron π-pulse [110]

$$R_{\left|-\frac{1}{2},+\frac{1}{2}\right\rangle\leftrightarrow\left|+\frac{1}{2},+\frac{1}{2}\right\rangle,\pi} \cdot R_{\left|+\frac{1}{2},-\frac{1}{2}\right\rangle\leftrightarrow\left|+\frac{1}{2},+\frac{1}{2}\right\rangle,-\pi} \tag{A.17}$$

Following the decoding transformation described in Section A.4.1.1, the uncorrupted component is already in the superposition given by the first term in Equation 6.18. The final decoding step is to tranfer the corrupted component from the $\left|-\frac{1}{2},-\frac{3}{2}\right\rangle, \left|-\frac{1}{2},+\frac{3}{2}\right\rangle$ superposition to the $\left|+\frac{1}{2},-\frac{1}{2}\right\rangle, \left|+\frac{1}{2},+\frac{1}{2}\right\rangle$ superposition. This is achieved through an alternating series of electron and nuclear π-pulses:

$$R_{\left|+\frac{1}{2},+\frac{3}{2}\right\rangle\leftrightarrow\left|+\frac{1}{2},+\frac{1}{2}\right\rangle,\pi} \cdot R_{\left|-\frac{1}{2},+\frac{3}{2}\right\rangle\leftrightarrow\left|+\frac{1}{2},+\frac{3}{2}\right\rangle,-\pi} \cdot R_{\left|+\frac{1}{2},-\frac{3}{2}\right\rangle\leftrightarrow\left|+\frac{1}{2},-\frac{1}{2}\right\rangle,-\pi} \cdot R_{\left|-\frac{1}{2},-\frac{3}{2}\right\rangle\leftrightarrow\left|+\frac{1}{2},-\frac{3}{2}\right\rangle,-\pi} \tag{A.18}$$

A.4.1.3 Swapping between electron and nuclear spin states

Owing to the lack of projective measurement in our apparatus, there is no value in our experiment implementing the full decoding described here. Instead we use a simpler but equivalent encoding, and we explore the dynamics of the encoded state by detecting various coherences as described in Sections 6.5.4 and A.4.5.

A.4.2 Nuclear coherence transfer via ENCT-3

While the ENCT-2 sequence was successful in sending coherence from one nuclear transition to another, it never recovered the coherence back to the electron transition. To fix it, we modify the ENCT-2 sequence by adding two additional pulses on the second RF transition analogous to those of the original ENCT-1. The resulting ENCT-3 sequence is shown in Figure A.1.

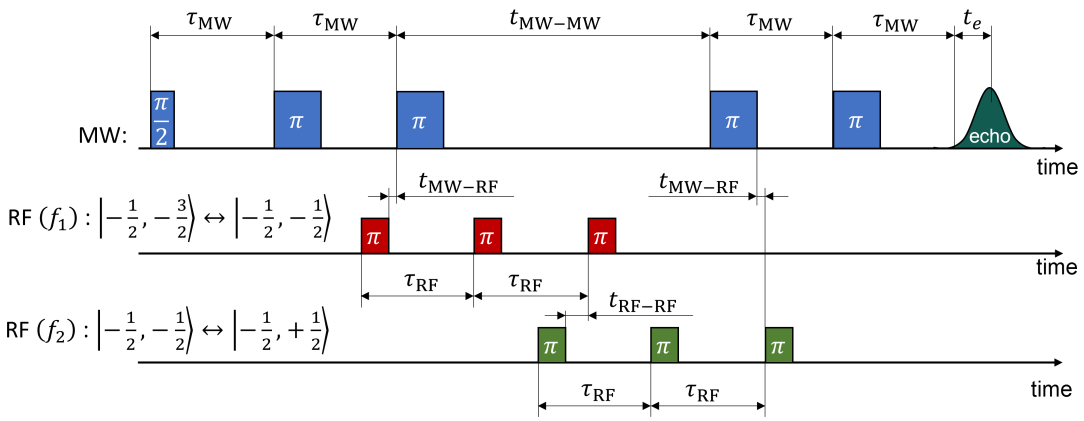

Figure A.1: ENCT-3 sequence.

First, ENCT-3 transforms the electron coherence to the nuclear coherence on transition $m_I : -3/2 \leftrightarrow -1/2$, then it transfers this coherence within the qudit to $m_I : -1/2 \leftrightarrow +1/2$, and finally it brings the coherence back to the electronic qubit for the spin-echo read-out. By analogy with the experiment in Figure 6.8, measuring the dependence of the read-out echo on the storage time reveals the phase coherence times for different nuclear qudit coherences. As shown in Figure A.2 we find that the phase memory time measured by ENCT-3 (1.31 ± 0.04 ms) matches the value found by the ENCT-1 sequence for $m_I : -1/2 \leftrightarrow +1/2$; this is exactly as we expect given that electronic T_{1e} processes are likely to be the dominant cause of the nuclear qudit de-phasing at this temperature.

These tests were accomplished on a sample different from that used in the main text of Chapter 6, and at a temperature of 30 K instead of 20 K. The purpose of the test was to check if the particular sequence of pulses that we designed was capable of transforming the coherence, storing it in the nuclear manifold and

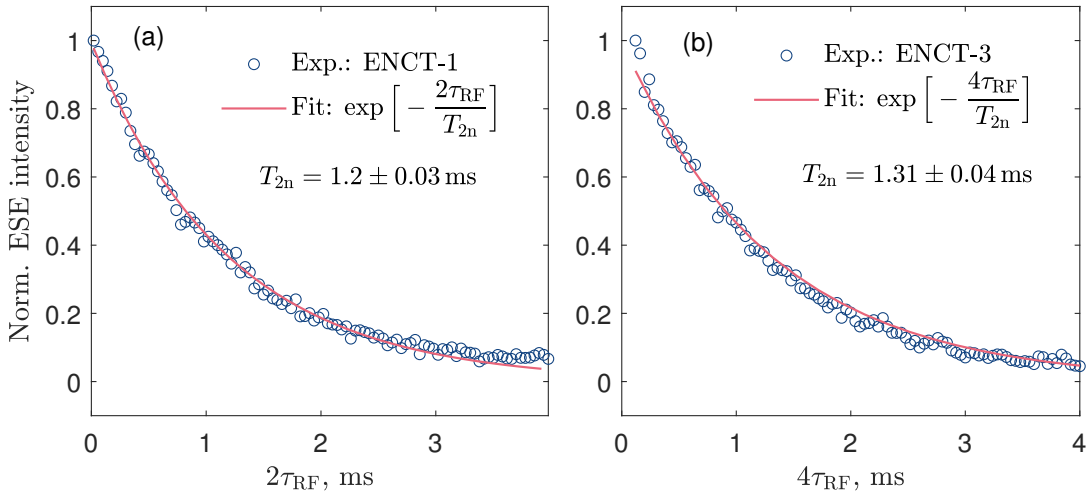

Figure A.2: Estimation of the nuclear spin-spin relaxation time at 30 K by means of (a) ENCT-1, and (b) ENCT-3 pulse sequences.

bringing it back to the electron manifold for measurement. Comparing the results of all three sequences, namely ENCT-1, ENCT-2 and ENCT-3, we conclude that the ENCT-3 sequence works as expected.

A.4.3 Phase shift induced by refocussing in ENCT-1

In order to ensure the effectiveness of manipulating coherence by the nuclear pulses in the ENCT-1 sequence, we have measured the phase of the final echo as a function of the phase θ of the nuclear refocussing π-pulse phase. As shown in Figure A.3, the echo gains an additional phase of 2θ in perfect agreement with Equation 2.79.

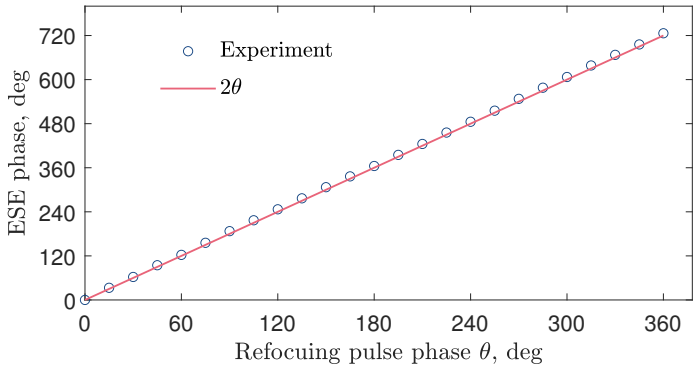

Figure A.3: The phase of the final electron spin echo as a function of the phase of the refocussing pulse in the ENCT-1 sequence.

A.4.4 Calibration of the artificial phase gate

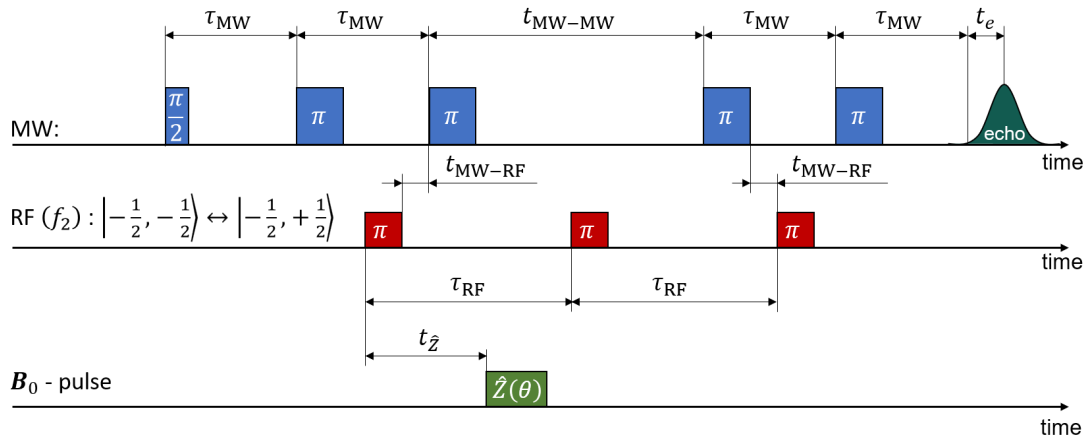

Figure A.4: Pulse sequence for the calibration of the artificial phase perturbation $\hat{Z}(\theta)$.

A controlled artificial phase perturbation, $\hat{Z}(\theta)$, was applied to investigate how the logical qubit evolves under a transient fluctuation of the magnetic field. This artificial phase perturbation is achieved by generating a transient magnetic field that is parallel to the static $\boldsymbol{B}_0$ field. We first calibrate $\hat{Z}(\theta)$ by measuring its effect on a standard nuclear coherence between two states.

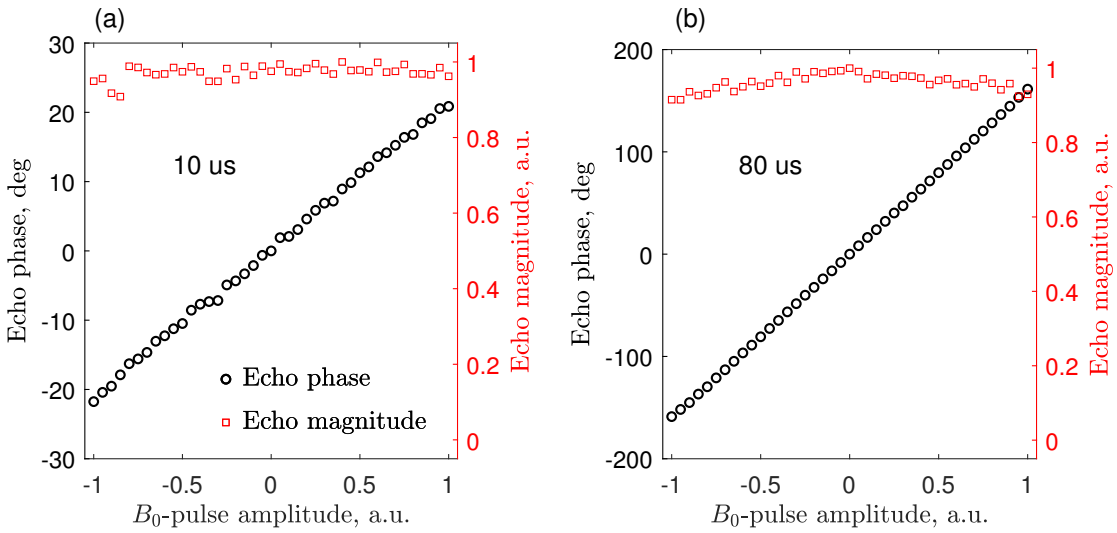

Figure A.5: The phase and the amplitude of the echo are measured while varying the amplitude of the B-field pulse $\hat{Z}(\theta)$ with a duration of 10 μs (a) and 80 μs (b).

The calibration sequence is shown in Figure A.4. The spin control pulses are the same as those in the ENCT-1 scheme(see Section 2.4.5) with a magnetic field

pulse $\hat{Z}(\theta)$ applied during the first free evolution period of the nuclear spin. Such a B-field pulse modifies the precession frequency for the nuclear spins, leading to a phase shift in the final echo. This effect is similar to that of the E-field pulses discussed in Chapters 4 and 5. The calibration results are shown in Figure A.5, for two values of the magnetic pulse duration 10 μs and 80 μs, and varying pulse amplitude. A linear phase dependence on the B-field pulse amplitude was observed for both pulse durations, with the effect of the 80 μs pulse approximately 8 times higher than that of the 10 μs pulse. The results confirm that the phase shift is proportional to both the duration and the amplitude of the applied B-field pulse. Furthermore, the amplitude of the echo remains stable throughout the experiment, with a maximum of 10% modulation observed for the strongest 80 μs B-field pulse. This confirms that the transient B-field applied during the pulse is reasonably homogeneous across the sample. Any inhomogeneity in this field would reduce the echo signal by introducing a phase distribution to the spin ensemble and damaging its coherence, similar to the processes described in Section A.4.5.4. This disturbance exists only during the B-field pulse, and therefore the decoherence of spins is not reversed by the refocussing pulse.

A.4.5 Full ENCT-8 sequence

Taking into account the static Hamiltonian 6.19, the propagators for electron and nuclear pulses with positive phases are

$$\hat{U}_{\mathrm{S}} = e^{-\mathrm{i}\theta\hat{S}_i} \tag{A.19a}$$

and

$$\hat{U}_{\mathrm{I}} = e^{\mathrm{i}\theta\hat{I}_i}. \tag{A.19b}$$

While applying the propagators, those components of the state vector for which the matrix has only zero entry in the corresponding line, should be left unchanged.

A.4.5.1 Encoding:

$$e^{-\mathrm{i}\frac{\pi}{2}S_x^{(14)}}\left|\psi\right\rangle(0)=\begin{pmatrix}\cos\left(\frac{\pi}{4}\right) & 0 & 0 & -\mathrm{i}\sin\left(\frac{\pi}{4}\right) & 0\\ 0 & 0 & 0 & 0 & 0\\ 0 & 0 & 0 & 0 & 0\\ -\mathrm{i}\sin\left(\frac{\pi}{4}\right) & 0 & 0 & \cos\left(\frac{\pi}{4}\right) & 0\\ 0 & 0 & 0 & 0 & 0\end{pmatrix}\begin{pmatrix}\mathrm{i}\\0\\0\\0\\0\end{pmatrix}=\frac{1}{\sqrt{2}}\begin{pmatrix}\mathrm{i}\\0\\0\\1\\0\end{pmatrix}=\begin{pmatrix}\alpha\\0\\0\\\beta\\0\end{pmatrix} \tag{A.20}$$

$$e^{-\mathrm{i}\pi S_x^{(14)}}\left|\psi\right\rangle=\begin{pmatrix}\cos\left(\frac{\pi}{2}\right) & 0 & 0 & -\mathrm{i}\sin\left(\frac{\pi}{2}\right) & 0\\ 0 & 0 & 0 & 0 & 0\\ 0 & 0 & 0 & 0 & 0\\ -\mathrm{i}\sin\left(\frac{\pi}{2}\right) & 0 & 0 & \cos\left(\frac{\pi}{2}\right) & 0\\ 0 & 0 & 0 & 0 & 0\end{pmatrix}\begin{pmatrix}\alpha\\0\\0\\\beta\\0\end{pmatrix}=\begin{pmatrix}-\mathrm{i}\beta\\0\\0\\-\mathrm{i}\alpha\\0\end{pmatrix} \tag{A.21}$$

$$e^{\mathrm{i}\pi I_x^{(34)}}\left|\psi\right\rangle=\begin{pmatrix}0 & 0 & 0 & 0 & 0\\ 0 & 0 & 0 & 0 & 0\\ 0 & 0 & \cos\left(\frac{\pi}{2}\right) & \mathrm{i}\sin\left(\frac{\pi}{2}\right) & 0\\ 0 & 0 & \mathrm{i}\sin\left(\frac{\pi}{2}\right) & \cos\left(\frac{\pi}{2}\right) & 0\\ 0 & 0 & 0 & 0 & 0\end{pmatrix}\begin{pmatrix}-\mathrm{i}\beta\\0\\0\\-\mathrm{i}\alpha\\0\end{pmatrix}=\begin{pmatrix}-\mathrm{i}\beta\\0\\\alpha\\0\\0\end{pmatrix} \tag{A.22}$$

$$e^{-\mathrm{i}\pi S_x^{(14)}}\left|\psi\right\rangle=\begin{pmatrix}\cos\left(\frac{\pi}{2}\right) & 0 & 0 & -\mathrm{i}\sin\left(\frac{\pi}{2}\right) & 0\\ 0 & 0 & 0 & 0 & 0\\ 0 & 0 & 0 & 0 & 0\\ -\mathrm{i}\sin\left(\frac{\pi}{2}\right) & 0 & 0 & \cos\left(\frac{\pi}{2}\right) & 0\\ 0 & 0 & 0 & 0 & 0\end{pmatrix}\begin{pmatrix}-\mathrm{i}\beta\\0\\\alpha\\0\\0\end{pmatrix}=\begin{pmatrix}0\\0\\\alpha\\-\beta\\0\end{pmatrix} \tag{A.23}$$

$$e^{\mathrm{i}\frac{\pi}{3}I_x^{(45)}}\left|\psi\right\rangle=\begin{pmatrix}0 & 0 & 0 & 0 & 0\\ 0 & 0 & 0 & 0 & 0\\ 0 & 0 & 0 & 0 & 0\\ 0 & 0 & 0 & \cos\left(\frac{\pi}{6}\right) & \mathrm{i}\sin\left(\frac{\pi}{6}\right)\\ 0 & 0 & 0 & \mathrm{i}\sin\left(\frac{\pi}{6}\right) & \cos\left(\frac{\pi}{6}\right)\end{pmatrix}\begin{pmatrix}0\\0\\\alpha\\-\beta\\0\end{pmatrix}=\begin{pmatrix}0\\0\\\alpha\\-\beta\sqrt{3}/2\\-\mathrm{i}\beta/2\end{pmatrix} \tag{A.24}$$

$$e^{\mathrm{i}\frac{\pi}{3}I_x^{(23)}}\left|\psi\right\rangle = \begin{pmatrix} 0 & 0 & 0 & 0 & 0 \\ 0 & \cos\left(\frac{\pi}{6}\right) & \mathrm{i}\sin\left(\frac{\pi}{6}\right) & 0 & 0 \\ 0 & \mathrm{i}\sin\left(\frac{\pi}{6}\right) & \cos\left(\frac{\pi}{6}\right) & 0 & 0 \\ 0 & 0 & 0 & 0 & 0 \\ 0 & 0 & 0 & 0 & 0 \end{pmatrix} \begin{pmatrix} 0 \\ 0 \\ \alpha \\ -\beta\sqrt{3}/2 \\ -\mathrm{i}\beta/2 \end{pmatrix} = \begin{pmatrix} 0 \\ \mathrm{i}\alpha/2 \\ \alpha\sqrt{3}/2 \\ -\beta\sqrt{3}/2 \\ -\mathrm{i}\beta/2 \end{pmatrix} \tag{A.25}$$

$$e^{\mathrm{i}(-\pi)I_x^{(34)}}\left|\psi\right\rangle = \begin{pmatrix} 0 & 0 & 0 & 0 & 0 \\ 0 & 0 & 0 & 0 & 0 \\ 0 & 0 & \cos\left(\frac{\pi}{2}\right) & -\mathrm{i}\sin\left(\frac{\pi}{2}\right) & 0 \\ 0 & 0 & -\mathrm{i}\sin\left(\frac{\pi}{2}\right) & \cos\left(\frac{\pi}{2}\right) & 0 \\ 0 & 0 & 0 & 0 & 0 \end{pmatrix} = \begin{pmatrix} 0 \\ \mathrm{i}\alpha/2 \\ \alpha\sqrt{3}/2 \\ -\beta\sqrt{3}/2 \\ -\mathrm{i}\beta/2 \end{pmatrix} = \begin{pmatrix} 0 \\ \mathrm{i}\alpha/2 \\ \mathrm{i}\beta\sqrt{3}/2 \\ -\mathrm{i}\alpha\sqrt{3}/2 \\ -\mathrm{i}\beta/2 \end{pmatrix} \tag{A.26}$$

A.4.5.2 1st free evolution period

$$\begin{pmatrix} 0 \\ \alpha/2 \\ \beta\sqrt{3}/2 \\ -\alpha\sqrt{3}/2 \\ -\beta/2 \end{pmatrix} \xrightarrow{\tau\hat{\mathcal{H}}} \begin{pmatrix} 0 \\ [\alpha/2]e^{-\mathrm{i}\tau\epsilon_3/\hbar} \\ [\beta\sqrt{3}/2]e^{-\mathrm{i}\tau\epsilon_2/\hbar} \\ -[\alpha\sqrt{3}/2]e^{-\mathrm{i}\tau\epsilon_1/\hbar} \\ -[\beta/2]e^{-\mathrm{i}\tau\epsilon_0/\hbar} \end{pmatrix} = e^{-\mathrm{i}\tau\epsilon_0/\hbar} \begin{pmatrix} 0 \\ [\alpha/2]e^{-\mathrm{i}\tau\Omega_3} \\ [\beta\sqrt{3}/2]e^{-\mathrm{i}\tau\Omega_2} \\ -[\alpha\sqrt{3}/2]e^{-\mathrm{i}\tau\Omega_1} \\ -[\beta/2] \end{pmatrix}, \tag{A.27}$$

where $\Omega_i = (\epsilon_i - \epsilon_0)/\hbar$.

A.4.5.3 Artificial phase error $\hat{Z}(\theta)$

$$\begin{pmatrix} 0 \\ [\alpha/2]e^{-\mathrm{i}\tau\Omega_3} \\ [\beta\sqrt{3}/2]e^{-\mathrm{i}\tau\Omega_2} \\ -[\alpha\sqrt{3}/2]e^{-\mathrm{i}\tau\Omega_1} \\ -[\beta/2] \end{pmatrix} = \begin{pmatrix} 0 \\ \Phi(+\frac{3}{2})[\alpha/2]e^{-\mathrm{i}\tau\Omega_3} \\ \Phi(+\frac{1}{2})[\beta\sqrt{3}/2]e^{-\mathrm{i}\tau\Omega_2} \\ -\Phi(-\frac{1}{2})[\alpha\sqrt{3}/2]e^{-\mathrm{i}\tau\Omega_1} \\ -\Phi(-\frac{3}{2})[\beta/2] \end{pmatrix} \tag{A.28}$$

Disregarding the global phase, let this state be equal to

$$\begin{pmatrix} 0 \\ \xi \\ \zeta \\ \eta \\ \lambda \end{pmatrix}. \tag{A.29}$$

A.4.5.4 Refocusing

$$5) e^{\mathrm{i}(+\pi)I_x^{(34)}}|\psi\rangle = \begin{pmatrix} 0 & 0 & 0 & 0 & 0 \\ 0 & 0 & 0 & 0 & 0 \\ 0 & 0 & \cos\left(\frac{\pi}{2}\right) & \mathrm{i}\sin\left(\frac{\pi}{2}\right) & 0 \\ 0 & 0 & \mathrm{i}\sin\left(\frac{\pi}{2}\right) & \cos\left(\frac{\pi}{2}\right) & 0 \\ 0 & 0 & 0 & 0 & 0 \end{pmatrix} \begin{pmatrix} 0 \\ \xi \\ \zeta \\ \eta \\ \lambda \end{pmatrix} = \begin{pmatrix} 0 \\ \xi \\ \mathrm{i}\eta \\ \mathrm{i}\zeta \\ \lambda \end{pmatrix} \tag{A.30}$$

$$6) e^{\mathrm{i}(\pm\pi)I_x^{(45)}}|\psi\rangle = \begin{pmatrix} 0 & 0 & 0 & 0 & 0 \\ 0 & 0 & 0 & 0 & 0 \\ 0 & 0 & 0 & 0 & 0 \\ 0 & 0 & 0 & \cos\left(\frac{\pi}{2}\right) & \pm\mathrm{i}\sin\left(\frac{\pi}{2}\right) \\ 0 & 0 & 0 & \pm\mathrm{i}\sin\left(\frac{\pi}{2}\right) & \cos\left(\frac{\pi}{2}\right) \end{pmatrix} \begin{pmatrix} 0 \\ \xi \\ \mathrm{i}\eta \\ \mathrm{i}\zeta \\ \lambda \end{pmatrix} = \begin{pmatrix} 0 \\ \xi \\ \mathrm{i}\eta \\ \pm\mathrm{i}\lambda \\ \mp\zeta \end{pmatrix} \tag{A.31}$$

$$7) e^{\mathrm{i}(+\pi)I_x^{(23)}}|\psi\rangle = \begin{pmatrix} 0 & 0 & 0 & 0 & 0 \\ 0 & \cos\left(\frac{\pi}{2}\right) & \mathrm{i}\sin\left(\frac{\pi}{2}\right) & 0 & 0 \\ 0 & \mathrm{i}\sin\left(\frac{\pi}{2}\right) & \cos\left(\frac{\pi}{2}\right) & 0 & 0 \\ 0 & 0 & 0 & 0 & 0 \\ 0 & 0 & 0 & 0 & 0 \end{pmatrix} \begin{pmatrix} 0 \\ \xi \\ \mathrm{i}\eta \\ \pm\mathrm{i}\lambda \\ \mp\zeta \end{pmatrix} = \begin{pmatrix} 0 \\ -\eta \\ \mathrm{i}\xi \\ \pm\mathrm{i}\lambda \\ \mp\zeta \end{pmatrix} \tag{A.32}$$

$$8) \quad e^{\mathrm{i}(+\pi)I_x^{(34)}}|\psi\rangle = \begin{pmatrix} 0 & 0 & 0 & 0 & 0 \\ 0 & 0 & 0 & 0 & 0 \\ 0 & 0 & \cos\left(\frac{\pi}{2}\right) & \mathrm{i}\sin\left(\frac{\pi}{2}\right) & 0 \\ 0 & 0 & \mathrm{i}\sin\left(\frac{\pi}{2}\right) & \cos\left(\frac{\pi}{2}\right) & 0 \\ 0 & 0 & 0 & 0 & 0 \end{pmatrix} \begin{pmatrix} 0 \\ -\eta \\ \mathrm{i}\xi \\ \pm\mathrm{i}\lambda \\ \mp\zeta \end{pmatrix} = \begin{pmatrix} 0 \\ -\eta \\ \mp\lambda \\ -\xi \\ \mp\zeta \end{pmatrix} \tag{A.33}$$

$$9) \quad e^{\mathrm{i}(\pm\pi)I_x^{(45)}}|\psi\rangle = \begin{pmatrix} 0 & 0 & 0 & 0 & 0 \\ 0 & 0 & 0 & 0 & 0 \\ 0 & 0 & 0 & 0 & 0 \\ 0 & 0 & 0 & \cos\left(\frac{\pi}{2}\right) & \pm\mathrm{i}\sin\left(\frac{\pi}{2}\right) \\ 0 & 0 & 0 & \pm\mathrm{i}\sin\left(\frac{\pi}{2}\right) & \cos\left(\frac{\pi}{2}\right) \end{pmatrix} \begin{pmatrix} 0 \\ -\eta \\ \mp\lambda \\ -\xi \\ \mp\zeta \end{pmatrix} = \begin{pmatrix} 0 \\ -\eta \\ \mp\lambda \\ -\mathrm{i}\zeta \\ \mp\mathrm{i}\xi \end{pmatrix} \tag{A.34}$$

$$10)\quad e^{\mathrm{i}(\pm\pi)I_x^{(23)}}\,|\psi\rangle = \begin{pmatrix} 0 & 0 & 0 & 0 & 0 \\ 0 & \cos\left(\frac{\pi}{2}\right) & \pm\mathrm{i}\sin\left(\frac{\pi}{2}\right) & 0 & 0 \\ 0 & \pm\mathrm{i}\sin\left(\frac{\pi}{2}\right) & \cos\left(\frac{\pi}{2}\right) & 0 & 0 \\ 0 & 0 & 0 & 0 & 0 \\ 0 & 0 & 0 & 0 & 0 \end{pmatrix} \begin{pmatrix} 0 \\ -\eta \\ \mp\lambda \\ -\mathrm{i}\zeta \\ \mp\mathrm{i}\xi \end{pmatrix} = \begin{pmatrix} 0 \\ -\mathrm{i}\lambda \\ \mp\mathrm{i}\eta \\ -\mathrm{i}\zeta \\ \mp\mathrm{i}\xi \end{pmatrix} \tag{A.35}$$

$$11)\quad e^{\mathrm{i}(-\pi)I_x^{(34)}}\,|\psi\rangle = \begin{pmatrix} 0 & 0 & 0 & 0 & 0 \\ 0 & 0 & 0 & 0 & 0 \\ 0 & 0 & \cos\left(\frac{\pi}{2}\right) & -\mathrm{i}\sin\left(\frac{\pi}{2}\right) & 0 \\ 0 & 0 & -\mathrm{i}\sin\left(\frac{\pi}{2}\right) & \cos\left(\frac{\pi}{2}\right) & 0 \\ 0 & 0 & 0 & 0 & 0 \end{pmatrix} \begin{pmatrix} 0 \\ -\mathrm{i}\lambda \\ \mp\mathrm{i}\eta \\ -\mathrm{i}\zeta \\ \mp\mathrm{i}\xi \end{pmatrix} = \begin{pmatrix} 0 \\ -\mathrm{i}\lambda \\ -\zeta \\ \mp\eta \\ \mp\mathrm{i}\xi \end{pmatrix} \tag{A.36}$$

$$12)\quad e^{\mathrm{i}(+\pi)I_x^{(34)}}\,|\psi\rangle = \begin{pmatrix} 0 & 0 & 0 & 0 & 0 \\ 0 & 0 & 0 & 0 & 0 \\ 0 & 0 & \cos\left(\frac{\pi}{2}\right) & \mathrm{i}\sin\left(\frac{\pi}{2}\right) & 0 \\ 0 & 0 & \mathrm{i}\sin\left(\frac{\pi}{2}\right) & \cos\left(\frac{\pi}{2}\right) & 0 \\ 0 & 0 & 0 & 0 & 0 \end{pmatrix} \begin{pmatrix} 0 \\ -\mathrm{i}\lambda \\ -\zeta \\ \mp\eta \\ \mp\mathrm{i}\xi \end{pmatrix} = \begin{pmatrix} 0 \\ -\mathrm{i}\lambda \\ \mp\mathrm{i}\eta \\ -\mathrm{i}\zeta \\ \mp\mathrm{i}\xi \end{pmatrix} \tag{A.37}$$

Removing the global phase $e^{i\pi/2}$ and turning back to α and β

$$\begin{pmatrix} 0 \\ -\lambda \\ \mp\eta \\ -\zeta \\ \mp\xi \end{pmatrix} = \begin{pmatrix} 0 \\ \Phi(-\frac{3}{2})[\beta/2] \\ \pm\Phi(-\frac{1}{2})[\alpha\sqrt{3}/2]e^{-\mathrm{i}\tau\Omega_1} \\ -\Phi(+\frac{1}{2})[\beta\sqrt{3}/2]e^{-\mathrm{i}\tau\Omega_2} \\ \mp\Phi(+\frac{3}{2})[\alpha/2]e^{-\mathrm{i}\tau\Omega_3} \end{pmatrix} \tag{A.38}$$

A.4.5.5 2nd free evolution period

$$\begin{pmatrix} 0 \\ \Phi(-\frac{3}{2})[\beta/2] \\ \pm\Phi(-\frac{1}{2})[\alpha\sqrt{3}/2]e^{-\mathrm{i}\tau\Omega_1} \\ -\Phi(+\frac{1}{2})[\beta\sqrt{3}/2]e^{-\mathrm{i}\tau\Omega_2} \\ \mp\Phi(+\frac{3}{2})[\alpha/2]e^{-\mathrm{i}\tau\Omega_3} \end{pmatrix} \xrightarrow{\tau\hat{\mathcal{H}}} \begin{pmatrix} 0 \\ \Phi(-\frac{3}{2})[\beta/2]e^{-\mathrm{i}\tau\Omega_3} \\ \pm\Phi(-\frac{1}{2})[\alpha\sqrt{3}/2]e^{-\mathrm{i}\tau(\Omega_1+\Omega_2)} \\ -\Phi(+\frac{1}{2})[\beta\sqrt{3}/2]e^{-\mathrm{i}\tau(\Omega_2+\Omega_1)} \\ \mp\Phi(+\frac{3}{2})[\alpha/2]e^{-\mathrm{i}\tau\Omega_3} \end{pmatrix} \tag{A.39}$$

The coherences on transitions $(3,4)$ and $(2,5)$ have the same global phase and can be transferred for read-out to the electron manifold using the decoding sequence.

A.4.5.6 Decoding

Let us introduce a short notation again:

$$\begin{pmatrix} 0 \\ \Phi(-\frac{3}{2})[\beta/2]e^{-\mathrm{i}\tau\Omega_3} \\ \pm\Phi(-\frac{1}{2})[\alpha\sqrt{3}/2]e^{-\mathrm{i}\tau(\Omega_1+\Omega_2)} \\ -\Phi(+\frac{1}{2})[\beta\sqrt{3}/2]e^{-\mathrm{i}\tau(\Omega_2+\Omega_1)} \\ \mp\Phi(+\frac{3}{2})[\alpha/2]e^{-\mathrm{i}\tau\Omega_3} \end{pmatrix} = \begin{pmatrix} 0, \\ \lambda \\ \eta \\ \zeta \\ \xi \end{pmatrix} \tag{A.40}$$

$$13) \quad e^{\mathrm{i}(+\pi)I_x^{(34)}}|\psi\rangle = \begin{pmatrix} 0 & 0 & 0 & 0 & 0 \\ 0 & 0 & 0 & 0 & 0 \\ 0 & 0 & \cos\left(\frac{\pi}{2}\right) & \mathrm{i}\sin\left(\frac{\pi}{2}\right) & 0 \\ 0 & 0 & \mathrm{i}\sin\left(\frac{\pi}{2}\right) & \cos\left(\frac{\pi}{2}\right) & 0 \\ 0 & 0 & 0 & 0 & 0 \end{pmatrix} \begin{pmatrix} 0, \\ \lambda \\ \eta \\ \zeta \\ \xi \end{pmatrix} = \begin{pmatrix} 0, \\ \lambda \\ \mathrm{i}\zeta \\ \mathrm{i}\eta \\ \xi \end{pmatrix} \tag{A.41}$$

From here, the decoding path divides into two. The first one does not contain pulses 14 and 15:

Measuring I_1

$$e^{-\mathrm{i}\pi S_x^{(14)}}|\psi\rangle = \begin{pmatrix} \cos\left(\frac{\pi}{2}\right) & 0 & 0 & -\mathrm{i}\sin\left(\frac{\pi}{2}\right) & 0 \\ 0 & 0 & 0 & 0 & 0 \\ 0 & 0 & 0 & 0 & 0 \\ -\mathrm{i}\sin\left(\frac{\pi}{2}\right) & 0 & 0 & \cos\left(\frac{\pi}{2}\right) & 0 \\ 0 & 0 & 0 & 0 & 0 \end{pmatrix} \begin{pmatrix} 0, \\ \lambda \\ \mathrm{i}\zeta \\ \mathrm{i}\eta \\ \xi \end{pmatrix} = \begin{pmatrix} \eta, \\ \lambda \\ \mathrm{i}\zeta \\ 0 \\ \xi \end{pmatrix} \tag{A.42}$$

$$16) \quad e^{\mathrm{i}(+\pi)I_x^{(34)}}|\psi\rangle = \begin{pmatrix} 0 & 0 & 0 & 0 & 0 \\ 0 & 0 & 0 & 0 & 0 \\ 0 & 0 & \cos\left(\frac{\pi}{2}\right) & \mathrm{i}\sin\left(\frac{\pi}{2}\right) & 0 \\ 0 & 0 & \mathrm{i}\sin\left(\frac{\pi}{2}\right) & \cos\left(\frac{\pi}{2}\right) & 0 \\ 0 & 0 & 0 & 0 & 0 \end{pmatrix} \begin{pmatrix} \eta, \\ \lambda \\ \mathrm{i}\zeta \\ 0 \\ \xi \end{pmatrix} = \begin{pmatrix} \eta, \\ \lambda \\ 0 \\ -\zeta \\ \xi \end{pmatrix} \tag{A.43}$$

$$e^{-\mathrm{i}\pi S_x^{(14)}}\,|\psi\rangle = \begin{pmatrix} \cos\left(\frac{\pi}{2}\right) & 0 & 0 & -\mathrm{i}\sin\left(\frac{\pi}{2}\right) & 0 \\ 0 & 0 & 0 & 0 & 0 \\ 0 & 0 & 0 & 0 & 0 \\ -\mathrm{i}\sin\left(\frac{\pi}{2}\right) & 0 & 0 & \cos\left(\frac{\pi}{2}\right) & 0 \\ 0 & 0 & 0 & 0 & 0 \end{pmatrix} \begin{pmatrix} \eta, \\ \lambda \\ 0 \\ -\zeta \\ \xi \end{pmatrix} = \begin{pmatrix} \mathrm{i}\zeta, \\ \lambda \\ 0 \\ -\mathrm{i}\eta \\ \xi \end{pmatrix} \tag{A.44}$$

Thus, the measured electron coherence is

$$\begin{pmatrix} \mathrm{i}\zeta \\ -\mathrm{i}\eta \end{pmatrix} = \begin{pmatrix} -\mathrm{i}\Phi(+\frac{1}{2})[\beta\sqrt{3}/2]e^{-\mathrm{i}\tau(\Omega_2+\Omega_1)} \\ \mp\mathrm{i}\Phi(-\frac{1}{2})[\alpha\sqrt{3}/2]e^{-\mathrm{i}\tau(\Omega_1+\Omega_2)} \end{pmatrix} \rightarrow \frac{\sqrt{3}}{2}\begin{pmatrix} \Phi\left(+\frac{1}{2}\right)\beta \\ \pm\Phi\left(-\frac{1}{2}\right)\alpha \end{pmatrix} \tag{A.45}$$

Measuring I_2

$$14)\quad e^{\mathrm{i}(+\pi)I_x^{(45)}}\,|\psi\rangle = \begin{pmatrix} 0 & 0 & 0 & 0 & 0 \\ 0 & 0 & 0 & 0 & 0 \\ 0 & 0 & 0 & 0 & 0 \\ 0 & 0 & 0 & \cos\left(\frac{\pi}{2}\right) & \mathrm{i}\sin\left(\frac{\pi}{2}\right) \\ 0 & 0 & 0 & \mathrm{i}\sin\left(\frac{\pi}{2}\right) & \cos\left(\frac{\pi}{2}\right) \end{pmatrix} \begin{pmatrix} 0, \\ \lambda \\ \mathrm{i}\zeta \\ \mathrm{i}\eta \\ \xi \end{pmatrix} = \begin{pmatrix} 0, \\ \lambda \\ \mathrm{i}\zeta \\ \mathrm{i}\xi \\ -\eta \end{pmatrix} \tag{A.46}$$

$$15)\quad e^{\mathrm{i}(+\pi)I_x^{(23)}}\,|\psi\rangle = \begin{pmatrix} 0 & 0 & 0 & 0 & 0 \\ 0 & \cos\left(\frac{\pi}{2}\right) & \mathrm{i}\sin\left(\frac{\pi}{2}\right) & 0 & 0 \\ 0 & \mathrm{i}\sin\left(\frac{\pi}{2}\right) & \cos\left(\frac{\pi}{2}\right) & 0 & 0 \\ 0 & 0 & 0 & 0 & 0 \\ 0 & 0 & 0 & 0 & 0 \end{pmatrix} \begin{pmatrix} 0, \\ \lambda \\ \mathrm{i}\zeta \\ \mathrm{i}\xi \\ -\eta \end{pmatrix} = \begin{pmatrix} 0, \\ -\zeta \\ \mathrm{i}\lambda \\ \mathrm{i}\xi \\ -\eta \end{pmatrix} \tag{A.47}$$

The rest is the same as for I_1:

$$e^{-\mathrm{i}\pi S_x^{(14)}}\,|\psi\rangle = \begin{pmatrix} \cos\left(\frac{\pi}{2}\right) & 0 & 0 & -\mathrm{i}\sin\left(\frac{\pi}{2}\right) & 0 \\ 0 & 0 & 0 & 0 & 0 \\ 0 & 0 & 0 & 0 & 0 \\ -\mathrm{i}\sin\left(\frac{\pi}{2}\right) & 0 & 0 & \cos\left(\frac{\pi}{2}\right) & 0 \\ 0 & 0 & 0 & 0 & 0 \end{pmatrix} \begin{pmatrix} 0, \\ -\zeta \\ \mathrm{i}\lambda \\ \mathrm{i}\xi \\ -\eta \end{pmatrix} = \begin{pmatrix} \xi, \\ -\zeta \\ \mathrm{i}\lambda \\ 0 \\ -\eta \end{pmatrix} \tag{A.48}$$

$$16)\quad e^{\mathrm{i}(+\pi)I_x^{(34)}}\,|\psi\rangle = \begin{pmatrix} 0 & 0 & 0 & 0 & 0 \\ 0 & 0 & 0 & 0 & 0 \\ 0 & 0 & \cos\left(\frac{\pi}{2}\right) & \mathrm{i}\sin\left(\frac{\pi}{2}\right) & 0 \\ 0 & 0 & \mathrm{i}\sin\left(\frac{\pi}{2}\right) & \cos\left(\frac{\pi}{2}\right) & 0 \\ 0 & 0 & 0 & 0 & 0 \end{pmatrix} \begin{pmatrix} \xi, \\ -\zeta \\ \mathrm{i}\lambda \\ 0 \\ -\eta \end{pmatrix} = \begin{pmatrix} \xi, \\ -\zeta \\ 0 \\ -\lambda \\ -\eta \end{pmatrix} \tag{A.49}$$

$$e^{-\mathrm{i}\pi S_x^{(14)}}\,|\psi\rangle = \begin{pmatrix} \cos\left(\frac{\pi}{2}\right) & 0 & 0 & -\mathrm{i}\sin\left(\frac{\pi}{2}\right) & 0 \\ 0 & 0 & 0 & 0 & 0 \\ 0 & 0 & 0 & 0 & 0 \\ -\mathrm{i}\sin\left(\frac{\pi}{2}\right) & 0 & 0 & \cos\left(\frac{\pi}{2}\right) & 0 \\ 0 & 0 & 0 & 0 & 0 \end{pmatrix} \begin{pmatrix} \xi, \\ -\zeta \\ 0 \\ -\lambda \\ -\eta \end{pmatrix} = \begin{pmatrix} \mathrm{i}\lambda, \\ -\zeta \\ 0 \\ -\mathrm{i}\xi \\ -\eta \end{pmatrix} \tag{A.50}$$

Thus, the measured electron coherence is

$$\begin{pmatrix} \mathrm{i}\lambda \\ -\mathrm{i}\xi \end{pmatrix} = \begin{pmatrix} \mathrm{i}\Phi(-\frac{3}{2})[\beta/2]e^{-\mathrm{i}\tau\Omega_3} \\ \pm\mathrm{i}\Phi(+\frac{3}{2})[\alpha/2]e^{-\mathrm{i}\tau\Omega_3} \end{pmatrix} \rightarrow \frac{1}{2}\begin{pmatrix} \Phi\left(-\frac{3}{2}\right)\beta \\ \pm\Phi\left(+\frac{3}{2}\right)\alpha \end{pmatrix} \tag{A.51}$$

A.4.6 Phase cycling of ENCT-8

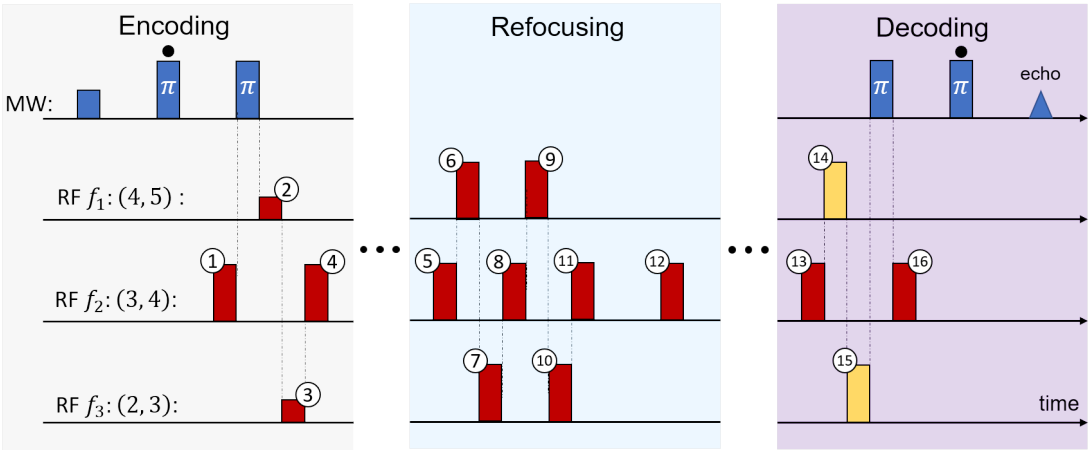

Figure A.6: The numbering of the pulses within the ENCT-8 sequence design for demonstrating the quantum error correction. The MW refocussing pulses are labelled with •. The MW pulses are aligned to the RF pulse 1 and 16 as indicated by the vertical dashed lines. The parameters of each RF pulse are presented in Table A.1.

Here we discuss the details of measuring the error-correcting sequence ENCT-8 from Section 6.5, whose simplified version is presented in Figure A.6. Table A.1

Pulse #	Frequency	Position	Ampl. & phase
1	f_2	0	$+\pi$
2	f_1	U	$+\pi/3$
3	f_3	$2U$	$+\pi/3$
4	f_2	$3U$	$-\pi$
5	f_2	$3U+\tau$	$+\pi$
6	f_1	$4U+\tau$	$\pm\pi$
7	f_3	$5U+\tau$	$+\pi$
8	f_2	$6U+\tau$	$+\pi$
9	f_1	$7U+\tau$	$\pm\pi$
10	f_3	$8U+\tau$	$\pm\pi$
11	f_2	$9U+\tau$	$-\pi$
12	f_2	$15U+\tau$	$+\pi$
13	f_2	$9U+2\tau$	$+\pi$
14	f_1	$10U+2\tau$	$+\pi$
15	f_3	$11U+2\tau$	$+\pi$
16	f_2	$12U+2\tau$	$+\pi$

Table A.1: Parameters for the RF pulses used in the phase cycling of the quantum error correction sequence ENCT-8.

shows the exact position of all RF pulses involved in the fault tolerant memory sequence. In experiment, we must account for the finite duration of the RF pulses and the ring down behaviour of the RF coil. To compensate for these effects, we introduced small delays between consecutive RF pulses, not shown in the diagram (though, see $t_{\mathrm{RF-RF}}$ in Figure 6.3, for instance). Together, this pause and the actual pulse duration compose the RF pulse unit U used in the table.

The phase of pulses 6, 9 and 10 is alternated between $+\pi$ and $-\pi$, which together with varying the phase of the first MW $\pi/2$-pulse, produces a four step phase cycling that reduces undesired echo contributions, similar to that of the ENCT-1 sequence discussed in Section 2.4.5.

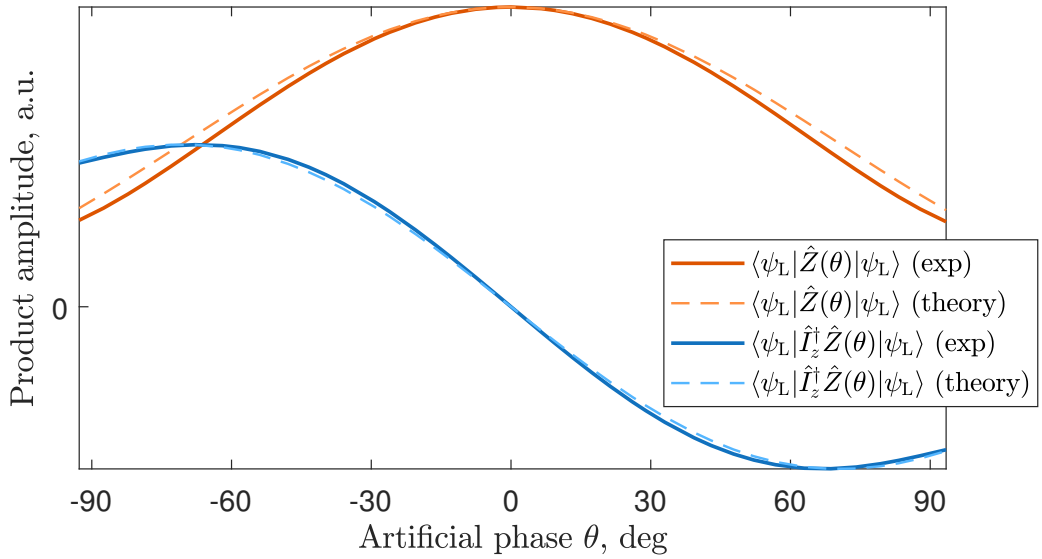

Figure A.7: Solid lines: Estimates of the quantities $\langle\psi_L|\hat{Z}(\theta)|\psi_L\rangle$ and $\langle\psi_L|\hat{I}_z^\dagger\hat{Z}(\theta)|\psi_L\rangle$ extracted from the parametrised fit to the experimental data. Dashed lines: exact theoretical evolution of the same quantities.

A.4.7 Overlap of logical qubit and error component with artificial error

In Figure A.7, we present the overlap of logical qubit $\langle\psi_L|\hat{Z}(\theta)|\psi_L\rangle$ and the error component $\langle\psi_L|\hat{I}_z^\dagger\hat{Z}(\theta)|\psi_L\rangle$ obtained (1) by theoretical calculation (dashed lines) and (2) from the fitting of experimental data (solid lines), as a function of the artificial error θ that we applied. The experimental curves were constructed from the fitting parameters A_n, $n = 0\ldots5$, while the theoretical curves were built using $A_n = 1$. In agreement with the results presented in Figure 6.13, for small θ, $\langle\psi_L|\hat{Z}(\theta)|\psi_L\rangle$ is independent of θ and $\langle\psi_L|\hat{I}_z^\dagger\hat{Z}(\theta)|\psi_L\rangle$ varies linearly with θ. This demonstrates the general point that using the parametrisation, we can explore the evolution of physically meaningful quantities that we cannot measure directly.

References

1. Chuang, I. L., Gershenfeld, N. & Kubinec, M. Experimental Implementation of Fast Quantum Searching. *Physical Review Letters* **80,** 3408–3411. doi:10.1103/PhysRevLett.80.3408 (1998).
2. Atom Computing. *Quantum startup Atom Computing first to exceed 1,000 qubits* https://atom-computing.com/quantum-startup-atom-computing-first-to-exceed-1000-qubits/. Accessed: April 28, 2025. (2023).
3. Castelvecchi, D. IBM releases first-ever 1,000-qubit quantum chip. *Nature* **624,** 238. https://www.nature.com/articles/d41586-023-03854-1 (2025).
4. Wikipedia contributors. *List of quantum processors — Wikipedia, The Free Encyclopedia* [Online; accessed 30-July-2025]. (2025). https://en.wikipedia.org/w/index.php?title=List_of_quantum_processors&oldid=1302874632.
5. Slussarenko, S. & Pryde, G. J. Photonic quantum information processing: A concise review. *Applied Physics Reviews* **6,** 041303. doi:10.1063/1.5115814 (2019).
6. Flamini, F., Spagnolo, N. & Sciarrino, F. Photonic quantum information processing: A review. *Reports on Progress in Physics* **82,** 016001. doi:10.1088/1361-6633/aad5b2 (2019).
7. Knill, E., Laflamme, R. & Milburn, G. J. A scheme for efficient quantum computation with linear optics. *Nature* **409,** 46–52. doi:10.1038/35051009 (2001).
8. Madsen, L. S. *et al.* Quantum computational advantage with a programmable photonic processor. *Nature* **606,** 75–81. doi:10.1038/s41586-022-04725-x (2022).
9. Häffner, H., Roos, C. F. & Blatt, R. Quantum computing with trapped ions. *Physics Reports* **469,** 155–203. doi:10.1016/j.physrep.2008.09.003 (2008).
10. Bernardini, F., Chakraborty, A. & Ordóñez, C. R. Quantum computing with trapped ions: a beginner's guide. *European Journal of Physics* **45,** 013001. doi:10.1088/1361-6404/ad06be (2024).
11. Schäfer, V. M. *et al.* Fast quantum logic gates with trapped-ion qubits. *Nature* **555,** 75–78. doi:10.1038/nature25737 (2018).
12. Blatt, R. & Wineland, D. Entangled states of trapped atomic ions. *Nature* **453,** 1008–1015. doi:10.1038/nature07125 (2008).
13. Jones, J. A. Quantum computing with NMR. *Progress in Nuclear Magnetic Resonance Spectroscopy* **59,** 91–120. doi:10.1016/j.pnmrs.2010.11.001 (2011).
14. Pla, J. J. *et al.* A single-atom electron spin qubit in silicon. *Nature* **489,** 541–545. doi:10.1038/nature11449 (2012).

15. Steger, M. *et al.* Quantum Information Storage for over 180 s Using Donor Spins in a 28 Si "Semiconductor Vacuum". *Science* **336,** 1280–1283. doi:10.1126/science.1217635 (2012).

16. Morley, G. W. *et al.* The initialization and manipulation of quantum information stored in silicon by bismuth dopants. *Nature Materials* **9,** 725–729. doi:10.1038/nmat2828 (2010).

17. Mayländer, M., Chen, S., Lorenzo, E. R., Wasielewski, M. R. & Richert, S. Exploring Photogenerated Molecular Quartet States as Spin Qubits and Qudits. *Journal of the American Chemical Society* **143,** 7050–7058. doi:10.1021/jacs.1c01620 (2021).

18. Hanson, R. & Awschalom, D. D. Coherent manipulation of single spins in semiconductors. *Nature* **453,** 1043–1049. doi:10.1038/nature07129 (2008).

19. Loss, D. & DiVincenzo, D. P. Quantum computation with quantum dots. *Physical Review A - Atomic, Molecular, and Optical Physics* **57,** 120–126. doi:10.1103/PhysRevA.57.120 (1998).

20. Dutt, M. V. G. *et al.* Quantum Register Based on Individual Electronic and Nuclear Spin Qubits in Diamond. *Science* **316,** 1312–1316. doi:10.1126/science.1139831 (2007).

21. Maurer, P. C. *et al.* Room-Temperature Quantum Bit Memory Exceeding One Second. *Science* **336,** 1283–1286. doi:10.1126/science.1220513 (2012).

22. Gulka, M. *et al.* Room-temperature control and electrical readout of individual nitrogen-vacancy nuclear spins. *Nature Communications* **12,** 4421. doi:10.1038/s41467-021-24494-x (2021).

23. Kjaergaard, M. *et al.* Superconducting Qubits: Current State of Play. *Annual Review of Condensed Matter Physics* **11,** 369–395. doi:10.1146/annurev-conmatphys-031119-050605 (2020).

24. Nayak, C., Simon, S. H., Stern, A., Freedman, M. & Sarma, S. D. Non-Abelian anyons and topological quantum computation. *Reviews of Modern Physics* **80,** 1083–1159. doi:10.1103/RevModPhys.80.1083 (2008).

25. Beenakker, C. W. Random-matrix theory of Majorana fermions and topological superconductors. *Reviews of Modern Physics* **87,** 1037–1066. doi:10.1103/RevModPhys.87.1037 (2015).

26. Nielsen, M. A. & Chuang, I. L. *Quantum computation and quantum information* 10th anniversary ed. (Cambridge University Press, Cambridge, 2010).

27. Jones, J. A. & Jaksch, D. *Quantum Information, Computation and Communication* (Cambridge University Press, United Kingdom, 2012).

28. Ladd, T. D. *et al.* Quantum computers. *Nature* **464,** 45–53. doi:10.1038/nature08812 (2010).

29. Moreno-Pineda, E., Godfrin, C., Balestro, F., Wernsdorfer, W. & Ruben, M. Molecular spin qudits for quantum algorithms. *Chemical Society Reviews* **47,** 501–513. doi:10.1039/C5CS00933B (2018).

30. Coronado, E. Molecular magnetism: from chemical design to spin control in molecules, materials and devices. *Nature Reviews Materials* **5,** 87–104. doi:10.1038/s41578-019-0146-8 (2020).

31. Leuenberger, M. N. & Loss, D. Quantum computing in molecular magnets. *Nature* **410,** 789–793. doi:10.1038/35071024 (2001).

32. Tejada, J., Chudnovsky, E. M., del Barco, E., Hernandez, J. M. & Spiller, T. P. Magnetic qubits as hardware for quantum computers. *Nanotechnology* **12,** 181. doi:10.1088/0957-4484/12/2/323 (2001).

33. Wedge, C. J. *et al.* Chemical engineering of molecular qubits. *Physical Review Letters* **108,** 107204. doi:10.1103/PhysRevLett.108.107204 (2012).

34. Ardavan, A. *et al.* Will spin-relaxation times in molecular magnets permit quantum information processing? *Physical Review Letters* **98,** 057201. doi:10.1103/PhysRevLett.98.057201 (2007).

35. Gaita-Ariño, A., Luis, F., Hill, S. & Coronado, E. Molecular spins for quantum computation. *Nature Chemistry* **11,** 301–309. doi:10.1038/s41557-019-0232-y (2019).

36. Wasielewski, M. R. *et al.* Exploiting chemistry and molecular systems for quantum information science. *Nature Reviews Chemistry* **4,** 490–504. doi:10.1038/s41570-020-0200-5 (2020).

37. Lim, S., Liu, J. & Ardavan, A. Fault-tolerant qubit encoding using a spin-7/2 qudit. *Physical Review A* **108,** 62403. doi:10.1103/PhysRevA.108.062403 (2023).

38. DiVincenzo, D. P. The Physical Implementation of Quantum Computation. *Fortschritte der Physik* **48,** 771–783. doi:10.1002/1521-3978(200009)48:9/11<771::AID-PROP771>3.0.CO;2-E (2000).

39. Zadrozny, J. M., Niklas, J., Poluektov, O. G. & Freedman, D. E. Millisecond coherence time in a tunable molecular electronic spin qubit. *ACS Central Science* **1,** 488–492. doi:10.1021/acscentsci.5b00338 (2015).

40. Atzori, M. *et al.* Quantum Coherence Times Enhancement in Vanadium(IV)-based Potential Molecular Qubits: The Key Role of the Vanadyl Moiety. *Journal of the American Chemical Society* **138,** 11234–11244. doi:10.1021/jacs.6b05574 (2016).

41. Shiddiq, M. *et al.* Enhancing coherence in molecular spin qubits via atomic clock transitions. *Nature* **531,** 348–351. doi:10.1038/nature16984 (2016).

42. Janković, D., Hartmann, J.-G., Ruben, M. & Hervieux, P.-A. Noisy qudit vs multiple qubits: conditions on gate efficiency for enhancing fidelity. *npj Quantum Information* **10,** 59. doi:10.1038/s41534-024-00829-6 (2024).

43. George, R. E., Edwards, J. P. & Ardavan, A. Coherent Spin Control by Electrical Manipulation of the Magnetic Anisotropy. *Physical Review Letters* **110,** 27601. doi:10.1103/PhysRevLett.110.027601 (2013).

44. Kane, B. E. A silicon-based nuclear spin quantum computer. *Nature* **393,** 133–137. doi:10.1038/30156 (1998).

45. Bardin, J. C., Slichter, D. H. & Reilly, D. J. Microwaves in Quantum Computing. *IEEE Journal of Microwaves* **1,** 403–427. doi:10.1109/JMW.2020.3034071 (2021).

46. Baumann, S. *et al.* Electron paramagnetic resonance of individual atoms on a surface. *Science* **350,** 417–420. doi:10.1126/science.aac8703 (2015).

47. Manipatruni, S. *et al.* Scalable energy-efficient magnetoelectric spin–orbit logic. *Nature* **565,** 35–42. doi:10.1038/s41586-018-0770-2 (2019).

48. Long, J. *et al.* Room temperature magnetoelectric coupling in a molecular ferroelectric ytterbium(III) complex. *Science* **367,** 671–676. doi:10.1126/science.aaz2795 (2020).

49. Spaldin, N. A. Multiferroics beyond electric-field control of magnetism. *Proceedings of the Royal Society A: Mathematical, Physical and Engineering Sciences* **476,** 20190542. doi:10.1098/rspa.2019.0542 (2020).

50. Yang, Y., Hong, L., Bellaiche, L. & Xiang, H. Toward Ultimate Memory with Single-Molecule Multiferroics. *Journal of the American Chemical Society* **145,** 25357–25364. doi:10.1021/jacs.3c09294 (2023).

51. Liu, J. *et al.* Electric Field Control of Spins in Molecular Magnets. *Physical Review Letters* **122,** 037202. doi:10.1103/PhysRevLett.122.037202 (2019).

52. Liu, J. *et al.* Coherent electric field manipulation of Fe3+ spins in PbTiO3. *Science Advances* **7,** eabf8103. doi:10.1126/sciadv.abf8103 (2021).

53. Mims, W. B. *The linear electric field effect in paramagnetic resonance* (Oxford University Press, 1976).

54. Trif, M., Troiani, F., Stepanenko, D. & Loss, D. Spin-electric coupling in molecular magnets. *Physical Review Letters* **101,** 217201. doi:10.1103/PhysRevLett.101.217201 (2008).

55. Liu, J. *et al.* Quantum coherent spin–electric control in a molecular nanomagnet at clock transitions. *Nature Physics* **17,** 1205–1209. doi:10.1038/s41567-021-01355-4 (2021).

56. Sato, K. *et al.* Implementation of molecular spin quantum computing by pulsed ENDOR technique: Direct observation of quantum entanglement and spinor. *Physica E: Low-Dimensional Systems and Nanostructures* **40,** 363–366. doi:10.1016/j.physe.2007.06.031 (2007).

57. Thiele, S. *et al.* Electrically driven nuclear spin resonance in single-molecule magnets. *Science* **344,** 1135–1138. doi:10.1126/science.1249802 (2014).

58. Godfrin, C. *et al.* Operating Quantum States in Single Magnetic Molecules: Implementation of Grover's Quantum Algorithm. *Physical Review Letters* **119,** 187702. doi:10.1103/PhysRevLett.119.187702 (2017).

59. Preskill, J. Quantum Computing in the NISQ era and beyond. *Quantum* **2,** 79. doi:10.22331/q-2018-08-06-79 (2018).

60. Noiri, A. *et al.* Fast universal quantum gate above the fault-tolerance threshold in silicon. *Nature* **601,** 338–342. doi:10.1038/s41586-021-04182-y (2022).

61. Xue, X. *et al.* Quantum logic with spin qubits crossing the surface code threshold. *Nature* **601,** 343–347. doi:10.1038/s41586-021-04273-w (2022).

62. Yoneda, J. *et al.* A quantum-dot spin qubit with coherence limited by charge noise and fidelity higher than 99.9%. *Nature Nanotechnology* **13,** 102–106. doi:10.1038/s41565-017-0014-x (2018).

63. Yang, C. H. *et al.* Silicon qubit fidelities approaching incoherent noise limits via pulse engineering. *Nature Electronics* **2,** 151–158. doi:10.1038/s41928-019-0234-1 (2019).

64. Arute, F. *et al.* Quantum supremacy using a programmable superconducting processor. *Nature* **574,** 505–510. doi:10.1038/s41586-019-1666-5 (2019).

65. Wu, Y. *et al.* Strong Quantum Computational Advantage Using a Superconducting Quantum Processor. *Physical Review Letters* **127,** 180501. doi:10.1103/PhysRevLett.127.180501 (2021).

66. Preskill, J. *Quantum computing 40 years later* (2023). arXiv: 2106.10522.

67. Terhal, B. M. Quantum error correction for quantum memories. *Reviews of Modern Physics* **87,** 307–346. doi:10.1103/RevModPhys.87.307 (2015).

68. Gottesman, D. *Stabilizer Codes and Quantum Error Correction* (1997). arXiv: quant-ph/9705052.

69. DiVincenzo, D. P. & Shor, P. W. Fault-Tolerant Error Correction with Efficient Quantum Codes. *Physical Review Letters* **77,** 3260–3263. doi:10.1103/PhysRevLett.77.3260 (1996).

70. Laflamme, R., Miquel, C., Paz, J. P. & Zurek, W. H. Perfect Quantum Error Correcting Code. *Physical Review Letters* **77,** 198–201. doi:10.1103/PhysRevLett.77.198 (1996).

71. Knill, E. & Laflamme, R. Theory of quantum error-correcting codes. *Physical Review A - Atomic, Molecular, and Optical Physics* **55,** 900–911. doi:10.1103/PhysRevA.55.900 (1997).

72. Knill, E., Laflamme, R., Martinez, R. & Tseng, C.-H. An algorithmic benchmark for quantum information processing. *Nature* **404,** 368–370. doi:10.1038/35006012 (2000).

73. Dennis, E., Kitaev, A., Landahl, A. & Preskill, J. Topological quantum memory. *Journal of Mathematical Physics* **43,** 4452–4505. doi:10.1063/1.1499754 (2002).

74. Google Quantum AI. Exponential suppression of bit or phase errors with cyclic error correction. *Nature* **595,** 383–387. doi:10.1038/s41586-021-03588-y (2021).

75. Gottesman, D., Kitaev, A. & Preskill, J. Encoding a qubit in an oscillator. *Physical Review A - Atomic, Molecular, and Optical Physics* **64,** 012310. doi:10.1103/PhysRevA.64.012310 (2001).

76. Pirandola, S., Mancini, S., Braunstein, S. L. & Vitali, D. Minimal qudit code for a qubit in the phase-damping channel. *Physical Review A - Atomic, Molecular, and Optical Physics* **77,** 032309. doi:10.1103/PhysRevA.77.032309 (2008).

77. Noh, K., Girvin, S. M. & Jiang, L. Encoding an Oscillator into Many Oscillators. *Physical Review Letters* **125,** 080503. doi:10.1103/PhysRevLett.125.080503 (2020).

78. Albert, V. V., Covey, J. P. & Preskill, J. Robust Encoding of a Qubit in a Molecule. *Physical Review X* **10,** 031050. doi:10.1103/PhysRevX.10.031050 (2020).

79. Royer, B., Singh, S. & Girvin, S. M. Stabilization of Finite-Energy Gottesman-Kitaev-Preskill States. *Physical Review Letters* **125,** 260509. doi:10.1103/PhysRevLett.125.260509 (2020).

80. Hu, L. *et al.* Quantum error correction and universal gate set operation on a binomial bosonic logical qubit. *Nature Physics* **15,** 503–508. doi:10.1038/s41567-018-0414-3 (2019).

81. Flühmann, C. & Home, J. P. Direct Characteristic-Function Tomography of Quantum States of the Trapped-Ion Motional Oscillator. *Physical Review Letters* **125,** 043602. doi:10.1103/PhysRevLett.125.043602 (2020).

82. Ofek, N. *et al.* Extending the lifetime of a quantum bit with error correction in superconducting circuits. *Nature* **536,** 441–445. doi:10.1038/nature18949 (2016).

83. Campagne-Ibarcq, P. *et al.* Quantum error correction of a qubit encoded in grid states of an oscillator. *Nature* **584,** 368–372. doi:10.1038/s41586-020-2603-3 (2020).

84. Heeres, R. W. *et al.* Implementing a universal gate set on a logical qubit encoded in an oscillator. *Nature Communications* **8,** 94. doi:10.1038/s41467-017-00045-1 (2017).

85. Gertler, J. M. *et al.* Protecting a bosonic qubit with autonomous quantum error correction. *Nature* **590,** 243–248. doi:10.1038/s41586-021-03257-0 (2021).

86. Chiesa, A. *et al.* Molecular Nanomagnets as Qubits with Embedded Quantum-Error Correction. *The Journal of Physical Chemistry Letters* **11,** 8610–8615. doi:10.1021/acs.jpclett.0c02213 (2020).

87. Semeghini, G. *et al.* Probing topological spin liquids on a programmable quantum simulator. *Science* **374,** 1242–1247. doi:10.1126/science.abi8794 (2021).

88. Mi, X. *et al.* Time-crystalline eigenstate order on a quantum processor. *Nature* **601,** 531–536. doi:10.1038/s41586-021-04257-w (2022).

89. Weil, J. A. & Bolton, J. R. *Electron paramagnetic resonance: elementary theory and practical applications* 2nd ed. (Wiley, Hoboken, N.J, 2007).

90. Schweiger, A. & Jeschke, G. *Principles of pulse electron paramagnetic resonance* (Oxford University Press, Oxford, 2001).

91. Abragam, A. & Bleaney, B. *Electron paramagnetic resonance of transition ions* (Oxford University Press, Oxford, 2012 - 1970).

92. Griffiths, D. J. & Schroeter, D. F. *Introduction to quantum mechanics* Third edition. (Cambridge University Press, Cambridge, 2018).

93. Binney, J. *The physics of quantum mechanics* (ed Skinner, D.) (Oxford University Press, Oxford, 2015).

94. Slichter, C. P. *Principles of magnetic resonance* 3rd ed. (Springer, Berlin, 1990).

95. Levitt, M. H. *Spin dynamics: basics of nuclear magnetic resonance* Second edition (John Wiley & Sons, Chichester, England, 2008).

96. Cory, D. G., Fahmy, A. F. & Havel, T. F. Ensemble quantum computing by NMR spectroscopy. *Proceedings of the National Academy of Sciences* **94,** 1634–1639. doi:10.1073/pnas.94.5.1634 (1997).

97. Eaton, S. S. & Eaton, G. R. Relaxation Times of Organic Radicals and Transition Metal Ions. in *Distance Measurements in Biological Systems by EPR* (eds Berliner, L. J., Eaton, S. S. & Eaton, G. R.) 29–154 (Springer US, Boston, MA, 2002).

98. Keeler, J. *Understanding NMR spectroscopy* 2nd ed. (John Wiley and Sons, Chichester, U.K, 2010).

99. Kuprov, I. *Spin: From Basic Symmetries to Quantum Optimal Control* 1st ed. (Springer International Publishing AG, Cham, 2023).

100. Redfield, A. G. Nuclear Magnetic Resonance Saturation and Rotary Saturation in Solids. *Physical Review* **98,** 1787–1809. doi:10.1103/PhysRev.98.1787 (1955).

101. Freeman, R., Frenkiel, T. A. & Levitt, M. H. Composite Z pulses. *Journal of Magnetic Resonance (1969)* **44,** 409–412. doi:10.1016/0022-2364(81)90181-5 (1981).

102. Mims, W. B. Electron Echo Methods in Spin Resonance Spectrometry. *Review of Scientific Instruments* **36,** 1472–1479. doi:10.1063/1.1719359 (1965).

103. Schenzle, A., Wong, N. C. & Brewer, R. G. Theorem on coherent transients. *Physical Review A* **22,** 635–637. doi:10.1103/PhysRevA.22.635 (1980).

104. Mossberg, T. W. & Hartmann, S. R. Coherent transients theorem: A comment. *Physical Review A* **24,** 2247–2249. doi:10.1103/PhysRevA.24.2247 (1981).

105. Stoll, S. & Schweiger, A. EasySpin, a comprehensive software package for spectral simulation and analysis in EPR. *Journal of Magnetic Resonance* **178,** 42–55. doi:10.1016/j.jmr.2005.08.013 (2006).

106. Gemperle, C. & Schweiger, A. Pulsed electron-nuclear double resonance methodology. *Chemical Reviews* **91,** 1481–1505. doi:10.1021/cr00007a011 (1991).

107. Davies, E. R. A new pulse endor technique. *Physics Letters A* **47,** 1–2. doi:10.1016/0375-9601(74)90078-4 (1974).

108. Mims, W. B. Pulsed endor experiments. *Proceedings of the Royal Society of London* **283,** 452–457. doi:10.1098/rspa.1965.0034 (1965).

109. Weber, R. T. *E 560-P User's Manual* version 2.0. Bruker BioSpin Corporation (May 2008). 258 pp.

110. Morton, J. J. L. *et al.* Solid-state quantum memory using the 31P nuclear spin. *Nature* **455,** 1085–1088. doi:10.1038/nature07295 (2008).

111. Brown, R. M. *et al.* Coherent State Transfer between an Electron and Nuclear Spin in ^{15}N@C$_{60}$. *Physical Review Letters* **106,** 110504. doi:10.1103/PhysRevLett.106.110504 (2011).

112. Wolfowicz, G. *et al.* Coherent Storage of Microwave Excitations in Rare-Earth Nuclear Spins. *Physical Review Letters* **114,** 170503. doi:10.1103/PhysRevLett.114.170503 (2015).

113. Mims, W. B. Measurement of the linear electric field effect in EPR using the spin echo method. *Review of Scientific Instruments* **45,** 1583–1591. doi:10.1063/1.1686567 (1974).

114. Blundell, S. *Magnetism in condensed matter* (Oxford University Press, Oxford, 2001).

115. Poole, C. P. *Electron spin resonance: a comprehensive treatise on experimental techniques* 2nd ed. (Wiley, New York, 1983).

116. Marki, F. & Marki, C. *Mixer basic primer. A tutorial for RF & microwave mixers* tech. rep. (Marki microwave, Inc, 215 Vineyard Court, Morgan Hill, CA 95037, 2010).

117. *MODEL SR830 DSP Lock-In Amplifier* 2.5. Standford Research Systems (1290-D Reamwood Avenue, Sunnyvale, California 94089, 2011).

118. Jorgesen, D. *IQ, IMAGE REJECT & single sideband Mixer Primer* tech. rep. (Marki microwave, Inc, 215 Vineyard Court, Morgan Hill, CA 95037, 2018).

119. Coey, J. M. D. *Magnetism and magnetic materials* (Cambridge University Press, 2010).

120. Pozar, D. M. *Microwave engineering* 4th ed. (Wiley, Hoboken, N.J., 2012).

121. Tseitlin, M., Quine, R. W., Rinard, G. A., Eaton, S. S. & Eaton, G. R. Combining absorption and dispersion signals to improve signal-to-noise for rapid-scan EPR imaging. *Journal of Magnetic Resonance* **203,** 305–310. doi:10.1016/j.jmr.2010.01.013 (2010).

122. Eaton, G. R. *Quantitative EPR* 1st ed. 2010. (Springer, New York, 2010).

123. Abe, E., Wu, H., Ardavan, A. & Morton, J. J. L. Electron spin ensemble strongly coupled to a three-dimensional microwave cavity. *Applied Physics Letters* **98,** 251108. doi:10.1063/1.3601930 (2011).

124. Mergenthaler, M. *et al.* Strong Coupling of Microwave Photons to Antiferromagnetic Fluctuations in an Organic Magnet. *Physical Review Letters* **119,** 147701. doi:10.1103/PhysRevLett.119.147701 (2017).

125. Griffiths, D. J. *Introduction to electrodynamics* Fifth edition. (Cambridge University Press, Cambridge, 2024).

126. Vaganov, M. V. *et al.* Chemical tuning of quantum spin–electric coupling in molecular magnets. *Nature Chemistry.* doi:10.1038/s41557-025-01926-5 (2025).

127. Ruamps, R. *et al.* Giant Ising-Type Magnetic Anisotropy in Trigonal Bipyramidal Ni(II) Complexes: Experiment and Theory. *Journal of the American Chemical Society* **135,** 3017–3026. doi:10.1021/ja308146e (2013).

128. Ruamps, R. *et al.* Ising-type magnetic anisotropy and single molecule magnet behaviour in mononuclear trigonal bipyramidal Co(ii) complexes. *Chemical Science* **5,** 3418–3424. doi:10.1039/C4SC00984C (2014).

129. Rubín-Osanz, M. *et al.* Chemical tuning of spin clock transitions in molecular monomers based on nuclear spin-free Ni(ii). *Chemical Science* **12,** 5123–5133. doi:10.1039/D0SC05856D (2021).

130. Glerup, J. & Weihe, H. Magnetic Susceptibility and EPR Spectra of (μ-Hydroxo)bis[pentaamminechromium(III)] Chloride Monohydrate. *Inorganic Chemistry* **36,** 2816–2819. doi:10.1021/ic970029c (1997).

131. Fang, Y.-H. *et al.* Spin-Electric Coupling with Anisotropy-Induced Vanishment and Enhancement in Molecular Ferroelectrics. *Journal of the American Chemical Society* **144,** 8605–8612. doi:10.1021/jacs.2c00484 (2022).

132. Kiel, A. & Mims, W. B. Electric field shift in electron paramagnetic resonance for Mn2+ in CaWO4. *Physical Review* **153,** 378–385. doi:10.1103/PhysRev.153.378 (1967).

133. Kiel, A. & Mims, W. B. Electric field effect in paramagnetic resonance for Mn2+ in SrWO4. *Physical Review B* **3,** 2878–2884. doi:10.1103/PhysRevB.3.2878 (1971).

134. Kiel, A., Mims, W. B. & Masuhr, G. J. Electric field effect in paramagnetic resonance for Mn2+ in PbMoO4. *Physical Review B* **7,** 1735–1739. doi:10.1103/PhysRevB.7.1735 (1973).

135. Pedersen, K. S. *et al.* Design of Single-Molecule Magnets: Insufficiency of the Anisotropy Barrier as the Sole Criterion. *Inorganic Chemistry* **54,** 7600–7606. doi:10.1021/acs.inorgchem.5b01209 (2015).

136. Bernhardt, P. V., Flanagan, B. M. & Riley, M. J. Completion of the isomorphous Ln(trensal) series. *Australian Journal of Chemistry* **54,** 229–232. doi:10.1071/CH01076 (2001).

137. Pedersen, K. S. *et al.* Modifying the properties of 4f single-ion magnets by peripheral ligand functionalisation. *Chemical Science* **5,** 1650–1660. doi:10.1039/C3SC53044B (4 2014).

138. Pedersen, K. S. *et al.* Toward Molecular 4f Single-Ion Magnet Qubits. *Journal of the American Chemical Society* **138,** 5801–5804. doi:10.1021/jacs.6b02702 (2016).

139. Bode, B. E. *et al.* Dipolar-Coupled Entangled Molecular 4f Qubits. *Journal of the American Chemical Society* **145,** 2877–2883. doi:10.1021/jacs.2c10902 (2023).

140. Ullah, A., Hu, Z., Cerdá, J., Aragó, J. & Gaita-Ariño, A. Electrical two-qubit gates within a pair of clock-qubit magnetic molecules. *npj Quantum Information* **8,** 133. doi:10.1038/s41534-022-00647-8 (2022).

141. Rudowicz, C. & Chung, C. Y. The generalization of the extended Stevens operators to higher ranks and spins, and a systematic review of the tables of the tensor operators and their matrix elements. *Journal of Physics: Condensed Matter* **16,** 5825. doi:10.1088/0953-8984/16/32/018 (2004).

142. Hussain, R. *et al.* Coherent Manipulation of a Molecular Ln-Based Nuclear Qudit Coupled to an Electron Qubit. *Journal of the American Chemical Society* **140,** 9814–9818. doi:10.1021/jacs.8b05934 (2018).

143. Rollano, V. *et al.* High cooperativity coupling to nuclear spins on a circuit quantum electrodynamics architecture. *Communications Physics* **5,** 246. doi:10.1038/s42005-022-01017-8 (2022).

144. Chicco, S. *et al.* Proof-of-Concept Quantum Simulator Based on Molecular Spin Qudits. *Journal of the American Chemical Society* **146,** 1053–1061. doi:10.1021/jacs.3c12008 (2024).

145. Hansen, S. H. *et al.* Probing decoherence in molecular 4f qubits. *Chemical Science* **15,** 20328–20337. doi:10.1039/D4SC05304D (2024).

146. Morrillo, W. T., Cumming, H. I. J., Mattioni, A., Staab, J. K. & Chilton, N. F. Ab Initio Design of Molecular Qubits with Electric Field Control. *Journal of the American Chemical Society* **146,** 25841–25851. doi:10.1021/jacs.4c09109 (2024).

147. Lim, S., Vaganov, M. V., Liu, J. & Ardavan, A. Demonstrating Experimentally the Encoding and Dynamics of an Error-Correctable Logical Qubit on a Hyperfine-Coupled Nuclear Spin Qudit. *Physical Review Letters* **134,** 70603. doi:10.1103/PhysRevLett.134.070603 (2025).

148. DiVincenzo, D. P. Quantum gates and circuits. *Proceedings of the Royal Society of London. Series A: Mathematical, Physical and Engineering Sciences* **454,** 261–276. doi:10.1098/rspa.1998.0159 (1998).

149. Lidar, D. A., Chuang, I. L. & Whaley, K. B. Decoherence-Free Subspaces for Quantum Computation. *Physical Review Letters* **81,** 2594–2597. doi:10.1103/PhysRevLett.81.2594 (1998).

150. Vincent, R., Klyatskaya, S., Ruben, M., Wernsdorfer, W. & Balestro, F. Electronic read-out of a single nuclear spin using a molecular spin transistor. *Nature* **488,** 357–360. doi:10.1038/nature11341 (2012).

151. Sigillito, A. J., Tyryshkin, A. M., Schenkel, T., Houck, A. A. & Lyon, S. A. All-electric control of donor nuclear spin qubits in silicon. *Nature Nanotechnology* **12,** 958–962. doi:10.1038/nnano.2017.154 (2017).

152. Omanakuttan, S., Mitra, A., Martin, M. J. & Deutsch, I. H. Quantum optimal control of ten-level nuclear spin qudits in ^{87}Sr. *Physical Review A* **104,** L060401. doi:10.1103/PhysRevA.104.L060401 (2021).

153. Sturgeon, B. E., Ball, J. A., Randall, D. W. & Britt, R. D. 55Mn Electron Spin Echo ENDOR of Mn2+ Complexes. *The Journal of Physical Chemistry* **98,** 12871–12883. doi:10.1021/j100100a012 (1994).

154. Böttcher, R. *et al.* 55Mn pulsed ENDOR spectroscopy of Mn2+ ions in ZnO thin films and single crystal. *Journal of Magnetic Resonance* **245,** 79–86. doi:10.1016/j.jmr.2014.05.012 (2014).

155. Gershenfeld, N. A. & Chuang, I. L. Bulk Spin-Resonance Quantum Computation. *Science* **275,** 350–356. doi:10.1126/science.275.5298.350 (1997).

156. Knill, E., Chuang, I. & Laflamme, R. Effective pure states for bulk quantum computation. *Physical Review A* **57,** 3348–3363. doi:10.1103/PhysRevA.57.3348 (1998).

157. Vitanov, N. V. Dynamical rephasing of ensembles of qudits. *Physical Review A* **92,** 22314. doi:10.1103/PhysRevA.92.022314 (2015).

158. Gross, J. A. Designing Codes around Interactions: The Case of a Spin. *Physical Review Letters* **127,** 10504. doi:10.1103/PhysRevLett.127.010504 (2021).

159. Suaud, N. *et al.* Playing with Magnetic Anisotropy in Hexacoordinated Mononuclear Ni(II) Complexes, An Interplay Between Symmetry and Geometry. *Applied Magnetic Resonance* **51,** 1215–1231. doi:10.1007/s00723-020-01228-8 (2020).

160. Duboc, C. *et al.* Origin of the Zero-Field Splitting in Mononuclear Octahedral Dihalide MnII Complexes: An Investigation by Multifrequency High-Field Electron Paramagnetic Resonance and Density Functional Theory. *Inorganic Chemistry* **46,** 4905–4916. doi:10.1021/ic0623841 (2007).

161. Tchougréeff, A. L. & Dronskowski, R. Nephelauxetic effect revisited. *International Journal of Quantum Chemistry* **109,** 2606–2621. doi:10.1002/qua.21989 (2009).